WAVE PROPAGATION IN METAMATERIAL STRUCTURES AND RETRIEVAL OF HOMOGENIZATION PARAMETERS

A THESIS

SUBMITTED TO THE DEPARTMENT OF ELECTRICAL AND

ELECTRONICS ENGINEERING

AND THE INSTITUTE OF ENGINEERING AND SCIENCES

OF BILKENT UNIVERSITY

IN PARTIAL FULFILLMENT OF THE REQUIREMENTS

FOR THE DEGREE OF

MASTER OF SCIENCE

By

Erdinç Ircı

August 2007

I certify that I have read this thesis and that in my opinion it is fully adequate, in scope and in quality, as a thesis for the degree of Master of Science.

Assist. Prof. Dr. Vakur B. Ertürk(Supervisor)

I certify that I have read this thesis and that in my opinion it is fully adequate, in scope and in quality, as a thesis for the degree of Master of Science.

Prof. Dr. Ayhan Altıntaş

I certify that I have read this thesis and that in my opinion it is fully adequate, in scope and in quality, as a thesis for the degree of Master of Science.

Assoc. Prof. Dr. Özlem Aydın Çivi

Approved for the Institute of Engineering and Sciences:

Prof. Dr. Mehmet Baray
Director of Institute of Engineering and Sciences

ABSTRACT

WAVE PROPAGATION IN METAMATERIAL STRUCTURES AND RETRIEVAL OF HOMOGENIZATION PARAMETERS

Erdinç Ircı
M.S. in Electrical and Electronics Engineering
Supervisor: Assist. Prof. Dr. Vakur B. Ertürk
August 2007

Electromagnetic wave propagation in metamaterial structures (metamaterial slabs, metamaterial cylinders, metamaterial coated conducting cylinders etc.) are investigated. Scattered and transmitted electromagnetic fields by these structures due to electric line sources or plane wave illuminations are found. A generic formulation of these wave propagation problems is done, enabling any kind of metamaterial or conventional material to be used, having any sign combination of constitutive parameters and having any electric and/or magnetic losses.

For one of these propagation problems i.e., metamaterial coated conducting cylinders illuminated normally with plane waves, achieving transparency and maximizing scattering are investigated thoroughly. It is found out that, rigorous derivation of transparency and resonance (scattering maximization) conditions for PEC core cylinder case under the sub-wavelength limitations yields the same conditions of two electrically small concentric layers of conjugately paired cylinders, given in the literature (when the inner core layer is also taken to the PEC limit). These transparency and resonance conditions are found to be heavily

dependent on the permittivity of the metamaterial coating (for TE polarization) and the ratio of core-shell radii. The relations between the permittivity of the coating and the ratio of core-shell radii are investigated for achieving transparency and scattering maximization. Numerical results show that these analytical relations are quite successful and work better when the cylindrical scatter is electrically very small.

A novel homogenization method for the retrieval of effective constitutive parameters of metamaterials is proposed and implemented. The method is based on the simple idea that the total reflection coefficient from a finite metamaterial structure has to resemble the reflection from an homogeneous equivalent. While implementing the method, 1, 2, ..., 20 unit cells of the same metamaterial structure are stacked and their reflection coefficients are collected. The homogenization quality of the metamaterial is evaluated in terms of various factors, which showed that the method is very successful to retrieve the effective constitutive parameters of the metamaterial.

Finally, another method has been proposed for the retrieval of surface wave propagation constants on any periodic or non-periodic grounded slab medium. As a preliminary, the method is applied to grounded dielectric slabs. The numerical results generally show good agreement with their theoretical counterparts.

Keywords: Metamaterials, Wave propagation, Scattering, Transmission, Metamaterial cylinders, Metamaterial coated conducting cylinders, Transparency, Resonance, Radar cross section, Homogenization, Parameter retrieval, Surface waves, Grounded Slabs.

ÖZET

METAMALZEME YAPILARDA DALGA YAYINIMI VE HOMOJENLEŞTİRME PARAMETRELERİNİN ELDE EDİLMESİ

Erdinç Ircı
Elektrik ve Elektronik Mühendisliği Bölümü Yüksek Lisans
Tez Yöneticisi: Yar. Doç. Dr. Vakur B. Ertürk
Ağustos 2007

Metamalzeme yapılarda (metamalzeme tabakalar, metamalzeme silindirler, metamalzeme kaplı iletken silindirler vb.) elektromanyetik dalga yayınımı incelendi. Çizgisel elektrik kaynaklarından ya da düzlem dalga aydınlatmalarından dolayı bu yapılardan saçılan ve bunlara iletilen elektromanyetik alanlar bulundu. Bu dalga yayınım problemlerinin genel formülasyonu, ortam parametrelerinin işaretlerinin herhangi kombinasyonu için, herhangi elektrik/manyetik kayba da sahip olabilecek şekilde metamalzemeler ya da sıradan malzemeler için yapıldı.

Bu yayınım problemlerinden biri olan düzlem dalga ile dik aydınlatılmış metamalzeme kaplı iletken silindirler, saydamlık ve saçılımın azamileştirilmesi açısından detaylıca incelendi. Saydamlık ve rezonans (saçılım azamileştirmesi) durumlarının dalgaboyu-altı sınırında türetilmesi, literatürdeki aynı eksenli, elektriksel olarak küçük, ters işaretli olarak eşleştirilmiş silindirlerle aynı durumu verdi (iç silindir iletken sınırına götürüldüğünde).

Bu saydamlık ve rezonans durumlarının daha çok metamalzeme kaplamanın elektriksel geçirgenliğine (TE polarizasyonu için) ve çekirdek-kaplama yarıçap

oranına bağlı olduğu bulundu. Saydamlık ve saçılım azamileştirmesi için, kaplamanın elektrik geçirgenliği ile çekirdek-kaplama yarıçap oranı arasındaki ilişkiler incelendi. Sayısal sonuçlar bu analitik ilişkilerin oldukça başarılı olduğunu ve silindirik saçıcı elektriksel olarak çok küçükken daha iyi çalıştığını gösterdi.

Metamalzemelerin etkin ortam parametrelerinin elde edilmesi için yeni bir homojenleştirme metodu ileri sürüldü ve uygulandı. Metod, sonlu bir metamalzeme yapının toplam yansıma katsayısının homojen denginin yansımasına benzeyeceği fikrine dayandırıldı. Metod uygulanırken metamalzemenin 1, 2, ..., 20 ünite hücresi art arda sıralandı ve yansıma katsayıları kaydedildi. Metamalzemenin homojenleştirme kalitesi değişik etkenler cinsinden incelendi ve metodun metamalzemenin etkin ortam parametrelerinin elde edilmesi için çok başarılı olduğu gözüktü.

Son olarak, bir başka metod da periyodik olan ya da olmayan herhangi bir topraklanmış tabaka üzerindeki yüzey dalga yayınım katsayılarının elde edilmesi için ileri sürüldü. Başlangıç olarak metod topraklanmış dielektrik tabakalara uygulandı. Sayısal sonuçlar genel olarak teorik karşılıklarıyla iyi uyum sergiledi.

Anahtar Kelimeler: Metamalzemeler, Dalga yayınımı, Saçılım, İletim, Metamalzeme silindirler, Metamalzeme kaplı iletken silindirler, Saydamlık, Rezonans, Radar kesit alanı, Homojenleştirme, Parametre elde edimi, Yüzey dalgaları, Topraklanmış tabakalar.

ACKNOWLEDGMENTS

I would like to express my sincere gratitude to my supervisor Asst. Prof. Vakur B. Ertürk for his invaluable guidance, suggestions, encouragement and support throughout the development of this thesis. He has always been a great mentor and teacher to me.

I would like to thank Prof. Ayhan Altıntaş and Assoc. Prof. Özlem Aydın Çivi from METU for being in my jury, reading the thesis and commenting on it.

I would like to thank Prof. M. İrşadi Aksun from Koç University for allowing us to collaborate in his research. Chapter 4 of this thesis is merely realization of his ingenious ideas.

I would also like to thank The Scientific and Technological Research Council of Turkey (TÜBİTAK) for supporting me with the graduate scholarship during my study.

Finally, I would like to thank my family, my friends Celal Alp Tunç, Onur Bakır, Aytaç Alparslan, Burak Güldoğan and many others, whom I can't all list here, for their understanding, encouragement, friendship and support.

Contents

List of Figures

List of Tables

Dedicated to my family.

Chapter 1

INTRODUCTION

Metamaterials are artificially engineered materials which can have negative effective electric permittivity and/or negative effective magnetic permeability. Different from conventional materials, which have both positive electric permittivity and positive magnetic permeability [i.e., double positive (DPS)], metamaterials show different electromagnetic and optical properties. For instance, when electric permittivity and magnetic permeability of the material are both negative [i.e., double negative (DNG)], negative refraction happens and direction of phase velocity is reversed. DNG metamaterials are also called Left Handed Materials (LHM) because electric field, magnetic field and the direction of phase velocity form a left handed coordinate system for these materials. On the other hand, when only one of the constitutive parameters of the metamaterial is negative [i.e., single negative (SNG)] evanescent waves appear.

In Chapter 2, electromagnetic scattering and transmission due to line sources or plane waves from different metamaterial structures is investigated. The metamaterial structures are chosen from simple canonical geometries, such as metamaterial slabs, metamaterial cylinders and metamaterial coated conducting cylinders, which have exact eigenfunction solutions.

After a complex analysis, the correct complex branches for the wave number and wave impedance of a metamaterial medium are selected. This choice of complex branches is found to be valid for all kinds of materials, which can have any combination of signs of constitutive parameters, or can have any electric and/or magnetic losses.

Due to their aforementioned exceptional properties, metamaterials are being investigated for many possible utilizations in different scientific and engineering applications, which otherwise cannot be easily accomplished with conventional materials. Recently, reducing scattering from various structures, and in the limit achieving transparency and building cloaking structures, have been investigated by many researchers [1–7]. On the other hand, resonant structures aimed at increasing the electromagnetic intensities, stored or radiated power levels have also been studied extensively [7–14]. Similarly, metamaterial layers have been proposed to enhance the power radiated by electrically small antennas [15–17].

While some of these studies are based on utilization of non-linear metamaterial structures, some of them rely on pairing slabs, spheres or cylinders with their electromagnetic conjugates (e.g., pairing/coating DPS materials with DNG metamaterials or mu-negative (MNG) metamaterials with epsilon-negative (ENG) metamaterials).

In Chapter 3, the transparency and resonance conditions for cylindrical structures are extended to the case where the core cylinder is particularly PEC. For achieving transparency or maximizing scattering, simple (i.e., homogeneous, isotropic and linear) metamaterial coatings are used. For both transparency and scattering maximization scenarios, the analytical relations between the ratio of core-coating radii and the constitutive parameters of the metamaterial coating are derived. These analytical relations are based on sub-wavelength approximations and they are valid especially when the cylindrical scatterers (i.e., PEC cylinders together with their metamaterial coatings) are electrically small. The

numerical simulations have showed the existence of transparency and resonance conditions in good agreement with the analytical expectations.

Although Chapter 3 is based on the assumptions that the metamaterial coating is homogeneous and isotropic, metamaterials currently produced are inhomogeneous, anisotropic and highly dispersive. However, there are many research efforts to obtain homogeneous and isotropic metamaterials.

Meanwhile, another branch of these research efforts is now focused on retrieval of the effective constitutive parameters of metamaterials, or in other words, obtaining homogeneous equivalents for essentially inhomogeneous metamaterials. The process of obtaining this homogeneous equivalent, with its all intermediate steps, is called homogenization. The homogenization processes present in the literature [18–22] are mainly based on utilization of transmission and reflection characteristics of the metamaterial structures, or field averaging. However, during these attempts for homogenization of metamaterials, usually transmission and reflection properties of only one unit cell of the metamaterial is taken into account. These methods are intrinsically unreliable since the unit cells, which form the metamaterial, are made up of metallic inclusions, which cause very strong electric and magnetic resonances. While using only one or two unit cells of the metamaterial, one loses the valuable information of periodicity of unit cells and their mutual interactions, therefore cannot represent the whole metamaterial structure correctly.

As a remedy to these inadequate methods, in Chapter 4 we present a novel method for the homogenization and parameter retrieval of metamaterials. If a metamaterial slab can be successfully homogenized, its reflection characteristics would mimic those of a homogeneous slab. Since total reflection from a homogeneous slab is the sum of a direct reflection term and other multiple reflection terms due to the waves bouncing inside the slab, with added phase delays, the

total reflection from the metamaterial slab can be written as a sum of exponentials. Also since the phase delays of the multiple reflections inside the slab are dependent on the thickness of the slab, utilization of different number of unit cells will yield different reflection results. Therefore, it becomes possible to obtain the constitutive parameters of a homogeneous medium using the reflection coefficients of the metamaterial medium, made up of different number of unit cells. In our method, we have used 1 to 20 unit cells. After the constitutive parameters are retrieved, the electromagnetic behavior of the metamaterial slab (e.g., its reflection and transmission properties, field distributions inside and outside the metamaterial) is compared with that of the homogeneous equivalent. Our numerical results show very good agreement between these two.

Again in Chapter 4, we aim to present another method for the retrieval of surface wave propagation constants on any periodic or non-periodic grounded slab medium. The method is basically based on the difference in spread factors of space and surface waves propagating on the surface of the slab. Since space wave contribution of the total electric field on the surface of the slab decays faster, multiplying the field data with the proper power of the lateral distance mainly leaves the surface wave contribution, for large lateral distances. The electric field data, then, can be approximated as a summation of complex exponentials, from which one can deduce how many surface wave modes are present and what their propagation constants are. At the present, the method is applied to a dielectric slab, for which the theoretical surface wave propagation constants are well known, and numerical results have shown good agreement to the theory.

In Chapter 5, conclusions of the thesis are drawn. Appendix A contains some properties of Bessel functions. In Appendix B, ϕ components of the magnetic and electric fields of Section 2.9 are derived from their z components. Derivations of the transparency and resonance conditions of Chapter 3 are given in Appendix C

and Appendix D, respectively. Throughout this thesis, an $e^{j\omega t}$ time dependence is assumed and suppressed.

Chapter 2

Wave Propagation in Metamaterial Structures

In this chapter, electromagnetic wave propagation in different metamaterial structures is investigated. The metamaterial geometries are chosen from simple canonical geometries, such that an exact analytical eigenfunction solution can be obtained.

Metamaterials are artificial materials which can have negative effective electric permittivity (ε_{eff}) and/or negative effective magnetic permeability (μ_{eff}). The signs of the aforementioned effective complex constitutive parameters are based on the signs of their real parts, whereas their imaginary parts indicate the presence of electric or magnetic losses, respectively. Therefore, metamaterials form four groups, depending on their constitutive parameters:

- Double Positive (DPS): $Re\{\varepsilon\} > 0$, $Re\{\mu\} > 0$
- Double Negative (DNG): $Re\{\varepsilon\} < 0$, $Re\{\mu\} < 0$
- Mu Negative (MNG): $Re\{\varepsilon\} > 0$, $Re\{\mu\} < 0$
- Epsilon Negative (ENG): $Re\{\varepsilon\} < 0$, $Re\{\mu\} > 0$

DNG metamaterials are also called Left Handed Materials (LHM) due to their unique electromagnetic/optical properties like negative refraction, negative phase velocity and negative Doppler shift, which follow a left hand rule system. MNG and ENG metamaterials are also called Single Negative (SNG) materials, because of the obvious fact that they have either negative effective magnetic permeability or negative effective electric permittivity, respectively.

2.1 Wave Number, Index of Refraction and Wave Impedance of Metamaterial Structures

Without loss of generality, the wave number, index of refraction and wave impedance of a medium are given as

$$k = \omega\sqrt{\mu\varepsilon}, \tag{2.1}$$

$$n = \sqrt{\mu_r\varepsilon_r}, \tag{2.2}$$

$$\eta = \sqrt{\frac{\mu}{\varepsilon}}, \tag{2.3}$$

respectively, where $\omega = 2\pi f$ is the angular frequency, $\mu_r = \mu/\mu_0$ and $\varepsilon_r = \varepsilon/\varepsilon_0$ are the relative constitutive parameters.

The square roots which appear in (2.1)-(2.3) create controversy, especially when DNG materials are considered. Since both constitutive parameters are complex quantities with their real parts being negative, the wave number, index of refraction and wave impedance of the medium heavily depend on which branch of the complex roots is selected. This controversy appeared in the scientific community after the idea of perfect lens [23] and discussions focused on validity of negative refraction and negative phase velocity [24].

The complex electric permittivity and the complex magnetic permeability of a metamaterial medium can be expressed in polar form, respectively, as

$$\varepsilon = |\varepsilon| e^{j\phi_\varepsilon}, \tag{2.4}$$

$$\mu = |\mu| e^{j\phi_\mu}. \tag{2.5}$$

Similarly, the wave number and the wave impedance of the metamaterial coating can be written as

$$k = \omega\sqrt{\mu\varepsilon} = |k| e^{j\phi_k}, \tag{2.6}$$

$$\eta = \sqrt{\mu/\varepsilon} = |\eta| e^{j\phi_\eta}, \tag{2.7}$$

respectively, where

$$|k| = \omega\sqrt{|\mu||\varepsilon|}, \tag{2.8}$$

$$|\eta| = \sqrt{|\mu|/|\varepsilon|}, \tag{2.9}$$

with

$$\phi_k = \frac{1}{2}(\phi_\mu + \phi_\varepsilon), \tag{2.10}$$

$$\phi_\eta = \frac{1}{2}(\phi_\mu - \phi_\varepsilon). \tag{2.11}$$

The choice of branches for the square roots in (2.10)-(2.11) is based on causality in a linear dispersive medium, the wave directions associated with reflection and transmission from the interfaces and the direction of electromagnetic power flow. This choice is given and examined in details in [25] for DNG metamaterials, first introducing infinitesimal electric and magnetic losses (as in the case of metamaterials approximated by Drude and Lorentz medium models [23, 25, 26]) and then deciding on which complex branch gives the physically correct solution. A similar analysis for DPS, MNG and ENG metamaterials [11] show that, the choice of branches for the square roots given in (2.10)-(2.11) still remains valid for these metamaterials. With the assumed $e^{j\omega t}$ time dependence in this thesis, and considering only passive media, the arguments of μ, ε, k and η for different types of metamaterials are tabulated in Table 2.1.

Table 2.1: Arguments of μ, ε, k and η for Different Types of Metamaterials

	ϕ_μ	ϕ_ε	ϕ_k	ϕ_η
DPS	$\left(-\frac{\pi}{2}, 0\right]$	$\left(-\frac{\pi}{2}, 0\right]$	$\left(-\frac{\pi}{2}, 0\right]$	$\left(-\frac{\pi}{4}, \frac{\pi}{4}\right)$
DNG	$\left[-\pi, -\frac{\pi}{2}\right)$	$\left[-\pi, -\frac{\pi}{2}\right)$	$\left[-\pi, -\frac{\pi}{2}\right)$	$\left(-\frac{\pi}{4}, \frac{\pi}{4}\right)$
MNG	$\left[-\pi, -\frac{\pi}{2}\right)$	$\left(-\frac{\pi}{2}, 0\right]$	$\left(-\frac{3\pi}{4}, -\frac{\pi}{4}\right)$	$\left[-\frac{\pi}{2}, 0\right)$
ENG	$\left(-\frac{\pi}{2}, 0\right]$	$\left[-\pi, -\frac{\pi}{2}\right)$	$\left(-\frac{3\pi}{4}, -\frac{\pi}{4}\right)$	$\left(0, \frac{\pi}{2}\right]$

Examination of Table 2.1 shows that for lossless DPS medium, wave number is real and positive. For lossless DNG medium, wave number is real and negative. For lossless DPS and DNG media, wave impedance is real and positive. For lossless MNG and ENG media, the wave number is negative and imaginary, which shows the presence of evanescent waves.

Remark: It is worthwhile to mention that when any of the constitutive parameters of a metamaterial medium is a negative real number, $-\pi$ should be selected as its argument instead of π, as shown in Table 2.1. This becomes important when intrinsic functions in a programming environment are directly used (e.g., `ANGLE`, `ATAN2`).

2.2 Normal Incidence of Plane Waves on a Metamaterial Slab

2.2.1 Introduction

Let us assume that a TEM^z plane wave is traveling in the $+z$ direction. An infinite length metamaterial slab of thickness d is placed between the $z = 0$ and $z = d$ planes in free space, without loss of generality. Here we will investigate the reflection and transmission properties of the metamaterial slab as well as

the waves traveling inside the metamaterial slab. The incident electric field is assumed to be in the $+x$ direction and the incident magnetic field is in $+y$ direction. The problem geometry is depicted in Fig. 2.1.

2.2.2 Problem Geometry

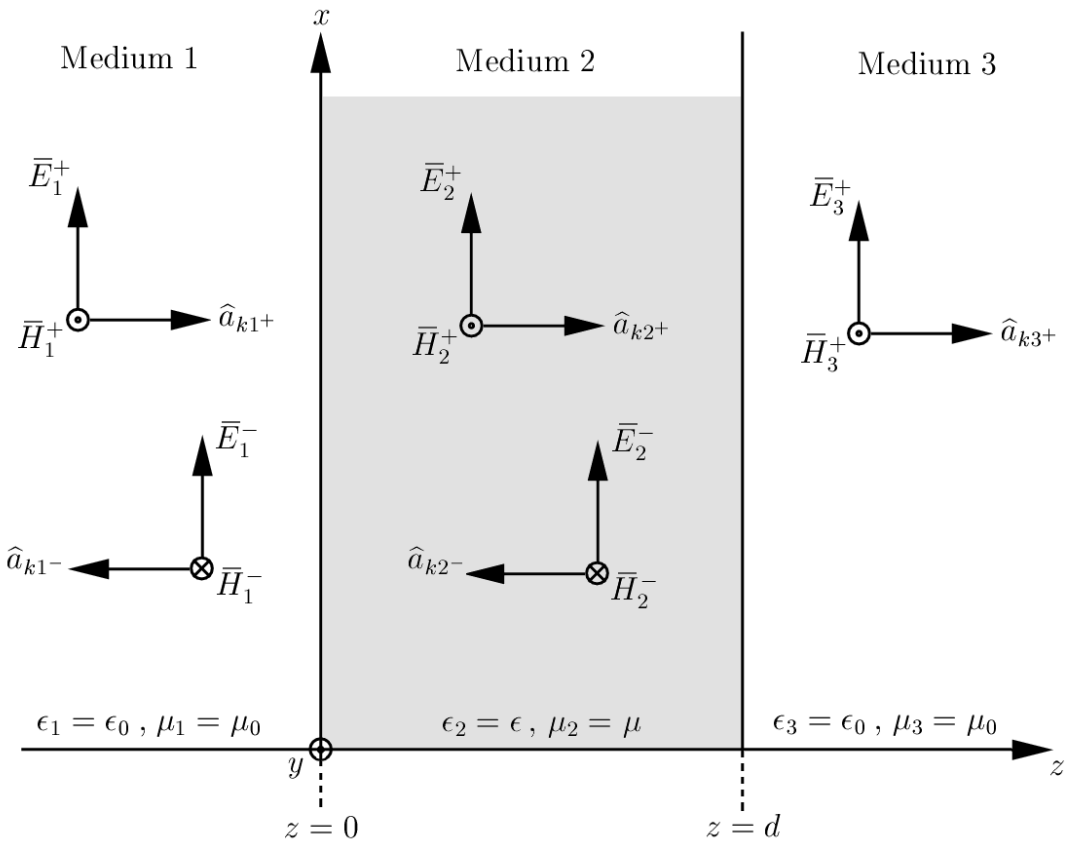

Figure 2.1: Uniform plane wave normally incident on a metamaterial slab.

2.2.3 Electric and Magnetic Fields

The total electric and magnetic fields in Medium 1 are

$$\mathbf{E_1} = \widehat{a}_x \left(E_1^+ e^{-jk_0 z} + E_1^- e^{jk_0 z} \right), \tag{2.12}$$

$$\mathbf{H_1} = \widehat{a}_y \left(\frac{E_1^+}{\eta_0} e^{-jk_0 z} - \frac{E_1^-}{\eta_0} e^{jk_0 z} \right), \tag{2.13}$$

respectively, where $k_0 = \omega\sqrt{\mu_0 \varepsilon_0}$ and $\eta_0 = \sqrt{\mu_0/\varepsilon_0}$.

The total electric and magnetic fields in Medium 2 are

$$\mathbf{E_2} = \widehat{a}_x \left(E_2^+ e^{-jkz} + E_2^- e^{jkz} \right), \tag{2.14}$$

$$\mathbf{H_2} = \widehat{a}_y \left(\frac{E_2^+}{\eta} e^{-jkz} - \frac{E_2^-}{\eta} e^{jkz} \right), \tag{2.15}$$

respectively, where $k = \omega\sqrt{\mu\varepsilon}$ and $\eta = \sqrt{\mu/\varepsilon}$.

The electric and magnetic fields in Medium 3 are

$$\mathbf{E_3} = \widehat{a}_x E_3^+ e^{-jk_0 z}, \tag{2.16}$$

$$\mathbf{H_3} = \widehat{a}_y \frac{E_3^+}{\eta_0} e^{-jk_0 z}, \tag{2.17}$$

respectively, where k_0 and η_0 are the same as in Medium 1.

2.2.4 Solution of Boundary Conditions

Boundary Conditions at $z = 0$:

$$E_1^+ + E_1^- = E_2^+ + E_2^-, \tag{2.18}$$

$$\frac{E_1^+}{\eta_0} - \frac{E_1^-}{\eta_0} = \frac{E_2^+}{\eta} - \frac{E_2^-}{\eta}. \tag{2.19}$$

Boundary Conditions at $z = d$:

$$E_2^+ e^{-jkd} + E_2^- e^{jkd} = E_3^+ e^{-jk_0 d}, \tag{2.20}$$

$$\frac{E_2^+}{\eta} e^{-jkd} - \frac{E_2^-}{\eta} e^{jkd} = \frac{E_3^+}{\eta_0} e^{-jk_0 d}. \tag{2.21}$$

Rearranging equations (2.18) - (2.21) we get:

$$-E_1^- + E_2^+ + E_2^- = E_1^+, \tag{2.22}$$

$$E_1^- + \frac{\eta_0}{\eta} E_2^+ - \frac{\eta_0}{\eta} E_2^- = E_1^+, \tag{2.23}$$

$$e^{-jkd} E_2^+ + e^{jkd} E_2^- - e^{-jk_0 d} E_3^+ = 0, \tag{2.24}$$

$$\frac{e^{-jkd}}{\eta} E_2^+ - \frac{e^{jkd}}{\eta} E_2^- - \frac{e^{-jk_0 d}}{\eta_0} E_3^+ = 0, \tag{2.25}$$

which can also be written in matrix form as follows:

$$\begin{bmatrix} -1 & 1 & 1 & 0 \\ 1 & \frac{\eta_0}{\eta} & -\frac{\eta_0}{\eta} & 0 \\ 0 & e^{-jkd} & e^{jkd} & -e^{-jk_0d} \\ 0 & \frac{e^{-jkd}}{\eta} & -\frac{e^{jkd}}{\eta} & -\frac{e^{-jk_0d}}{\eta_0} \end{bmatrix} \begin{bmatrix} E_1^- \\ E_2^+ \\ E_2^- \\ E_3^+ \end{bmatrix} = \begin{bmatrix} E_1^+ \\ E_1^+ \\ 0 \\ 0 \end{bmatrix}. \tag{2.26}$$

Using Symbolic Math Toolbox of MATLAB, the solution to this system of equations can be found as:

$$E_1^- = \frac{j(\eta^2 - \eta_0^2)\sin kd}{2\eta\eta_0\cos kd + j(\eta^2 + \eta_0^2)\sin kd}\ E_1^+, \tag{2.27}$$

$$E_2^+ = \frac{\eta(\eta + \eta_0)e^{jkd}}{2\eta\eta_0\cos kd + j(\eta^2 + \eta_0^2)\sin kd}\ E_1^+, \tag{2.28}$$

$$E_2^- = \frac{\eta(\eta_0 - \eta)e^{-jkd}}{2\eta\eta_0\cos kd + j(\eta^2 + \eta_0^2)\sin kd}\ E_1^+, \tag{2.29}$$

$$E_3^+ = \frac{2\eta\eta_0 e^{jk_0d}}{2\eta\eta_0\cos kd + j(\eta^2 + \eta_0^2)\sin kd}\ E_1^+. \tag{2.30}$$

Defining

$$\zeta = \frac{\eta}{\eta_0} = \sqrt{\frac{\mu_r}{\varepsilon_r}}, \tag{2.31}$$

and using relation (2.31), equations (2.27)-(2.30) can be reduced to:

$$E_1^- = \frac{j(\zeta^2 - 1)\sin kd}{2\zeta\cos kd + j(\zeta^2 + 1)\sin kd}\ E_1^+, \tag{2.32}$$

$$E_2^+ = \frac{(\zeta^2 + \zeta)e^{jkd}}{2\zeta\cos kd + j(\zeta^2 + 1)\sin kd}\ E_1^+, \tag{2.33}$$

$$E_2^- = \frac{(\zeta - \zeta^2)e^{-jkd}}{2\zeta\cos kd + j(\zeta^2 + 1)\sin kd}\ E_1^+, \tag{2.34}$$

$$E_3^+ = \frac{2\zeta e^{jk_0d}}{2\zeta\cos kd + j(\zeta^2 + 1)\sin kd}\ E_1^+. \tag{2.35}$$

Note that, the solutions (2.27)-(2.30) or (2.32)-(2.35) are valid for all four types of metamaterials (i.e., DPS, DNG, MNG and ENG) provided that k and η are calculated as in Section 2.1.

2.3 Infinite Length Metamaterial Cylinder Near an Infinite Length Electric Line Source: TM^z Polarization

2.3.1 Introduction

An infinite line of constant electric current is placed in the vicinity of a circular metamaterial cylinder of infinite length. The scattering and transmission by the metamaterial cylinder is examined for TM^z polarization. The problem geometry is given in Fig. 2.2.

2.3.2 Problem Geometry

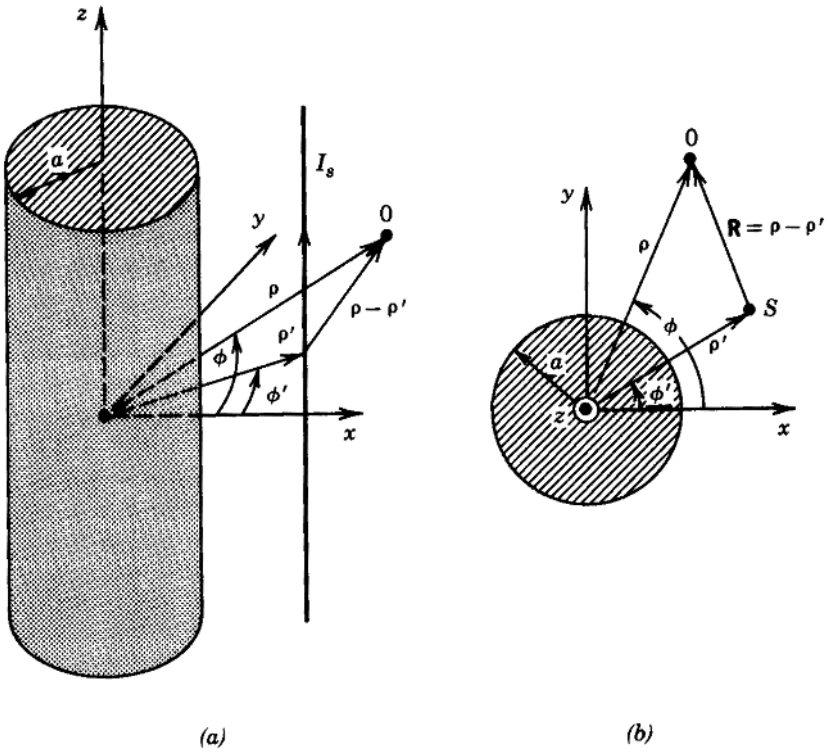

Figure 2.2: Metamaterial cylinder near an electric line source. (a) Side view, (b) Top view.

2.3.3 Electric Line Source and Incident Electric Field

For the line source of constant electric current, I_e, in Fig. 2.2, the electric field generated everywhere by the source in the absence of the cylinder is given as [27]

$$E_z^i = -\frac{k_0^2 I_e}{4\omega\varepsilon_0} H_0^{(2)}(k_0|\bar{\rho} - \bar{\rho}'|), \tag{2.36}$$

which we will refer as the incident electric field. Using the addition theorem for Hankel functions [28], (2.36) can be written in the series expansion form as follows [27]:

$$E_z^i = -\frac{k_0^2 I_e}{4\omega\varepsilon_0} \sum_{n=-\infty}^{+\infty} J_n(k_0\rho) H_n^{(2)}(k_0\rho') e^{jn(\phi-\phi')} \qquad \rho \leq \rho', \tag{2.37}$$

$$E_z^i = -\frac{k_0^2 I_e}{4\omega\varepsilon_0} \sum_{n=-\infty}^{+\infty} J_n(k_0\rho') H_n^{(2)}(k_0\rho) e^{jn(\phi-\phi')} \qquad \rho \geq \rho'. \tag{2.38}$$

2.3.4 Scattered and Transmitted Electric Fields

Similar to the incident field expressions in (2.37) and (2.38), we will define the scattered and transmitted electric fields in series expansion form, respectively as

$$E_z^s = -\frac{k_0^2 I_e}{4\omega\varepsilon_0} \sum_{n=-\infty}^{+\infty} c_n H_n^{(2)}(k_0\rho) e^{jn(\phi-\phi')} \qquad a \leq \rho \leq \rho' \,,\, \rho \geq \rho', \tag{2.39}$$

$$E_z^t = -\frac{k_0^2 I_e}{4\omega\varepsilon_0} \sum_{n=-\infty}^{+\infty} d_n J_n(k\rho) e^{jn(\phi-\phi')} \qquad 0 \leq \rho \leq a. \tag{2.40}$$

For the scattered field, our definition should include $H_n^{(2)}(k_0\rho)$ term which represents $+\widehat{\rho}$ wave propagation. For the transmitted field, our definition should include $J_n(k\rho)$ term which represents a standing wave and also avoids a blow up at $\rho = 0$ (due to Y_n). The fields are 2π periodic in ϕ, so $e^{jn(\phi-\phi')}$ term is inserted to show this and to be in accordance with the incident field expressions and also for convenience. The $-\frac{k_0^2 I_e}{4\omega\varepsilon_0}$ terms are just for convenience in calculations, which in fact could be included in c_n and/or d_n.

2.3.5 Boundary Conditions for Electric Fields

The tangential components of the electric fields are continuous at the surface of the cylinder, due to the boundary conditions. Therefore,

$$E_z^i(\rho = a) + E_z^s(\rho = a) = E_z^t(\rho = a), \tag{2.41}$$

$$\begin{aligned} -\frac{k_0^2 I_e}{4\omega\varepsilon_0} \sum_{n=-\infty}^{+\infty} \left[J_n(k_0 a) H_n^{(2)}(k_0\rho') + c_n H_n^{(2)}(k_0 a) \right] e^{jn(\phi-\phi')} \\ = -\frac{k_0^2 I_e}{4\omega\varepsilon_0} \sum_{n=-\infty}^{+\infty} d_n J_n(ka) e^{jn(\phi-\phi')}, \end{aligned} \tag{2.42}$$

$$J_n(k_0 a) H_n^{(2)}(k_0\rho') + c_n H_n^{(2)}(k_0 a) = d_n J_n(ka), \tag{2.43}$$

$$d_n = \frac{J_n(k_0 a) H_n^{(2)}(k_0\rho') + c_n H_n^{(2)}(k_0 a)}{J_n(ka)}. \tag{2.44}$$

2.3.6 Incident, Scattered and Transmitted Magnetic Fields

The radial and tangential components of the magnetic fields are derived from the electric fields using the Maxwell's equation:

$$\mathbf{H} = -\frac{1}{j\omega\mu} \nabla \times \mathbf{E}, \tag{2.45}$$

$$\mathbf{E} = \widehat{a}_z E_z, \tag{2.46}$$

$$\mathbf{H} = -\frac{1}{j\omega\mu} \left(\widehat{a}_\rho \frac{1}{\rho} \frac{\partial E_z}{\partial \phi} - \widehat{a}_\phi \frac{\partial E_z}{\partial \rho} \right), \tag{2.47}$$

$$H_\rho = -\frac{1}{j\omega\mu} \frac{1}{\rho} \frac{\partial E_z}{\partial \phi}, \tag{2.48}$$

$$H_\phi = \frac{1}{j\omega\mu} \frac{\partial E_z}{\partial \rho}. \tag{2.49}$$

Since H_ϕ is the only component of the magnetic fields we will utilize in boundary conditions, we are only interested in equation (2.49).

One important point where attention must be paid is the partial derivative of E_z with respect to ρ. Since in our E_z definitions we have the Bessel and Hankel functions, their derivatives should be taken with respect to the entire argument of the corresponding Bessel and Hankel functions.

Let $F(\beta\rho)$ be a function representing the Bessel and Hankel functions. Then,

$$\frac{\partial F(\beta\rho)}{\partial \rho} = \frac{\partial(\beta\rho)}{\partial \rho}\frac{\partial F(\beta\rho)}{\partial(\beta\rho)} = \beta\frac{\partial F(\beta\rho)}{\partial(\beta\rho)}. \tag{2.50}$$

Utilizing (2.49) and (2.50), and also keeping in mind that the derivatives are all with respect to the entire arguments, the tangential components of the magnetic fields are obtained as follows:

$$H_\phi^i = -\frac{k_0^2 I_e}{4\omega\varepsilon_0}\frac{1}{j\omega\mu_0}k_0\sum_{n=-\infty}^{+\infty} J_n'(k_0\rho)H_n^{(2)}(k_0\rho')e^{jn(\phi-\phi')} \qquad \rho \le \rho', \tag{2.51}$$

$$H_\phi^i = -\frac{k_0^2 I_e}{4\omega\varepsilon_0}\frac{1}{j\omega\mu_0}k_0\sum_{n=-\infty}^{+\infty} J_n(k_0\rho')H_n^{(2)'}(k_0\rho)e^{jn(\phi-\phi')} \qquad \rho \ge \rho', \tag{2.52}$$

$$H_\phi^s = -\frac{k_0^2 I_e}{4\omega\varepsilon_0}\frac{1}{j\omega\mu_0}k_0\sum_{n=-\infty}^{+\infty} c_n H_n^{(2)'}(k_0\rho)e^{jn(\phi-\phi')} \qquad a \le \rho \le \rho'\,,\, \rho \ge \rho', \tag{2.53}$$

$$H_\phi^t = -\frac{k_0^2 I_e}{4\omega\varepsilon_0}\frac{1}{j\omega\mu}k\sum_{n=-\infty}^{+\infty} d_n J_n'(k\rho)e^{jn(\phi-\phi')} \qquad 0 \le \rho \le a. \tag{2.54}$$

2.3.7 Boundary Conditions for Magnetic Fields

The tangential components of the magnetic fields are continuous at the surface of the cylinder due to the boundary conditions. Therefore,

$$H_\phi^i(\rho = a) + H_\phi^s(\rho = a) = H_\phi^t(\rho = a), \tag{2.55}$$

$$-\frac{k_0^2 I_e}{4\omega\varepsilon_0}\frac{1}{j\omega\mu_0}k_0\sum_{n=-\infty}^{+\infty}\left[J_n'(k_0a)H_n^{(2)}(k_0\rho') + c_n H_n^{(2)'}(k_0a)\right]e^{jn(\phi-\phi')}$$
$$= -\frac{k_0^2 I_e}{4\omega\varepsilon_0}\frac{1}{j\omega\mu}k\sum_{n=-\infty}^{+\infty} d_n J_n'(ka)e^{jn(\phi-\phi')}, \tag{2.56}$$

$$\frac{k_0}{\mu_0}\left[J_n'(k_0a)H_n^{(2)}(k_0\rho') + c_nH_n^{(2)'}(k_0a)\right] = \frac{k}{\mu}d_nJ_n'(ka). \tag{2.57}$$

Expressing

$$\frac{k}{\mu} = \frac{k_0}{\mu_0}\frac{\sqrt{\mu_r\varepsilon_r}}{\mu_r} = \frac{k_0}{\mu_0}\sqrt{\frac{\varepsilon_r}{\mu_r}} = \frac{k_0}{\mu_0}\frac{1}{\zeta}, \tag{2.58}$$

where $\zeta = \sqrt{\mu_r/\varepsilon_r}$ as previously defined in (2.31), and substituting (2.58) in (2.57), we get:

$$\zeta\left[J_n'(k_0a)H_n^{(2)}(k_0\rho') + c_nH_n^{(2)'}(k_0a)\right] = d_nJ_n'(ka), \tag{2.59}$$

$$d_n = \frac{\zeta\left[J_n'(k_0a)H_n^{(2)}(k_0\rho') + c_nH_n^{(2)'}(k_0a)\right]}{J_n'(ka)}. \tag{2.60}$$

2.3.8 Simultaneous Solution of the Boundary Conditions for Electric and Magnetic Fields

Now we have two equations for d_n: (2.44) and (2.60), which are derived from the boundary conditions for the electric and magnetic fields, respectively. Our next step will be to equate these equations:

$$d_n = \frac{J_n(k_0a)H_n^{(2)}(k_0\rho') + c_nH_n^{(2)}(k_0a)}{J_n(ka)} = \frac{\zeta\left[J_n'(k_0a)H_n^{(2)}(k_0\rho') + c_nH_n^{(2)'}(k_0a)\right]}{J_n'(ka)}, \tag{2.61}$$

$$\begin{aligned} &J_n'(ka)\left[J_n(k_0a)H_n^{(2)}(k_0\rho') + c_nH_n^{(2)}(k_0a)\right] \\ &\quad = \zeta J_n(ka)\left[J_n'(k_0a)H_n^{(2)}(k_0\rho') + c_nH_n^{(2)'}(k_0a)\right], \end{aligned} \tag{2.62}$$

$$\begin{aligned} &J_n'(ka)J_n(k_0a)H_n^{(2)}(k_0\rho') + c_nJ_n'(ka)H_n^{(2)}(k_0a) \\ &\quad = \zeta J_n(ka)J_n'(k_0a)H_n^{(2)}(k_0\rho') + c_n\zeta J_n(ka)H_n^{(2)'}(k_0a), \end{aligned} \tag{2.63}$$

$$\begin{aligned} &c_nJ_n'(ka)H_n^{(2)}(k_0a) - c_n\zeta J_n(ka)H_n^{(2)'}(k_0a) \\ &\quad = \zeta J_n(ka)J_n'(k_0a)H_n^{(2)}(k_0\rho') - J_n'(ka)J_n(k_0a)H_n^{(2)}(k_0\rho'), \end{aligned} \tag{2.64}$$

$$c_n \left[J_n'(ka) H_n^{(2)}(k_0 a) - \zeta J_n(ka) H_n^{(2)'}(k_0 a) \right]$$
$$= \zeta J_n(ka) J_n'(k_0 a) H_n^{(2)}(k_0 \rho') - J_n'(ka) J_n(k_0 a) H_n^{(2)}(k_0 \rho'), \tag{2.65}$$

$$c_n = \frac{\zeta J_n(ka) J_n'(k_0 a) H_n^{(2)}(k_0 \rho') - J_n'(ka) J_n(k_0 a) H_n^{(2)}(k_0 \rho')}{J_n'(ka) H_n^{(2)}(k_0 a) - \zeta J_n(ka) H_n^{(2)'}(k_0 a)}, \tag{2.66}$$

$$c_n = \frac{\zeta J_n(ka) J_n'(k_0 a) - J_n'(ka) J_n(k_0 a)}{J_n'(ka) H_n^{(2)}(k_0 a) - \zeta J_n(ka) H_n^{(2)'}(k_0 a)} H_n^{(2)}(k_0 \rho'), \tag{2.67}$$

where d_n can be found from (2.44)

$$d_n = \frac{J_n(k_0 a) H_n^{(2)}(k_0 \rho') + c_n H_n^{(2)}(k_0 a)}{J_n(ka)}, \tag{2.68}$$

or from (2.60)

$$d_n = \frac{\zeta \left[J_n'(k_0 a) H_n^{(2)}(k_0 \rho') + c_n H_n^{(2)'}(k_0 a) \right]}{J_n'(ka)}. \tag{2.69}$$

Now, the incident, scattered and transmitted electric and magnetic fields can be calculated using (2.37)-(2.40) and (2.51)-(2.54), respectively.

Remark: Note that, since the electric line source is placed outside the metamaterial cylinder, when applying the boundary conditions for electric and magnetic fields at $\rho = a$, (2.37) and (2.51) are used, respectively. If the line source is placed inside the cylinder, boundary conditions should be written using (2.38) and (2.52).

2.3.9 Calculation of the Radiation Patterns

To calculate the radiation patterns, the following large argument approximation for Hankel functions of the second kind is used:

$$\lim_{k_0 \rho \to \infty} H_n^{(2)}(k_0 \rho) = \sqrt{\frac{2}{\pi k_0 \rho}} e^{-j[k_0 \rho - \pi/4 - n(\pi/2)]}. \tag{2.70}$$

The total electric field for $\rho > \rho'$ can be written as:

$$E_z^r(\rho,\phi) = E_z^i(\rho,\phi) + E_z^s(\rho,\phi) = -\frac{k_0^2 I_e}{4\omega\varepsilon_0} \sum_{n=-\infty}^{+\infty} \left[J_n(k_0\rho') + c_n\right] H_n^{(2)}(k_0\rho) e^{jn(\phi-\phi')}. \tag{2.71}$$

Using (2.70),

$$\lim_{k_0\rho\to\infty} E_z^r(\rho,\phi) = -\frac{k_0^2 I_e}{4\omega\varepsilon_0} \sum_{n=-\infty}^{+\infty} \left[J_n(k_0\rho') + c_n\right] \sqrt{\frac{2}{\pi k_0\rho}} e^{-j[k_0\rho-\pi/4-n(\pi/2)]} e^{jn(\phi-\phi')}, \tag{2.72}$$

$$\lim_{k_0\rho\to\infty} E_z^r(\rho,\phi) = -\frac{k_0^2 I_e}{4\omega\varepsilon_0} \sqrt{\frac{2}{\pi k_0\rho}} e^{-j(k_0\rho-\pi/4)} \sum_{n=-\infty}^{+\infty} \left[J_n(k_0\rho') + c_n\right] e^{jn(\phi-\phi'+\pi/2)}. \tag{2.73}$$

The radiation density is:

$$W_{rad}(\rho,\phi) = \lim_{k_0\rho\to\infty} \frac{\left|E_z^r(\rho,\phi)\right|^2}{2\eta_0} = \frac{k_0^3 I_e^2}{16\eta_0\omega^2\varepsilon_0^2\pi\rho} \left| \sum_{n=-\infty}^{+\infty} \left[J_n(k_0\rho') + c_n\right] e^{jn(\phi-\phi'+\pi/2)} \right|^2. \tag{2.74}$$

The radiation intensity is:

$$U(\phi) = \rho W_{rad}(\rho,\phi) = \frac{k_0^3 I_e^2}{16\eta_0\omega^2\varepsilon_0^2\pi} \left| \sum_{n=-\infty}^{+\infty} \left[J_n(k_0\rho') + c_n\right] e^{jn(\phi-\phi'+\pi/2)} \right|^2. \tag{2.75}$$

2.3.10 Numerical Results

Fig. 2.3 shows the magnitude of electric field for different choices of constitutive parameters when $f = 30\text{GHz}$, $\lambda_0 = 0.01\text{m}$, $a = \lambda_0$, $\rho' = 1.5\lambda_0$, $\phi' = 0^\circ$.

For DNG cases, focusing towards the line source and inside the metamaterial cylinder is noticed. In Fig. 2.3 (a), this focusing occurs on the surface of the cylinder. These unique focusing properties of DNG metamaterials are mainly results of negative refraction.

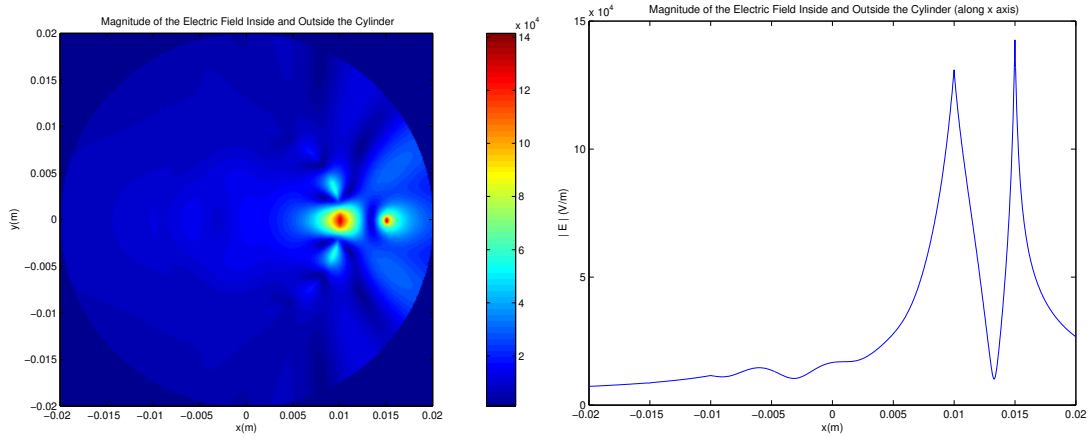

(a) (b)

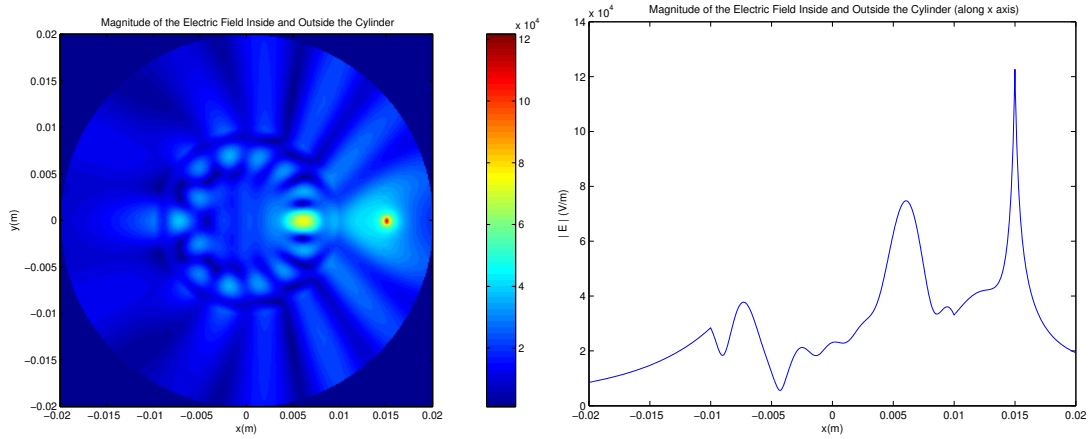

(c) (d)

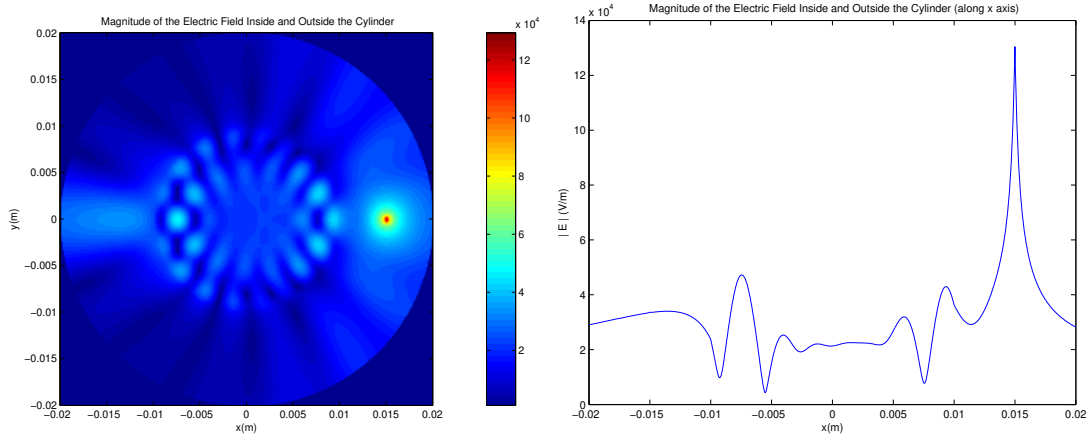

(e) (f)

Figure 2.3: Magnitude of the electric field inside and outside the cylinder. (a)-(b) $\varepsilon_r = -1$, $\mu_r = -1$, (c)-(d) $\varepsilon_r = -2$, $\mu_r = -2$, (e)-(f) $\varepsilon_r = 2$, $\mu_r = 2$

2.4 Normally Incident Plane Wave Scattering by an Infinite Length Metamaterial Cylinder: TM^z Polarization

2.4.1 Introduction

A uniform plane wave is normally incident on a metamaterial cylinder of infinite length. The plane wave travels in the $-x$ direction. We will examine here the scattering and transmission by the cylinder in the case the polarization of the plane wave is TM^z. For the $-x$ propagation direction and TM^z polarization, electric field is directed along the $+z$ axis and magnetic field is directed along the $+y$ axis. The problem geometry is given in Fig. 2.4.

2.4.2 Problem Geometry

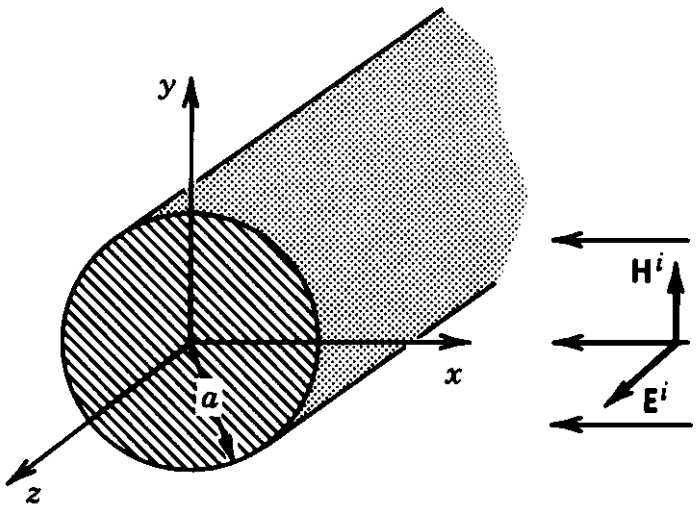

Figure 2.4: Uniform plane wave incident on a metamaterial cylinder: TM^z Polarization.

2.4.3 Uniform Plane Wave and Incident Electric Field

Let us assume that a TM^z polarized uniform plane wave is traveling in the $-x$ direction. This means electric field is directed along the $+z$ axis and magnetic field is directed along the $+y$ axis. Therefore the electric field can be written as [27]

$$E_z^i = E_0 e^{jk_0 x} = E_0 e^{jk_0 \rho \cos\phi}. \tag{2.76}$$

By wave transformations and utilizing orthogonality condition [27,28], (2.76) can be written in the series expansion form as follows [27]:

$$E_z^i = E_0 \sum_{n=-\infty}^{+\infty} j^n J_n(k_0\rho) e^{jn\phi} \qquad \rho \geq a. \tag{2.77}$$

2.4.4 Scattered and Transmitted Electric Fields

Similar to the incident field expression in (2.77), we will define the scattered and transmitted electric fields in series expansion form, respectively, as

$$E_z^s = E_0 \sum_{n=-\infty}^{+\infty} j^n c_n H_n^{(2)}(k_0\rho) e^{jn\phi} \qquad \rho \geq a, \tag{2.78}$$

$$E_z^t = E_0 \sum_{n=-\infty}^{+\infty} j^n d_n J_n(k\rho) e^{jn\phi} \qquad 0 \leq \rho \leq a. \tag{2.79}$$

For the scattered field, our definition should include $H_n^{(2)}(k_0\rho)$ term which represents $+\widehat{\rho}$ wave propagation. For the transmitted field, our definition should include $J_n(k\rho)$ term which represents a standing wave and also avoids a blow up at $\rho = 0$ (due to Y_n). The fields are 2π periodic in ϕ, so $e^{jn\phi}$ term is inserted to show this and to be in accordance with the incident field expressions and also for convenience. The j^n terms are just for convenience in calculations, which in fact could be included in c_n and/or d_n.

2.4.5 Boundary Conditions for Electric Fields

The tangential components of the electric fields are continuous at the surface of the cylinder due to the boundary conditions. Therefore,

$$E_z^i(\rho = a) + E_z^s(\rho = a) = E_z^t(\rho = a), \tag{2.80}$$

$$E_0 \sum_{n=-\infty}^{+\infty} j^n \left[J_n(k_0 a) + c_n H_n^{(2)}(k_0 a) \right] e^{jn\phi} = E_0 \sum_{n=-\infty}^{+\infty} j^n d_n J_n(ka) e^{jn\phi}, \tag{2.81}$$

$$J_n(k_0 a) + c_n H_n^{(2)}(k_0 a) = d_n J_n(ka), \tag{2.82}$$

$$d_n = \frac{J_n(k_0 a) + c_n H_n^{(2)}(k_0 a)}{J_n(ka)}. \tag{2.83}$$

2.4.6 Incident, Scattered and Transmitted Magnetic Fields

Utilizing (2.49) and (2.50), the tangential components of the magnetic fields are obtained as

$$H_\phi^i = E_0 \frac{1}{j\omega\mu_0} k_0 \sum_{n=-\infty}^{+\infty} j^n J_n'(k_0\rho) e^{jn\phi} \qquad \rho \geq a, \tag{2.84}$$

$$H_\phi^s = E_0 \frac{1}{j\omega\mu_0} k_0 \sum_{n=-\infty}^{+\infty} j^n c_n H_n^{(2)'}(k_0\rho) e^{jn\phi} \qquad \rho \geq a, \tag{2.85}$$

$$H_\phi^t = E_0 \frac{1}{j\omega\mu} k \sum_{n=-\infty}^{+\infty} j^n d_n J_n'(k\rho) e^{jn\phi} \qquad 0 \leq \rho \leq a. \tag{2.86}$$

The derivatives in (2.197)-(2.199) are again with respect to the entire arguments.

2.4.7 Boundary Conditions for Magnetic Fields

The tangential components of the magnetic fields are continuous at the surface of the cylinder due to the boundary conditions. Therefore,

$$H_\phi^i(\rho = a) + H_\phi^s(\rho = a) = H_\phi^t(\rho = a), \tag{2.87}$$

$$E_0 \frac{1}{j\omega\mu_0} k_0 \sum_{n=-\infty}^{+\infty} j^n \left[J_n'(k_0 a) + c_n H_n^{(2)'}(k_0 a) \right] e^{jn\phi} = E_0 \frac{1}{j\omega\mu} k \sum_{n=-\infty}^{+\infty} j^n d_n J_n'(ka) e^{jn\phi}, \tag{2.88}$$

$$\frac{k_0}{\mu_0} \left[J_n'(k_0 a) + c_n H_n^{(2)'}(k_0 a) \right] = \frac{k}{\mu} d_n J_n'(ka). \tag{2.89}$$

Using (2.58) in (2.231),

$$\zeta \left[J_n'(k_0 a) + c_n H_n^{(2)'}(k_0 a) \right] = d_n J_n'(ka), \tag{2.90}$$

$$d_n = \frac{\zeta \left[J_n'(k_0 a) + c_n H_n^{(2)'}(k_0 a) \right]}{J_n'(ka)}. \tag{2.91}$$

2.4.8 Simultaneous Solution of the Boundary Conditions for Electric and Magnetic Fields

Now we have two equations for d_n: (2.83) and (2.91), which are derived from the boundary conditions for the electric and magnetic fields, respectively. Our next step will be to equate these equations:

$$d_n = \frac{J_n(k_0 a) + c_n H_n^{(2)}(k_0 a)}{J_n(ka)} = \frac{\zeta \left[J_n'(k_0 a) + c_n H_n^{(2)'}(k_0 a) \right]}{J_n'(ka)}, \tag{2.92}$$

$$J_n'(ka) \left[J_n(k_0 a) + c_n H_n^{(2)}(k_0 a) \right] = \zeta J_n(ka) \left[J_n'(k_0 a) + c_n H_n^{(2)'}(k_0 a) \right], \tag{2.93}$$

$$J_n'(ka) J_n(k_0 a) + c_n J_n'(ka) H_n^{(2)}(k_0 a) = \zeta J_n(ka) J_n'(k_0 a) + c_n \zeta J_n(ka) H_n^{(2)'}(k_0 a), \tag{2.94}$$

$$c_n J_n'(ka)H_n^{(2)}(k_0a) - c_n\zeta J_n(ka)H_n^{(2)'}(k_0a) = \zeta J_n(ka)J_n'(k_0a) - J_n'(ka)J_n(k_0a), \tag{2.95}$$

$$c_n\left[J_n'(ka)H_n^{(2)}(k_0a) - \zeta J_n(ka)H_n^{(2)'}(k_0a)\right] = \zeta J_n(ka)J_n'(k_0a) - J_n'(ka)J_n(k_0a), \tag{2.96}$$

$$c_n = \frac{\zeta J_n(ka)J_n'(k_0a) - J_n'(ka)J_n(k_0a)}{J_n'(ka)H_n^{(2)}(k_0a) - \zeta J_n(ka)H_n^{(2)'}(k_0a)}, \tag{2.97}$$

where

$$d_n = \frac{J_n(k_0a) + c_nH_n^{(2)}(k_0a)}{J_n(ka)}, \tag{2.98}$$

or

$$d_n = \frac{\zeta\left[J_n'(k_0a) + c_nH_n^{(2)'}(k_0a)\right]}{J_n'(ka)}. \tag{2.99}$$

2.4.9 Numerical Results

Fig. 2.5 shows the numerical results for $f = 30\text{GHz}$, $\lambda_0 = 0.01\text{m}$, $a = \lambda_0$. In Fig. 2.5 (a), there are three foci close to the interface and inside the metamaterial cylinder. In Fig. 2.5 (b), there is one dominant focus inside the cylinder, while the other two diminish. Finally in Fig. 2.5 (c) there is one focus inside the cylinder and another outside. Both foci are at the other side of the cylinder (w.r.t plane wave illumination) as predicted for a DPS dielectric lens.

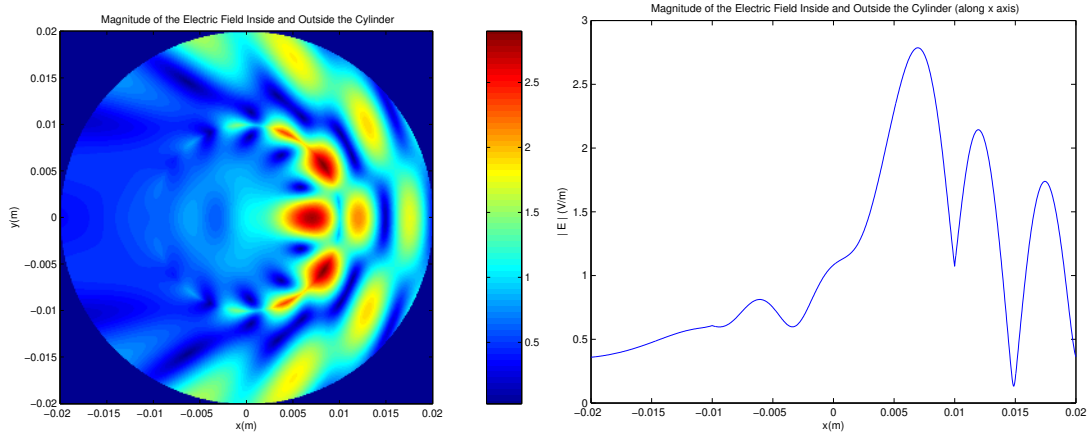

(a) (b)

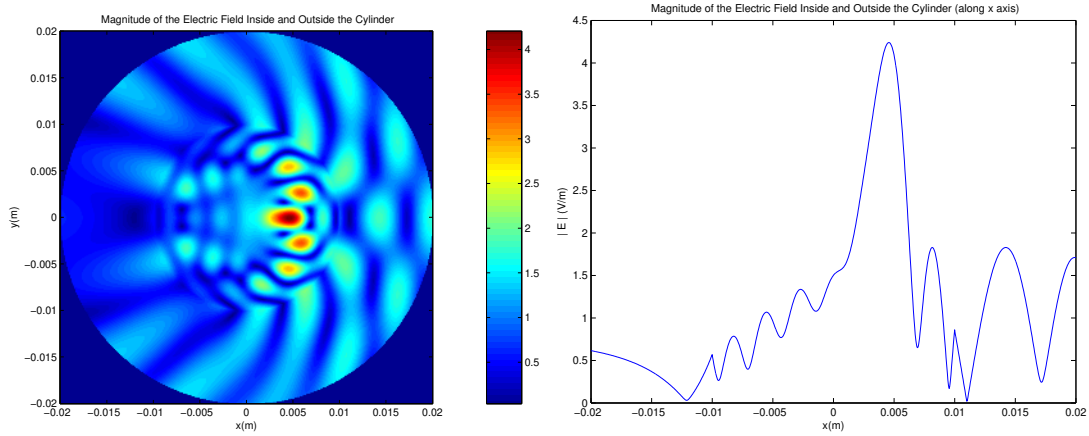

(c) (d)

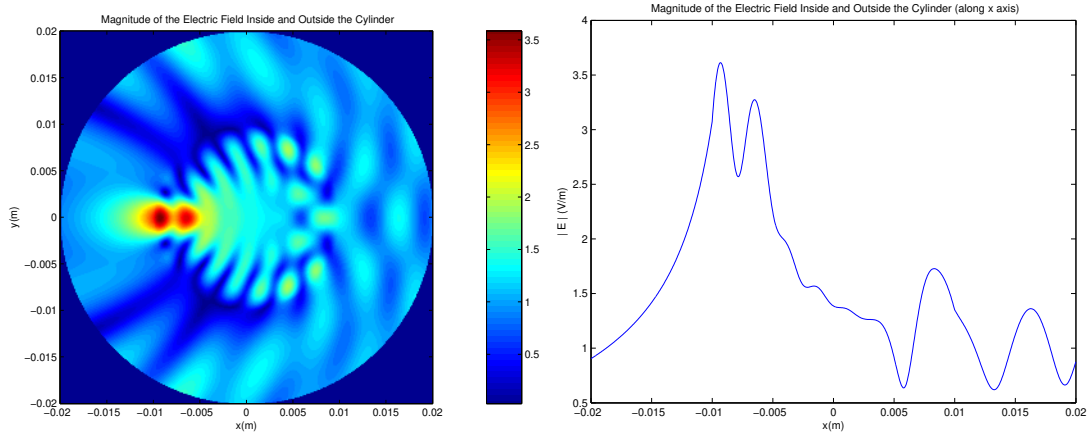

(e) (f)

Figure 2.5: Magnitude of the electric field inside and outside the cylinder. (a)-(b) $\varepsilon_r = -1$, $\mu_r = -1$, (c)-(d) $\varepsilon_r = -2$, $\mu_r = -2$, (e)-(f) $\varepsilon_r = 2$, $\mu_r = 2$

2.5 Normally Incident Plane Wave Scattering by an Infinite Length Metamaterial Cylinder: TE^z Polarization

2.5.1 Introduction

A uniform plane wave is normally incident on a metamaterial cylinder of infinite length, traveling in the $-x$ direction, as in Section 2.4. We will examine here the scattering and transmission by the cylinder in the case the polarization of the plane wave is TE^z. For the $-x$ propagation direction and TE^z polarization, magnetic field is directed along the $+z$ axis and electric field is directed along the $-y$ axis. The problem geometry is depicted in Fig. 2.6.

2.5.2 Problem Geometry

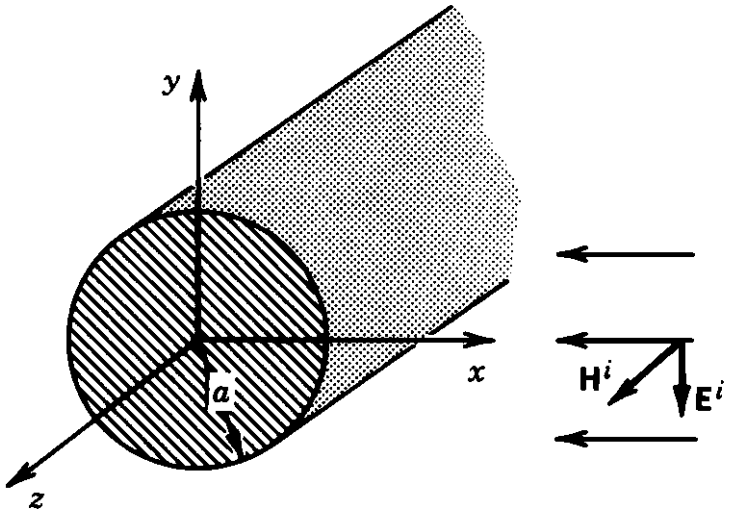

Figure 2.6: Uniform plane wave incident on a metamaterial cylinder: TE^z Polarization.

2.5.3 Uniform Plane Wave and Incident Magnetic Field

Let us assume that a TE^z polarized uniform plane wave is traveling in the $-x$ direction, which means the magnetic field is directed along the $+z$ axis and the electric field is directed along the $-y$ axis. Therefore, the magnetic field can be written as [27]

$$H_z^i = H_0 e^{jk_0 x} = H_0 e^{jk_0 \rho \cos\phi}. \tag{2.100}$$

By wave transformations and utilizing orthogonality condition [27,28], (2.100) can be written in series expansion form as [27]

$$H_z^i = H_0 \sum_{n=-\infty}^{+\infty} j^n J_n(k_0\rho) e^{jn\phi} \qquad \rho \geq a. \tag{2.101}$$

2.5.4 Scattered and Transmitted Magnetic Fields

Similar to the incident field expression in (2.101), we will define the scattered and transmitted magnetic fields in series expansion form respectively as follows:

$$H_z^s = H_0 \sum_{n=-\infty}^{+\infty} j^n c_n H_n^{(2)}(k_0\rho) e^{jn\phi} \qquad \rho \geq a, \tag{2.102}$$

$$H_z^t = H_0 \sum_{n=-\infty}^{+\infty} j^n d_n J_n(k\rho) e^{jn\phi} \qquad 0 \leq \rho \leq a. \tag{2.103}$$

2.5.5 Boundary Conditions for Magnetic Fields

The tangential components of the magnetic fields are continuous at the surface of the cylinder due to the boundary conditions. Hence,

$$H_z^i(\rho = a) + H_z^s() = H_z^t(\rho = a), \tag{2.104}$$

$$H_0 \sum_{n=-\infty}^{+\infty} j^n \left[J_n(k_0 a) + c_n H_n^{(2)}(k_0 a) \right] e^{jn\phi} = H_0 \sum_{n=-\infty}^{+\infty} j^n d_n J_n(ka) e^{jn\phi}, \tag{2.105}$$

$$J_n(k_0a) + c_n H_n^{(2)}(k_0a) = d_n J_n(ka), \tag{2.106}$$

$$d_n = \frac{J_n(k_0a) + c_n H_n^{(2)}(k_0a)}{J_n(ka)}. \tag{2.107}$$

2.5.6 Incident, Scattered and Transmitted Electric Fields

The radial and tangential components of the electric fields are derived from the magnetic fields using the Maxwell's equation:

$$\mathbf{E} = \frac{1}{j\omega\varepsilon}\nabla \times \mathbf{H}, \tag{2.108}$$

$$\mathbf{H} = \widehat{a}_z H_z, \tag{2.109}$$

$$\mathbf{E} = \frac{1}{j\omega\varepsilon}\left(\widehat{a}_\rho \frac{1}{\rho}\frac{\partial H_z}{\partial \phi} - \widehat{a}_\phi \frac{\partial H_z}{\partial \rho}\right), \tag{2.110}$$

$$E_\rho = \frac{1}{j\omega\varepsilon}\frac{1}{\rho}\frac{\partial H_z}{\partial \phi}, \tag{2.111}$$

$$E_\phi = -\frac{1}{j\omega\varepsilon}\frac{\partial H_z}{\partial \rho}. \tag{2.112}$$

Since E_ϕ is the only component of the electric fields we will utilize in boundary conditions, we are only interested in equation (2.112).

Utilizing (2.112), tangential components of the electric fields are obtained as

$$E_\phi^i = H_0 \frac{-1}{j\omega\varepsilon_0} k_0 \sum_{n=-\infty}^{+\infty} j^n J_n'(k_0\rho) e^{jn\phi} \qquad \rho \geq a, \tag{2.113}$$

$$E_\phi^s = H_0 \frac{-1}{j\omega\varepsilon_0} k_0 \sum_{n=-\infty}^{+\infty} j^n c_n H_n^{(2)'}(k_0\rho) e^{jn\phi} \qquad \rho \geq a, \tag{2.114}$$

$$E_\phi^t = H_0 \frac{-1}{j\omega\varepsilon} k \sum_{n=-\infty}^{+\infty} j^n d_n J_n'(k\rho) e^{jn\phi} \qquad 0 \leq \rho \leq a. \tag{2.115}$$

2.5.7 Boundary Conditions for Electric Fields

The tangential components of the electric fields are continuous at the surface of the cylinder due to the boundary conditions. For this reason,

$$E_\phi^i(\rho = a) + E_\phi^s(\rho = a) = E_\phi^t(\rho = a), \tag{2.116}$$

$$H_0 \frac{-1}{j\omega\varepsilon_0} k_0 \sum_{n=-\infty}^{+\infty} j^n \left[J_n'(k_0 a) + c_n H_n^{(2)'}(k_0 a) \right] e^{jn\phi} = H_0 \frac{-1}{j\omega\varepsilon} k \sum_{n=-\infty}^{+\infty} j^n d_n J_n'(ka) e^{jn\phi}, \tag{2.117}$$

$$\frac{k_0}{\varepsilon_0} \left[J_n'(k_0 a) + c_n H_n^{(2)'}(k_0 a) \right] = \frac{k}{\varepsilon} d_n J_n'(ka). \tag{2.118}$$

Expressing,

$$\frac{k}{\varepsilon} = \frac{k_0}{\varepsilon_0} \frac{\sqrt{\mu_r \varepsilon_r}}{\varepsilon_r} = \frac{k_0}{\varepsilon_0} \sqrt{\frac{\mu_r}{\varepsilon_r}} = \frac{k_0}{\varepsilon_0} \zeta, \tag{2.119}$$

and substituting (2.119) in (2.118),

$$J_n'(k_0 a) + c_n H_n^{(2)'}(k_0 a) = d_n \zeta J_n'(ka), \tag{2.120}$$

$$d_n = \frac{J_n'(k_0 a) + c_n H_n^{(2)'}(k_0 a)}{\zeta J_n'(ka)}. \tag{2.121}$$

2.5.8 Simultaneous Solution of the Boundary Conditions for Magnetic and Electric Fields

Now we have two equations for d_n: (2.107) and (2.121), which are derived from the boundary conditions for the magnetic and electric fields, respectively. Our next step will be to equate these equations:

$$d_n = \frac{J_n(k_0 a) + c_n H_n^{(2)}(k_0 a)}{J_n(ka)} = \frac{J_n'(k_0 a) + c_n H_n^{(2)'}(k_0 a)}{\zeta J_n'(ka)}, \tag{2.122}$$

$$\zeta J_n'(ka) \left[J_n(k_0 a) + c_n H_n^{(2)}(k_0 a) \right] = J_n(ka) \left[J_n'(k_0 a) + c_n H_n^{(2)'}(k_0 a) \right], \tag{2.123}$$

$$\zeta J_n'(ka) J_n(k_0 a) + c_n \zeta J_n'(ka) H_n^{(2)}(k_0 a) = J_n(ka) J_n'(k_0 a) + c_n J_n(ka) H_n^{(2)'}(k_0 a), \tag{2.124}$$

$$c_n\zeta J_n'(ka)H_n^{(2)}(k_0a) - c_nJ_n(ka)H_n^{(2)'}(k_0a) = J_n(ka)J_n'(k_0a) - \zeta J_n'(ka)J_n(k_0a), \tag{2.125}$$

$$c_n\left[\zeta J_n'(ka)H_n^{(2)}(k_0a) - J_n(ka)H_n^{(2)'}(k_0a)\right] = J_n(ka)J_n'(k_0a) - \zeta J_n'(ka)J_n(k_0a), \tag{2.126}$$

$$c_n = \frac{J_n(ka)J_n'(k_0a) - \zeta J_n'(ka)J_n(k_0a)}{\zeta J_n'(ka)H_n^{(2)}(k_0a) - J_n(ka)H_n^{(2)'}(k_0a)}, \tag{2.127}$$

where

$$d_n = \frac{J_n(k_0a) + c_nH_n^{(2)}(k_0a)}{J_n(ka)}, \tag{2.128}$$

or

$$d_n = \frac{J_n'(k_0a) + c_nH_n^{(2)'}(k_0a)}{\zeta J_n'(ka)}. \tag{2.129}$$

2.5.9 Numerical Results

Using duality, interchanging μ_r and ε_r, the same results in Fig. 2.5 can be obtained (for magnitude of the magnetic field).

2.6 Infinite Length Metamaterial Coated Conducting Cylinder Near an Infinite Length Electric Line Source: TM^z Polarization

2.6.1 Introduction

An infinite line of constant electric current is placed in the vicinity of an infinite length metamaterial coated conducting cylinder. The scattering and transmission by the metamaterial coated conducting cylinder is examined for TM^z polarization. The problem geometry is shown in Fig. 2.7.

2.6.2 Problem Geometry

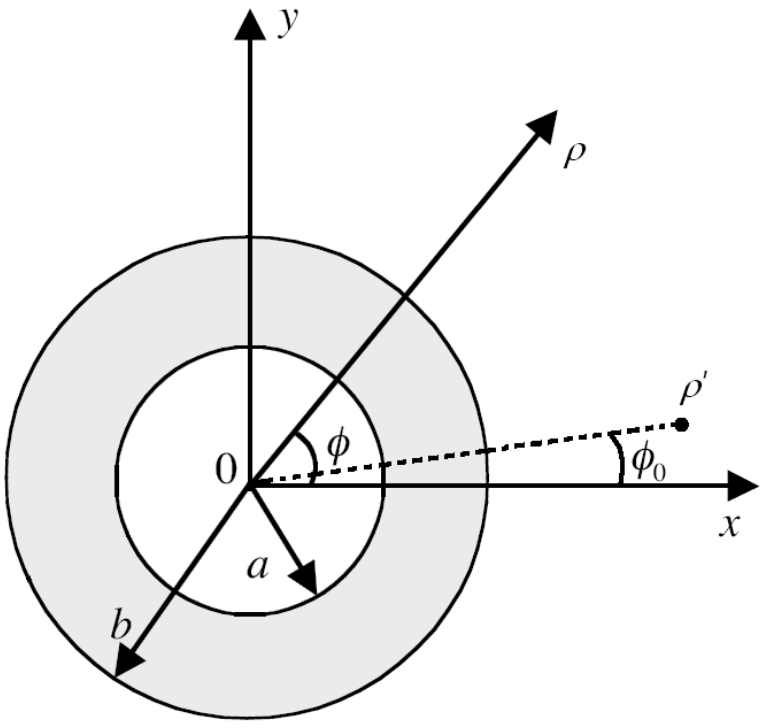

Figure 2.7: Metamaterial coated conducting cylinder near an electric line source (Cross section view).

2.6.3 Electric Line Source and Incident Electric Field

For the line source of constant electric current, I_e, in Fig. 2.7, the electric field generated everywhere by the source in the absence of the cylinder is given as [27]

$$E_z^i = -\frac{k_0^2 I_e}{4\omega\varepsilon_0} H_0^{(2)}(k_0|\bar{\rho} - \bar{\rho}'|), \tag{2.130}$$

which is our incident electric field. By the addition theorem for Hankel functions [28], (2.130) can be written in the series expansion form as [27]

$$E_z^i = -\frac{k_0^2 I_e}{4\omega\varepsilon_0} \sum_{n=-\infty}^{+\infty} J_n(k_0\rho) H_n^{(2)}(k_0\rho') e^{jn(\phi-\phi')} \qquad \rho \leq \rho', \tag{2.131}$$

$$E_z^i = -\frac{k_0^2 I_e}{4\omega\varepsilon_0} \sum_{n=-\infty}^{+\infty} J_n(k_0\rho') H_n^{(2)}(k_0\rho) e^{jn(\phi-\phi')} \qquad \rho \geq \rho'. \tag{2.132}$$

2.6.4 Scattered and Transmitted Electric Fields

Similar to the incident field expressions in (2.131) and (2.132), we will define the scattered and transmitted electric fields in series expansion form, respectively, as

$$E_z^s = -\frac{k_0^2 I_e}{4\omega\varepsilon_0} \sum_{n=-\infty}^{+\infty} c_n H_n^{(2)}(k_0\rho) e^{jn(\phi-\phi_0)}, \tag{2.133}$$

$$E_z^t = -\frac{k_0^2 I_e}{4\omega\varepsilon_0} \sum_{n=-\infty}^{+\infty} \left[a_n J_n(k\rho) + b_n Y_n(k\rho)\right] e^{jn(\phi-\phi_0)}. \tag{2.134}$$

For the scattered field, our definition should include $H_n^{(2)}(k_0\rho)$ term which represents $+\widehat{\rho}$ wave propagation. For the transmitted field, our definition should include $J_n(k\rho)$ and $Y_n(k\rho)$ terms which represent standing waves. The fields are 2π periodic in ϕ, so $e^{jn(\phi-\phi_0)}$ term is inserted to show this and to be in accordance with the incident field expressions and also for convenience. The $-\frac{k_0^2 I_e}{4\omega\varepsilon_0}$ terms are just for convenience in calculations, which in fact could be included in a_n and/or b_n and/or c_n.

2.6.5 Boundary Conditions for Electric Fields

The tangential components of the electric fields are continuous on the outer surface of the metamaterial coating, due to the boundary conditions. Also, on the inner surface of the metamaterial coating (i.e., on the conducting cylinder surface) tangential electric field should vanish. Therefore,

$$E_z^t(\rho = a) = 0, \tag{2.135}$$

$$-\frac{k_0^2 I_e}{4\omega\varepsilon_0} \sum_{n=-\infty}^{+\infty} \left[a_n J_n(k\rho) + b_n Y_n(k\rho)\right] e^{jn(\phi-\phi_0)} \Bigg|_{\rho=a} = 0, \tag{2.136}$$

$$a_n J_n(ka) + b_n Y_n(ka) = 0, \tag{2.137}$$

$$E_z^i(\rho = b) + E_z^s(\rho = b) = E_z^t(\rho = b), \tag{2.138}$$

$$-\frac{k_0^2 I_e}{4\omega\varepsilon_0} \sum_{n=-\infty}^{+\infty} \left[J_n(k_0 b) H_n^{(2)}(k_0\rho') + c_n H_n^{(2)}(k_0 b)\right] e^{jn(\phi-\phi_0)}$$
$$= -\frac{k_0^2 I_e}{4\omega\varepsilon_0} \sum_{n=-\infty}^{+\infty} \left[a_n J_n(kb) + b_n Y_n(kb)\right] e^{jn(\phi-\phi_0)}, \tag{2.139}$$

$$J_n(k_0 b) H_n^{(2)}(k_0\rho') + c_n H_n^{(2)}(k_0 b) = a_n J_n(kb) + b_n Y_n(kb). \tag{2.140}$$

2.6.6 Incident, Scattered and Transmitted Magnetic Fields

Utilizing (2.49) and (2.50), the tangential components of the magnetic fields are obtained as

$$H_\phi^i = -\frac{k_0^2 I_e}{4\omega\varepsilon_0} \frac{1}{j\omega\mu_0} k_0 \sum_{n=-\infty}^{+\infty} J_n'(k_0\rho) H_n^{(2)}(k_0\rho') e^{jn(\phi-\phi_0)}, \tag{2.141}$$

$$H_\phi^s = -\frac{k_0^2 I_e}{4\omega\varepsilon_0} \frac{1}{j\omega\mu_0} k_0 \sum_{n=-\infty}^{+\infty} c_n H_n^{(2)'}(k_0\rho) e^{jn(\phi-\phi_0)}, \tag{2.142}$$

$$H_\phi^t = -\frac{k_0^2 I_e}{4\omega\varepsilon_0}\frac{1}{j\omega\mu}k\sum_{n=-\infty}^{+\infty}\left[a_n J_n'(k\rho) + b_n Y_n'(k\rho)\right]e^{jn(\phi-\phi_0)}. \tag{2.143}$$

2.6.7 Boundary Conditions for Magnetic Fields

Tangential components of the magnetic fields are continuous on the outer surface of the metamaterial coating, due to the boundary conditions. Therefore,

$$H_\phi^i(\rho=b) + H_\phi^s(\rho=b) = H_\phi^t(\rho=b), \tag{2.144}$$

$$\begin{aligned}-\frac{k_0^2 I_e}{4\omega\varepsilon_0}\frac{1}{j\omega\mu_0}k_0\sum_{n=-\infty}^{+\infty}\left[J_n'(k_0b)H_n^{(2)}(k_0\rho') + c_n H_n^{(2)'}(k_0b)\right]e^{jn(\phi-\phi_0)}& \\ = -\frac{k_0^2 I_e}{4\omega\varepsilon_0}\frac{1}{j\omega\mu}k\sum_{n=-\infty}^{+\infty}\left[a_n J_n'(kb) + b_n Y_n'(kb)\right]e^{jn(\phi-\phi_0)},&\end{aligned} \tag{2.145}$$

$$\frac{k_0}{\mu_0}\left[J_n'(k_0b)H_n^{(2)}(k_0\rho') + c_n H_n^{(2)'}(k_0b)\right] = \frac{k}{\mu}\left[a_n J_n'(kb) + b_n Y_n'(kb)\right]. \tag{2.146}$$

Substituting (2.58) in (2.146),

$$\zeta J_n'(k_0b)H_n^{(2)}(k_0\rho') + c_n\zeta H_n^{(2)'}(k_0b) = a_n J_n'(kb) + b_n Y_n'(kb). \tag{2.147}$$

2.6.8 Simultaneous Solution of the Boundary Conditions for Electric and Magnetic Fields

Now we have three unknowns and three equations. Rearranging equations (2.137), (2.140) and (2.147) we get:

$$J_n(ka)a_n + Y_n(ka)b_n = 0, \tag{2.148}$$

$$J_n(kb)a_n + Y_n(kb)b_n - H_n^{(2)}(k_0b)c_n = J_n(k_0b)H_n^{(2)}(k_0\rho'), \tag{2.149}$$

$$J_n'(kb)a_n + Y_n'(kb)b_n - \zeta H_n^{(2)'}(k_0b)c_n = \zeta J_n'(k_0b)H_n^{(2)}(k_0\rho'), \tag{2.150}$$

which can also be written in matrix form as:

$$\begin{bmatrix} J_n(ka) & Y_n(ka) & 0 \\ J_n(kb) & Y_n(kb) & -H_n^{(2)}(k_0b) \\ J_n'(kb) & Y_n'(kb) & -\zeta H_n^{(2)'}(k_0b) \end{bmatrix} \begin{bmatrix} a_n \\ b_n \\ c_n \end{bmatrix} = \begin{bmatrix} 0 \\ J_n(k_0b)H_n^{(2)}(k_0\rho') \\ \zeta J_n'(k_0b)H_n^{(2)}(k_0\rho') \end{bmatrix}. \quad (2.151)$$

Using Symbolic Math Toolbox of MATLAB, the solution to this system of equations can be found as:

$$a_n = \frac{\zeta Y_n(ka)\left[H_n^{(2)}(k_0b)J_n'(k_0b) - H_n^{(2)'}(k_0b)J_n(k_0b)\right]}{D} H_n^{(2)}(k_0\rho'), \quad (2.152)$$

$$b_n = \frac{\zeta J_n(ka)\left[J_n(k_0b)H_n^{(2)'}(k_0b) - J_n'(k_0b)H_n^{(2)}(k_0b)\right]}{D} H_n^{(2)}(k_0\rho'), \quad (2.153)$$

$$c_n = \frac{N}{D} H_n^{(2)}(k_0\rho'), \quad (2.154)$$

where

$$\begin{aligned} N = {} & J_n(k_0b)\left[J_n(ka)Y_n'(kb) - J_n'(kb)Y_n(ka)\right] \\ & -\zeta J_n'(k_0b)\left[J_n(ka)Y_n(kb) - J_n(kb)Y_n(ka)\right], \end{aligned} \quad (2.155)$$

$$\begin{aligned} D = {} & \zeta H_n^{(2)'}(k_0b)\left[J_n(ka)Y_n(kb) - J_n(kb)Y_n(ka)\right] \\ & -H_n^{(2)}(k_0b)\left[J_n(ka)Y_n'(kb) - J_n'(kb)Y_n(ka)\right]. \end{aligned} \quad (2.156)$$

Using the following Wronskian will further simplify a_n and b_n:

$$J_n(x)H_n^{(2)'}(x) - J_n'(x)H_n^{(2)}(x) = \frac{-2j}{\pi x}. \quad (2.157)$$

2.6.9 Electric Line Source Inside the Metamaterial Coating

When the electric line source is placed inside the metamaterial coating, the formulation given up to here has to be modified. This is mainly due to the electric

field definition of the electric line source. Utilizing the previous procedure, it can be seen that (2.137), (2.140) and (2.147) have to be modified as

$$J_n(ka)H_n^{(2)}(k\rho') + a_n J_n(ka) + b_n Y_n(ka) = 0, \tag{2.158}$$

$$J_n(k\rho')H_n^{(2)}(kb) + a_n J_n(kb) + b_n Y_n(kb) = c_n H_n^{(2)}(k_0 b), \tag{2.159}$$

$$J_n(k\rho')H_n^{(2)'}(kb) + a_n J_n'(kb) + b_n Y_n'(kb) = c_n \zeta H_n^{(2)'}(k_0 b), \tag{2.160}$$

respectively. The system of equations can be written in matrix form as

$$\begin{bmatrix} J_n(ka) & Y_n(ka) & 0 \\ J_n(kb) & Y_n(kb) & -H_n^{(2)}(k_0 b) \\ J_n'(kb) & Y_n'(kb) & -\zeta H_n^{(2)'}(k_0 b) \end{bmatrix} \begin{bmatrix} a_n \\ b_n \\ c_n \end{bmatrix} = \begin{bmatrix} -J_n(ka)H_n^{(2)}(k\rho') \\ -J_n(k\rho')H_n^{(2)}(kb) \\ -J_n(k\rho')H_n^{(2)'}(kb) \end{bmatrix}. \tag{2.161}$$

Using Symbolic Math Toolbox of MATLAB, the solution to this system of equations can be found as

$$a_n = \frac{A_1 + A_2}{D}, \tag{2.162}$$

$$b_n = \frac{B_1 + B_2}{D}, \tag{2.163}$$

$$c_n = \frac{C_1 + C_2 + C_3}{D}, \tag{2.164}$$

where

$$A_1 = \left[H_n^{(2)}(k_0 b)Y_n'(kb) - \zeta H_n^{(2)'}(k_0 b)Y_n(kb)\right] J_n(ka)H_n^{(2)}(k\rho'), \tag{2.165}$$

$$A_2 = \left[\zeta H_n^{(2)}(kb)H_n^{(2)'}(k_0 b) - H_n^{(2)'}(kb)H_n^{(2)}(k_0 b)\right] Y_n(ka)J_n(k\rho'), \tag{2.166}$$

$$B_1 = \left[\zeta J_n(kb)H_n^{(2)'}(k_0 b) - J_n'(kb)H_n^{(2)}(k_0 b)\right] J_n(ka)H_n^{(2)}(k\rho'), \tag{2.167}$$

$$B_2 = \left[H_n^{(2)}(k_0 b)H_n^{(2)'}(kb) - \zeta H_n^{(2)'}(k_0 b)H_n^{(2)}(kb)\right] J_n(ka)J_n(k\rho'), \tag{2.168}$$

$$C_1 = \left[J_n(kb)Y_n'(kb) - J_n'(kb)Y_n(kb)\right] J_n(ka)H_n^{(2)}(k\rho'), \tag{2.169}$$

$$C_2 = \left[Y_n(ka)J_n'(kb) - Y_n'(kb)J_n(ka)\right] J_n(k\rho')H_n^{(2)}(kb), \tag{2.170}$$

$$C_3 = \left[J_n(ka)Y_n(kb) - J_n(kb)Y_n(ka)\right] J_n(k\rho')H_n^{(2)'}(kb), \tag{2.171}$$

$$\begin{aligned} D = \zeta H_n^{(2)'}(k_0 b) \left[J_n(ka)Y_n(kb) - J_n(kb)Y_n(ka)\right] \\ -H_n^{(2)}(k_0 b) \left[J_n(ka)Y_n'(kb) - J_n'(kb)Y_n(ka)\right]. \end{aligned} \tag{2.172}$$

2.6.10 Numerical Results

Some of the numerical results are shown in Fig. 2.8 for $f = 30\text{GHz}$, $\lambda_0 = 0.01\text{m}$, $a = 0.5\lambda_0$, $b = \lambda_0$, $\rho' = 1.5\lambda_0$, $\phi' = 0^\circ$. In Fig. 2.8 (a) there is a strong focus on the outer surface of the metamaterial. In Fig. 2.8 (b), focus point moves inside the cylinder. Finally in Fig. 2.8 (c) for the DPS case no focusing can be observed.

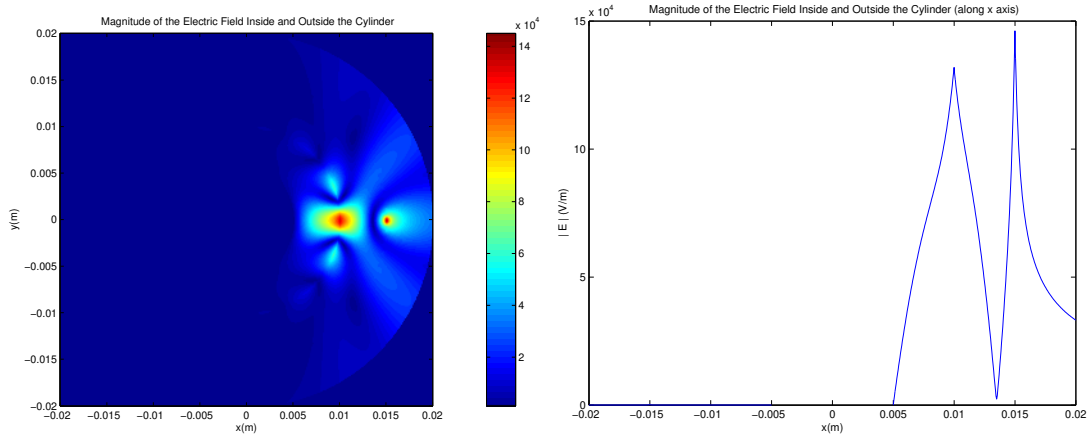

(a) (b)

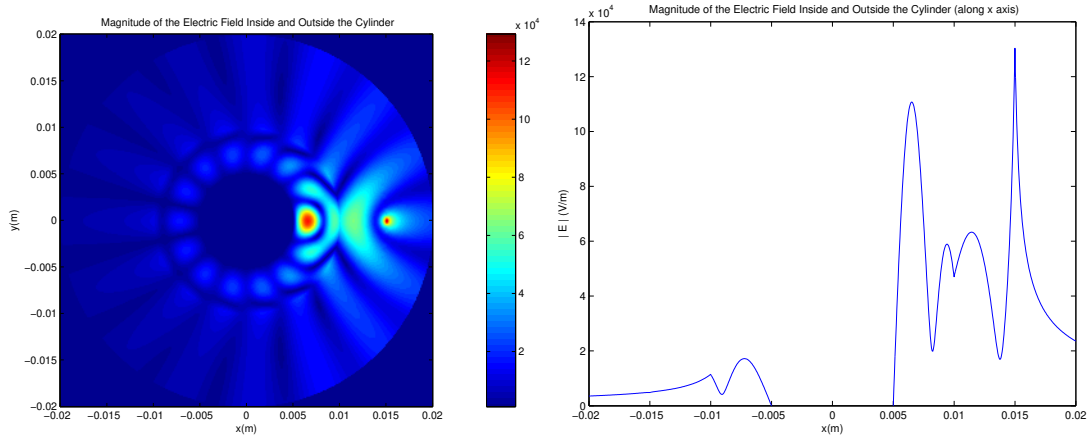

(c) (d)

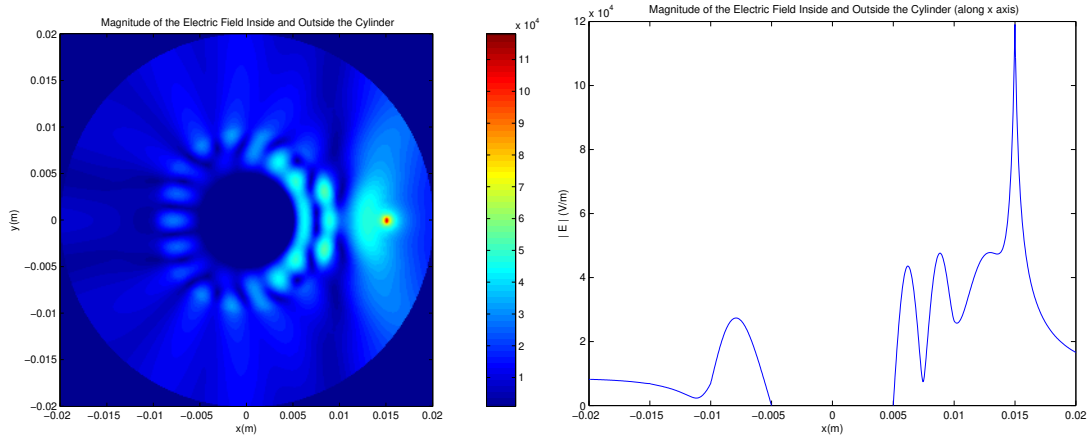

(e) (f)

Figure 2.8: Magnitude of the electric field inside and outside the cylinder. (a)-(b) $\varepsilon_r = -1$, $\mu_r = -1$, (c)-(d) $\varepsilon_r = -2$, $\mu_r = -2$, (e)-(f) $\varepsilon_r = 2$, $\mu_r = 2$

2.7 Normally Incident Plane Wave Scattering by an Infinite Length Metamaterial Coated Conducting Cylinder: TM^z Polarization

2.7.1 Introduction

A uniform plane wave is normally incident on a metamaterial coated conducting cylinder of infinite length. The plane wave travels in the direction which makes an angle ϕ_0 with the $+x$ axis. We will examine here the scattering and transmission by the metamaterial coated conducting cylinder in the case the polarization of the plane wave is TM^z. In the numerical results of this section, the angle of incidence ϕ_0 is selected as π. This corresponds to a plane wave traveling in the $-x$ direction, which is the case we have investigated in Section 2.4. The problem geometry is depicted in Fig. 2.9.

2.7.2 Problem Geometry

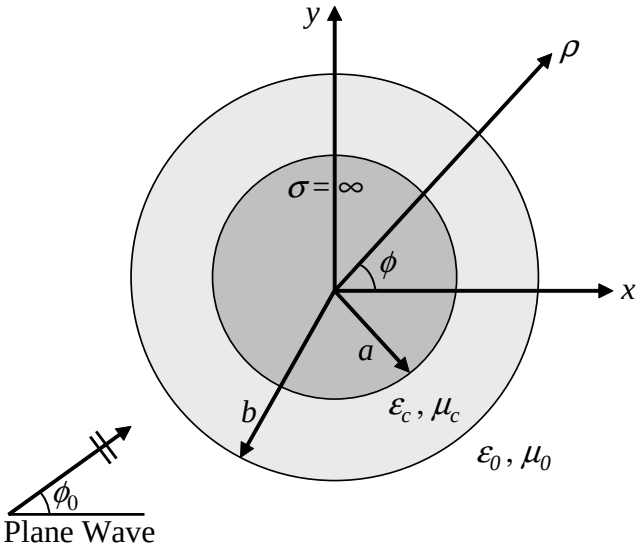

Figure 2.9: Plane wave normally incident on a metamaterial coated conducting cylinder.

2.7.3 Uniform Plane Wave and Incident Electric Field

Let us assume that a TM^z polarized uniform plane wave is traveling in the direction which makes an angle ϕ_0 with the $+x$ axis. Electric field is directed along the $+z$ axis. Referring to Figure 2.9 the electric field can be written as

$$E_z^i = E_0 e^{-jk_0(x\cos\phi_0 + y\sin\phi_0)}, \tag{2.173}$$

where

$$x = \rho\cos\phi \ , \ y = \rho\sin\phi. \tag{2.174}$$

Therefore,

$$\begin{aligned} E_z^i &= E_0 e^{-jk_0(\rho\cos\phi\cos\phi_0 + \rho\sin\phi\sin\phi_0)}, \\ &= E_0 e^{-jk_0\rho(\cos\phi\cos\phi_0 + \sin\phi\sin\phi_0)}, \\ &= E_0 e^{-jk_0\rho\cos(\phi-\phi_0)}. \end{aligned} \tag{2.175}$$

The plane wave can be represented by an infinite sum of cylindrical wave functions:

$$E_z^i = E_0 e^{-jk_0\rho\cos(\phi-\phi_0)} = E_0 \sum_{n=-\infty}^{+\infty} a_n J_n(k_0\rho) e^{jn\phi}, \tag{2.176}$$

since it must be 2π periodic in ϕ and finite at $\rho = 0$. Our next step is to find the coefficients a_n. Multiplying both sides of (2.176) by $e^{jm\phi}$, where m is an integer, and integrating from 0 to 2π,

$$E_0 \int_0^{2\pi} e^{-j(k_0\rho\cos(\phi-\phi_0)+m\phi)} d\phi = E_0 \int_0^{2\pi} \left[\sum_{n=-\infty}^{+\infty} a_n J_n(k_0\rho) e^{j(n-m)\phi} \right] d\phi. \tag{2.177}$$

Dropping 'E_0's and interchanging the integration and summation, we have

$$\int_0^{2\pi} e^{-j(k_0\rho\cos(\phi-\phi_0)+m\phi)} d\phi = \sum_{n=-\infty}^{+\infty} a_n J_n(k_0\rho) \int_0^{2\pi} e^{j(n-m)\phi} d\phi. \tag{2.178}$$

Utilizing the orthogonality condition of

$$\int_0^{2\pi} e^{j(n-m)\phi} d\phi = \begin{cases} 2\pi, & n = m \\ 0\ , & n \neq m \end{cases}, \tag{2.179}$$

the right hand side of (2.178) reduces to

$$\sum_{n=-\infty}^{+\infty} a_n J_n(k_0\rho) \int_0^{2\pi} e^{j(n-m)\phi} d\phi = 2\pi a_m J_m(k_0\rho). \tag{2.180}$$

Using the integral of

$$\int_0^{2\pi} e^{j(z\cos\phi + n\phi)} d\phi = 2\pi j^n J_n(z), \tag{2.181}$$

and by a simple transformation $\varphi = \phi - \phi_0$, the left side of (2.178) can be written as

$$\int_0^{2\pi} e^{-j(k_0\rho\cos(\phi-\phi_0)+m\phi)} d\phi = e^{-jm\phi_0} 2\pi j^{-m} J_{-m}(-k_0\rho). \tag{2.182}$$

Since

$$J_{-m}(x) = (-1)^m J_m(x), \tag{2.183}$$

and

$$J_m(-x) = (-1)^m J_m(x), \tag{2.184}$$

(2.182) can be written as

$$\begin{aligned} \int_0^{2\pi} e^{-j(k_0\rho\cos(\phi-\phi_0)+m\phi)} d\phi &= e^{-jm\phi_0} 2\pi j^{-m} J_{-m}(-k_0\rho), \\ &= e^{-jm\phi_0} 2\pi j^{-m} J_m(k_0\rho). \end{aligned} \tag{2.185}$$

Using (2.180) and (2.185) reduces (2.178) to

$$e^{-jm\phi_0} 2\pi j^{-m} J_m(k_0\rho) = 2\pi a_m J_m(k_0\rho). \tag{2.186}$$

Thus

$$a_m = j^{-m} e^{-jm\phi_0}. \tag{2.187}$$

Therefore (2.176) can be written as

$$\begin{aligned} E_z^i &= E_0 e^{-jk_0\rho\cos(\phi-\phi_0)}, \\ &= E_0 \sum_{n=-\infty}^{+\infty} a_n J_n(k_0\rho) e^{jn\phi}, \\ &= E_0 \sum_{n=-\infty}^{+\infty} j^{-n} J_n(k_0\rho) e^{jn(\phi-\phi_0)}. \end{aligned} \tag{2.188}$$

2.7.4 Scattered and Transmitted Electric Fields

Similar to the incident field expression in (2.188), we will define the scattered and transmitted electric fields in series expansion form, respectively as follows:

$$E_z^s = E_0 \sum_{n=-\infty}^{+\infty} j^{-n} c_n H_n^{(2)}(k_0\rho) e^{jn(\phi-\phi_0)}, \tag{2.189}$$

$$E_z^t = E_0 \sum_{n=-\infty}^{+\infty} j^{-n} \left[a_n J_n(k_c\rho) + b_n Y_n(k_c\rho)\right] e^{jn(\phi-\phi_0)}. \tag{2.190}$$

2.7.5 Boundary Conditions for Electric Fields

The tangential components of the electric fields are continuous on the outer surface of the metamaterial coating, due to the boundary conditions. Also, on the inner surface of the metamaterial coating (i.e., on the conducting cylinder surface) tangential electric field should vanish. Therefore,

$$E_z^t(\rho = a) = 0, \tag{2.191}$$

$$E_0 \sum_{n=-\infty}^{+\infty} j^{-n} \left[a_n J_n(k_c\rho) + b_n Y_n(k_c\rho)\right] e^{jn(\phi-\phi_0)}\Big|_{\rho=a} = 0, \tag{2.192}$$

$$a_n J_n(k_c a) + b_n Y_n(k_c a) = 0, \tag{2.193}$$

$$E_z^i(\rho = b) + E_z^s(\rho = b) = E_z^t(\rho = b), \tag{2.194}$$

$$E_0 \sum_{n=-\infty}^{+\infty} j^{-n} \left[J_n(k_0 b) + c_n H_n^{(2)}(k_0 b)\right] e^{jn(\phi-\phi_0)} = E_0 \sum_{n=-\infty}^{+\infty} j^{-n} \left[a_n J_n(k_c b) + b_n Y_n(k_c b)\right] e^{jn(\phi-\phi_0)}, \tag{2.195}$$

$$J_n(k_0 b) + c_n H_n^{(2)}(k_0 b) = a_n J_n(k_c b) + b_n Y_n(k_c b). \tag{2.196}$$

2.7.6 Incident, Scattered and Transmitted Magnetic Fields

Utilizing (2.49) and (2.50), the tangential components of the magnetic fields are obtained as

$$H_\phi^i = E_0 \frac{1}{j\omega\mu_0} k_0 \sum_{n=-\infty}^{+\infty} j^{-n} J_n'(k_0\rho) e^{jn(\phi-\phi_0)}, \tag{2.197}$$

$$H_\phi^s = E_0 \frac{1}{j\omega\mu_0} k_0 \sum_{n=-\infty}^{+\infty} j^{-n} c_n H_n^{(2)'}(k_0\rho) e^{jn(\phi-\phi_0)}, \tag{2.198}$$

$$H_\phi^t = E_0 \frac{1}{j\omega\mu} k_c \sum_{n=-\infty}^{+\infty} j^{-n} \left[a_n J_n'(k_c\rho) + b_n Y_n'(k_c\rho)\right] e^{jn(\phi-\phi_0)}. \tag{2.199}$$

2.7.7 Boundary Conditions for Magnetic Fields

Tangential components of the magnetic fields are continuous on the outer surface of the metamaterial coating, due to the boundary conditions. Therefore,

$$H_\phi^i(\rho=b) + H_\phi^s(\rho=b) = H_\phi^t(\rho=b), \tag{2.200}$$

$$\begin{aligned} E_0 \frac{1}{j\omega\mu_0} k_0 \sum_{n=-\infty}^{+\infty} j^{-n} \left[J_n'(k_0 b) + c_n H_n^{(2)'}(k_0 b)\right] e^{jn(\phi-\phi_0)} \\ = E_0 \frac{1}{j\omega\mu} k_c \sum_{n=-\infty}^{+\infty} j^{-n} \left[a_n J_n'(k_c b) + b_n Y_n'(k_c b)\right] e^{jn(\phi-\phi_0)} \end{aligned} \tag{2.201}$$

$$\frac{k_0}{\mu_0}\left[J_n'(k_0 b) + c_n H_n^{(2)'}(k_0 b)\right] = \frac{k_c}{\mu}\left[a_n J_n'(k_c b) + b_n Y_n'(k_c b)\right] \tag{2.202}$$

Using (2.58) in (2.231),

$$\zeta J_n'(k_0 b) + c_n \zeta H_n^{(2)'}(k_0 b) = a_n J_n'(k_c b) + b_n Y_n'(k_c b). \tag{2.203}$$

2.7.8 Simultaneous Solution of the Boundary Conditions for Electric and Magnetic Fields

Now we have three unknowns and three equations. Rearranging equations (2.228), (2.222) and (2.232) we get

$$J_n(k_c a)a_n + Y_n(k_c a)b_n = 0, \tag{2.204}$$

$$J_n(k_c b)a_n + Y_n(k_c b)b_n - H_n^{(2)}(k_0 b)c_n = J_n(k_0 b), \tag{2.205}$$

$$J_n'(k_c b)a_n + Y_n'(k_c b)b_n - \zeta H_n^{(2)'}(k_0 b)c_n = \zeta J_n'(k_0 b), \tag{2.206}$$

or in matrix form

$$\begin{bmatrix} J_n(k_c a) & Y_n(k_c a) & 0 \\ J_n(k_c b) & Y_n(k_c b) & -H_n^{(2)}(k_0 b) \\ J_n'(k_c b) & Y_n'(k_c b) & -\zeta H_n^{(2)'}(k_0 b) \end{bmatrix} \begin{bmatrix} a_n \\ b_n \\ c_n \end{bmatrix} = \begin{bmatrix} 0 \\ J_n(k_0 b) \\ \zeta J_n'(k_0 b) \end{bmatrix}. \tag{2.207}$$

Using Symbolic Math Toolbox of MATLAB, the solution to this system of equations can be found as:

$$a_n = \frac{\zeta Y_n(k_c a)\left[H_n^{(2)}(k_0 b)J_n'(k_0 b) - H_n^{(2)'}(k_0 b)J_n(k_0 b)\right]}{D}, \tag{2.208}$$

$$b_n = \frac{\zeta J_n(k_c a)\left[J_n(k_0 b)H_n^{(2)'}(k_0 b) - J_n'(k_0 b)H_n^{(2)}(k_0 b)\right]}{D}, \tag{2.209}$$

$$c_n = \frac{N}{D}, \tag{2.210}$$

where

$$\begin{aligned} N = {} & J_n(k_0 b)\left[J_n(k_c a)Y_n'(k_c b) - J_n'(k_c b)Y_n(k_c a)\right] \\ & - \zeta J_n'(k_0 b)\left[J_n(k_c a)Y_n(k_c b) - J_n(k_c b)Y_n(k_c a)\right], \end{aligned} \tag{2.211}$$

$$\begin{aligned} D = {} & \zeta H_n^{(2)'}(k_0 b)\left[J_n(k_c a)Y_n(k_c b) - J_n(k_c b)Y_n(k_c a)\right] \\ & - H_n^{(2)}(k_0 b)\left[J_n(k_c a)Y_n'(k_c b) - J_n'(k_c b)Y_n(k_c a)\right]. \end{aligned} \tag{2.212}$$

Using the following Wronskian will further simplify a_n and b_n:

$$J_n(x)H_n^{(2)'}(x) - J_n'(x)H_n^{(2)}(x) = \frac{-2j}{\pi x}. \tag{2.213}$$

2.7.9 Numerical Results

Fig. 2.10 shows some of the numerical results when $f = 30\text{GHz}$, $\lambda_0 = 0.01\text{m}$, $a = 0.5\lambda_0$, $b = \lambda_0$. In Fig. 2.10 (a) there are two foci: one of them is inside the metamaterial and the other one is outside. In Fig. 2.10 (b) there are three foci inside the metamaterial close to the conducting cylinder. In Fig. 2.10 (c) the foci are distributed inside the cylinder. Though, one of them is stronger.

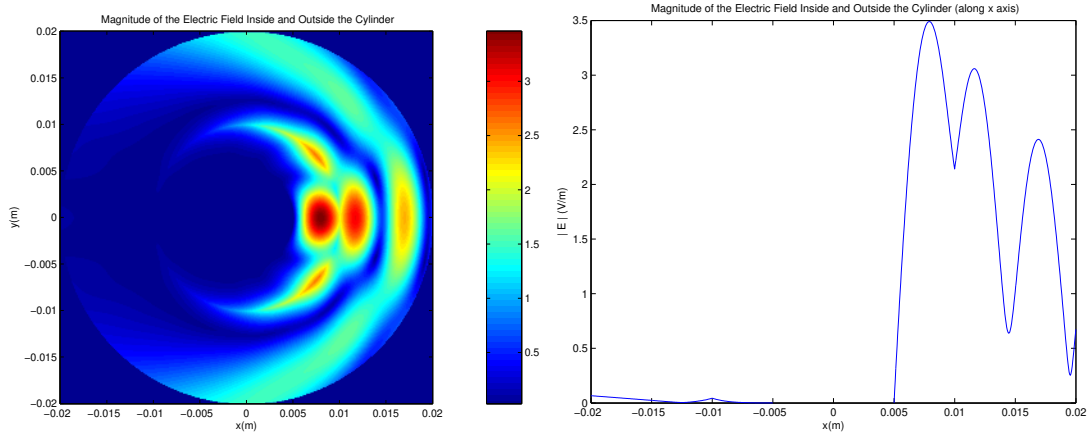

(a) (b)

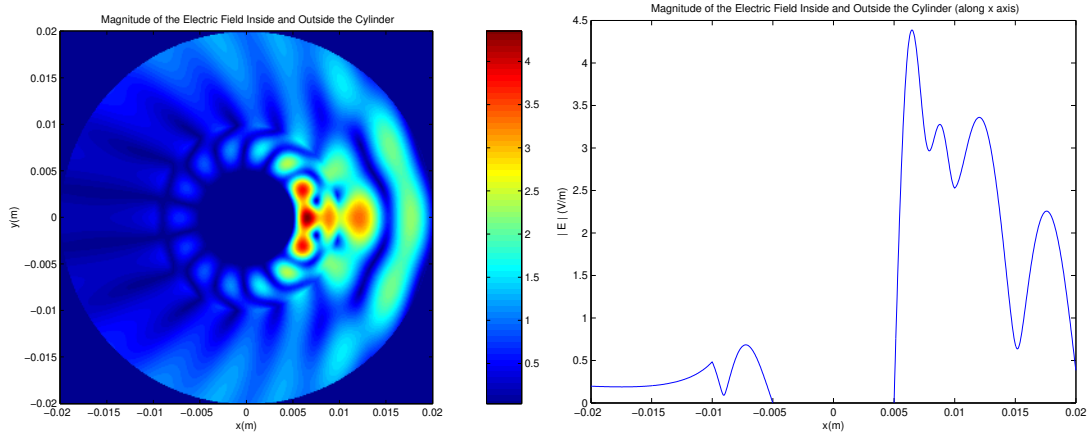

(c) (d)

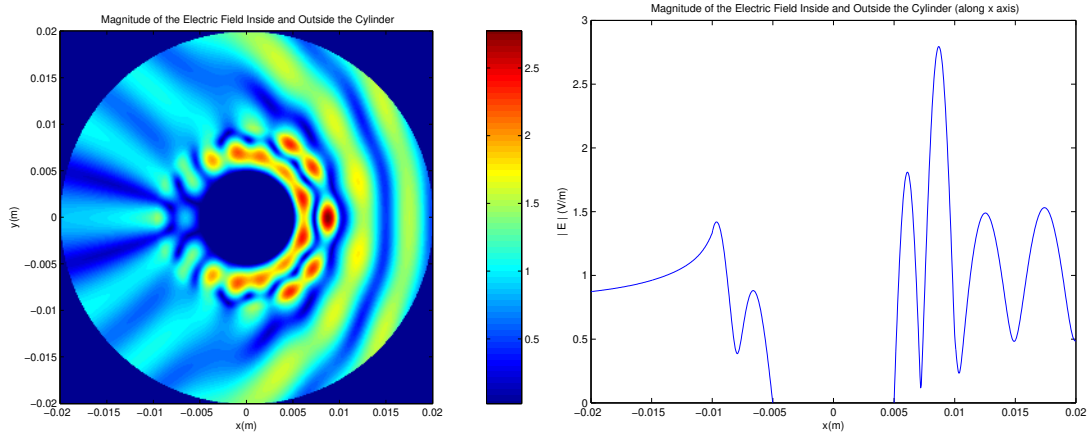

(e) (f)

Figure 2.10: Magnitude of the electric field inside and outside the cylinder. (a)-(b) $\varepsilon_r = -1$, $\mu_r = -1$, (c)-(d) $\varepsilon_r = -2$, $\mu_r = -2$, (e)-(f) $\varepsilon_r = 2$, $\mu_r = 2$

2.8 Normally Incident Plane Wave Scattering by an Infinite Length Metamaterial Coated Conducting Cylinder: TE^z Polarization

2.8.1 Introduction

A uniform plane wave is normally incident on a metamaterial coated conducting cylinder of infinite length. The plane wave travels in the direction which makes an angle ϕ_0 with the $+x$ axis. We will examine here the scattering and transmission by the metamaterial coated conducting cylinder in the case the polarization of the plane wave is TE^z. The problem geometry is depicted in Fig. 2.11.

2.8.2 Problem Geometry

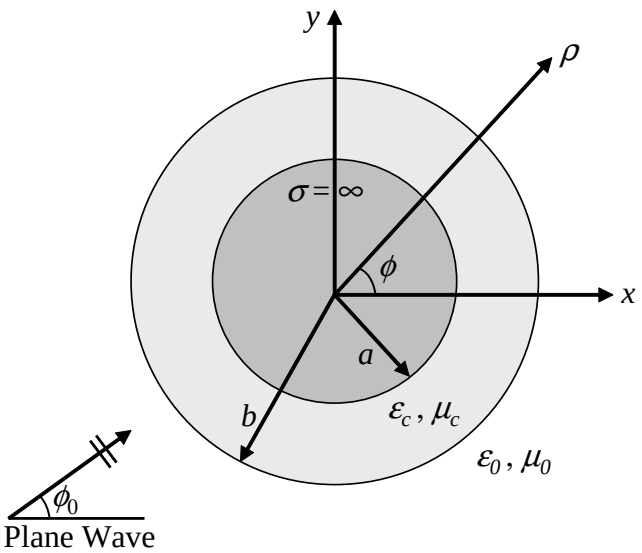

Figure 2.11: Plane wave normally incident on a metamaterial coated conducting cylinder.

2.8.3 Uniform Plane Wave and Incident Magnetic Field

Let us assume that a TE^z polarized uniform plane wave is traveling in the direction which makes an angle ϕ_0 with the $+x$ axis. Magnetic field is directed along the $+z$ axis. Referring to Figure 2.11 the magnetic field can be written as

$$H_z^i = H_0 e^{-jk_0(x\cos\phi_0 + y\sin\phi_0)}, \tag{2.214}$$

where

$$x = \rho\cos\phi \ , \ y = \rho\sin\phi. \tag{2.215}$$

Therefore,

$$\begin{aligned} H_z^i &= H_0 e^{-jk_0(\rho\cos\phi\cos\phi_0 + \rho\sin\phi\sin\phi_0)}, \\ &= H_0 e^{-jk_0\rho(\cos\phi\cos\phi_0 + \sin\phi\sin\phi_0)}, \\ &= H_0 e^{-jk_0\rho\cos(\phi-\phi_0)}. \end{aligned} \tag{2.216}$$

Following the same procedure in Section 2.7, incident magnetic field can be written as

$$\begin{aligned} H_z^i &= H_0 e^{-jk_0\rho\cos(\phi-\phi_0)}, \\ &= H_0 \sum_{n=-\infty}^{+\infty} j^{-n} J_n(k_0\rho) e^{jn(\phi-\phi_0)}. \end{aligned} \tag{2.217}$$

2.8.4 Scattered and Transmitted Magnetic Fields

Similar to the incident field expression in (2.217), we will define the scattered and transmitted magnetic fields in series expansion form respectively as follows:

$$H_z^s = H_0 \sum_{n=-\infty}^{+\infty} j^{-n} c_n H_n^{(2)}(k_0\rho) e^{jn(\phi-\phi_0)}, \tag{2.218}$$

$$H_z^t = H_0 \sum_{n=-\infty}^{+\infty} j^{-n} \left[a_n J_n(k_c\rho) + b_n Y_n(k_c\rho)\right] e^{jn(\phi-\phi_0)}. \tag{2.219}$$

2.8.5 Boundary Conditions for Magnetic Fields

The tangential components of the magnetic fields are continuous on the outer surface of the metamaterial coating, due to the boundary conditions. Therefore,

$$H_z^i(\rho = b) + H_z^s(\rho = b) = H_z^t(\rho = b), \tag{2.220}$$

$$H_0 \sum_{n=-\infty}^{+\infty} j^{-n} \left[J_n(k_0 b) + c_n H_n^{(2)}(k_0 b) \right] e^{jn(\phi-\phi_0)} = H_0 \sum_{n=-\infty}^{+\infty} j^{-n} \left[a_n J_n(k_c b) + b_n Y_n(k_c b) \right] e^{jn(\phi-\phi_0)}, \tag{2.221}$$

$$J_n(k_0 b) + c_n H_n^{(2)}(k_0 b) = a_n J_n(k_c b) + b_n Y_n(k_c b). \tag{2.222}$$

2.8.6 Incident, Scattered and Transmitted Electric Fields

Utilizing (2.112) and (2.50), the tangential components of the electric fields are obtained as

$$E_\phi^i = H_0 \frac{-1}{j\omega\varepsilon_0} k_0 \sum_{n=-\infty}^{+\infty} j^{-n} J_n'(k_0\rho) e^{jn(\phi-\phi_0)}, \tag{2.223}$$

$$E_\phi^s = H_0 \frac{-1}{j\omega\varepsilon_0} k_0 \sum_{n=-\infty}^{+\infty} j^{-n} c_n H_n^{(2)'}(k_0\rho) e^{jn(\phi-\phi_0)}, \tag{2.224}$$

$$E_\phi^t = H_0 \frac{-1}{j\omega\varepsilon} k_c \sum_{n=-\infty}^{+\infty} j^{-n} \left[a_n J_n'(k_c\rho) + b_n Y_n'(k_c\rho) \right] e^{jn(\phi-\phi_0)}. \tag{2.225}$$

2.8.7 Boundary Conditions for Electric Fields

The tangential components of the electric fields are continuous on the outer surface of the metamaterial coating, due to the boundary conditions. Also, on the inner surface of the metamaterial coating (i.e., on the conducting cylinder surface) tangential electric field should vanish. Therefore,

$$E_\phi^t(\rho = a) = 0, \tag{2.226}$$

$$H_0 \frac{-1}{j\omega\varepsilon} k_c \sum_{n=-\infty}^{+\infty} j^{-n} \left[a_n J_n'(k_c\rho) + b_n Y_n'(k_c\rho) \right] e^{jn(\phi-\phi_0)} \Bigg|_{\rho=a} = 0, \tag{2.227}$$

$$a_n J_n'(k_c a) + b_n Y_n'(k_c a) = 0, \tag{2.228}$$

$$E_\phi^i(\rho = b) + E_\phi^s(\rho = b) = E_\phi^t(\rho = b), \tag{2.229}$$

$$\begin{aligned} H_0 \frac{-1}{j\omega\varepsilon_0} k_0 \sum_{n=-\infty}^{+\infty} j^{-n} \left[J_n'(k_0 b) + c_n H_n^{(2)'}(k_0 b) \right] e^{jn(\phi-\phi_0)} \\ = H_0 \frac{-1}{j\omega\varepsilon} k_c \sum_{n=-\infty}^{+\infty} j^{-n} \left[a_n J_n'(k_c b) + b_n Y_n'(k_c b) \right] e^{jn(\phi-\phi_0)} \end{aligned} \tag{2.230}$$

$$\frac{k_0}{\varepsilon_0} \left[J_n'(k_0 b) + c_n H_n^{(2)'}(k_0 b) \right] = \frac{k_c}{\varepsilon} \left[a_n J_n'(k_c b) + b_n Y_n'(k_c b) \right] \tag{2.231}$$

Using (2.119) in (2.231),

$$J_n'(k_0 b) + c_n H_n^{(2)'}(k_0 b) = a_n \zeta J_n'(k_c b) + b_n \zeta Y_n'(k_c b). \tag{2.232}$$

2.8.8 Simultaneous Solution of the Boundary Conditions for Electric and Magnetic Fields

Now we have three unknowns and three equations. Rearranging equations (2.228), (2.222) and (2.232) we get

$$J_n'(k_c a) a_n + Y_n'(k_c a) b_n = 0, \tag{2.233}$$

$$J_n(k_c b) a_n + Y_n(k_c b) b_n - H_n^{(2)}(k_0 b) c_n = J_n(k_0 b), \tag{2.234}$$

$$\zeta J_n'(k_c b) a_n + \zeta Y_n'(k_c b) b_n - H_n^{(2)'}(k_0 b) c_n = J_n'(k_0 b), \tag{2.235}$$

or in matrix form

$$\begin{bmatrix} J_n'(k_c a) & Y_n'(k_c a) & 0 \\ J_n(k_c b) & Y_n(k_c b) & -H_n^{(2)}(k_0 b) \\ \zeta J_n'(k_c b) & \zeta Y_n'(k_c b) & -H_n^{(2)'}(k_0 b) \end{bmatrix} \begin{bmatrix} a_n \\ b_n \\ c_n \end{bmatrix} = \begin{bmatrix} 0 \\ J_n(k_0 b) \\ J_n'(k_0 b) \end{bmatrix}. \tag{2.236}$$

Using Symbolic Math Toolbox of MATLAB, the solution to this system of equations can be found as:

$$a_n = \frac{Y_n'(k_c a)\left[H_n^{(2)}(k_0 b)J_n'(k_0 b) - H_n^{(2)'}(k_0 b)J_n(k_0 b)\right]}{D}, \tag{2.237}$$

$$b_n = \frac{J_n'(k_c a)\left[J_n(k_0 b)H_n^{(2)'}(k_0 b) - J_n'(k_0 b)H_n^{(2)}(k_0 b)\right]}{D}, \tag{2.238}$$

$$c_n = \frac{N}{D}, \tag{2.239}$$

where

$$\begin{aligned} N = {} & \zeta J_n(k_0 b)\left[J_n'(k_c a)Y_n'(k_c b) - J_n'(k_c b)Y_n'(k_c a)\right] \\ & - J_n'(k_0 b)\left[J_n'(k_c a)Y_n(k_c b) - J_n(k_c b)Y_n'(k_c a)\right], \end{aligned} \tag{2.240}$$

$$\begin{aligned} D = {} & H_n^{(2)'}(k_0 b)\left[J_n'(k_c a)Y_n(k_c b) - J_n(k_c b)Y_n'(k_c a)\right] \\ & - \zeta H_n^{(2)}(k_0 b)\left[J_n'(k_c a)Y_n'(k_c b) - J_n'(k_c b)Y_n'(k_c a)\right]. \end{aligned} \tag{2.241}$$

Using the following Wronskian will further simplify a_n and b_n:

$$J_n(x)H_n^{(2)'}(x) - J_n'(x)H_n^{(2)}(x) = \frac{-2j}{\pi x}. \tag{2.242}$$

2.9 Obliquely Incident Plane Wave Scattering by an Infinite Length Metamaterial Cylinder: TM^z Polarization

2.9.1 Introduction

A uniform plane wave is obliquely incident on a metamaterial cylinder of infinite length. The plane wave travels in the direction which makes an angle ϕ_0 with the $+x$ axis and θ_0 with the $-z$ axis. We will examine here the scattering and transmission by the metamaterial cylinder in the case the polarization of the plane wave is TM^z. The problem geometry is depicted in Fig. 2.12.

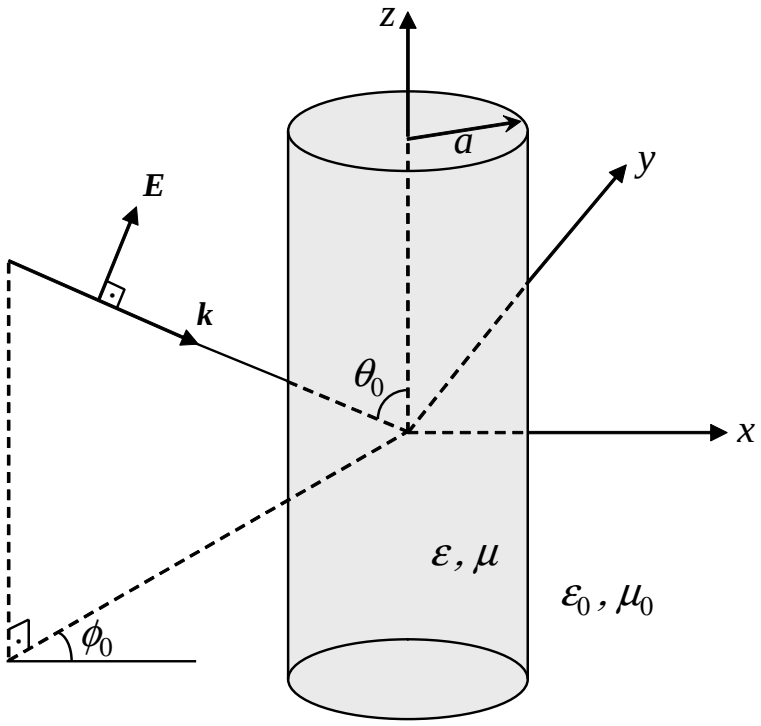

Figure 2.12: Uniform plane wave obliquely incident on a metamaterial cylinder: TM^z Polarization.

2.9.2 Incident, Scattered and Transmitted Electric Fields (z components)

Referring to Fig. 2.12, the incident electric field can be written as

$$\mathbf{E}^i = (\widehat{a}_x E_0 \cos\theta_0 \cos\phi_0 + \widehat{a}_y E_0 \cos\theta_0 \sin\phi_0 + \widehat{a}_z E_0 \sin\theta_0) .e^{-jk_0 x \sin\theta_0 \cos\phi_0} e^{-jk_0 y \sin\theta_0 \sin\phi_0} e^{jk_0 z \cos\theta_0}, \tag{2.243}$$

also since $x = \rho\cos\phi$ and $y = \rho\sin\phi$, the z component of the electric field can be expressed as

$$\begin{aligned} E_z^i &= E_0 \sin\theta_0 e^{-jk_0\rho\sin\theta_0(\cos\phi\cos\phi_0+\sin\phi\sin\phi_0)} e^{jk_0 z\cos\theta_0} \\ &= E_0 \sin\theta_0 e^{-jk_0\rho\sin\theta_0\cos(\phi-\phi_0)} e^{jk_0 z\cos\theta_0}. \end{aligned} \tag{2.244}$$

In Section 2.7 Eqn. (2.188), we have previously derived that

$$E_0 e^{-jk_0\rho\cos(\phi-\phi_0)} = E_0 \sum_{n=-\infty}^{+\infty} j^{-n} J_n(k_0\rho) e^{jn(\phi-\phi_0)}. \tag{2.245}$$

Utilizing (2.245), (2.244) can be written as

$$E_z^i = E_0 \sin\theta_0 e^{jk_0 z\cos\theta_0} \sum_{n=-\infty}^{+\infty} j^{-n} J_n(k_0\rho\sin\theta_0) e^{jn(\phi-\phi_0)}. \tag{2.246}$$

Since the cylinder is of infinite length, the fields are periodic in the z direction and vary according to the factor $e^{jk_0 z\cos\theta_0}$ [29]. The z components of the scattered and transmitted electric fields are expressed similar to (2.246) as

$$E_z^s = E_0 \sin\theta_0 e^{jk_0 z\cos\theta_0} \sum_{n=-\infty}^{+\infty} j^{-n} c_n H_n^{(2)}(k_0\rho\sin\theta_0) e^{jn(\phi-\phi_0)}, \tag{2.247}$$

$$E_z^t = E_0 \sin\theta_0 e^{jk_0 z\cos\theta_0} \sum_{n=-\infty}^{+\infty} j^{-n} a_n J_n(k\rho\sin\theta_1) e^{jn(\phi-\phi_0)}. \tag{2.248}$$

The obliquely incident wave travels both in longitudinal and transverse directions, as shown in Fig. 2.13. Due to phase matching, the propagation constant in

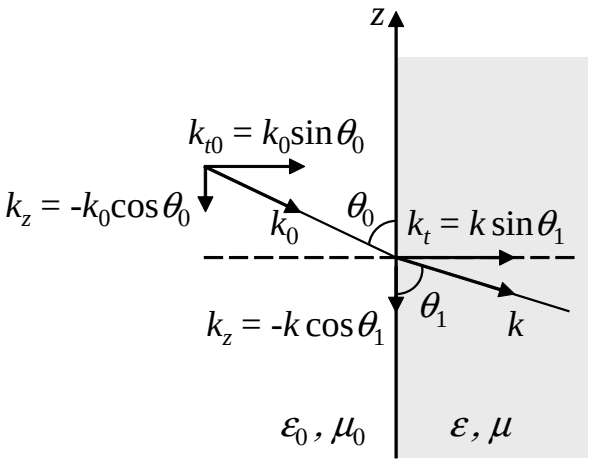

Figure 2.13: Longitudinal and transverse components of the incident and transmitted fields.

the longitudinal direction, k_z, should be the same for free space and metamaterial media. Therefore,

$$k_0 \cos\theta_0 = k \cos\theta_1, \tag{2.249}$$

$$\cos\theta_1 = \frac{k_0}{k} \cos\theta_0, \tag{2.250}$$

$$\sin\theta_1 = \begin{cases} \sqrt{1 - \left(\frac{k_0}{k}\right)^2 \cos^2\theta_0} & |\frac{k_0}{k} \cos\theta_0| \leq 1, \\ -j\sqrt{\left(\frac{k_0}{k}\right)^2 \cos^2\theta_0 - 1} & |\frac{k_0}{k} \cos\theta_0| > 1, \end{cases} \tag{2.251}$$

and

$$k_t = k \sin\theta_1 \tag{2.252}$$

is the transverse propagation constant in metamaterial medium. The arguments of the Bessel and Hankel functions in (2.246)-(2.248) basically include the transverse propagation constants.

Remark: Note that, since the metamaterial medium we consider here is not limited to only DPS metamaterials, (2.252) should not be further simplified to:

$$k_t = \begin{cases} \sqrt{k^2 - k_0^2 \cos^2\theta_0} & |\frac{k_0}{k} \cos\theta_0| \leq 1, \\ -j\sqrt{k_0^2 \cos^2\theta_0 - k^2} & |\frac{k_0}{k} \cos\theta_0| > 1. \end{cases} \tag{2.253}$$

As an example, consider a DNG medium with $k = -k_0$ at normal incidence ($\theta_0 = \pi/2$). Since the propagation is only in the transverse direction, (2.252) gives $k_t = -k_0$, which is the correct solution. However, the aforementioned simplification in (2.253) would yield $k_t = k_0$, which is wrong.

2.9.3 Incident, Scattered and Transmitted Magnetic Fields (z components)

Smooth perfectly conducting infinite cylinders do not depolarize obliquely incident waves. However, for scattering by dielectric or dielectric coated conducting cylinders, depolarization is inevitable in order to satisfy the Maxwell's equations [27, 29]. Therefore, there exist longitudinal magnetic field components for the scattered and transmitted waves:

$$H_z^i = 0, \tag{2.254}$$

$$H_z^s = E_0 \sin\theta_0 e^{jk_0 z\cos\theta_0} \sum_{n=-\infty}^{+\infty} j^{-n}\widetilde{c}_n H_n^{(2)}(k_0\rho\sin\theta_0)e^{jn(\phi-\phi_0)}, \tag{2.255}$$

$$H_z^t = E_0 \sin\theta_0 e^{jk_0 z\cos\theta_0} \sum_{n=-\infty}^{+\infty} j^{-n}\widetilde{a}_n J_n(k\rho\sin\theta_1)e^{jn(\phi-\phi_0)}. \tag{2.256}$$

2.9.4 ϕ Components of the Incident, Scattered and Transmitted Electric and Magnetic Fields

The ϕ components of the incident, scattered and transmitted electric and magnetic fields are derived from their z components, utilizing Maxwell's Equations, in Appendix B. They are found to be:

$$E_\phi^i = -\frac{E_0\cos\theta_0}{k_0\rho\sin\theta_0} e^{jk_0 z\cos\theta_0} \sum_{n=-\infty}^{+\infty} nj^{-n}J_n(k_0\rho\sin\theta_0)e^{jn(\phi-\phi_0)}, \tag{2.257}$$

$$E_{\phi}^{s} = -\frac{E_0 \cos\theta_0}{k_0 \rho \sin\theta_0} e^{jk_0 z\cos\theta_0} \sum_{n=-\infty}^{+\infty} n j^{-n} c_n H_n^{(2)}(k_0\rho\sin\theta_0) e^{jn(\phi-\phi_0)}$$
$$+ jE_0\eta_0 e^{jk_0 z\cos\theta_0} \sum_{n=-\infty}^{+\infty} j^{-n} \widetilde{c}_n H_n^{(2)'}(k_0\rho\sin\theta_0) e^{jn(\phi-\phi_0)}, \tag{2.258}$$

$$E_{\phi}^{t} = -\frac{E_0 k_0 \sin\theta_0 \cos\theta_0}{k^2 \rho \sin^2\theta_1} e^{jk_0 z\cos\theta_0} \sum_{n=-\infty}^{+\infty} n j^{-n} a_n J_n(k\rho\sin\theta_1) e^{jn(\phi-\phi_0)}$$
$$+ jE_0\zeta\eta_0 \frac{\sin\theta_0}{\sin\theta_1} e^{jk_0 z\cos\theta_0} \sum_{n=-\infty}^{+\infty} j^{-n} \widetilde{a}_n J_n'(k\rho\sin\theta_1) e^{jn(\phi-\phi_0)}, \tag{2.259}$$

$$H_{\phi}^{i} = -j\frac{E_0}{\eta_0} e^{jk_0 z\cos\theta_0} \sum_{n=-\infty}^{+\infty} j^{-n} J_n'(k_0\rho\sin\theta_0) e^{jn(\phi-\phi_0)}, \tag{2.260}$$

$$H_{\phi}^{s} = -\frac{E_0 \cos\theta_0}{k_0 \rho \sin\theta_0} e^{jk_0 z\cos\theta_0} \sum_{n=-\infty}^{+\infty} n j^{-n} \widetilde{c}_n H_n^{(2)}(k_0\rho\sin\theta_0) e^{jn(\phi-\phi_0)}$$
$$- j\frac{E_0}{\eta_0} e^{jk_0 z\cos\theta_0} \sum_{n=-\infty}^{+\infty} j^{-n} c_n H_n^{(2)'}(k_0\rho\sin\theta_0) e^{jn(\phi-\phi_0)}, \tag{2.261}$$

$$H_{\phi}^{t} = -\frac{E_0 k_0 \sin\theta_0 \cos\theta_0}{k^2 \rho \sin^2\theta_1} e^{jk_0 z\cos\theta_0} \sum_{n=-\infty}^{+\infty} n j^{-n} \widetilde{a}_n J_n(k\rho\sin\theta_1) e^{jn(\phi-\phi_0)}$$
$$- j\frac{E_0}{\zeta\eta_0} \frac{\sin\theta_0}{\sin\theta_1} e^{jk_0 z\cos\theta_0} \sum_{n=-\infty}^{+\infty} j^{-n} a_n J_n'(k\rho\sin\theta_1) e^{jn(\phi-\phi_0)}. \tag{2.262}$$

2.9.5 Boundary Conditions and Their Solution

Tangential components of the electric and magnetic fields should be continuous on the surface of the metamaterial cylinder. Therefore,

$$E_z^i(\rho=a) + E_z^s(\rho=a) = E_z^t(\rho=a), \tag{2.263}$$

$$H_z^i(\rho=a) + H_z^s(\rho=a) = H_z^t(\rho=a), \tag{2.264}$$

$$E_{\phi}^i(\rho=a) + E_{\phi}^s(\rho=a) = E_{\phi}^t(\rho=a), \tag{2.265}$$

$$H_{\phi}^i(\rho=a) + H_{\phi}^s(\rho=a) = H_{\phi}^t(\rho=a), \tag{2.266}$$

which leads to

$$J_n(k_0 a\sin\theta_0) + c_n H_n^{(2)}(k_0 a\sin\theta_0) = a_n J_n(ka\sin\theta_1), \tag{2.267}$$

$$\widetilde{c}_n H_n^{(2)}(k_0 a\sin\theta_0) = \widetilde{a}_n J_n(ka\sin\theta_1), \tag{2.268}$$

$$\begin{aligned}
&-\frac{E_0\cos\theta_0}{k_0 a\sin\theta_0} n J_n(k_0 a\sin\theta_0) - \frac{E_0\cos\theta_0}{k_0 a\sin\theta_0} n c_n H_n^{(2)}(k_0 a\sin\theta_0) + jE_0\eta_0\widetilde{c}_n H_n^{(2)'}(k_0 a\sin\theta_0) \\
&= -\frac{E_0 k_0\sin\theta_0\cos\theta_0}{k^2 a\sin^2\theta_1} n a_n J_n(ka\sin\theta_1) + jE_0\zeta\eta_0\frac{\sin\theta_0}{\sin\theta_1}\widetilde{a}_n J_n'(ka\sin\theta_1),
\end{aligned} \tag{2.269}$$

$$\begin{aligned}
&-j\frac{E_0}{\eta_0} J_n'(k_0 a\sin\theta_0) - \frac{E_0\cos\theta_0}{k_0 a\sin\theta_0} n\widetilde{c}_n H_n^{(2)}(k_0 a\sin\theta_0) - j\frac{E_0}{\eta_0} c_n H_n^{(2)'}(k_0 a\sin\theta_0) \\
&= -\frac{E_0 k_0\sin\theta_0\cos\theta_0}{k^2 a\sin^2\theta_1} n\widetilde{a}_n J_n(ka\sin\theta_1) - j\frac{E_0}{\zeta\eta_0}\frac{\sin\theta_0}{\sin\theta_1} a_n J_n'(ka\sin\theta_1).
\end{aligned} \tag{2.270}$$

As we have done in previous sections, the equations are converted into matrix form and solved. The unknown coefficients are found to be:

$$\begin{aligned}
a_n = &\frac{1}{D}\zeta a^2 k_0^2 k_1^4 \sin^2\theta_0 \sin^3\theta_1 \\
&. \left[J_n(k_0 a\sin\theta_0) H_n^{(2)'}(k_0 a\sin\theta_0) - J_n'(k_0 a\sin\theta_0) H_n^{(2)}(k_0 a\sin\theta_0)\right] \\
&. \left[\sin\theta_1 J_n(ka\sin\theta_1) H_n^{(2)'}(k_0 a\sin\theta_0) - \zeta\sin\theta_0 J_n'(ka\sin\theta_1) H_n^{(2)}(k_0 a\sin\theta_0)\right],
\end{aligned} \tag{2.271}$$

$$\begin{aligned}
\widetilde{a}_n = &j\frac{1}{D}\frac{1}{\eta_0}\zeta a n k_0 k_1^2 \sin\theta_0 \sin^2\theta_1 \cos\theta_0 \\
&. \left(k_0^2\sin^2\theta_0 - k^2\sin^2\theta_1\right) J_n(ka\sin\theta_1) H_n^{(2)}(k_0 a\sin\theta_0) \\
&. \left[J_n(k_0 a\sin\theta_0) H_n^{(2)'}(k_0 a\sin\theta_0) - J_n'(k_0 a\sin\theta_0) H_n^{(2)}(k_0 a\sin\theta_0)\right],
\end{aligned} \tag{2.272}$$

$$c_n = \frac{a_n J_n(ka\sin\theta_1) - J_n(k_0 a\sin\theta_0)}{H_n^{(2)}(k_0 a\sin\theta_0)}, \tag{2.273}$$

$$\widetilde{c}_n = \frac{J_n(ka\sin\theta_1)}{H_n^{(2)}(k_0 a\sin\theta_0)}\widetilde{a}_n, \tag{2.274}$$

where

$$\begin{aligned}
D = &-\left(J_n(ka\sin\theta_1)\right)^2 \left(H_n^{(2)}(k_0 a\sin\theta_0)\right)^2 \cos^2\theta_0 n^2\zeta \left(k_0^2\sin^2\theta_0 - k^2\sin^2\theta_1\right)^2 \\
&+ \left[\sin\theta_1 J_n(ka\sin\theta_1) H_n^{(2)'}(k_0 a\sin\theta_0) - \zeta\sin\theta_0 J_n'(ka\sin\theta_1) H_n^{(2)}(k_0 a\sin\theta_0)\right] \\
&. \left[\zeta\sin\theta_1 J_n(ka\sin\theta_1) H_n^{(2)'}(k_0 a\sin\theta_0) - \sin\theta_0 J_n'(ka\sin\theta_1) H_n^{(2)}(k_0 a\sin\theta_0)\right] \\
&. a^2 k_0^2 k_1^4 \sin^2\theta_0 \sin^2\theta_1.
\end{aligned} \tag{2.275}$$

2.9.6 Calculation of the Radar Cross Section

2D echo width can be found from either

$$\sigma = \lim_{\rho\to\infty}\left(2\pi\rho\frac{|\mathbf{E}^s|^2}{|\mathbf{E}^i|^2}\right), \tag{2.276}$$

or

$$\sigma = \lim_{\rho\to\infty}\left(2\pi\rho\frac{|\mathbf{H}^s|^2}{|\mathbf{H}^i|^2}\right). \tag{2.277}$$

Let us use the definition in (2.277). The magnitude of the scattered magnetic field is

$$|\mathbf{H}^s| = \sqrt{|H_\rho^s|^2 + |H_\phi^s|^2 + |H_z^s|^2}, \tag{2.278}$$

and the magnitude of the incident magnetic field is

$$|\mathbf{H}^i| = \frac{|E_0|}{\eta_0}. \tag{2.279}$$

From Appendix B,

$$\begin{aligned} H_\rho^s = &-\frac{E_0\sin\theta_0}{\omega\mu_0\rho}e^{jk_0z\cos\theta_0}\sum_{n=-\infty}^{+\infty} nj^{-n}c_nH_n^{(2)}(k_0\rho\sin\theta_0)e^{jn(\phi-\phi_0)} \\ &-\frac{k_0\cos\theta_0}{\omega\mu_0}\frac{E_0\cos\theta_0}{k_0\rho\sin\theta_0}e^{jk_0z\cos\theta_0}\sum_{n=-\infty}^{+\infty} nj^{-n}c_nH_n^{(2)}(k_0\rho\sin\theta_0)e^{jn(\phi-\phi_0)} \\ &-\frac{k_0\cos\theta_0}{\omega\mu_0}\frac{E_0k_0}{j\omega\varepsilon_0}e^{jk_0z\cos\theta_0}\sum_{n=-\infty}^{+\infty} j^{-n}\widetilde{c}_nH_n^{(2)'}(k_0\rho\sin\theta_0)e^{jn(\phi-\phi_0)}. \end{aligned} \tag{2.280}$$

Note that, large argument forms of the Hankel functions and their derivatives have the spread factor of $\rho^{-1/2}$. Therefore, the first and second terms in (2.280) decay with $\rho^{-3/2}$, whereas the third term decays with $\rho^{-1/2}$ and becomes dominant in the far zone. Therefore, when $\rho\to\infty$

$$\begin{aligned} H_\rho^s &\approx -\frac{k_0\cos\theta_0}{\omega\mu_0}\frac{E_0k_0}{j\omega\varepsilon_0}e^{jk_0z\cos\theta_0}\sum_{n=-\infty}^{+\infty} j^{-n}\widetilde{c}_nH_n^{(2)'}(k_0\rho\sin\theta_0)e^{jn(\phi-\phi_0)}, \\ &= -E_0\cos\theta_0e^{jk_0z\cos\theta_0}\sum_{n=-\infty}^{+\infty} j^{-n-1}\widetilde{c}_nH_n^{(2)'}(k_0\rho\sin\theta_0)e^{jn(\phi-\phi_0)}. \end{aligned} \tag{2.281}$$

Since when $\rho \to \infty$

$$H_n^{(2)'}(k_0\rho\sin\theta_0) \approx -\sqrt{\frac{2j}{\pi k_0\rho\sin\theta_0}}j^{n+1}e^{-jk_0\rho\sin\theta_0}, \tag{2.282}$$

(2.281) becomes

$$H_\rho^s \approx E_0\cos\theta_0 e^{jk_0(z\cos\theta_0-\rho\sin\theta_0)}\sqrt{\frac{2j}{\pi k_0\rho\sin\theta_0}}\sum_{n=-\infty}^{+\infty}\widetilde{c}_n e^{jn(\phi-\phi_0)}. \tag{2.283}$$

Therefore,

$$|H_\rho^s|^2 \approx |E_0|^2\cos^2\theta_0\frac{2}{\pi k_0\rho\sin\theta_0}\left|\sum_{n=-\infty}^{+\infty}\widetilde{c}_n e^{jn(\phi-\phi_0)}\right|^2. \tag{2.284}$$

We will follow similar steps for H_ϕ^s:

$$\begin{aligned} H_\phi^s = &-\frac{E_0\cos\theta_0}{k_0\rho\sin\theta_0}e^{jk_0z\cos\theta_0}\sum_{n=-\infty}^{+\infty}nj^{-n}\widetilde{c}_n H_n^{(2)}(k_0\rho\sin\theta_0)e^{jn(\phi-\phi_0)} \\ &+\frac{E_0}{j\eta_0}e^{jk_0z\cos\theta_0}\sum_{n=-\infty}^{+\infty}j^{-n}c_n H_n^{(2)'}(k_0\rho\sin\theta_0)e^{jn(\phi-\phi_0)}. \end{aligned} \tag{2.285}$$

When $\rho \to \infty$,

$$\begin{aligned} H_\phi^s &\approx \frac{E_0}{\eta_0}e^{jk_0z\cos\theta_0}\sum_{n=-\infty}^{+\infty}j^{-n-1}c_n H_n^{(2)'}(k_0\rho\sin\theta_0)e^{jn(\phi-\phi_0)}, \\ &\approx -\frac{E_0}{\eta_0}e^{jk_0(z\cos\theta_0-\rho\sin\theta_0)}\sqrt{\frac{2j}{\pi k_0\rho\sin\theta_0}}\sum_{n=-\infty}^{+\infty}c_n e^{jn(\phi-\phi_0)}, \end{aligned} \tag{2.286}$$

$$|H_\phi^s|^2 \approx \frac{|E_0|^2}{\eta_0^2}\frac{2}{\pi k_0\rho\sin\theta_0}\left|\sum_{n=-\infty}^{+\infty}c_n e^{jn(\phi-\phi_0)}\right|^2. \tag{2.287}$$

$$H_z^s = E_0\sin\theta_0 e^{jk_0z\cos\theta_0}\sum_{n=-\infty}^{+\infty}j^{-n}\widetilde{c}_n H_n^{(2)}(k_0\rho\sin\theta_0)e^{jn(\phi-\phi_0)}. \tag{2.288}$$

Using the large argument approximation

$$H_n^{(2)}(k_0\rho\sin\theta_0) \approx \sqrt{\frac{2j}{\pi k_0\rho\sin\theta_0}}j^n e^{-jk_0\rho\sin\theta_0}, \tag{2.289}$$

when $\rho \to \infty$,

$$H_z^s \approx E_0 \sin\theta_0 e^{jk_0(z\cos\theta_0 - \rho\sin\theta_0)} \sqrt{\frac{2j}{\pi k_0 \rho \sin\theta_0}} \sum_{n=-\infty}^{+\infty} \widetilde{c}_n e^{jn(\phi-\phi_0)}, \tag{2.290}$$

$$|H_z^s|^2 \approx |E_0|^2 \sin^2\theta_0 \frac{2}{\pi k_0 \rho \sin\theta_0} \left| \sum_{n=-\infty}^{+\infty} \widetilde{c}_n e^{jn(\phi-\phi_0)} \right|^2. \tag{2.291}$$

$$\begin{aligned}
|\mathbf{H}^s|^2 &= |H_\rho^s|^2 + |H_\phi^s|^2 + |H_z^s|^2, \\
&\approx |E_0|^2 \cos^2\theta_0 \frac{2}{\pi k_0 \rho \sin\theta_0} \left| \sum_{n=-\infty}^{+\infty} \widetilde{c}_n e^{jn(\phi-\phi_0)} \right|^2 \\
&\quad + \frac{|E_0|^2}{\eta_0^2} \frac{2}{\pi k_0 \rho \sin\theta_0} \left| \sum_{n=-\infty}^{+\infty} c_n e^{jn(\phi-\phi_0)} \right|^2 \\
&\quad + |E_0|^2 \sin^2\theta_0 \frac{2}{\pi k_0 \rho \sin\theta_0} \left| \sum_{n=-\infty}^{+\infty} \widetilde{c}_n e^{jn(\phi-\phi_0)} \right|^2 \\
&= |E_0|^2 \frac{2}{\pi k_0 \rho \sin\theta_0} \left\{ \frac{1}{\eta_0^2} \left| \sum_{n=-\infty}^{+\infty} c_n e^{jn(\phi-\phi_0)} \right|^2 + \left| \sum_{n=-\infty}^{+\infty} \widetilde{c}_n e^{jn(\phi-\phi_0)} \right|^2 \right\}.
\end{aligned} \tag{2.292}$$

From (2.277),

$$\begin{aligned}
\sigma &= \frac{4}{k_0 \sin\theta_0} \left\{ \left| \sum_{n=-\infty}^{+\infty} c_n e^{jn(\phi-\phi_0)} \right|^2 + \eta_0^2 \left| \sum_{n=-\infty}^{+\infty} \widetilde{c}_n e^{jn(\phi-\phi_0)} \right|^2 \right\}, \\
&= \frac{2\lambda_0}{\pi \sin\theta_0} \left\{ \left| \sum_{n=-\infty}^{+\infty} c_n e^{jn(\phi-\phi_0)} \right|^2 + \eta_0^2 \left| \sum_{n=-\infty}^{+\infty} \widetilde{c}_n e^{jn(\phi-\phi_0)} \right|^2 \right\}.
\end{aligned} \tag{2.293}$$

The normalized (with respect to λ_0) echo width is

$$\sigma/\lambda_0 = \frac{2}{\pi} \frac{1}{\sin\theta_0} \left\{ \left| \sum_{n=-\infty}^{+\infty} c_n e^{jn(\phi-\phi_0)} \right|^2 + \eta_0^2 \left| \sum_{n=-\infty}^{+\infty} \widetilde{c}_n e^{jn(\phi-\phi_0)} \right|^2 \right\}, \tag{2.294}$$

which at normal incidence special case becomes

$$\sigma/\lambda_0 = \frac{2}{\pi} \left| \sum_{n=-\infty}^{+\infty} c_n e^{jn(\phi-\phi_0)} \right|^2. \tag{2.295}$$

2.10 Obliquely Incident Plane Wave Scattering by an Infinite Length Metamaterial Cylinder: TE^z Polarization

2.10.1 Introduction

The solution for the TE^z polarization case can be obtained from the TM^z case utilizing duality. The field expressions and RCS calculations are similar to the TM^z case. Hence, in this section only key equations will be given for completeness of the problem.

2.10.2 Incident, Scattered and Transmitted Magnetic Fields (z components)

$$H_z^i = H_0 \sin\theta_0 e^{jk_0 z\cos\theta_0} \sum_{n=-\infty}^{+\infty} j^{-n} J_n(k_0\rho\sin\theta_0) e^{jn(\phi-\phi_0)}, \tag{2.296}$$

$$H_z^s = H_0 \sin\theta_0 e^{jk_0 z\cos\theta_0} \sum_{n=-\infty}^{+\infty} j^{-n} c_n H_n^{(2)}(k_0\rho\sin\theta_0) e^{jn(\phi-\phi_0)}, \tag{2.297}$$

$$H_z^t = H_0 \sin\theta_0 e^{jk_0 z\cos\theta_0} \sum_{n=-\infty}^{+\infty} j^{-n} a_n J_n(k\rho\sin\theta_1) e^{jn(\phi-\phi_0)}. \tag{2.298}$$

2.10.3 Incident, Scattered and Transmitted Electric Fields (z components)

$$E_z^i = 0, \tag{2.299}$$

$$E_z^s = H_0 \sin\theta_0 e^{jk_0 z\cos\theta_0} \sum_{n=-\infty}^{+\infty} j^{-n} \widetilde{c}_n H_n^{(2)}(k_0\rho\sin\theta_0) e^{jn(\phi-\phi_0)}, \tag{2.300}$$

$$E_z^t = H_0 \sin\theta_0 e^{jk_0 z\cos\theta_0} \sum_{n=-\infty}^{+\infty} j^{-n} \widetilde{a}_n J_n(k\rho\sin\theta_1) e^{jn(\phi-\phi_0)}. \tag{2.301}$$

2.10.4 ϕ Components of the Incident, Scattered and Transmitted Magnetic and Electric Fields

$$H_\phi^i = -\frac{H_0 \cos\theta_0}{k_0 \rho \sin\theta_0} e^{jk_0 z\cos\theta_0} \sum_{n=-\infty}^{+\infty} n j^{-n} J_n(k_0\rho\sin\theta_0) e^{jn(\phi-\phi_0)}, \tag{2.302}$$

$$\begin{aligned} H_\phi^s = &-\frac{H_0 \cos\theta_0}{k_0 \rho \sin\theta_0} e^{jk_0 z\cos\theta_0} \sum_{n=-\infty}^{+\infty} n j^{-n} c_n H_n^{(2)}(k_0\rho\sin\theta_0) e^{jn(\phi-\phi_0)} \\ &-j\frac{H_0}{\eta_0} e^{jk_0 z\cos\theta_0} \sum_{n=-\infty}^{+\infty} j^{-n} \widetilde{c}_n H_n^{(2)'}(k_0\rho\sin\theta_0) e^{jn(\phi-\phi_0)}, \end{aligned} \tag{2.303}$$

$$\begin{aligned} H_\phi^t = &-\frac{H_0 k_0 \sin\theta_0\cos\theta_0}{k^2\rho\sin^2\theta_1} e^{jk_0 z\cos\theta_0} \sum_{n=-\infty}^{+\infty} n j^{-n} a_n J_n(k\rho\sin\theta_1) e^{jn(\phi-\phi_0)} \\ &-j\frac{H_0}{\zeta\eta_0}\frac{\sin\theta_0}{\sin\theta_1} e^{jk_0 z\cos\theta_0} \sum_{n=-\infty}^{+\infty} j^{-n} \widetilde{a}_n J_n'(k\rho\sin\theta_1) e^{jn(\phi-\phi_0)}, \end{aligned} \tag{2.304}$$

$$E_\phi^i = jH_0\eta_0 e^{jk_0 z\cos\theta_0} \sum_{n=-\infty}^{+\infty} j^{-n} J_n'(k_0\rho\sin\theta_0) e^{jn(\phi-\phi_0)}, \tag{2.305}$$

$$\begin{aligned} E_\phi^s = &-\frac{H_0 \cos\theta_0}{k_0 \rho \sin\theta_0} e^{jk_0 z\cos\theta_0} \sum_{n=-\infty}^{+\infty} n j^{-n} \widetilde{c}_n H_n^{(2)}(k_0\rho\sin\theta_0) e^{jn(\phi-\phi_0)} \\ &+jH_0\eta_0 e^{jk_0 z\cos\theta_0} \sum_{n=-\infty}^{+\infty} j^{-n} c_n H_n^{(2)'}(k_0\rho\sin\theta_0) e^{jn(\phi-\phi_0)}, \end{aligned} \tag{2.306}$$

$$\begin{aligned} E_\phi^t = &-\frac{H_0 k_0 \sin\theta_0\cos\theta_0}{k^2\rho\sin^2\theta_1} e^{jk_0 z\cos\theta_0} \sum_{n=-\infty}^{+\infty} n j^{-n} \widetilde{a}_n J_n(k\rho\sin\theta_1) e^{jn(\phi-\phi_0)} \\ &+jH_0\zeta\eta_0\frac{\sin\theta_0}{\sin\theta_1} e^{jk_0 z\cos\theta_0} \sum_{n=-\infty}^{+\infty} j^{-n} a_n J_n'(k\rho\sin\theta_1) e^{jn(\phi-\phi_0)}. \end{aligned} \tag{2.307}$$

2.10.5 Boundary Conditions and Their Solution

Tangential components of the electric and magnetic fields should be continuous on the surface of the metamaterial cylinder. Therefore,

$$H_z^i(\rho=a) + H_z^s(\rho=a) = H_z^t(\rho=a), \tag{2.308}$$

$$H_z^i(\rho = a) + H_z^s(\rho = a) = H_z^t(\rho = a), \tag{2.309}$$

$$H_\phi^i(\rho = a) + H_\phi^s(\rho = a) = H_\phi^t(\rho = a), \tag{2.310}$$

$$H_\phi^i(\rho = a) + H_\phi^s(\rho = a) = H_\phi^t(\rho = a), \tag{2.311}$$

which leads to

$$J_n(k_0 a \sin\theta_0) + c_n H_n^{(2)}(k_0 a \sin\theta_0) = a_n J_n(ka \sin\theta_1), \tag{2.312}$$

$$\widetilde{c}_n H_n^{(2)}(k_0 a \sin\theta_0) = \widetilde{a}_n J_n(ka \sin\theta_1), \tag{2.313}$$

$$\begin{aligned} &-\frac{H_0 \cos\theta_0}{k_0 a \sin\theta_0} n J_n(k_0 a \sin\theta_0) - \frac{H_0 \cos\theta_0}{k_0 a \sin\theta_0} n c_n H_n^{(2)}(k_0 a \sin\theta_0) - j\frac{H_0}{\eta_0}\widetilde{c}_n H_n^{(2)'}(k_0 a \sin\theta_0) \\ &= -\frac{H_0 k_0 \sin\theta_0 \cos\theta_0}{k^2 a \sin^2\theta_1} n a_n J_n(ka \sin\theta_1) - j\frac{H_0}{\zeta\eta_0}\frac{\sin\theta_0}{\sin\theta_1}\widetilde{a}_n J_n'(ka \sin\theta_1), \end{aligned} \tag{2.314}$$

$$\begin{aligned} &jH_0\eta_0 J_n'(k_0 a \sin\theta_0) - \frac{H_0 \cos\theta_0}{k_0 a \sin\theta_0} n\widetilde{c}_n H_n^{(2)}(k_0 a \sin\theta_0) + jH_0\eta_0 c_n H_n^{(2)'}(k_0 a \sin\theta_0) \\ &= -\frac{H_0 k_0 \sin\theta_0 \cos\theta_0}{k^2 a \sin^2\theta_1} n\widetilde{a}_n J_n(ka \sin\theta_1) + jH_0\zeta\eta_0\frac{\sin\theta_0}{\sin\theta_1} a_n J_n'(ka \sin\theta_1). \end{aligned} \tag{2.315}$$

As we have done in previous sections, the equations are converted into matrix form and solved. The unknown coefficients are found to be:

$$\begin{aligned} a_n = &\frac{1}{D} a^2 k_0^2 k_1^4 \sin^2\theta_0 \sin^3\theta_1 \\ &. \left[J_n(k_0 a \sin\theta_0) H_n^{(2)'}(k_0 a \sin\theta_0) - J_n'(k_0 a \sin\theta_0) H_n^{(2)}(k_0 a \sin\theta_0) \right] \\ &. \left[\zeta \sin\theta_1 J_n(ka \sin\theta_1) H_n^{(2)'}(k_0 a \sin\theta_0) - \sin\theta_0 J_n'(ka \sin\theta_1) H_n^{(2)}(k_0 a \sin\theta_0) \right], \end{aligned} \tag{2.316}$$

$$\begin{aligned} \widetilde{a}_n = &-j\frac{1}{D}\zeta\eta_0 a n k_0 k_1^2 \sin\theta_0 \sin^2\theta_1 \cos\theta_0 \\ &. \left(k_0^2 \sin^2\theta_0 - k^2 \sin^2\theta_1\right) J_n(ka \sin\theta_1) H_n^{(2)}(k_0 a \sin\theta_0) \\ &. \left[J_n(k_0 a \sin\theta_0) H_n^{(2)'}(k_0 a \sin\theta_0) - J_n'(k_0 a \sin\theta_0) H_n^{(2)}(k_0 a \sin\theta_0) \right], \end{aligned} \tag{2.317}$$

$$c_n = \frac{a_n J_n(ka \sin\theta_1) - J_n(k_0 a \sin\theta_0)}{H_n^{(2)}(k_0 a \sin\theta_0)}, \tag{2.318}$$

$$\widetilde{c}_n = \frac{J_n(ka \sin\theta_1)}{H_n^{(2)}(k_0 a \sin\theta_0)}\widetilde{a}_n, \tag{2.319}$$

where

$$D = -\left(J_n(ka\sin\theta_1)\right)^2\left(H_n^{(2)}(k_0a\sin\theta_0)\right)^2\cos^2\theta_0 n^2\zeta\left(k_0^2\sin^2\theta_0 - k^2\sin^2\theta_1\right)^2$$
$$+\left[\sin\theta_1 J_n(ka\sin\theta_1)H_n^{(2)'}(k_0a\sin\theta_0) - \zeta\sin\theta_0 J_n'(ka\sin\theta_1)H_n^{(2)}(k_0a\sin\theta_0)\right]$$
$$.\left[\zeta\sin\theta_1 J_n(ka\sin\theta_1)H_n^{(2)'}(k_0a\sin\theta_0) - \sin\theta_0 J_n'(ka\sin\theta_1)H_n^{(2)}(k_0a\sin\theta_0)\right]$$
$$.\ a^2k_0^2k_1^4\sin^2\theta_0\sin^2\theta_1. \tag{2.320}$$

2.10.6 Calculation of the Radar Cross Section

Normalized echo width can be found using (2.276) as:

$$\sigma/\lambda_0 = \frac{2}{\pi}\frac{1}{\sin\theta_0}\left\{\left|\sum_{n=-\infty}^{+\infty} c_n e^{jn(\phi-\phi_0)}\right|^2 + \frac{1}{\eta_0^2}\left|\sum_{n=-\infty}^{+\infty}\widetilde{c}_n e^{jn(\phi-\phi_0)}\right|^2\right\}, \tag{2.321}$$

which at normal incidence case becomes

$$\sigma/\lambda_0 = \frac{2}{\pi}\left|\sum_{n=-\infty}^{+\infty} c_n e^{jn(\phi-\phi_0)}\right|^2. \tag{2.322}$$

2.11 Obliquely Incident Plane Wave Scattering by an Infinite Length Metamaterial Coated Conducting Cylinder: TM^z Polarization

2.11.1 Introduction

A uniform plane wave is obliquely incident on a metamaterial coated conducting cylinder of infinite length. The plane wave illumination and polarization is the same with Section 2.9. The problem geometry is depicted in Fig. 2.14.

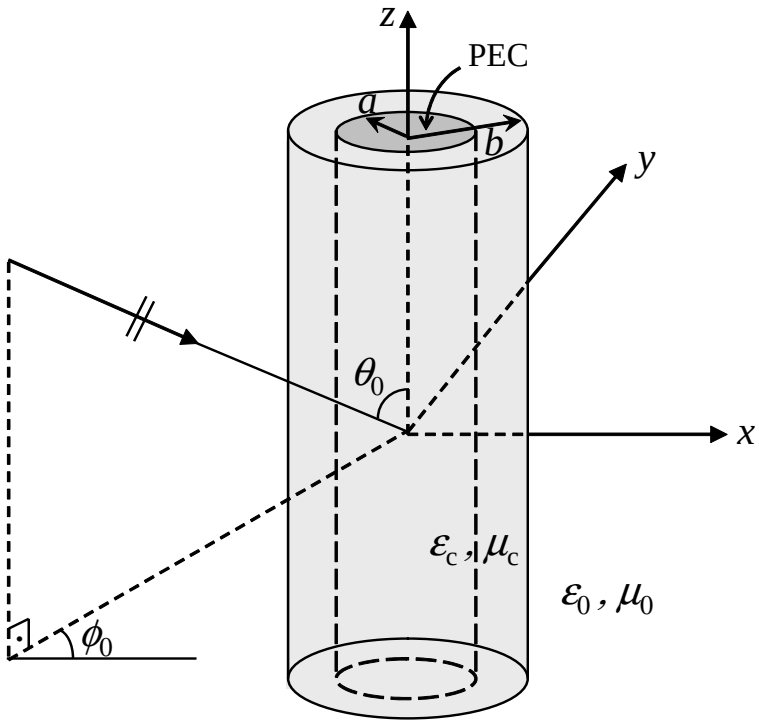

Figure 2.14: Uniform plane wave obliquely incident on a metamaterial coated conducting cylinder: TM^z Polarization.

Due to the conducting cylinder centered at the origin, the fields inside the metamaterial coating are written not only in terms of Bessel functions of the first kind (i.e., $J_n(.)$) but also in terms of Bessel functions of the second kind (i.e.,

$Y_n(.)$), and their derivatives. This is the only difference in formulation, from Section 2.9. Therefore, in this section only key equations are given.

2.11.2 Incident, Scattered and Transmitted Electric Fields (z components)

$$E_z^i = E_0 \sin\theta_0 e^{jk_0 z\cos\theta_0} \sum_{n=-\infty}^{+\infty} j^{-n} J_n(k_0\rho\sin\theta_0) e^{jn(\phi-\phi_0)}, \tag{2.323}$$

$$E_z^s = E_0 \sin\theta_0 e^{jk_0 z\cos\theta_0} \sum_{n=-\infty}^{+\infty} j^{-n} c_n H_n^{(2)}(k_0\rho\sin\theta_0) e^{jn(\phi-\phi_0)}, \tag{2.324}$$

$$E_z^t = E_0 \sin\theta_0 e^{jk_0 z\cos\theta_0} \sum_{n=-\infty}^{+\infty} j^{-n} \left[a_n J_n(k_c\rho\sin\theta_1) + b_n Y_n(k_c\rho\sin\theta_1)\right] e^{jn(\phi-\phi_0)}. \tag{2.325}$$

2.11.3 Incident, Scattered and Transmitted Magnetic Fields (z components)

$$H_z^i = 0, \tag{2.326}$$

$$H_z^s = E_0 \sin\theta_0 e^{jk_0 z\cos\theta_0} \sum_{n=-\infty}^{+\infty} j^{-n} \widetilde{c}_n H_n^{(2)}(k_0\rho\sin\theta_0) e^{jn(\phi-\phi_0)}, \tag{2.327}$$

$$H_z^t = E_0 \sin\theta_0 e^{jk_0 z\cos\theta_0} \sum_{n=-\infty}^{+\infty} j^{-n} \left[\widetilde{a}_n J_n(k_c\rho\sin\theta_1) + \widetilde{b}_n Y_n(k_c\rho\sin\theta_1)\right] e^{jn(\phi-\phi_0)}. \tag{2.328}$$

2.11.4 ϕ Components of the Incident, Scattered and Transmitted Electric and Magnetic Fields

$$E_\phi^i = -\frac{E_0\cos\theta_0}{k_0\rho\sin\theta_0} e^{jk_0 z\cos\theta_0} \sum_{n=-\infty}^{+\infty} n j^{-n} J_n(k_0\rho\sin\theta_0) e^{jn(\phi-\phi_0)}, \tag{2.329}$$

$$E_\phi^s = -\frac{E_0 \cos\theta_0}{k_0 \rho \sin\theta_0} e^{jk_0 z\cos\theta_0} \sum_{n=-\infty}^{+\infty} n j^{-n} c_n H_n^{(2)}(k_0\rho\sin\theta_0) e^{jn(\phi-\phi_0)}$$
$$+ jE_0\eta_0 e^{jk_0 z\cos\theta_0} \sum_{n=-\infty}^{+\infty} j^{-n} \widetilde{c}_n H_n^{(2)'}(k_0\rho\sin\theta_0) e^{jn(\phi-\phi_0)}, \tag{2.330}$$

$$E_\phi^t = -\frac{E_0 k_0 \sin\theta_0 \cos\theta_0}{k_c^2 \rho \sin^2\theta_1} e^{jk_0 z\cos\theta_0} \tag{2.331}$$
$$. \sum_{n=-\infty}^{+\infty} n j^{-n} \left[a_n J_n(k_c\rho\sin\theta_1) + b_n Y_n(k_c\rho\sin\theta_1)\right] e^{jn(\phi-\phi_0)}$$
$$+ jE_0\zeta\eta_0 \frac{\sin\theta_0}{\sin\theta_1} e^{jk_0 z\cos\theta_0}$$
$$. \sum_{n=-\infty}^{+\infty} j^{-n} \left[\widetilde{a}_n J_n'(k_c\rho\sin\theta_1) + \widetilde{b}_n Y_n'(k_c\rho\sin\theta_1)\right] e^{jn(\phi-\phi_0)},$$

$$H_\phi^i = -j\frac{E_0}{\eta_0} e^{jk_0 z\cos\theta_0} \sum_{n=-\infty}^{+\infty} j^{-n} J_n'(k_0\rho\sin\theta_0) e^{jn(\phi-\phi_0)}, \tag{2.332}$$

$$H_\phi^s = -\frac{E_0 \cos\theta_0}{k_0 \rho \sin\theta_0} e^{jk_0 z\cos\theta_0} \sum_{n=-\infty}^{+\infty} n j^{-n} \widetilde{c}_n H_n^{(2)}(k_0\rho\sin\theta_0) e^{jn(\phi-\phi_0)}$$
$$- j\frac{E_0}{\eta_0} e^{jk_0 z\cos\theta_0} \sum_{n=-\infty}^{+\infty} j^{-n} c_n H_n^{(2)'}(k_0\rho\sin\theta_0) e^{jn(\phi-\phi_0)}, \tag{2.333}$$

$$H_\phi^t = -\frac{E_0 k_0 \sin\theta_0 \cos\theta_0}{k_c^2 \rho \sin^2\theta_1} e^{jk_0 z\cos\theta_0} \tag{2.334}$$
$$. \sum_{n=-\infty}^{+\infty} n j^{-n} \left[\widetilde{a}_n J_n(k_c\rho\sin\theta_1) + \widetilde{b}_n Y_n(k_c\rho\sin\theta_1)\right] e^{jn(\phi-\phi_0)}$$
$$- j\frac{E_0}{\zeta\eta_0} \frac{\sin\theta_0}{\sin\theta_1} e^{jk_0 z\cos\theta_0}$$
$$. \sum_{n=-\infty}^{+\infty} j^{-n} \left[a_n J_n'(k_c\rho\sin\theta_1) + b_n Y_n'(k_c\rho\sin\theta_1)\right] e^{jn(\phi-\phi_0)}.$$

2.11.5 Boundary Conditions and Their Solution

Tangential components of the electric and magnetic fields are continuous on the outer surface of the metamaterial coating. Also, on the inner surface of

the metamaterial coating (i.e., on the conducting cylinder surface) tangential components of the electric field should vanish. Therefore,

$$E_z^i(\rho=b)+E_z^s(\rho=b)=E_z^t(\rho=b), \tag{2.335}$$

$$H_z^i(\rho=b)+H_z^s(\rho=b)=H_z^t(\rho=b), \tag{2.336}$$

$$E_\phi^i(\rho=b)+E_\phi^s(\rho=b)=E_\phi^t(\rho=b), \tag{2.337}$$

$$H_\phi^i(\rho=b)+H_\phi^s(\rho=b)=H_\phi^t(\rho=b), \tag{2.338}$$

$$E_z^t(\rho=a)=0, \tag{2.339}$$

$$E_\phi^t(\rho=a)=0, \tag{2.340}$$

which leads to

$$J_n(k_0b\sin\theta_0)+c_nH_n^{(2)}(k_0b\sin\theta_0)=a_nJ_n(k_cb\sin\theta_1)+b_nY_n(k_cb\sin\theta_1), \tag{2.341}$$

$$\widetilde{c}_nH_n^{(2)}(k_0b\sin\theta_0)=\widetilde{a}_nJ_n(k_cb\sin\theta_1)+\widetilde{b}_nY_n(k_cb\sin\theta_1), \tag{2.342}$$

$$\begin{aligned}&-\frac{E_0\cos\theta_0}{k_0b\sin\theta_0}nJ_n(k_0b\sin\theta_0)-\frac{E_0\cos\theta_0}{k_0b\sin\theta_0}nc_nH_n^{(2)}(k_0b\sin\theta_0)+jE_0\eta_0\widetilde{c}_nH_n^{(2)\prime}(k_0b\sin\theta_0)\\&=-\frac{E_0k_0\sin\theta_0\cos\theta_0}{k_c^2b\sin^2\theta_1}na_nJ_n(k_cb\sin\theta_1)-\frac{E_0k_0\sin\theta_0\cos\theta_0}{k_c^2b\sin^2\theta_1}nb_nY_n(k_cb\sin\theta_1)\\&\quad+jE_0\zeta\eta_0\frac{\sin\theta_0}{\sin\theta_1}\widetilde{a}_nJ_n'(k_cb\sin\theta_1)+jE_0\zeta\eta_0\frac{\sin\theta_0}{\sin\theta_1}\widetilde{b}_nY_n'(k_cb\sin\theta_1),\end{aligned} \tag{2.343}$$

$$\begin{aligned}&-j\frac{E_0}{\eta_0}J_n'(k_0b\sin\theta_0)-\frac{E_0\cos\theta_0}{k_0b\sin\theta_0}n\widetilde{c}_nH_n^{(2)}(k_0b\sin\theta_0)-j\frac{E_0}{\eta_0}c_nH_n^{(2)\prime}(k_0b\sin\theta_0)\\&=-\frac{E_0k_0\sin\theta_0\cos\theta_0}{k_c^2b\sin^2\theta_1}n\widetilde{a}_nJ_n(k_cb\sin\theta_1)-\frac{E_0k_0\sin\theta_0\cos\theta_0}{k_c^2b\sin^2\theta_1}n\widetilde{b}_nY_n(k_cb\sin\theta_1)\\&\quad-j\frac{E_0}{\zeta\eta_0}\frac{\sin\theta_0}{\sin\theta_1}a_nJ_n'(k_cb\sin\theta_1)-j\frac{E_0}{\zeta\eta_0}\frac{\sin\theta_0}{\sin\theta_1}b_nY_n'(k_cb\sin\theta_1),\end{aligned} \tag{2.344}$$

$$a_nJ_n(k_ca\sin\theta_1)+b_nY_n(k_ca\sin\theta_1)=0, \tag{2.345}$$

$$\begin{aligned}&-\frac{E_0k_0\sin\theta_0\cos\theta_0}{k_c^2a\sin^2\theta_1}na_nJ_n(k_ca\sin\theta_1)-\frac{E_0k_0\sin\theta_0\cos\theta_0}{k_c^2a\sin^2\theta_1}nb_nY_n(k_ca\sin\theta_1)\\&+jE_0\zeta\eta_0\frac{\sin\theta_0}{\sin\theta_1}\widetilde{a}_nJ_n'(k_ca\sin\theta_1)+jE_0\zeta\eta_0\frac{\sin\theta_0}{\sin\theta_1}\widetilde{b}_nY_n'(k_ca\sin\theta_1)=0.\end{aligned} \tag{2.346}$$

As we have done in previous sections, the equations are converted into matrix form and solved. The unknown coefficients are found to be:

$$\begin{aligned} a_n = & -\frac{1}{D} Y_n(k_c a \sin\theta_1) \zeta k_0^2 k_1^4 b^2 \sin^2\theta_0 \sin^3\theta_1 \\ & . \left[J_n(k_0 b \sin\theta_0) H_n^{(2)'}(k_0 b \sin\theta_0) - J_n'(k_0 b \sin\theta_0) H_n^{(2)}(k_0 b \sin\theta_0) \right] \\ & . \Big(\sin\theta_1 H_n^{(2)'}(k_0 b \sin\theta_0) \\ & \quad . \left[J_n(k_c b \sin\theta_1) Y_n'(k_c a \sin\theta_1) - J_n'(k_c a \sin\theta_1) Y_n(k_c b \sin\theta_1) \right] \\ & \quad -\zeta \sin\theta_0 H_n^{(2)}(k_0 b \sin\theta_0) \\ & \quad . \left[J_n'(k_c b \sin\theta_1) Y_n'(k_c a \sin\theta_1) - J_n'(k_c a \sin\theta_1) Y_n'(k_c b \sin\theta_1) \right] \Big) \end{aligned} \tag{2.347}$$

$$\begin{aligned} \widetilde{a}_n = & \, j \frac{1}{D} \frac{1}{\eta_0} \zeta b n k_0 k_1^2 \sin\theta_0 \sin^2\theta_1 \cos\theta_0 \\ & . \left(k_0^2 \sin^2\theta_0 - k_c^2 \sin^2\theta_1 \right) Y_n'(k_c a \sin\theta_1) H_n^{(2)}(k_0 b \sin\theta_0) \\ & . \left[J_n(k_c a \sin\theta_1) Y_n(k_c b \sin\theta_1) - J_n(k_c b \sin\theta_1) Y_n(k_c a \sin\theta_1) \right] \\ & . \left[J_n(k_0 b \sin\theta_0) H_n^{(2)'}(k_0 b \sin\theta_0) - J_n'(k_0 b \sin\theta_0) H_n^{(2)}(k_0 b \sin\theta_0) \right], \end{aligned} \tag{2.348}$$

$$b_n = -\frac{J_n(k_c a \sin\theta_1)}{Y_n(k_c a \sin\theta_1)} a_n, \tag{2.349}$$

$$\widetilde{b}_n = -\frac{J_n'(k_c a \sin\theta_1)}{Y_n'(k_c a \sin\theta_1)} \widetilde{a}_n, \tag{2.350}$$

$$c_n = \frac{a_n J_n(k_c b \sin\theta_1) + b_n Y_n(k_c b \sin\theta_1) - J_n(k_0 b \sin\theta_0)}{H_n^{(2)}(k_0 b \sin\theta_0)}, \tag{2.351}$$

$$\widetilde{c}_n = \frac{\widetilde{a}_n J_n(k_c b \sin\theta_1) + \widetilde{b}_n Y_n(k_c b \sin\theta_1)}{H_n^{(2)}(k_0 b \sin\theta_0)}, \tag{2.352}$$

where

$$D = D_1 + D_2, \tag{2.353}$$

$$\begin{aligned} D_1 = & \, \zeta \cos^2\theta_0 n^2 \left(H_n^{(2)}(k_0 b \sin\theta_0) \right)^2 \left(k_0^2 \sin^2\theta_0 - k_c^2 \sin^2\theta_1 \right)^2 \\ & . \left[J_n(k_c b \sin\theta_1) Y_n(k_c a \sin\theta_1) - J_n(k_c a \sin\theta_1) Y_n(k_c b \sin\theta_1) \right] \\ & . \left[J_n(k_c b \sin\theta_1) Y_n'(k_c a \sin\theta_1) - J_n'(k_c a \sin\theta_1) Y_n(k_c b \sin\theta_1) \right], \end{aligned} \tag{2.354}$$

$$
\begin{aligned}
D_2 = -b^2 k_0^2 k_1^4 \sin^2\theta_0 \sin^2\theta_1 \qquad (2.355)\\
\cdot \Big(J_n'(k_c a \sin\theta_1) \Big[\sin\theta_1 Y_n(k_c b \sin\theta_1) H_n^{(2)'}(k_0 b \sin\theta_0) \\
-\zeta \sin\theta_0 Y_n'(k_c b \sin\theta_1) H_n^{(2)}(k_0 b \sin\theta_0) \Big] \\
-Y_n'(k_c a \sin\theta_1) \Big[\sin\theta_1 J_n(k_c b \sin\theta_1) H_n^{(2)'}(k_0 b \sin\theta_0) \\
-\zeta \sin\theta_0 J_n'(k_c b \sin\theta_1) H_n^{(2)}(k_0 b \sin\theta_0) \Big] \Big) \\
\cdot \Big(J_n(k_c a \sin\theta_1) \Big[\zeta \sin\theta_1 Y_n(k_c b \sin\theta_1) H_n^{(2)'}(k_0 b \sin\theta_0) \\
-\sin\theta_0 Y_n'(k_c b \sin\theta_1) H_n^{(2)}(k_0 b \sin\theta_0) \Big] \\
-Y_n(k_c a \sin\theta_1) \Big[\zeta \sin\theta_1 J_n(k_c b \sin\theta_1) H_n^{(2)'}(k_0 b \sin\theta_0) \\
-\sin\theta_0 J_n'(k_c b \sin\theta_1) H_n^{(2)}(k_0 b \sin\theta_0) \Big] \Big)
\end{aligned}
$$

2.11.6 Calculation of the Radar Cross Section

Calculation of the Radar Cross Section is the same as in Section 2.9. The normalized echo width is given in (2.294).

2.12 Obliquely Incident Plane Wave Scattering by an Infinite Length Metamaterial Coated Conducting Cylinder: TE^z Polarization

2.12.1 Introduction

A uniform plane wave is obliquely incident on a metamaterial coated conducting cylinder of infinite length. The plane wave illumination and polarization is the same with Section 2.10. The problem geometry is as depicted in Fig. 2.14. As in Section 2.11, due to the conducting cylinder centered at the origin, the fields inside the metamaterial coating are written not only in terms of Bessel functions of the first kind (i.e., $J_n(.)$) but also in terms of Bessel functions of the second kind (i.e., $Y_n(.)$), and their derivatives. This is the only difference in formulation, from Section 2.10. Therefore, in this section only key equations are given.

2.12.2 Incident, Scattered and Transmitted Magnetic Fields (z components)

$$H_z^i = H_0 \sin\theta_0 e^{jk_0 z\cos\theta_0} \sum_{n=-\infty}^{+\infty} j^{-n} J_n(k_0\rho\sin\theta_0) e^{jn(\phi-\phi_0)}, \tag{2.356}$$

$$H_z^s = H_0 \sin\theta_0 e^{jk_0 z\cos\theta_0} \sum_{n=-\infty}^{+\infty} j^{-n} c_n H_n^{(2)}(k_0\rho\sin\theta_0) e^{jn(\phi-\phi_0)}, \tag{2.357}$$

$$H_z^t = H_0 \sin\theta_0 e^{jk_0 z\cos\theta_0} \sum_{n=-\infty}^{+\infty} j^{-n} \left[a_n J_n(k_c\rho\sin\theta_1) + b_n Y_n(k_c\rho\sin\theta_1)\right] e^{jn(\phi-\phi_0)}. \tag{2.358}$$

2.12.3 Incident, Scattered and Transmitted Electric Fields (z components)

$$E_z^i = 0, \tag{2.359}$$

$$E_z^s = H_0 \sin\theta_0 e^{jk_0 z\cos\theta_0} \sum_{n=-\infty}^{+\infty} j^{-n}\widetilde{c}_n H_n^{(2)}(k_0\rho\sin\theta_0)e^{jn(\phi-\phi_0)}, \tag{2.360}$$

$$E_z^t = H_0 \sin\theta_0 e^{jk_0 z\cos\theta_0} \sum_{n=-\infty}^{+\infty} j^{-n}\left[\widetilde{a}_n J_n(k_c\rho\sin\theta_1) + \widetilde{b}_n Y_n(k_c\rho\sin\theta_1)\right] e^{jn(\phi-\phi_0)}. \tag{2.361}$$

2.12.4 ϕ Components of the Incident, Scattered and Transmitted Magnetic and Electric Fields

$$H_\phi^i = -\frac{H_0\cos\theta_0}{k_0\rho\sin\theta_0} e^{jk_0 z\cos\theta_0} \sum_{n=-\infty}^{+\infty} nj^{-n}J_n(k_0\rho\sin\theta_0)e^{jn(\phi-\phi_0)}, \tag{2.362}$$

$$\begin{aligned} H_\phi^s = &-\frac{H_0\cos\theta_0}{k_0\rho\sin\theta_0} e^{jk_0 z\cos\theta_0} \sum_{n=-\infty}^{+\infty} nj^{-n}c_n H_n^{(2)}(k_0\rho\sin\theta_0)e^{jn(\phi-\phi_0)} \\ &-j\frac{H_0}{\eta_0} e^{jk_0 z\cos\theta_0} \sum_{n=-\infty}^{+\infty} j^{-n}\widetilde{c}_n H_n^{(2)\prime}(k_0\rho\sin\theta_0)e^{jn(\phi-\phi_0)}, \end{aligned} \tag{2.363}$$

$$\begin{aligned} H_\phi^t = &-\frac{H_0 k_0\sin\theta_0\cos\theta_0}{k_c^2\rho\sin^2\theta_1} e^{jk_0 z\cos\theta_0} \\ &\cdot \sum_{n=-\infty}^{+\infty} nj^{-n}\left[a_n J_n(k_c\rho\sin\theta_1) + b_n Y_n(k_c\rho\sin\theta_1)\right] e^{jn(\phi-\phi_0)} \\ &-j\frac{H_0}{\zeta\eta_0}\frac{\sin\theta_0}{\sin\theta_1} e^{jk_0 z\cos\theta_0} \\ &\cdot \sum_{n=-\infty}^{+\infty} j^{-n}\left[\widetilde{a}_n J_n'(k_c\rho\sin\theta_1) + \widetilde{b}_n Y_n'(k_c\rho\sin\theta_1)\right] e^{jn(\phi-\phi_0)}, \end{aligned} \tag{2.364}$$

$$E_\phi^i = jH_0\eta_0 e^{jk_0 z\cos\theta_0} \sum_{n=-\infty}^{+\infty} j^{-n}J_n'(k_0\rho\sin\theta_0)e^{jn(\phi-\phi_0)}, \tag{2.365}$$

$$E_{\phi}^{s} = -\frac{H_0 \cos\theta_0}{k_0 \rho \sin\theta_0} e^{jk_0 z\cos\theta_0} \sum_{n=-\infty}^{+\infty} n j^{-n} \widetilde{c}_n H_n^{(2)}(k_0\rho\sin\theta_0) e^{jn(\phi-\phi_0)}$$
$$+ jH_0\eta_0 e^{jk_0 z\cos\theta_0} \sum_{n=-\infty}^{+\infty} j^{-n} c_n H_n^{(2)'}(k_0\rho\sin\theta_0) e^{jn(\phi-\phi_0)}, \tag{2.366}$$

$$E_{\phi}^{t} = -\frac{H_0 k_0 \sin\theta_0 \cos\theta_0}{k_c^2 \rho \sin^2\theta_1} e^{jk_0 z\cos\theta_0} \tag{2.367}$$
$$. \sum_{n=-\infty}^{+\infty} n j^{-n} \left[\widetilde{a}_n J_n(k_c\rho\sin\theta_1) + \widetilde{b}_n Y_n(k_c\rho\sin\theta_1)\right] e^{jn(\phi-\phi_0)}$$
$$+ jH_0\zeta\eta_0 \frac{\sin\theta_0}{\sin\theta_1} e^{jk_0 z\cos\theta_0}$$
$$. \sum_{n=-\infty}^{+\infty} j^{-n} \left[a_n J_n'(k_c\rho\sin\theta_1) + b_n Y_n'(k_c\rho\sin\theta_1)\right] e^{jn(\phi-\phi_0)}.$$

2.12.5 Boundary Conditions and Their Solution

Tangential components of the magnetic and electric fields are continuous on the outer surface of the metamaterial coating. Also, on the inner surface of the metamaterial coating (i.e., on the conducting cylinder surface) tangential components of the electric field should vanish. Therefore,

$$H_z^i(\rho=b) + H_z^s(\rho=b) = H_z^t(\rho=b), \tag{2.368}$$

$$E_z^i(\rho=b) + E_z^s(\rho=b) = E_z^t(\rho=b), \tag{2.369}$$

$$H_\phi^i(\rho=b) + H_\phi^s(\rho=b) = H_\phi^t(\rho=b), \tag{2.370}$$

$$E_\phi^i(\rho=b) + E_\phi^s(\rho=b) = E_\phi^t(\rho=b), \tag{2.371}$$

$$E_z^t(\rho=a) = 0, \tag{2.372}$$

$$E_\phi^t(\rho=a) = 0, \tag{2.373}$$

which leads to

$$J_n(k_0 b\sin\theta_0) + c_n H_n^{(2)}(k_0 b\sin\theta_0) = a_n J_n(k_c b\sin\theta_1) + b_n Y_n(k_c b\sin\theta_1), \tag{2.374}$$

$$\widetilde{c}_n H_n^{(2)}(k_0 b\sin\theta_0) = \widetilde{a}_n J_n(k_c b\sin\theta_1) + \widetilde{b}_n Y_n(k_c b\sin\theta_1), \tag{2.375}$$

$$-\frac{H_0\cos\theta_0}{k_0 b\sin\theta_0}nJ_n(k_0 b\sin\theta_0)-\frac{H_0\cos\theta_0}{k_0 b\sin\theta_0}nc_nH_n^{(2)}(k_0 b\sin\theta_0)-j\frac{H_0}{\eta_0}\widetilde{c}_nH_n^{(2)'}(k_0 b\sin\theta_0)$$
$$=-\frac{H_0k_0\sin\theta_0\cos\theta_0}{k_c^2 b\sin^2\theta_1}na_nJ_n(k_c b\sin\theta_1)-\frac{H_0k_0\sin\theta_0\cos\theta_0}{k_c^2 b\sin^2\theta_1}nb_nY_n(k_c b\sin\theta_1)$$
$$-j\frac{H_0}{\zeta\eta_0}\frac{\sin\theta_0}{\sin\theta_1}\widetilde{a}_nJ_n'(k_c b\sin\theta_1)-j\frac{H_0}{\zeta\eta_0}\frac{\sin\theta_0}{\sin\theta_1}\widetilde{b}_nY_n'(k_c b\sin\theta_1), \tag{2.376}$$

$$jH_0\eta_0J_n'(k_0 b\sin\theta_0)-\frac{H_0\cos\theta_0}{k_0 b\sin\theta_0}n\widetilde{c}_nH_n^{(2)}(k_0 b\sin\theta_0)+jH_0\eta_0c_nH_n^{(2)'}(k_0 b\sin\theta_0)$$
$$=-\frac{H_0k_0\sin\theta_0\cos\theta_0}{k_c^2 b\sin^2\theta_1}n\widetilde{a}_nJ_n(k_c b\sin\theta_1)-\frac{H_0k_0\sin\theta_0\cos\theta_0}{k_c^2 b\sin^2\theta_1}n\widetilde{b}_nY_n(k_c b\sin\theta_1)$$
$$+jH_0\zeta\eta_0\frac{\sin\theta_0}{\sin\theta_1}a_nJ_n'(k_c b\sin\theta_1)+jH_0\zeta\eta_0\frac{\sin\theta_0}{\sin\theta_1}b_nY_n'(k_c b\sin\theta_1), \tag{2.377}$$

$$\widetilde{a}_nJ_n(k_c a\sin\theta_1)+\widetilde{b}_nY_n(k_c a\sin\theta_1)=0, \tag{2.378}$$

$$-\frac{H_0k_0\sin\theta_0\cos\theta_0}{k_c^2 a\sin^2\theta_1}n\widetilde{a}_nJ_n(k_c a\sin\theta_1)-\frac{H_0k_0\sin\theta_0\cos\theta_0}{k_c^2 a\sin^2\theta_1}n\widetilde{b}_nY_n(k_c a\sin\theta_1)$$
$$+jH_0\zeta\eta_0\frac{\sin\theta_0}{\sin\theta_1}a_nJ_n'(k_c a\sin\theta_1)+jH_0\zeta\eta_0\frac{\sin\theta_0}{\sin\theta_1}b_nY_n'(k_c a\sin\theta_1)=0. \tag{2.379}$$

As we have done in previous sections, the equations are converted into matrix form and solved. The unknown coefficients are found to be:

$$a_n=\frac{1}{D}Y_n'(k_c a\sin\theta_1)k_0^2k_1^4b^2\sin^2\theta_0\sin^3\theta_1 \tag{2.380}$$
$$.\left[J_n(k_0 b\sin\theta_0)H_n^{(2)'}(k_0 b\sin\theta_0)-J_n'(k_0 b\sin\theta_0)H_n^{(2)}(k_0 b\sin\theta_0)\right]$$
$$.\Big(\zeta\sin\theta_1H_n^{(2)'}(k_0 b\sin\theta_0)$$
$$.\left[J_n(k_c b\sin\theta_1)Y_n(k_c a\sin\theta_1)-J_n(k_c a\sin\theta_1)Y_n(k_c b\sin\theta_1)\right]$$
$$-\sin\theta_0H_n^{(2)}(k_0 b\sin\theta_0)$$
$$.\left[J_n'(k_c b\sin\theta_1)Y_n(k_c a\sin\theta_1)-J_n(k_c a\sin\theta_1)Y_n'(k_c b\sin\theta_1)\right]\Big)$$

$$\widetilde{a}_n=j\frac{1}{D}\zeta\eta_0bnk_0k_1^2\sin\theta_0\sin^2\theta_1\cos\theta_0 \tag{2.381}$$
$$.\left(k_0^2\sin^2\theta_0-k_c^2\sin^2\theta_1\right)Y_n(k_c a\sin\theta_1)H_n^{(2)}(k_0 b\sin\theta_0)$$
$$.\left[J_n'(k_c a\sin\theta_1)Y_n(k_c b\sin\theta_1)-J_n(k_c b\sin\theta_1)Y_n'(k_c a\sin\theta_1)\right]$$
$$.\left[J_n(k_0 b\sin\theta_0)H_n^{(2)'}(k_0 b\sin\theta_0)-J_n'(k_0 b\sin\theta_0)H_n^{(2)}(k_0 b\sin\theta_0)\right],$$

$$b_n = -\frac{J_n'(k_c a \sin\theta_1)}{Y_n'(k_c a \sin\theta_1)} a_n, \tag{2.382}$$

$$\widetilde{b}_n = -\frac{J_n(k_c a \sin\theta_1)}{Y_n(k_c a \sin\theta_1)} \widetilde{a}_n, \tag{2.383}$$

$$c_n = \frac{a_n J_n(k_c b \sin\theta_1) + b_n Y_n(k_c b \sin\theta_1) - J_n(k_0 b \sin\theta_0)}{H_n^{(2)}(k_0 b \sin\theta_0)}, \tag{2.384}$$

$$\widetilde{c}_n = \frac{\widetilde{a}_n J_n(k_c b \sin\theta_1) + \widetilde{b}_n Y_n(k_c b \sin\theta_1)}{H_n^{(2)}(k_0 b \sin\theta_0)}, \tag{2.385}$$

where

$$D = D_1 + D_2, \tag{2.386}$$

$$\begin{aligned} D_1 = &-\zeta \cos^2\theta_0 n^2 \left(H_n^{(2)}(k_0 b \sin\theta_0)\right)^2 \left(k_0^2 \sin^2\theta_0 - k_c^2 \sin^2\theta_1\right)^2 \\ &. \left[J_n(k_c b \sin\theta_1) Y_n(k_c a \sin\theta_1) - J_n(k_c a \sin\theta_1) Y_n(k_c b \sin\theta_1)\right] \\ &. \left[J_n(k_c b \sin\theta_1) Y_n'(k_c a \sin\theta_1) - J_n'(k_c a \sin\theta_1) Y_n(k_c b \sin\theta_1)\right], \end{aligned} \tag{2.387}$$

$$\begin{aligned} D_2 = &\, b^2 k_0^2 k_1^4 \sin^2\theta_0 \sin^2\theta_1 \\ &. \Bigg(J_n'(k_c a \sin\theta_1) \Big[\sin\theta_1 Y_n(k_c b \sin\theta_1) H_n^{(2)'}(k_0 b \sin\theta_0) \\ &\qquad -\zeta \sin\theta_0 Y_n'(k_c b \sin\theta_1) H_n^{(2)}(k_0 b \sin\theta_0)\Big] \\ &\quad -Y_n'(k_c a \sin\theta_1) \Big[\sin\theta_1 J_n(k_c b \sin\theta_1) H_n^{(2)'}(k_0 b \sin\theta_0) \\ &\qquad -\zeta \sin\theta_0 J_n'(k_c b \sin\theta_1) H_n^{(2)}(k_0 b \sin\theta_0)\Big] \Bigg) \\ &. \Bigg(J_n(k_c a \sin\theta_1) \Big[\zeta \sin\theta_1 Y_n(k_c b \sin\theta_1) H_n^{(2)'}(k_0 b \sin\theta_0) \\ &\qquad -\sin\theta_0 Y_n'(k_c b \sin\theta_1) H_n^{(2)}(k_0 b \sin\theta_0)\Big] \\ &\quad -Y_n(k_c a \sin\theta_1) \Big[\zeta \sin\theta_1 J_n(k_c b \sin\theta_1) H_n^{(2)'}(k_0 b \sin\theta_0) \\ &\qquad -\sin\theta_0 J_n'(k_c b \sin\theta_1) H_n^{(2)}(k_0 b \sin\theta_0)\Big] \Bigg) \end{aligned} \tag{2.388}$$

2.12.6 Calculation of the Radar Cross Section

Calculation of the Radar Cross Section is the same as in Section 2.10. The normalized echo width is given in (2.321).

Chapter 3

Achieving Transparency and Maximizing Scattering with Metamaterial Coated Conducting Cylinders

3.1 Introduction

In this chapter, the electromagnetic interaction of plane waves with infinitely long metamaterial coated conducting cylinders is considered. Different from "conjugate" pairing of double-positive (DPS) and double-negative (DNG) or epsilon-negative (ENG) and mu-negative (MNG) concentric cylinders [5,7–12], achieving transparency and maximizing scattering are separately achieved by covering perfect electric conductor (PEC) cylinders with simple (i.e., homogeneous, isotropic and linear) metamaterial coatings. As in the case of "conjugate" pairing, transparency and resonance are found to be heavily dependent on the ratio of core-coating radii, instead of the total size of the cylindrical structure.

In our work we show that, for TE polarization, the metamaterial coating should have $0 < \varepsilon_c < \varepsilon_0$ as its permittivity to achieve transparency, whereas the coating permittivity has to be in the $-\varepsilon_0 < \varepsilon_c < 0$ interval for resonance so that scattering maximization can be achieved. For both transparency and resonance conditions, we derive the analytical relation between the ratio of core-coating radii and the permittivity of the metamaterial coating in the TE polarization case. The numerical results show the validity of these analytical relations, especially when the cylindrical scatterers (i.e., PEC cylinders together with their metamaterial coatings) are electrically small.

Besides, notice that because the core cylinder is PEC, unlike the aforementioned "conjugate" pairing cases, the analytical relations we have derived for TE polarization cannot be used for TM polarization by interchanging ε with μ (and vice versa), unless the core cylinder is replaced with perfect magnetic conductor (PMC). Yet, both transparency and resonant peaks can be achieved for TM polarization. Here, we show numerically that for electrically small PEC cylinders transparency can be obtained by covering them with metamaterial covers having large $|\mu_c|$, whereas resonant peaks are observed when $\mu_c < 0$.

The theory and formulation for TM and TE polarizations have been previously given in Sections 2.7 and 2.8, respectively.

3.2 Transparency Condition

The transparency condition for TE^z polarization is derived in Appendix C by setting the numerator of the scattering coefficient c_n^{TE} given in (2.240) to zero. In the sub-wavelength limit, assuming $|k_c|a < |k_c|b \ll 1, k_0 b \ll 1$ and utilizing the small argument forms of Bessel and Hankel functions, the following transparency

condition is obtained:

$$\gamma = \sqrt[2n]{\frac{\varepsilon_0 - \varepsilon_c}{\varepsilon_0 + \varepsilon_c}} \quad \text{for} \quad n \neq 0. \tag{3.1}$$

where $\gamma = a/b$ is the ratio of core-shell radii, n is the index of series summation.

Alternatively, one can use the transparency condition for an electrically small cylindrical scatterer, which is composed of two concentric layers of different isotropic materials, given in [5] for the TE^z polarization as

$$\gamma = \sqrt[2n]{\frac{(\varepsilon_c - \varepsilon_0)(\varepsilon_c + \varepsilon)}{(\varepsilon_c - \varepsilon)(\varepsilon_c + \varepsilon_0)}} \quad \text{for} \quad n \neq 0, \tag{3.2}$$

$$\gamma = \sqrt{\frac{\mu_c - \mu_0}{\mu_c - \mu}} \quad \text{for} \quad n = 0, \tag{3.3}$$

where (ε, μ) are constitutive parameters of the core cylinder and (ε_c, μ_c) are constitutive parameters of the coating (shell) layer.

When the core cylinder is PEC, $\varepsilon \to -j\infty$ and $\mu = \mu_0$. In this case (3.3) becomes

$$\gamma = \sqrt{\frac{\mu_c - \mu_0}{\mu_c - \mu_0}} = 1 \quad \text{for} \quad \mu_c \neq \mu_0, \; n = 0, \tag{3.4}$$

which means there would be no coating. However, (3.2) can still be used in the limiting case, yielding the same transparency condition in (3.1) as

$$\gamma \to \sqrt[2n]{\frac{(\varepsilon_c - \varepsilon_0)(\varepsilon_c - j\infty)}{(\varepsilon_c + j\infty)(\varepsilon_c + \varepsilon_0)}} = \sqrt[2n]{\frac{\varepsilon_0 - \varepsilon_c}{\varepsilon_0 + \varepsilon_c}} \quad \text{for} \quad n \neq 0. \tag{3.5}$$

The root in (3.1) is of even degree of n (i.e., $2n$), which implies that the argument of the root must be positive. On the other hand, when there is a coating γ should vary between 0 and 1. Therefore,

$$0 < \frac{\varepsilon_0 - \varepsilon_c}{\varepsilon_0 + \varepsilon_c} < 1, \tag{3.6}$$

which leads to

$$0 < \frac{\varepsilon_0 - \varepsilon_c}{\varepsilon_0 + \varepsilon_c} \Rightarrow -\varepsilon_0 < \varepsilon_c < \varepsilon_0, \tag{3.7}$$

and

$$\frac{\varepsilon_0 - \varepsilon_c}{\varepsilon_0 + \varepsilon_c} < 1 \Rightarrow \varepsilon_c < -\varepsilon_0 \quad \text{or} \quad 0 < \varepsilon_c. \tag{3.8}$$

From (3.7) and (3.8), the proper choice for ε_c lies in

$$0 < \varepsilon_c < \varepsilon_0. \tag{3.9}$$

As it can be seen from (3.1)-(3.9), for the TE^z case, the transparency condition for the PEC cylinder is independent of the permeability of its metamaterial coating. As a matter of fact, this is true when the cylindrical scatterer is electrically small and the scattering problem is consequently "quasielectrostatic". Simply we will choose $\mu_c = \mu_0$ in the numerical experiments for convenience.

For a specific coating permittivity ε_c, utilizing (3.1), one can analytically find the core-coating ratio γ at which transparency can be obtained. Similarly, one can rewrite (3.1) as

$$\varepsilon_c = \frac{1 - \gamma^{2n}}{1 + \gamma^{2n}} \varepsilon_0, \tag{3.10}$$

to find the coating permittivity for a desired γ, again analytically. In the numerical experiments, the following procedure is applied to test the accuracy of the transparency condition: for a desired γ value, we analytically find what the coating permittivity, ε_c, should be. Then, using this coating permittivity, we numerically find at which γ value transparency is actually obtained.

In Table 3.1, for certain outer shell radii some γ values are selected where transparency is desired to be observed. The permittivities of the metamaterial coating corresponding to these γ values after (3.10) [by setting $n = 1$ in (3.10)] are tabulated in Table 3.1. Based on numerical results, transparency is obtained at different γ values (reasonably below desired values), which are also tabulated in Table 3.1. One way to explain this deviation (i.e., the difference between desired and obtained γ values where transparency occurs) is when the sub-wavelength limit assumptions are performed, expressions leading to ε_c given in (3.10) [or (3.1)] are overly simplified, particularly in terms of a and b. Interestingly, when

the core cylinder is replaced with a core-dielectric, ε_c given in (3.2) yields accurate results as mentioned in [5] for electrically small cylinders. It is also observed that as the electrical size of the cylindrical scatterer increases, deviation of the obtained γ values from the the desired γ values increases. This is an expected result since the accuracy of (3.10) decreases as the electrical size of the scatterer increases.

Table 3.1: Desired and Obtained γ for Achieving Transparency Using (3.10)

		$b = \lambda_0/100$	$b = \lambda_0/10$	$b = \lambda_0/5$
Desired γ	$\varepsilon_c/\varepsilon_0$	Obtained γ	Obtained γ	Obtained γ
0.2	0.923	0.165	0.15	0.105
0.5	0.6	0.41	0.39	0.31
0.7	0.342	0.595	0.575	0.51
0.9	0.105	0.81	0.805	0.78

Based on Table 3.1 and noticing that the deviation between desired and obtained γ values usually increases as the value of γ increases, we heuristically modify (3.10) as

$$\varepsilon_c = \frac{1-\gamma^{(2n-\gamma)}}{1+\gamma^{(2n-\gamma)}}\varepsilon_0, \tag{3.11}$$

to find ε_c for a desired γ value, analytically. In (3.11), the dependence of ε_c to a and b is more strongly pronounced. Similar to Table 3.1, desired γ values, the corresponding ε_c values and obtained γ values where transparency occurs after (3.11) [again by setting $n = 1$ in (3.11)] are tabulated in Table 3.2. As it can be seen from Table 3.2, our heuristic formula decreases the deviation successfully, especially when $b \leq \lambda_0/10$.

The transparency condition for the initial cylindrical structure for the TM^z polarization can be found from (3.2) and (3.3) utilizing duality:

$$\gamma = \sqrt[2n]{\frac{(\mu_c-\mu_0)(\mu_c+\mu)}{(\mu_c-\mu)(\mu_c+\mu_0)}} \quad \text{for} \quad n \neq 0, \tag{3.12}$$

Table 3.2: Desired and Obtained γ for Achieving Transparency Using (3.11)

		$b = \lambda_0/100$	$b = \lambda_0/10$	$b = \lambda_0/5$
Desired γ	$\varepsilon_c/\varepsilon_0$	Obtained γ	Obtained γ	Obtained γ
0.2	0.895	0.19	0.175	0.125
0.5	0.478	0.49	0.47	0.395
0.7	0.228	0.68	0.67	0.625
0.9	0.0579	0.875	0.875	0.86

$$\gamma = \sqrt{\frac{\varepsilon_c - \varepsilon_0}{\varepsilon_c - \varepsilon}} \quad \text{for} \quad n = 0. \tag{3.13}$$

After replacing the core cylinder with a PEC one, (3.12)-(3.13) become

$$\gamma = \sqrt[2n]{\frac{(\mu_c - \mu_0)(\mu_c + \mu_0)}{(\mu_c - \mu_0)(\mu_c + \mu_0)}} = 1 \quad \text{for} \quad \begin{matrix} \mu_c \neq \mu_0 \\ \mu_c \neq -\mu_0 \end{matrix}, \; n \neq 0, \tag{3.14}$$

$$\gamma = \sqrt{\frac{\varepsilon_c - \varepsilon_0}{\varepsilon_c - \varepsilon}} \to \sqrt{\frac{\varepsilon_c - \varepsilon_0}{\varepsilon_c + j\infty}} \quad \text{for} \quad n = 0. \tag{3.15}$$

It can be deduced from (3.14)-(3.15) that the transparency condition for the TM^z polarization does not lead to any reasonable outcome due to the core being PEC. It is obvious that in DPS-DNG or ENG-MNG pairing no such difficulty arises since duality can be simply applied. To be able to achieve transparency for the TM^z polarization utilizing similar transparency conditions we have derived for TE^z polarization, the core should be PMC instead of PEC. Theoretical analysis or simply duality shows that in such a case one can use the dual of transparency condition for TE^z polarization by interchanging any permittivity with the corresponding permeability. Yet, even if the core cylinder is PEC, our numerical investigations show that polarization can be obtained for electrically small cylinders with metamaterial coatings having large $|\mu_c|$. Examples of this situation are illustrated in Section 3.4 (Numerical Results and Discussion).

3.3 Resonance (Scattering Maximization) Condition

The resonance condition, which increases the scattering drastically for an electrically small cylindrical scatterer, is derived in Appendix D by setting the denominator of the scattering coefficient c_n^{TE} in (2.241) to zero, again in the sub-wavelength limit. This yields the following resonance condition:

$$\gamma = \sqrt[2n]{\frac{\varepsilon_0 + \varepsilon_c}{\varepsilon_0 - \varepsilon_c}} \quad \text{for} \quad n \neq 0. \tag{3.16}$$

Alternatively, one can use the resonance condition given in [8] for the TE^z polarization

$$\gamma = \sqrt[2n]{\frac{(\varepsilon_c + \varepsilon_0)(\varepsilon_c + \varepsilon)}{(\varepsilon_c - \varepsilon_0)(\varepsilon_c - \varepsilon)}} \quad \text{for} \quad n > 0. \tag{3.17}$$

When the core cylinder is PEC, (3.17) becomes

$$\gamma \to \sqrt[2n]{\frac{(\varepsilon_c + \varepsilon_0)(\varepsilon_c - j\infty)}{(\varepsilon_c - \varepsilon_0)(\varepsilon_c + j\infty)}} = \sqrt[2n]{\frac{\varepsilon_0 + \varepsilon_c}{\varepsilon_0 - \varepsilon_c}} \quad \text{for} \quad n > 0. \tag{3.18}$$

Since the root in (3.16) is of even degree of n (i.e., $2n$) and $0<\gamma<1$ should be, then

$$0 < \frac{\varepsilon_0 + \varepsilon_c}{\varepsilon_0 - \varepsilon_c} < 1, \tag{3.19}$$

which leads to

$$0 < \frac{\varepsilon_0 + \varepsilon_c}{\varepsilon_0 - \varepsilon_c} \Rightarrow -\varepsilon_0 < \varepsilon_c < \varepsilon_0, \tag{3.20}$$

and

$$\frac{\varepsilon_0 + \varepsilon_c}{\varepsilon_0 - \varepsilon_c} < 1 \Rightarrow \varepsilon_c < 0 \quad \text{or} \quad \varepsilon_c > \varepsilon_0. \tag{3.21}$$

From (3.20) and (3.21), the proper choice for ε_c lies in

$$-\varepsilon_0 < \varepsilon_c < 0. \tag{3.22}$$

Then, the ratio of core-shell radii γ, to maximize scattering from a metamaterial coated PEC cylinder, can be found analytically from the permittivity of the

coating ε_c utilizing (3.16), and vice versa:

$$\varepsilon_c = \frac{\gamma^{2n} - 1}{\gamma^{2n} + 1}\varepsilon_0. \tag{3.23}$$

In our numerical experiments with scattering maximization, we follow the same procedure as in the transparency condition (i.e., we find the coating permittivity for a desired γ value analytically and then use it in the numerical experiment). Our numerical experiments show that, for electrically small cylindrical scatterers, (3.23) works quite well (by setting $n = 1$). Therefore, we do not modify it as we have modified the analytical transparency relation.

Interestingly, comparison of (3.10) with (3.23) for a desired γ value shows that, the permittivity of the coating to maximize scattering should be the negative of the coating permittivity which makes the cylinder transparent. For the TE^z case, since the scattering maximization condition is independent of the permeability of its coating and for electrically small cylindrical scatterers we are dealing with the "quasielectrostatic" problem, we can safely choose $\mu_c = \mu_0$. Therefore, coatings we use here for scattering maximization are ENG metamaterials (or plasmonic materials).

To understand how this resonance condition occurs, consider a PEC cylinder which is illuminated by a TE^z polarized plane wave. If the cylinder is electrically small, the $n = 0$ term becomes dominant. However, the $n = \pm 1$ terms cannot be neglected since they radiate more efficiently [28]. It has been shown in [28] that the $n = 0$ term is equivalent to a z-directed magnetic line source, while the $n = \pm 1$ terms, which are referred as dipolar terms in [11], correspond to a y-directed electric dipole. Due to its electrically small size, this electric dipole behaves like a capacitive element. If there is also an ENG coating present, the coating will act like an inductive element. Therefore, the whole cylindrical scatterer will form an inductor-capacitor (LC) resonator. A similar scenario is investigated in [17] for electrically small antennas enclosed by metamaterial

shells. As the size of the scatterer increases, quadrupolar (i.e., $n = 2$), octopolar (i.e., $n = 3$) and any higher order terms also emerge as resonant terms [11].

The resonance condition for the same cylindrical structure for the TM^z polarization, which can be derived from (3.17) utilizing duality, is given in [8] as

$$\gamma = \sqrt[2n]{\frac{(\mu_c + \mu_0)(\mu_c + \mu)}{(\mu_c - \mu_0)(\mu_c - \mu)}} \quad \text{for} \quad n > 0. \tag{3.24}$$

After replacing the core cylinder with a PEC one, (3.24) becomes

$$\gamma = \sqrt[n]{\left|\frac{\mu_c + \mu_0}{\mu_c - \mu_0}\right|} \quad \text{for} \quad \mu_c \neq \mu_0, \quad n > 0. \tag{3.25}$$

Although (3.25) states a resonance relation between a desired γ value and μ_c for the TM^z polarization, our numerical investigations show that μ_c values obtained via (3.25) (i.e., from the desired γ values) yield resonance (i.e., maximum scattering) at γ values different from the desired ones. On the other hand, similar to the transparency condition, if PEC core is replaced by a PMC core, then dual of (3.22) (i.e, $-\mu_0 < \mu_c < 0$) yields a resonance at the desired γ value for the TM^z polarization.

Note that, all the formulations used for transparency and scattering maximization conditions are independent of the electrical size of the cylindrical scatterer (i.e., a and b). However, the formulations are expected to work well for electrically very small cylinders (i.e., $|k_c|b \ll 1$, $k_0 b \ll 1$), such that only a few modes of the infinite series summation is enough to represent the whole radar cross section. Although the aforementioned theoretical analysis is based on electrically small cylinders and a few modes of the infinite series is assumed to be dominant, in the computation of the normalized echo widths we use sufficiently many modes to be accurate. In other words, our numerical results do not include any assumption in this sense.

3.4 Numerical Results and Discussion

To assess the accuracy of our numerical routines, we have duplicated one of the numerical results (normalized monostatic echo width of a metamaterial coated PEC cylinder at 1GHz with PEC radius $a = 50$mm and coating radius $b = 70$mm) in [1], which is shown in Fig. 3.1. In addition to the DPS and DNG coatings investigated in [1], we also included ENG and MNG coatings. As seen in Fig. 3.1, we have excellent agreement with the results of [1]. Moreover, a perfect continuation in the monostatic echo width values is observed (as expected) when the coating medium becomes single-negative (SNG) from a DPS or DNG coating. In the previous sections, expanding the transparency condition given in

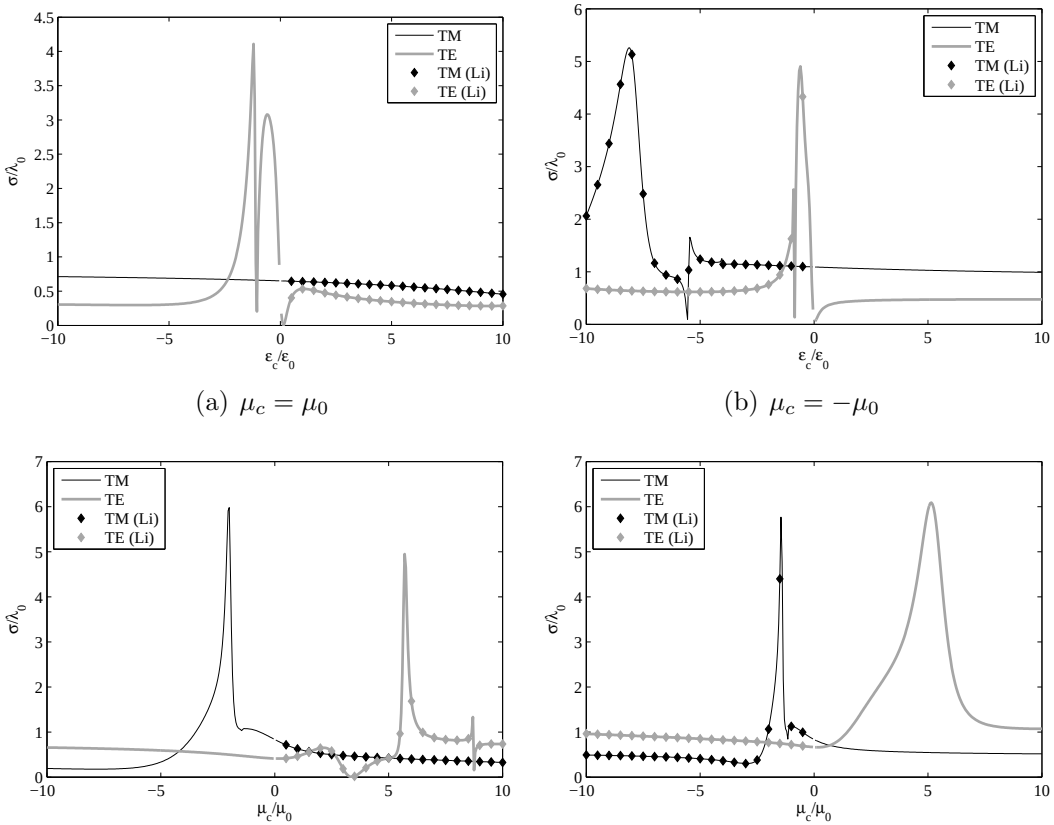

(a) $\mu_c = \mu_0$ (b) $\mu_c = -\mu_0$

(c) $\varepsilon_c = 2.2\varepsilon_0$ (d) $\varepsilon_c = -2.2\varepsilon_0$

Figure 3.1: Normalized monostatic echo width of a metamaterial coated PEC cylinder ($a = 50$mm, $b = 70$mm, $f = 1$GHz). Diamond marks show the DPS and DNG coating cases in [1].

[5], we have found that it is possible to make PEC cylinders transparent for

the TE^z polarization by covering them with metamaterial covers which exhibit the material property given by (3.9). By transparency we mean the significant reduction and minimization of scattering in the backscattering direction. As it has been explained previously, the transparency condition is expected to work well for electrically very small cylinders. Therefore, we start with an electrically very small PEC cylinder (in the cross-sectional sense) covered with our proposed metamaterial coating such that the outer radius of the coating is $b = \lambda_0/100$. Then, for some γ values, where transparency is desired to be observed, the corresponding permittivities are analytically found using (3.11) as tabulated in Table 3.2. Finally, the normalized monostatic echo widths are calculated and depicted in Figs. 3.2(a)-3.2(d) for these permittivities. One can see that transparency is indeed obtained for PEC cylinders almost at the desired γ values. The normalized monostatic echo widths for un-coated PEC cylinders (i.e., with radius a) are shown with dashed lines to visualize the reduction in scattering when proposed metamaterial coatings are used. Note that for the un-coated case small γ values mean extremely small PEC cylinders. Naturally, as a goes to zero, no scattering is supposed to take place. As the next step, we investigate what happens to the transparency as the electrical size of the scatterer increases. For this purpose, we gradually increase the outer radius of the cylindrical scatterer. The normalized monostatic echo widths are calculated and depicted in Figs. 3.2(e)-3.2(h), when the outer radius of the scatterer is increased to $b = \lambda_0/10$. From Figs. 3.2(e)-3.2(h) we see that increasing the electrical size of the cylindrical scatterer from $b = \lambda_0/100$ to $b = \lambda_0/10$ increases the RCS considerably (e.g., the largest normalized monostatic echo width increases roughly from -40dB to -5dB). Despite this huge increase in RCS, as it can be seen from Figs. 3.2(e)-3.2(h) and Table 3.2, transparency can be achieved at the desired γ values. Similarly, we can still achieve transparency close to desired γ values (as tabulated in Table 3.2) when the outer radius of the scatterer is increased to $b = \lambda_0/5$.

Fig. 3.2 and Table 3.2 show that as the permittivity of the coating is decreased from $\varepsilon_c = \varepsilon_0$ to $\varepsilon_c = 0$, the core-coating ratio where transparency occurs moves from $\gamma = 0$ to $\gamma = 1$. To explain this phenomenon, we can treat the metamaterial coating as a cover which cancels out the electromagnetic response of the PEC core. When the permittivity of the metamaterial coating is close to ε_0, this cancellation is quite weak (i.e., metamaterial cover behaves like free space). In this case, the PEC core should be considerably small with respect to the coating such that a full cancellation can occur. However, when the permittivity of the coating is decreased towards 0, the cancellation of the coating will become stronger, which means that with even thinner coatings it becomes possible to make larger PEC cores transparent. Note that a similar discussion is made in [5] to explain the cancellation phenomenon for metamaterial coated dielectric spheres. For both the dielectric core and the metamaterial cover, their polarization vectors are defined, respectively as $\mathbf{P} = (\varepsilon - \varepsilon_0)\mathbf{E}$ and $\mathbf{P_c} = (\varepsilon_c - \varepsilon_0)\mathbf{E}$. The transparency condition is attributed to the cancellation of these antiparallel polarization vectors, which happens when $\varepsilon_c < \varepsilon_0$. In our scenario, since the core cylinder is PEC, the problem has a less degree of freedom and the analytical solution shows that to achieve transparency $0 < \varepsilon_c < \varepsilon_0$ should be.

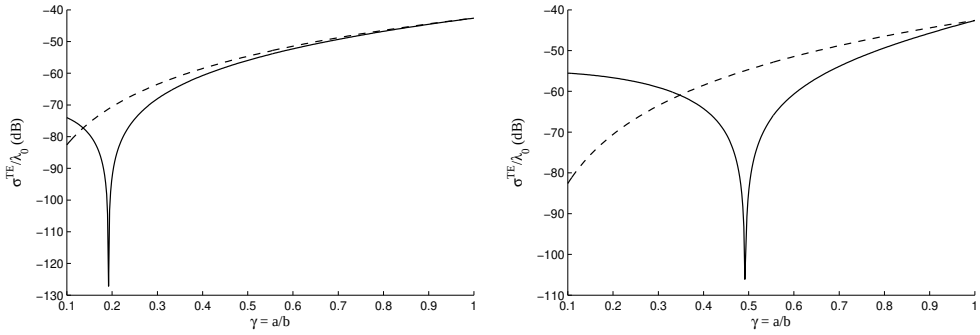

(a) $\varepsilon_c = 0.895\varepsilon_0, \mu_c = \mu_0$ (b) $\varepsilon_c = 0.478\varepsilon_0, \mu_c = \mu_0$

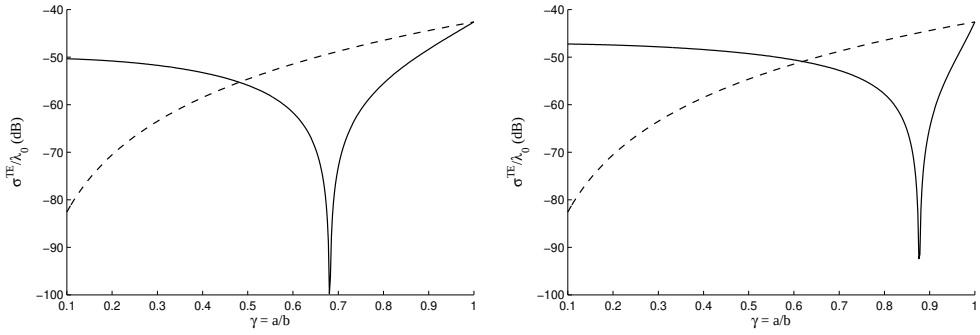

(c) $\varepsilon_c = 0.228\varepsilon_0, \mu_c = \mu_0$ (d) $\varepsilon_c = 0.0579\varepsilon_0, \mu_c = \mu_0$

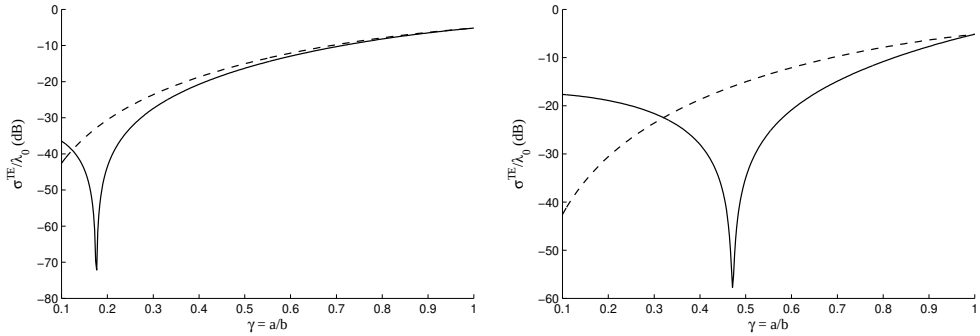

(e) $\varepsilon_c = 0.895\varepsilon_0, \mu_c = \mu_0$ (f) $\varepsilon_c = 0.478\varepsilon_0, \mu_c = \mu_0$

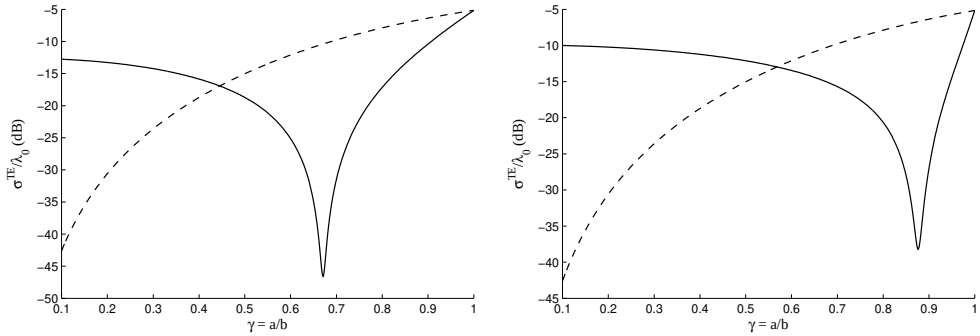

(g) $\varepsilon_c = 0.228\varepsilon_0, \mu_c = \mu_0$ (h) $\varepsilon_c = 0.0579\varepsilon_0, \mu_c = \mu_0$

Figure 3.2: Normalized monostatic echo width of a metamaterial coated PEC cylinder for the TE^z polarization case, versus the core-coating ratio for coatings with different constitutive parameters. The outer radius of the coating is selected as (a)-(d) $b = \lambda_0/100$, (e)-(h) $b = \lambda_0/10$. Dashed line shows the un-coated PEC case, with radius a.

To see the limitations on the electrical size of the cylindrical scatterers for achieving transparency, we will consider relatively larger scatterers. Since these scatterers are electrically large, available analytical relations between γ and ε_c do not hold any longer. Therefore, for these large scatterers we choose ε_c in a trial & error process. Figs. 3.3(a)-3.3(c) show the results when the outer radius of the scatterer is increased to $b = \lambda_0/2$. In Figs. 3.3(d)-3.3(f) this outer radius is further increased to $b = \lambda_0$. As it is seen in Fig. 3.3(a) and Fig. 3.3(d), the normalized monostatic echo width makes two dips at some γ. As the permittivity of the coating is decreased towards 0, the dips move towards $\gamma = 1$, destructively interfering with each other. Finally, the minimum value of the normalized echo width (σ^{TE}/λ_0 drops from 4dB to -25dB) is achieved when the permittivity is very close to zero but positive, and γ being between 0.9 and 1. Therefore, larger cylinders require coatings having permittivities much closer to zero. Since monostatic echo width is minimized in the $0.9 < \gamma < 1$ region, the PEC core can be quite large.

Next, we turn our attention to investigate the validity of scattering maximization condition. Hence, we follow a procedure similar to the one we have done for the transparency condition. We again start with electrically very small cylindrical scatterers and gradually increase their outer radii. We use the same γ in Table 3.1 as our desired γ values, but this time to maximize scattering. Hence, the coating permittivities are the negatives of coating permittivities tabulated in Table 3.1, as a result of (3.23). Figs. 3.4(a)-3.4(d) show the normalized monostatic echo widths for ENG coated PEC cylinders when the outer radius of the scatterer is $b = \lambda_0/100$. As it can be seen from the figures, RCS increases drastically at the desired γ values, making peaks, depending on the permittivity of the coating. This is mainly due to the resonance of dipolar terms which we have explained previously. When the outer radius is $b = \lambda_0/50$, the RCS peaks can still be clearly seen in Figs. 3.4(e)-3.4(h). But, this time the peaks are wider and the peak centers deviate a little from their desired locations. Also note a

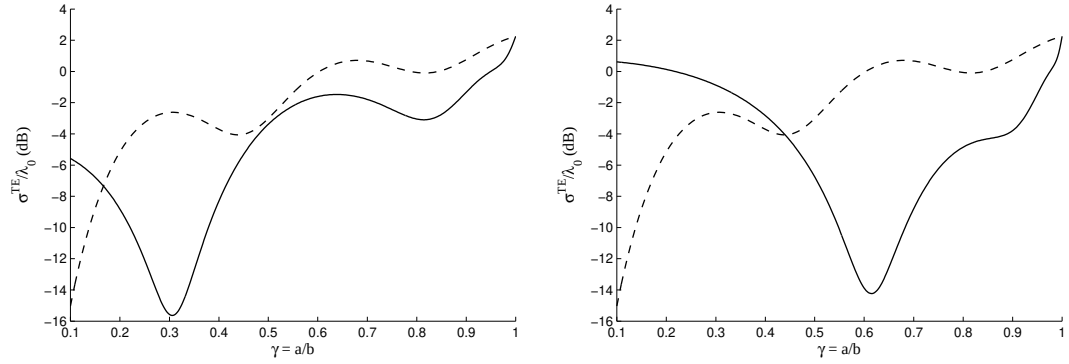

(a) $\varepsilon_c = 0.2\varepsilon_0, \mu_c = \mu_0$

(b) $\varepsilon_c = 0.1\varepsilon_0, \mu_c = \mu_0$

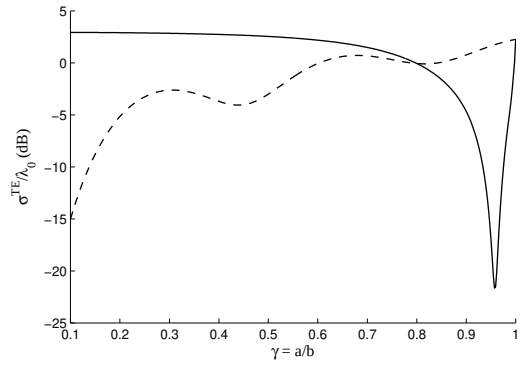

(c) $\varepsilon_c = 0.01\varepsilon_0, \mu_c = \mu_0$

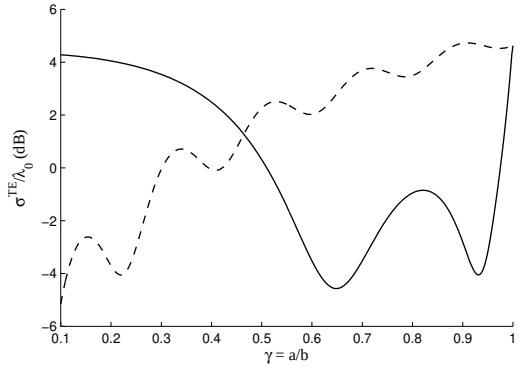

(d) $\varepsilon_c = 0.03\varepsilon_0, \mu_c = \mu_0$

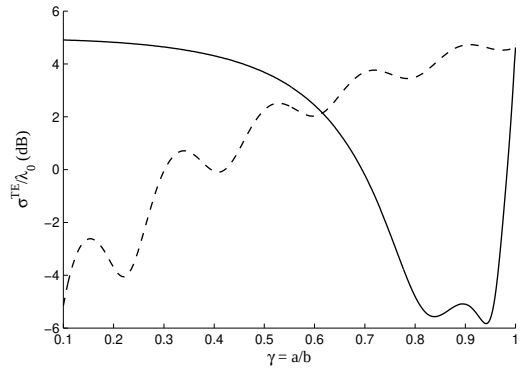

(e) $\varepsilon_c = 0.02\varepsilon_0, \mu_c = \mu_0$

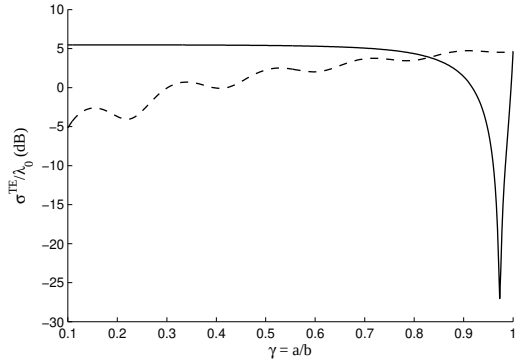

(f) $\varepsilon_c = 0.005\varepsilon_0, \mu_c = \mu_0$

Figure 3.3: Normalized monostatic echo width of a metamaterial coated PEC cylinder for the TE^z polarization case, versus the core-coating ratio for coatings with different constitutive parameters. The outer radius of the coating is selected as (a)-(c) $b = \lambda_0/2$, (d)-(f) $b = \lambda_0$. Dashed line shows the un-coated PEC case, with radius a.

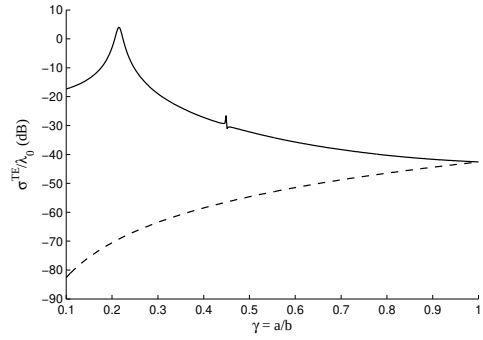

(a) $\varepsilon_c = -0.923\varepsilon_0, \mu_c = \mu_0$

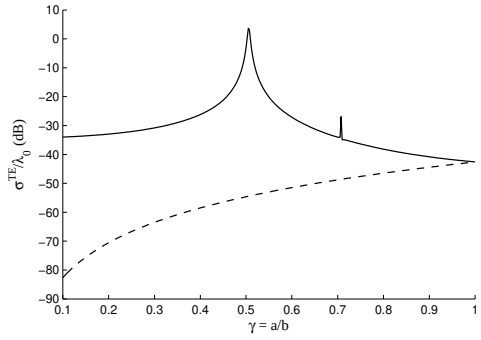

(b) $\varepsilon_c = -0.6\varepsilon_0, \mu_c = \mu_0$

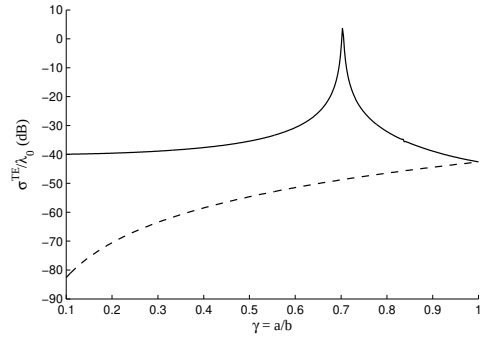

(c) $\varepsilon_c = -0.342\varepsilon_0, \mu_c = \mu_0$

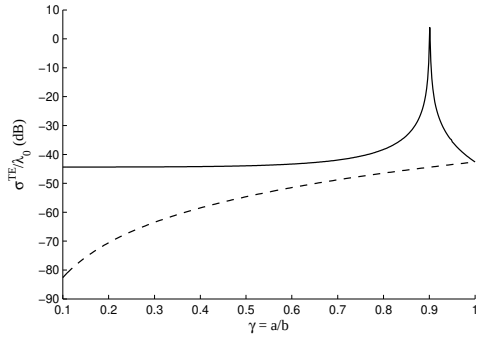

(d) $\varepsilon_c = -0.105\varepsilon_0, \mu_c = \mu_0$

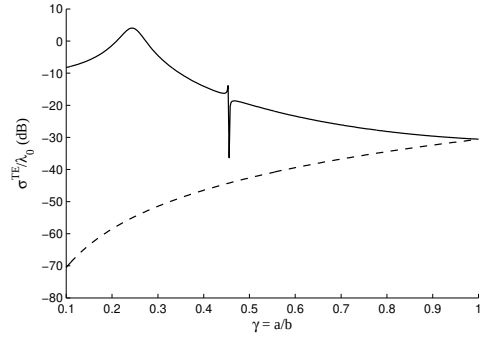

(e) $\varepsilon_c = -0.923\varepsilon_0, \mu_c = \mu_0$

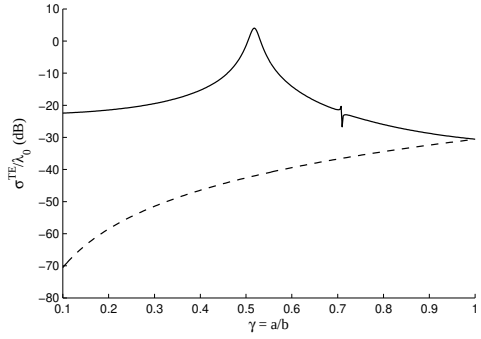

(f) $\varepsilon_c = -0.6\varepsilon_0, \mu_c = \mu_0$

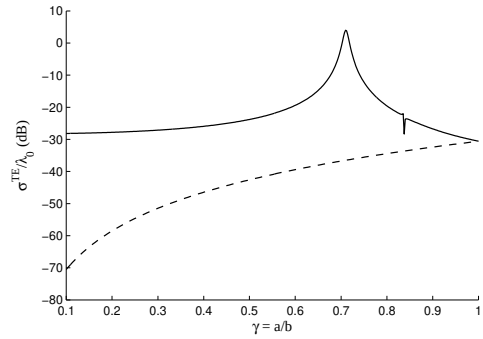

(g) $\varepsilon_c = -0.342\varepsilon_0, \mu_c = \mu_0$

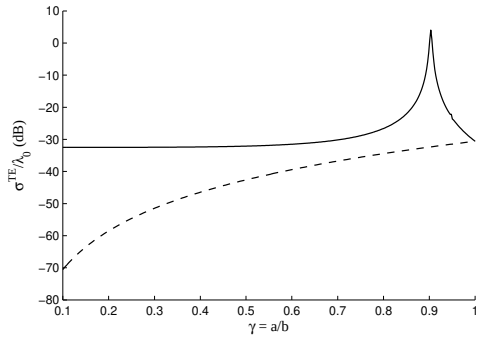

(h) $\varepsilon_c = -0.105\varepsilon_0, \mu_c = \mu_0$

Figure 3.4: Normalized monostatic echo width of an ENG coated PEC cylinder for the TE^z polarization case, versus the core-coating ratio for coatings with different constitutive parameters. The outer radius of the coating is selected as (a)-(d) $b = \lambda_0/100$, (e)-(h) $b = \lambda_0/50$. Dashed line shows the un-coated PEC case, with radius a.

second small peak which just emerges in Fig. 3.4(e) due to the quadrupolar terms. These quadrupolar terms become more observable in Figs. 3.5(a)-3.5(d) where $b = \lambda_0/20$. When the outer radius is increased to $b = \lambda_0/10$, effects of other higher order terms can be observed from Figs. 3.5(e)-3.5(h). In summary, Figs. 3.4-3.5 suggest that as the electrical size of the scatterer increases the peak due to the dipolar term becomes wider and moves towards $\gamma = 1$. Also, due to the increased size, quadrupolar and higher order modes emerge. However, the peak due to the dipolar term is much more dominant and can be safely used to maximize RCS of objects.

To see whether any transparency or scattering maximization condition can be obtained for the TM^z polarization, we consider an electrically very small cylindrical scatterer with outer radius $b = \lambda_0/100$. For various γ values, we calculate the monostatic echo widths when μ_c/μ_0 is in the $[-20\ 20]$ interval, as shown in Fig. 3.6. For this "quasimagnetostatic" problem, we have chosen $\varepsilon_c = \varepsilon_0$ for convenience. Fig. 3.6 shows the existence of resonant modes which maximize the RCS considerably, when $\mu_c < 0$. Transparency can be obtained with coatings having large permeabilities in the absolute sense as seen in Figs. 3.6(a)-3.6(c). For $\gamma = 0.9$, transparency is possible if μ_c is positive and very large.

As we have mentioned previously, the huge increase in the RCS of an ENG coated PEC cylinder is due to high resonance. However, transparency we have achieved using DPS coatings is not a result of such resonance, but simple cancellation. This can be best observed from the changes in RCS with respect to γ, when Figs. 3.2-3.3 are plotted in linear scale. In this case, it can be seen that RCS is not very sensitive to γ near the transparency point. On the contrary, in Fig. 3.4 we see high γ sensitivity. Since transparency condition is not a result of resonation, we also expect it not to be very sensitive to ohmic losses. For the ENG coated cases, however, there would be high sensitivity to ohmic losses near

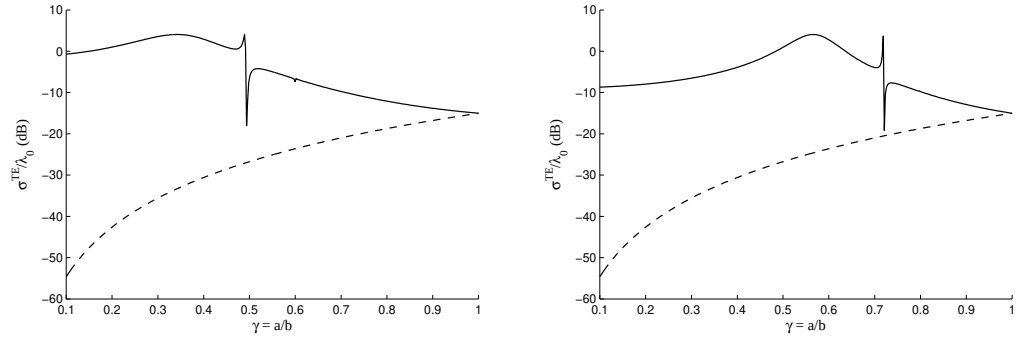

(a) $\varepsilon_c = -0.923\varepsilon_0, \mu_c = \mu_0$ (b) $\varepsilon_c = -0.6\varepsilon_0, \mu_c = \mu_0$

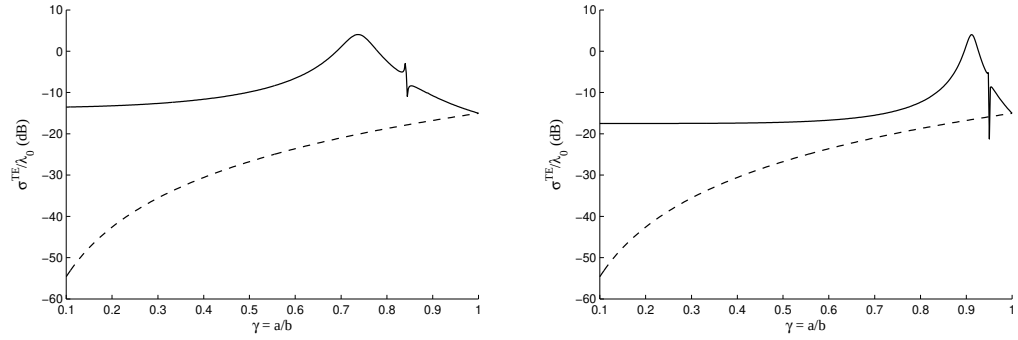

(c) $\varepsilon_c = -0.342\varepsilon_0, \mu_c = \mu_0$ (d) $\varepsilon_c = -0.105\varepsilon_0, \mu_c = \mu_0$

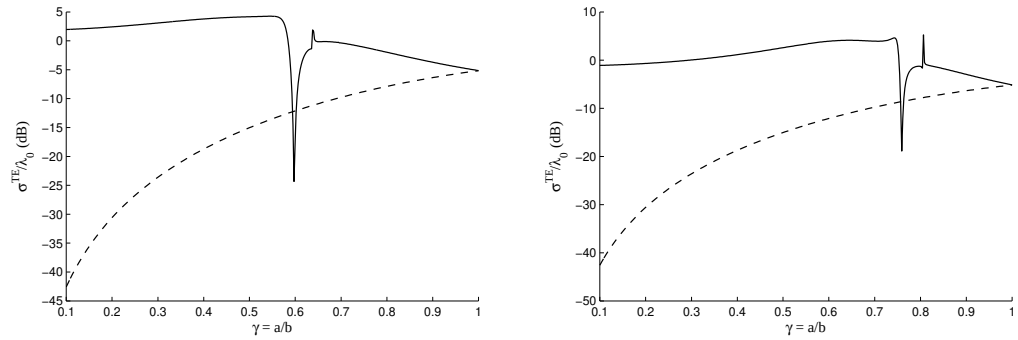

(e) $\varepsilon_c = -0.923\varepsilon_0, \mu_c = \mu_0$ (f) $\varepsilon_c = -0.6\varepsilon_0, \mu_c = \mu_0$

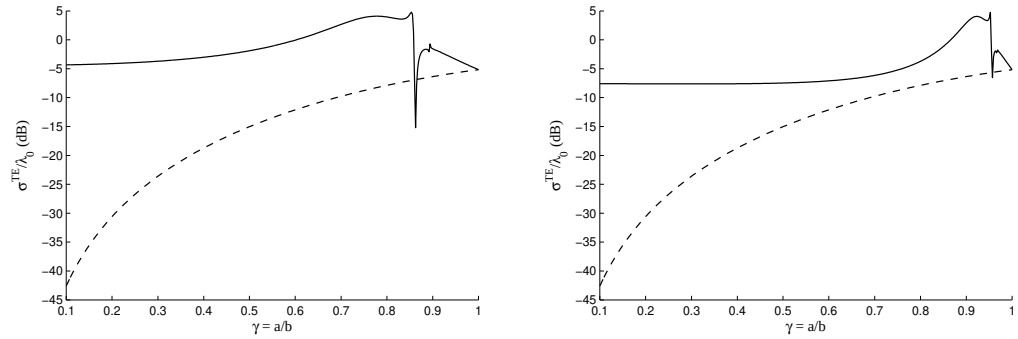

(g) $\varepsilon_c = -0.342\varepsilon_0, \mu_c = \mu_0$ (h) $\varepsilon_c = -0.105\varepsilon_0, \mu_c = \mu_0$

Figure 3.5: Normalized monostatic echo width of an ENG coated PEC cylinder for the TE^z polarization case, versus the core-coating ratio for coatings with different constitutive parameters. The outer radius of the coating is selected as (a)-(d) $b = \lambda_0/20$, (e)-(h) $b = \lambda_0/10$. Dashed line shows the un-coated PEC case, with radius a.

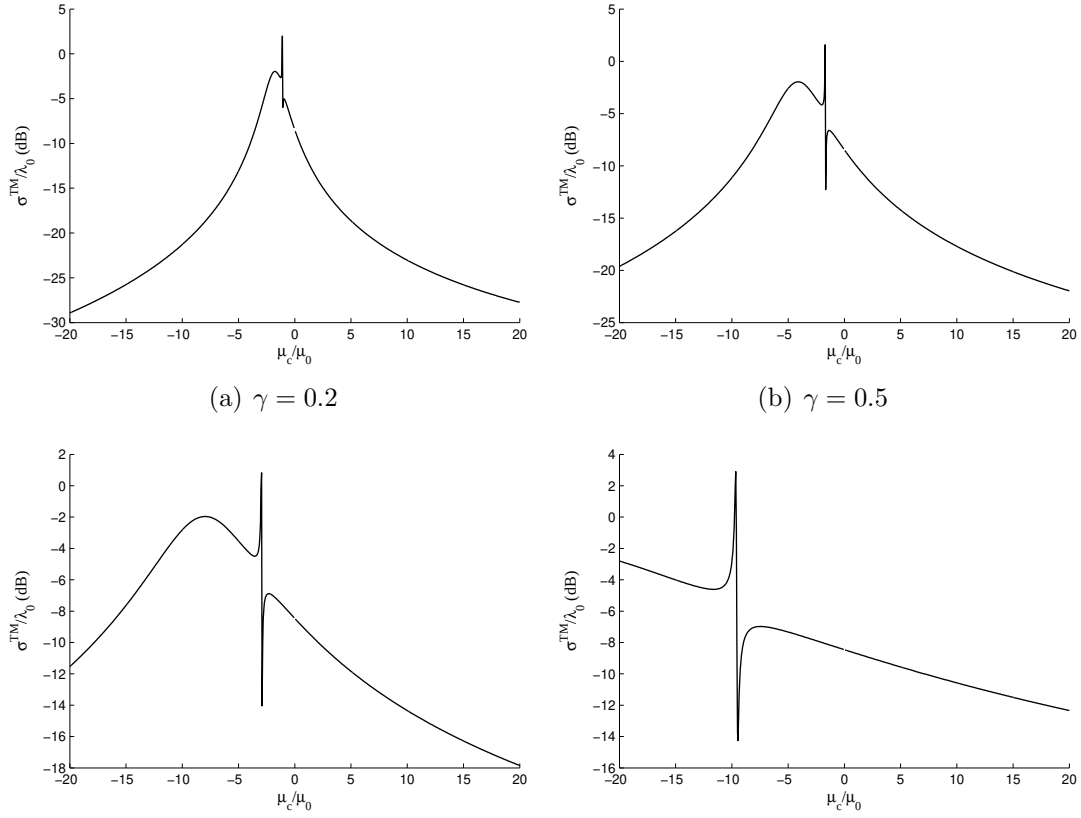

(a) $\gamma = 0.2$ (b) $\gamma = 0.5$

(c) $\gamma = 0.7$ (d) $\gamma = 0.9$

Figure 3.6: Normalized monostatic echo width of a metamaterial coated PEC cylinder for the TM^z polarization case, versus the coating permeability μ_c for different core-coating ratios. The outer radius of the coating is $b = \lambda_0/100$ and the coating permittivity is $\varepsilon_c = \varepsilon_0$.

the resonant modes. The effects of small ohmic losses, as in the Drude or Lorentz medium models, are shown in Fig. 3.7. As predicted, there is very little ohmic sensitivity for transparency condition in Fig. 3.7(a). On the other hand, the high sensitivity to ohmic losses can be seen clearly at the resonance location in Fig. 3.7(b). Again in Fig. 3.7(b), despite the decrease in the monostatic echo width due to the ohmic losses, metamaterial coating provides at least approximately 65dB increase in the echo width at the resonance location, when compared with the un-coated case. In the numerical results we have shown up to here, we have considered the normalized monostatic echo widths (i.e., back scattering). To visualize the far-zone field distribution in the xy-plane, bistatic echo widths can be calculated. Fig. 3.8 illustrates the bistatic scattering scenarios for transparency

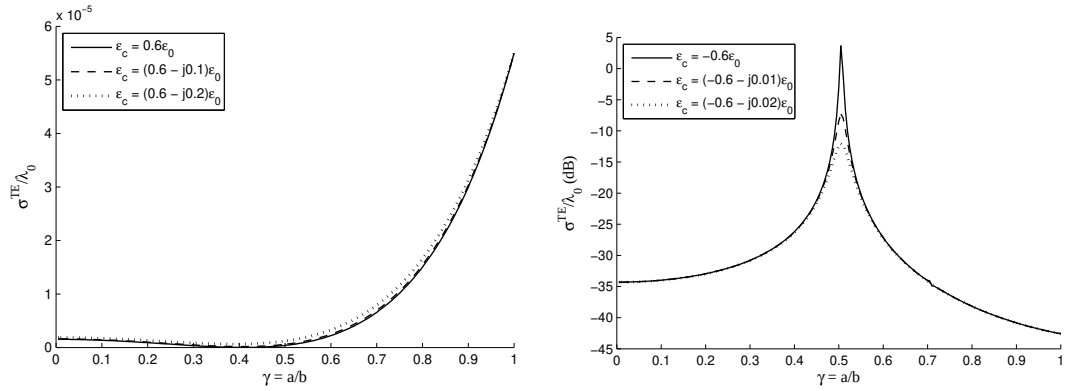

(a) $\varepsilon_c = 0.6\varepsilon_0, \mu_c = \mu_0$ (b) $\varepsilon_c = -0.6\varepsilon_0, \mu_c = \mu_0$

Figure 3.7: Effects of ohmic losses on normalized monostatic echo width for (a) DPS [transparency] (b) ENG [Scattering maximization] cases. The outer radius of the coating is selected as $b = \lambda_0/100$.

and scattering maximization for the TE polarization considering a metamaterial coated PEC cylinder with $b = \lambda_0/100$. The angle of incidence is set to $\phi_0 = 0°$. In Fig. 3.8(a), for the values of $\varepsilon_c = 0.6\varepsilon_0$, $\mu_c = \mu_0$ and $\gamma = 0.41$, it is seen that RCS increases gradually from backscattering direction ($\phi = 180°$) towards direction of incidence ($\phi = 0°$). Therefore, while little portion of the incident wave is reflected back, the much larger portion will continue traveling in the direction of incidence. Indeed, this is the expected situation for transparency. In Fig. 3.8(b), for $\varepsilon_c = -0.6\varepsilon_0$, $\mu_c = \mu_0$ and $\gamma = 0.505$, RCS is maximized in the backscattering and incidence directions, however it reduces towards $\phi = 90°$, finally becoming effectively zero in this direction. In other words, RCS is not only maximized in the backscattering direction, but also in the direction of incidence. Fig. 3.9(a) shows the contour plot of the axial component of the total magnetic field (i.e., $H_z^i + H_z^s$) in the presence of single PEC cylinder, with radius $a = \lambda_0/200$. In Fig. 3.9(b), the PEC cylinder is coated with a DPS metamaterial coating having $b = \lambda_0/100$, $\varepsilon_c = 0.6\varepsilon_0$ and $\mu_c = \mu_0$. Comparison of Fig. 3.9(a) and Fig. 3.9(b) shows the decrease in RCS with the proposed metamaterial coating, especially in the backscattering direction. The case for the resonant ENG coating, for $b = \lambda_0/100$, $\varepsilon_c = -0.6\varepsilon_0$ and $\mu_c = \mu_0$, which increases the RCS dramatically, is

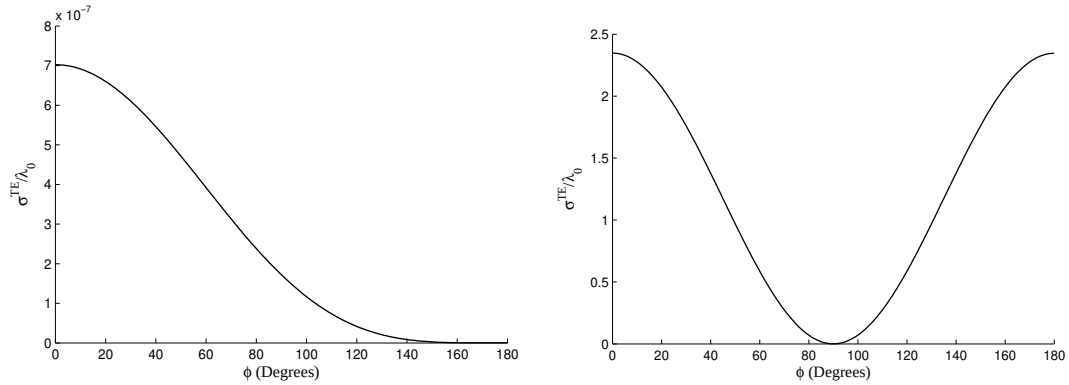

(a) $\varepsilon_c = 0.6\varepsilon_0, \mu_c = \mu_0, \gamma = 0.41$ (b) $\varepsilon_c = -0.6\varepsilon_0, \mu_c = \mu_0, \gamma = 0.505$

Figure 3.8: Normalized bistatic echo widths for (a) DPS coated (b) ENG coated PEC cylinder for the TE^z polarization case. The outer radius of the coating is selected as $b = \lambda_0/100$. The angle of incidence is $\phi_0 = 0^\circ$.

shown in Fig. 3.9(c). The field distribution confirms the strong resonance in the radiation of a y-directed electric dipole.

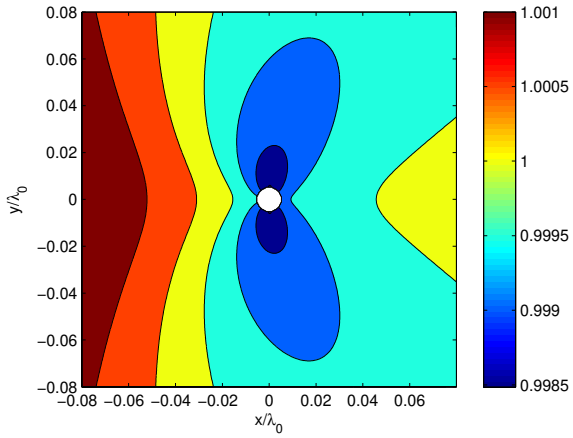

(a) No coating

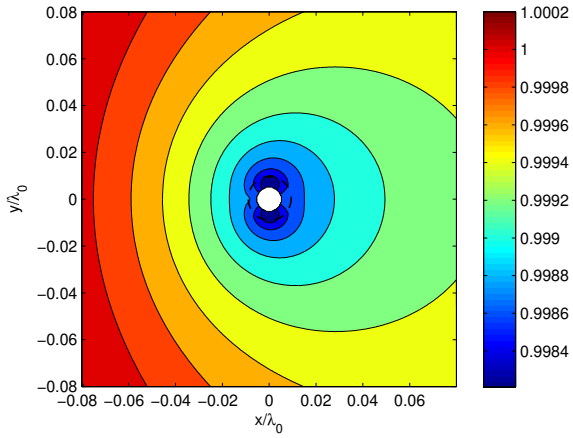

(b) $\varepsilon_c = 0.6\varepsilon_0, \mu_c = \mu_0$

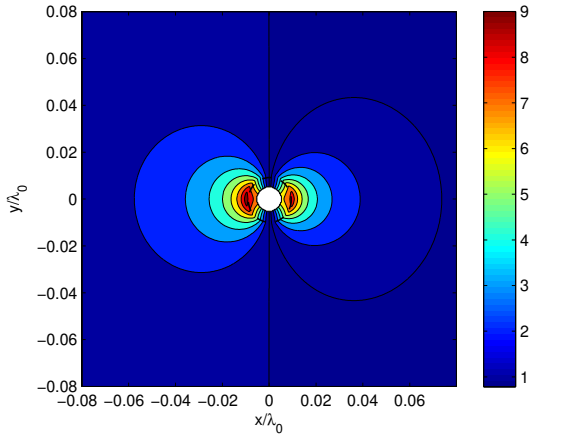

(c) $\varepsilon_c = -0.6\varepsilon_0, \mu_c = \mu_0$

Figure 3.9: Contour plots of axial component of the total magnetic field (i.e., $H_z^i + H_z^s$) outside the PEC cylinder when there is (a) No coating, (b) DPS coating, (c) ENG coating. Outer boundaries of the coatings are shown by dashed lines ($a = \lambda_0/200$, $b = \lambda_0/100$). Plane wave illumination is along the $+x$-axis.

Fig. 3.10 shows the preliminary results for the oblique incidence case. It can be observed that, the angle of oblique incidence changes the transparency condition, however, resonance condition is affected very slightly.

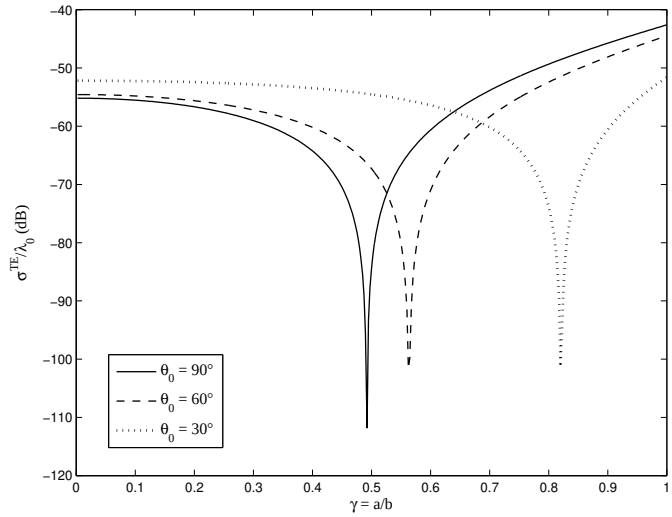

(a) $\varepsilon_c = 0.478\varepsilon_0, \mu_c = \mu_0$

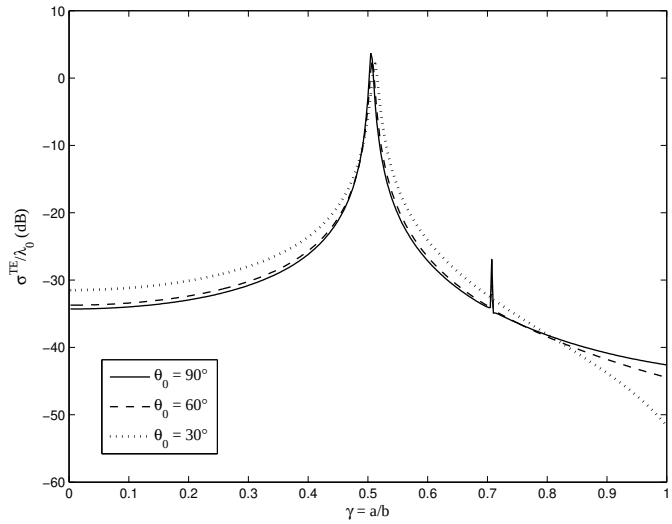

(b) $\varepsilon_c = -0.6\varepsilon_0, \mu_c = \mu_0$

Figure 3.10: Normalized monostatic echo widths for (a) DPS coated (b) ENG coated PEC cylinder for the TE^z polarization, oblique incidence case. The outer radius of the coating is selected as $b = \lambda_0/100$.

Chapter 4

Retrieval of Homogenization Parameters

4.1 Homogenization of Metamaterial Structures and Retrieval of Effective Constitutive Parameters

4.1.1 Introduction

The physical properties of matter together with the underlying mathematics (e.g., Bloch's Theorem, Lyapunov-Floquet Theorem) lead to extraordinary phenomena when structures are aligned periodically. Photonic and electromagnetic band gap materials, frequency selective surfaces and yet metamaterials are some artificial structures which make use of the periodicity. With their unnatural behavior, these structures are highly exploited for engineering purposes. In engineering, the use of periodic alignment can also be seen in antennas, cMUTs, optical

gratings etc., to increase the overall performance of a system or to establish a predefined task.

For the analysis and design of periodic materials and structures, to be able to practically incorporate them in larger systems, their overall equivalents have to be calculated. As an example, for an array of antennas an array factor can be defined. The overall response of the antenna array can be calculated by multiplying this array factor with the response of a single antenna. However, most of the time the contribution of the interactions between these antennas cannot be easily neglected. To obtain accurate results, full wave analysis of the system is necessary. Similarly, for periodic materials an equivalent homogeneous material can be defined which exhibits the same properties with the material of interest. The process of obtaining this homogeneous equivalent, with its all intermediate steps, is called homogenization. For periodic materials, obtaining the homogeneous equivalent from the basic building block of the material is obviously simpler and more towards the design of actual material of interest. Most of the time, the building block of the periodic material is not canonical and a full wave analysis may be required to obtain the behavior of a building block itself. Once the response of a single building block is obtained, the overall structure can be modeled analytically from the results of the building block. The homogenization processes present in the literature [18–22] are usually examples of such processes.

However, the interactions between the many building blocks, which form the periodic structure, must not be simply neglected. Especially for periodic structures, the periodicity of the structure and therefore the presence of periodic building blocks are of utmost importance. Hence, for accurate homogenization of periodic structures, a rigorous method has to be formed to successfully represent the whole periodic structure. The method we introduce in this work is intended to accomplish this idea.

4.1.2 Homogenization of Metamaterials

In this section, we will focus on the homogenization of metamaterials. However, the method we present here is not only restricted to metamaterials, therefore it can be applied to any finite or semi-infinite periodic structure. Although the method is quite versatile and applicable to oblique incidence scenarios, in this work we will consider the normal incidence case for a three dimensional metamaterial structure.

In general, metamaterials are inhomogeneous, anisotropic and highly dispersive materials. With the homogenization process we obviously remove the inhomogeneity, however the material maintains its anisotropic and dispersive state. Therefore the homogenization process for metamaterials is inherently anisotropic and dispersive. For this reason, the homogenization process can be applied at a single direction (θ_0, ϕ_0) and at a single frequency, a time.

Metamaterial Geometry:

The building blocks for metamaterials are usually cubic cells, which are also called unit cells. The unit cell is basically composed of a Split Ring Resonator (SRR), a wire and a substrate on which the SRR and wire are mounted. The SRR is formed by two circular or rectangular loops, one within another, with gaps located at the opposite locations on these loops. A typical unit cell for a metamaterial is shown in Fig. 4.1.

For metamaterials, the SRRs provide negative effective magnetic permeability and the wires provide negative effective electric permittivity. However, this extraordinary behavior can be observed with the proper polarization of electric and magnetic fields with respect to the SRR structure, such that the magnetic field should be perpendicular to the SRRs and the electric field should reside in the plane parallel to the SRRs. A typical case is shown in Fig. 4.2.

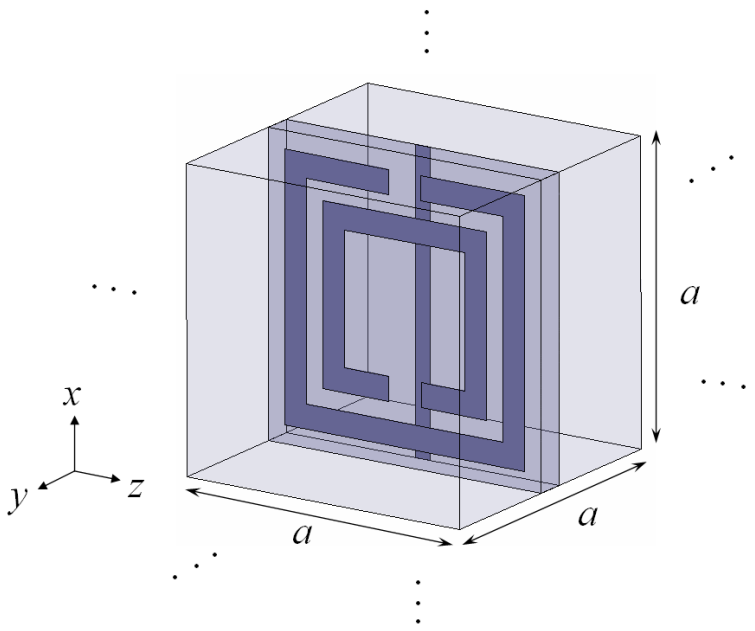

Figure 4.1: Metamaterial unit cell.

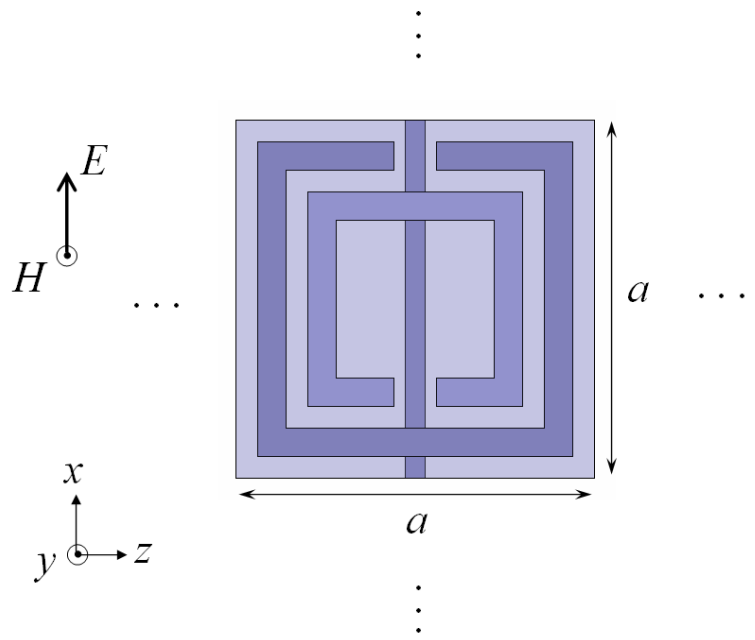

Figure 4.2: Direction of **E** and **H** fields for a unit cell.

In a right handed medium, for the TEM mode, the directions of **E** and **H** fields in Fig. 4.2 suggest the direction of propagation to be in the $+z$ direction. However, in a left handed medium the phase velocity will be in the $-z$ direction, whereas the energy flow will be again in the $+z$ direction. The direction of propagation, to avoid ambiguity, should refer to the direction of energy flow (i.e., direction of the Poynting vector) for both right handed and left handed media.

Implementation of Boundary Conditions and Excitation:

Consider Fig. 4.3 where a metamaterial of thickness d is placed in air and a plane wave is normally incident. The metamaterial medium (i.e., Medium 2) is composed of metamaterial unit cells depicted in Fig. 4.2. Let N_x, N_y, and N_z denote the number of unit cells stratified in the x, y and z directions, respectively. The metamaterial medium is assumed to be of infinite extent in the transverse direction (i.e., $N_x \to \infty, N_y \to \infty,$). Practically this is the case for $N_x \gg N_z$ and $N_y \gg N_z$.

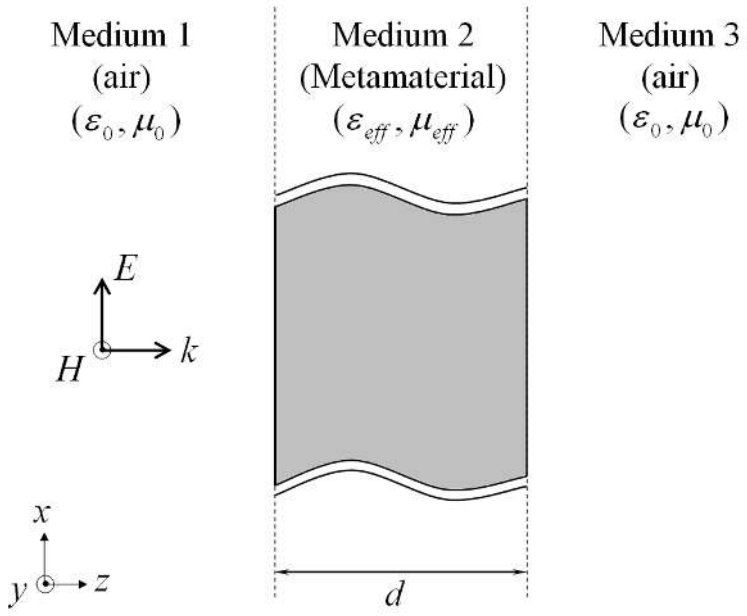

Figure 4.3: Direction of **E** and **H** fields for a unit cell.

Let x_{max}, x_{min}, y_{max} and y_{min} denote the four surfaces of a unit cell, referring to Fig. 4.1 and Fig. 4.2. If the four neighboring cells around a unit cell in the

transverse direction are considered, for their touching surfaces, x_{max}, x_{min}, y_{max} and y_{min} surfaces of the unit cell at the center are identical to x_{min}, x_{max}, y_{min} and y_{max} surfaces of the corresponding neighboring cells, respectively. This is due to the fact that unit cells are indistinguishable in the transverse direction. Therefore x_{max} and x_{min} surfaces of a unit cell are identical to each other, as y_{max} and y_{min} surfaces of the unit cell are identical to each other. Hence, a periodic boundary condition for the x_{max} and x_{min} surfaces with zero phase and another periodic boundary condition for the y_{max} and y_{min} surfaces with zero phase can be used to simulate the periodicity in the transverse direction.

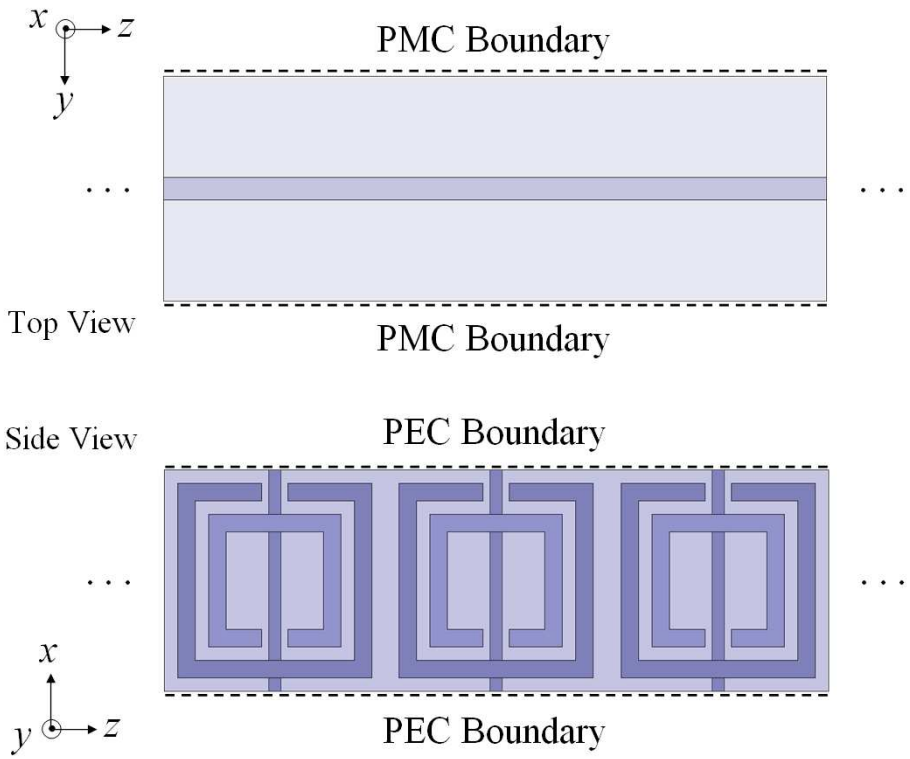

Figure 4.4: Alignment of unit cells inside the PEC-PMC waveguide.

Another, and computationally more efficient, method has been suggested in [30] for the simulation of SRR+wire metamaterial structures. Unit cells of the metamaterial structure are placed in a PEC-PMC waveguide and stratified in the z direction as seen in Fig. 4.4. The PMC walls are parallel to the SRR structure and force the magnetic field to be perpendicular to themselves and also to the SRR structure. The PEC walls are perpendicular to the SRR structure such

that the electric field becomes parallel to the SRR structure. The electric and magnetic fields forced by the PEC-PMC waveguide are in full accordance with the plane wave polarization seen in Fig. 4.3.

In our computer simulations, we used High Frequency Structure Simulator (HFSS) of Ansoft Inc., which is a Finite Element Method (FEM) based electromagnetic simulator, and we implemented the aforementioned PEC-PMC waveguide method. The problem geometry is depicted in Fig. 4.5.

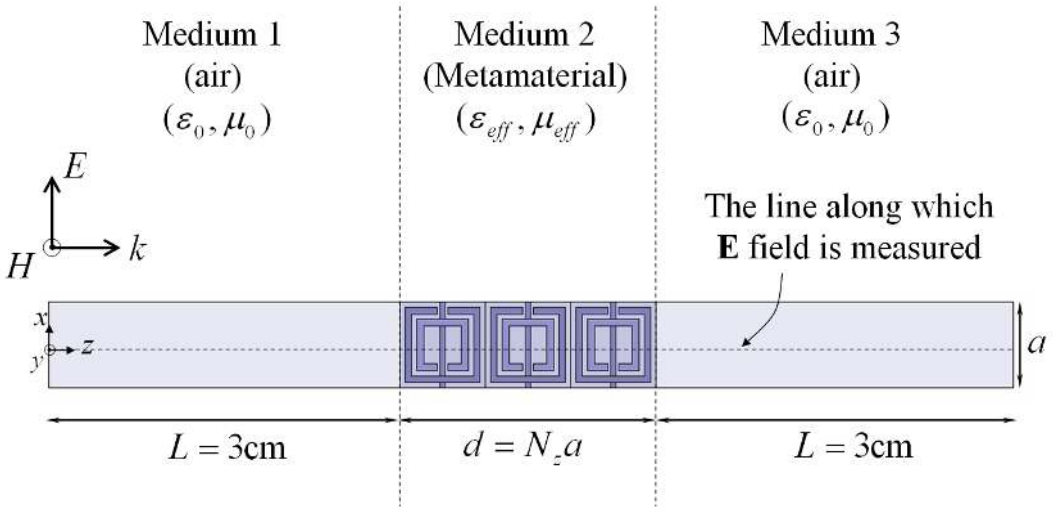

Figure 4.5: Problem geometry (cross-section view, for $N_z = 3$).

The metamaterial unit cell we use is the same with the symmetric unit cell given in [21] except only that the SRR and wire structures are assumed to have zero thicknesses and are applied Perfect Electric boundary condition (i.e., treated as PEC) to reduce the required memory and the computation cost.

The thickness of the metamaterial structure d depends on the number of unit cells stratified in the z direction N_z, such that $d = N_z a$, where $a = 2.5$mm is the unit cell size.

With the coordinate system given in Fig. 4.5, the $x = a/2$ and $x = -a/2$ surfaces of Medium 1, Medium 2 and Medium 3 are applied the PEC boundary condition, whereas their $y = a/2$ and $y = -a/2$ surfaces are applied the PMC

boundary condition, in accordance with the PEC-PMC waveguide method explained previously. The two ends of the geometry (i.e., $z = 0$ and $z = 2L + d$ surfaces) are applied the Radiation Boundary Condition, where $L = 3$cm is the length of Medium 1 and Medium 3.

The structure is illuminated with a plane wave which originates at $z = 0$ surface, with its polarization and propagation direction as shown in Fig. 4.5. The plane wave has magnitude 1 and phase 0 at the $z = 0$ surface, where it originates.

Homogeneous Equivalent :

If the metamaterial medium (Medium 2) can be successfully represented with its homogeneous equivalent, we can define a Generalized Reflection Coefficient (GRC) at the interface between Medium 1 and Medium 2 as given in [31],

$$\begin{aligned}\Gamma_{in}(z = L) &= \Gamma_{12} + T_{12}T_{21}\Gamma_{23}e^{-j2k_{z2}d} + T_{12}T_{21}\Gamma_{21}\Gamma_{23}^2e^{-j4k_{z2}d} + \cdots \\ &= \Gamma_{12} + \frac{T_{12}T_{21}\Gamma_{23}e^{-j2k_{z2}d}}{1 - \Gamma_{23}\Gamma_{21}e^{-j2k_{z2}d}},\end{aligned} \tag{4.1}$$

where k_{z2} is the wave number in z direction in Medium 2, Γ_{ij} and T_{ij} are the direct reflection and transmission coefficients at the interface between layers i and j, respectively. Note that, (4.1) is valid for the more general oblique incidence case. For the normal incidence case, $k_{z2} = k_2$.

Extraction of Electric Field Data:

After the simulation, x component of the electric field (i.e., E_x) is measured on the line passing through the centers of the unit cells. The begin and end points of this line are $(0, 0, 0)$ and $(0, 0, 2L + d)$ respectively. A typical magnitude plot of the x component of the electric field is shown in Fig. 4.5. It should be noted that the electric field plotted in Fig. 4.5 is the scattered electric field (i.e., [total electric field − incident electric field] in Medium 1, 2 and 3). Since we use the

PEC-PMC waveguide method, the y and z components of the electric field are nearly zero.

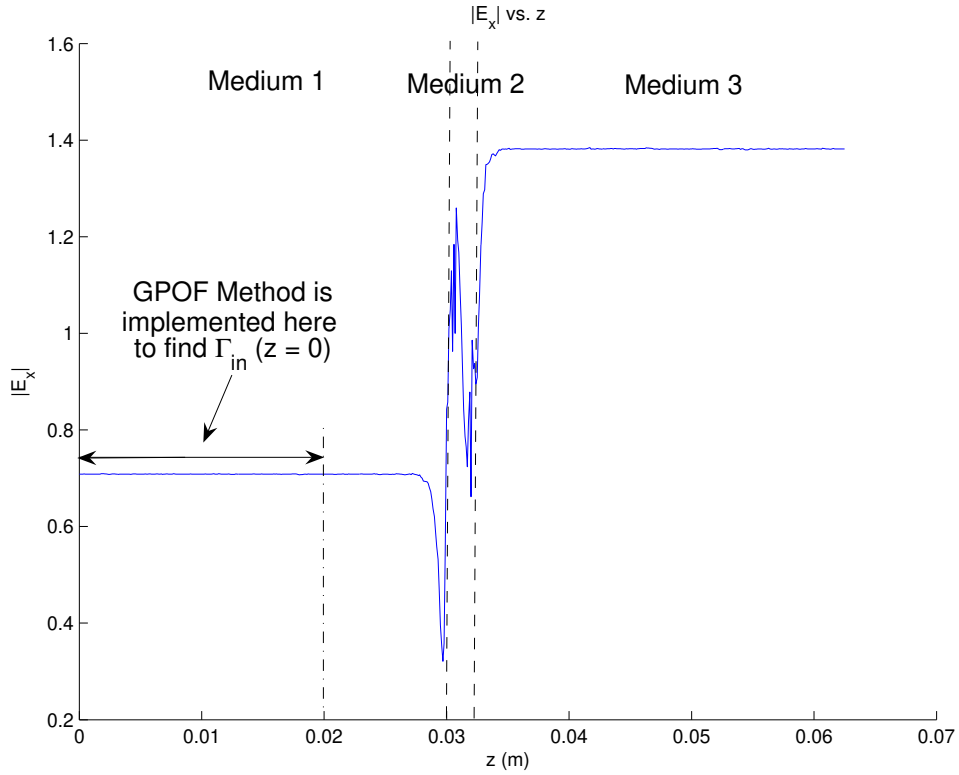

Figure 4.6: $|E_x|$ vs. z $(f = 10GHz, N_z = 1)$.

The scattered field in Medium 1 is basically a plane wave traveling in the $-z$ direction. In Medium 3, the transmitted field travels in the $+z$ direction. However, as seen in Fig. 4.5, there are transition regions near the boundaries of metamaterial medium (i.e., Medium 2). This is mainly due to discontinuities inside the PEC-PMC waveguide and mode conversions. However these non-TEM modes decay fast. Therefore the scattered and transmitted fields away from the metamaterial medium, in Medium 1 and Medium 3 respectively, are TEM waves.

Obtaining the Reflection Coefficients:

GPOF Method [32] is one of the many methods used in approximating a complex function in terms of complex exponentials. Other methods used for this purpose are various forms of the Prony's Method such as Least Square Prony's Method, Total Least Square Prony's Method and Singular Value Decomposition

Prony's Method. Another method is the Pencil of Function Method which forms the basis of the Generalized Pencil of Function Method. In GPOF Method, basically, a generalized eigenvalue problem is solved and subspace decomposition is employed. GPOF Method is superior to aforementioned methods in its less noise sensitivity and computational efficiency [33].

The reflection coefficient $\Gamma_{in}(z = 0)$ in Medium 1 is found by applying the Generalized Pencil of Function (GPOF) method to the E_x field component data in $z = [0, 2L/3]$ interval and fitting it by 1 exponential. The propagation constant of the scattered wave in Medium 1, obtained via GPOF method, is verified to be $-k_1$, where k_1 is the free space propagation constant in Medium 1 (propagating in the $+z$ direction). The $z = [0, 2L/3]$ interval is selected by inspection because, for all frequencies of interest, the electric field data in this interval does not overlap with the aforementioned transition region. Due to the non-uniform meshing of the geometry and numerical noise, applying the GPOF method in this interval is more reliable than simply dividing the scattered field at $z = 0$ to the incident field at the same point (which is $1 + j0$). GPOF method basically removes the numerical noise in the data.

To find $\Gamma_{in}(z = L)$ given in (4.1), which is the S_{11} of the metamaterial structure, we use the following relation:

$$S_{11} = \Gamma_{in}(z = L) = \Gamma_{in}(z = 0)e^{j2k_1L}. \tag{4.2}$$

To find the s-parameters of the metamaterial structure, we could only use Medium 2 with two wave ports attached to its input and output surfaces to set up the excitations. In this setup, we have run simulations with different number of modes for the waveguide $(1, 2, \ldots)$. However, S_{11} results of these simulations vary noticeably from our setup, maybe because of the aforementioned fast decaying non-TEM modes are still existent. Our simulation setup seems more reasonable and it is closer to a real life scenario. However, in the wave ports setup, the voltages or powers are calculated over the entire surfaces. In

our setup, instead of measuring the electric field in only one line, which passes through the midpoints of unit cells, we could take different parallel lines to this line and average the results. As we will present with the results, another line which passes through the edge of the unit cells gives the same electric field distribution in Mediums 1 and 3, while differing from Medium 2 because it does not go through the dielectric in the unit cell, but air.

Fresnel Reflection:

Γ_{12}, the first term in (4.1), is called the Fresnel reflection term. Fresnel reflection occurs when electromagnetic wave passes from one medium to a different medium. Therefore, Fresnel reflection term is obviously expected at the interface of two homogeneous and different media. The nice thing about the Fresnel reflection is its time causality. In other words, Fresnel reflection term is just a result of discontinuity of the medium in which the wave travels, independent of whatever the wave will experience in the future. If we consider Fig. 4.7, the Fresnel reflections for (a) and (b) are the same. Therefore, to find the Fresnel reflection term at the interface of two media, the medium in which the wave is transmitted can be taken as semi-infinite and all layers beyond this medium can be neglected. All contributions of these layers will be present in the GRC, as other terms except the Fresnel reflection term.

The Fresnel coefficient can be easily calculated for Fig. 4.7 (b). However the Fresnel reflection term will take two different forms for the decoupled TE and TM modes [31]:

$$\Gamma_{12}^{TE} = \frac{\mu_2 k_{z1} - \mu_1 k_{z2}}{\mu_2 k_{z1} + \mu_1 k_{z2}}, \tag{4.3}$$

$$\Gamma_{12}^{TM} = \frac{\varepsilon_2 k_{z1} - \varepsilon_1 k_{z2}}{\varepsilon_2 k_{z1} + \varepsilon_1 k_{z2}}. \tag{4.4}$$

For the TEM wave in Fig. 4.7, at normal incidence ($k_{z1} = k_1$ and $k_{z2} = k_2$), either (4.3) for E_x or (4.4) for H_y can be used. In our work we have checked both methods and they gave the same result as expected.

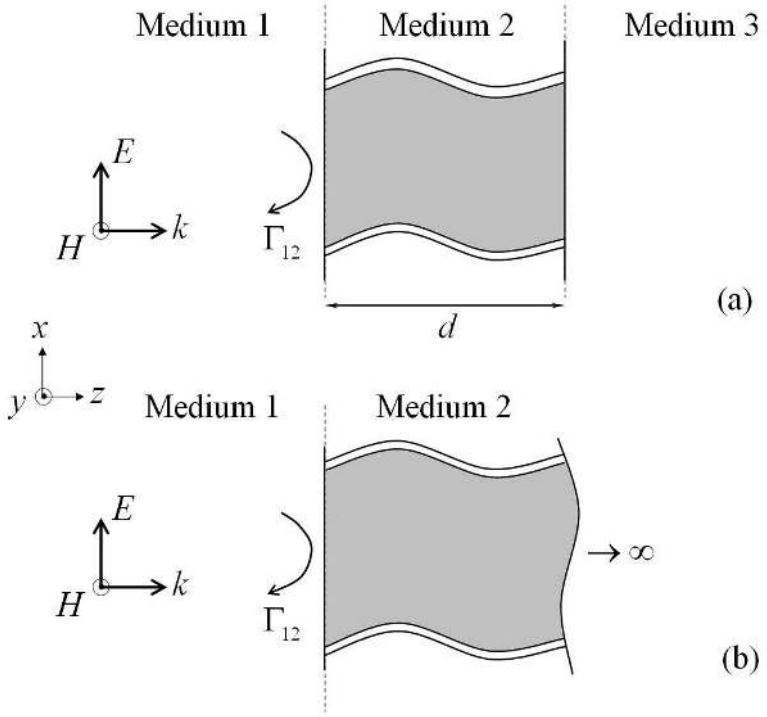

Figure 4.7: Fresnel reflection at (a) three layered media, (b) two layered media.

Expressing S_{11} as Summation of Complex Exponentials:

Let us rewrite the GRC equation in (4.1):

$$S_{11} = \Gamma_{12} + T_{12}T_{21}\Gamma_{23}e^{-j2k_{z2}d} + T_{12}T_{21}\Gamma_{21}\Gamma_{23}^2 e^{-j4k_{z2}d} + \cdots. \tag{4.5}$$

As seen in (4.5), S_{11} is actually a function of $d = N_z a$. In our method we vary N_z and record the S_{11}s correspondingly. In other words, we have the S_{11} vs. N_z response of the metamaterial medium and we express it as a summation of complex exponentials:

$$S_{11}(N_z) \approx \sum_{i=1}^{M} b_i e^{s_i N_z a}, \qquad N_z = N_0, N_0 + 1, \ldots, N_0 + N - 1 \tag{4.6}$$

where b_i's are the complex residues, s_i's are the complex exponents, M is the number of exponentials to represent the GRC with truncating the infinite series, N_0 is the initial number of unit cells stratified in the z direction and N is total number of unit cells used. Fitting the GRC with M exponentials is done using the GPOF Method.

We have obtained the reflection coefficients, S_{11}, for metamaterial stacks made up of $N_z = 1, 2, \ldots, 20$ unit cells. For each stack, and each frequency from 5GHz to 15GHz (with 200MHz steps) S_{11} are calculated as explained previously. Referring to (4.6):

$$\begin{aligned} S_{11}(N_0) &\approx b_1 e^{js_1 N_0 a} + b_2 e^{js_2 N_0 a} + \cdots + b_M e^{js_M N_0 a}, \\ S_{11}(N_0+1) &\approx b_1 e^{js_1 (N_0+1) a} + b_2 e^{js_2 (N_0+1) a} + \cdots + b_M e^{js_M (N_0+1) a}, \\ &\vdots \\ S_{11}(N_0+N-1) &\approx b_1 e^{js_1 (N_0+N-1) a} + b_2 e^{js_2 (N_0+N-1) a} + \cdots + b_M e^{js_M (N_0+N-1) a}, \end{aligned} \tag{4.7}$$

where $N_0 \geq 1$ but not necessarily $N_0 = 1$ and $N_0 + N - 1 = 20$. (4.7) can also be written as

$$\begin{aligned} S_{11}(N_0) &\approx b'_1 e^{js'_1 0a} + b'_2 e^{js'_2 0a} + \cdots + b'_M e^{js'_M 0a}, \\ S_{11}(N_0+1) &\approx b'_1 e^{js'_1 1a} + b'_2 e^{js'_2 1a} + \cdots + b'_M e^{js'_M 1a}, \\ &\vdots \\ S_{11}(N_0+N-1) &\approx b'_1 e^{js'_1 (N-1) a} + b'_2 e^{js'_2 (N-1) a} + \cdots + b'_M e^{js'_M (N-1) a}. \end{aligned} \tag{4.8}$$

When we apply the GPOF method to a vector such as:

$[S_{11}(N_0)\ S_{11}(N_0+1) \ldots\ S_{11}(N_0+N-1)]$, and fit it with M exponentials, we actually obtain b'_i and $s'_i.a$, the complex residues and exponentials in (4.8), respectively. This is because GPOF method treats the index of the first entry in a vector as zero, in our case as $N_0 = 0$. However, our aim is to find b_i and $s_i.a$ in (4.7) where $N_0 \neq 0$ is the number of unit cells used as bias. Therefore we should relate these complex residues and exponentials to each other. Comparison of (4.7) with (4.8) shows that

$$b_i = b'_i e^{-js'_i N_0 a} \quad , \quad s_i = s'_i. \tag{4.9}$$

Now we have found b_i and s_i correctly, to approximate S_{11} given in (4.5) as a summation of complex exponentials expressed in (4.6). Comparison of two

equations term by term shows that:

$$\begin{aligned} b_1 &= \Gamma_{12}, & s_1 &= 0, \\ b_2 &= T_{12}T_{21}\Gamma_{23}, & s_2 &= -j2k_{z2}, \\ b_3 &= T_{12}T_{21}\Gamma_{21}\Gamma_{23}^2, & s_3 &= -j4k_{z2}, \\ &\vdots & &\vdots \end{aligned} \tag{4.10}$$

which means b_1 is the Fresnel reflection term, s_1 is the complex exponential corresponding to the Fresnel reflection term and should be zero, $s_2 = -j2k_{z2}$, $s_3 = -j4k_{z2}$, ... can be used to calculate k_{z2}.

The propagation constant k_{z2}, found from each of the complex exponential terms s_i, $i \geq 2$, should be the same, such that the $k_{z2}.a$ product calculated using each exponent is the same and remains in the reduced Brillouin zone $[-\pi, \pi]$. The following derivations explain the reduction of the complex propagation constant, k_{z2}, to the reduced Brillouin zone.

Reduction to the Reduced Brillouin Zone:

Consider the second and third complex exponentials of the GPOF approximation in (4.10), assuming $M > 2$.

$$e^{-j2k_{z2}a} = e^{s_2 a}e^{-j2\pi m} = e^{s_2 a - j2\pi m}, \tag{4.11}$$

$$e^{-j4k_{z2}a} = e^{s_3 a}e^{-j2\pi n} = e^{s_3 a - j2\pi n}, \tag{4.12}$$

where m, n are integers. Then,

$$-j2k_{z2}a = s_2 a - j2\pi m, \tag{4.13}$$

$$-j4k_{z2}a = s_3 a - j2\pi n. \tag{4.14}$$

$$-j2(\mathrm{Re}\{k_{z2}\} + j\mathrm{Im}\{k_{z2}\})a = (\mathrm{Re}\{s_2\} + j\mathrm{Im}\{s_2\})a - j2\pi m, \tag{4.15}$$

$$-j4(\mathrm{Re}\{k_{z2}\} + j\mathrm{Im}\{k_{z2}\})a = (\mathrm{Re}\{s_3\} + j\mathrm{Im}\{s_3\})a - j2\pi n. \tag{4.16}$$

$$2\text{Im}\{k_{z2}\}a - j2\text{Re}\{k_{z2}\}a = \text{Re}\{s_2\}a + j\text{Im}\{s_2\}a - j2\pi m, \tag{4.17}$$

$$4\text{Im}\{k_{z2}\}a - j4\text{Re}\{k_{z2}\}a = \text{Re}\{s_3\}a + j\text{Im}\{s_3\}a - j2\pi n. \tag{4.18}$$

Therefore,

$$-2\text{Re}\{k_{z2}\}a = \text{Im}\{s_2\}a - 2\pi m \;\rightarrow\; \text{Re}\{k_{z2}\}a = -\frac{1}{2}\text{Im}\{s_2\}a + \pi m, \tag{4.19}$$

$$-4\text{Re}\{k_{z2}\}a = \text{Im}\{s_3\}a - 2\pi n \;\rightarrow\; \text{Re}\{k_{z2}\}a = -\frac{1}{4}\text{Im}\{s_3\}a + \frac{\pi}{2}n. \tag{4.20}$$

$$2\text{Im}\{k_{z2}\}a = \text{Re}\{s_2\}a \;\rightarrow\; \text{Im}\{k_{z2}\}a = \frac{1}{2}\text{Re}\{s_2\}a, \tag{4.21}$$

$$4\text{Im}\{k_{z2}\}a = \text{Re}\{s_3\}a \;\rightarrow\; \text{Im}\{k_{z2}\}a = \frac{1}{4}\text{Re}\{s_3\}a. \tag{4.22}$$

The integers m, n in (4.19)-(4.20) are selected such that the $\text{Re}\{k_{z2}\}a$ product calculated using each exponential s_i, $i = 2, 3$ is the same and remains in the reduced Brillouin zone $[-\pi, \pi]$. The procedure is similar for exponentials s_i, $i > 3$.

Finding the Effective Constitutive Parameters:

After Γ_{12} and k_{z2} have been found out, for TEM polarization at normal incidence, either (4.3) for TE polarized E_x or (4.4) for TM polarized H_y can be used to find the effective relative μ_r or ε_r of the homogeneous medium respectively. In our method we used E_x component of the electric field, therefore utilizing (4.3):

$$\mu_r = \frac{(1+\Gamma_{12})k_{z2}}{(1-\Gamma_{12})k_{z1}}, \tag{4.23}$$

where $k_{z1} = k_1 = \omega\sqrt{\mu_0\varepsilon_0}$ is the wave number in Medium 1 (air).

Since

$$k_2 = \omega\sqrt{\mu_2\varepsilon_2} = 2\pi f\sqrt{\mu_r\varepsilon_r}\sqrt{\mu_0\varepsilon_0} = \frac{2\pi f}{c}\sqrt{\mu_r\varepsilon_r}, \tag{4.24}$$

$$\varepsilon_r = \frac{\left(\frac{c}{2\pi f}\right)^2 (k_{t2}^2 + k_{z2}^2)}{\mu_r}, \tag{4.25}$$

where $k_{t2} = k_{t1} = k_1 \sin\theta_i$ is the wave number in transverse direction in Medium 2, $\sin\theta_i$ being the angle of oblique incidence. $\theta_i = 0°$, $k_{z2} = k_2$ for normal incidence.

Replacing the Metamaterial with its Homogeneous Equivalent:

Once μ_r and ε_r of the homogeneous equivalent for the metamaterial structure have been obtained, we can replace the metamaterial structure with its homogeneous equivalent. Since the metamaterial structure is dispersive, its homogeneous equivalent is also dispersive. Therefore, the obtained μ_r and ε_r values are frequency dependent and can be better written as $\mu_r(\omega)$ and $\varepsilon_r(\omega)$. It is worthwhile to mention that $\mu_r(\omega)$ and $\varepsilon_r(\omega)$ are complex quantities.

In HFSS, electric permittivity and magnetic permeability of a material cannot be directly assigned complex numbers. However, relative permittivity (ε'_r) and dielectric loss tangent ($\tan\delta_d$) together with relative permeability (μ'_r) and magnetic loss tangent ($\tan\delta_m$) can be used alternatively.

$$\varepsilon_r(\omega) = \varepsilon'_r(\omega) - j\varepsilon''_r(\omega) \tag{4.26}$$

$$\tan\delta_d(\omega) = \frac{\varepsilon''_r(\omega)}{\varepsilon'_r(\omega)} \tag{4.27}$$

$$\mu_r(\omega) = \mu'_r(\omega) - j\mu''_r(\omega) \tag{4.28}$$

$$\tan\delta_m(\omega) = \frac{\mu''_r(\omega)}{\mu'_r(\omega)} \tag{4.29}$$

Both positive and negative real numbers can be assigned to relative permittivity, dielectric loss tangent, relative permeability and magnetic loss tangent. Other properties of the material are left at their defaults:

Bulk Conductivity = 0 S/m, Magnetic Saturation = 0 T

Lande G factor = 2, Delta H = 0 A/m.

Speeding up the process: Although the homogeneous equivalent is much simpler than the metamaterial structure, due to the size of problem, it takes

considerable amount of time to run the geometry in HFSS and to obtain the electric field data and reflection coefficient (in the order of several hours). To solve this problem, we used the slab problem of Section 2.2. Since the PEC-PMC waveguide method enforces TEM wave propagation in the normal direction, using a slab with constitutive parameters μ_r and ε_r, the reflection coefficient of the slab as well as electric fields in Medium 1, 2 and 3 are obtained, in very good agreement with the HFSS results and in seconds. This allowed us to build an efficient optimization algorithm.

Optimization Algorithm:

Since metamaterials are highly dispersive, their homogeneous equivalents are also expected to be highly dispersive. Hence, the effective constitutive parameters of the homogeneous equivalent change with frequency, sometimes rapidly. If a homogeneous slab is considered at a single frequency, the effective constitutive parameters of the slab play an important role on the number of exponentials to be used, to approximate the generalized reflection coefficient successfully, as in Discrete Complex Image Method (DCIM). Therefore, the number of exponentials to successfully represent the generalized reflection coefficient is expected to change from one frequency to another, based on the effective constitutive parameters of the homogeneous equivalent at that frequency.

On the other hand, suppose the following vector is used in the GPOF method, at a single frequency: $[S_{11}(N_0)\ S_{11}(N_0+1)\ldots\ S_{11}(N_0+N-1)]$. The variation of physical length along this vector corresponds to $(N-1)a$. The electrical length variation for the same vector should be sufficiently large, such that the samples of the vector do not reside very close to each other and hence cause singularity. Usually, the electrical path length variation along the vector, $k_{z2}(N-1)a$, is expected to be larger than π for successful approximation with complex exponentials.

Another aspect of the homogenization problem in metamaterials is the highly resonant properties of the unit cells which build the metamaterial structure. The wire and split ring resonators inside the unit cell of a metamaterial cause electric and magnetic resonances, which are very dominant near their resonant frequencies. When the unit cells are stacked, the mutual interactions between these unit cells are very high. Now, consider only one unit cell. If another unit cell is added, the electromagnetic response of the metamaterial slab will change abruptly. When a third unit cell is also added, the response is also expected to change, but less abruptly. As unit cells are added, after some point, the interaction of the newly added unit cell with the very first unit cells (at the other end of the stack) will be quite weak. Therefore, in the homogeneous state, the interaction of a newly added unit cell is expected to be dominant only with the unit cells in its neighborhood. Also, when another unit cell is added, the interaction of the new unit cell with its neighbors should be at the same amount as in the case of previously added unit cell. In summary, the metamaterial slab can be said to be homogeneous when it has sufficiently large number of unit cells. This also means that if the metamaterial structure is not acting homogeneous, using generalized reflection coefficients for this structure will contaminate the retrieved constitutive parameters. Therefore, the generalized reflection coefficients used in the GPOF vector should begin from a sufficiently large number of unit cells, which we have defined previously as N_0: number of unit cells used as bias.

To sum up, the two important parameters in the homogenization process are:

1. Number of unit cells used as bias: N_0,

2. Number of complex exponentials: M.

Therefore, we have developed an optimization algorithm which finds the optimum (N_0, M) combinations using the S_{11} data obtained from stacks made up of $N_z = 1, 2, \ldots, 20$ unit cells. In our optimization code we follow these steps:

i. Select N_0 (from 1 to 17). This means that the length of the vector used in the GPOF method is $N = 20 - N_0 + 1$.

ii. Select M (from 2 to $\lfloor \frac{N}{2} \rfloor$).

iii. Apply GPOF method to the vector and fit with M exponentials. Obtain (b_i', s_i').

iv. Obtain (b_i, s_i) from (b_i', s_i') using (4.9).

v. Sort $|s_i|$ in an increasing manner. Re-index s_i and b_i vectors in the same sequence with the sorted $|s_i|$.

vi. Obtain the Fresnel term from b_1. (s_1 should be very close to zero, if homogenization is successful.)

vii. Drop b_1 and s_1 from b_i and s_i vectors, respectively.

viii. Sort new $|b_i|$ vector in a decreasing manner. Re-index b_i and s_i vectors in the same sequence with the sorted $|b_i|$. The entries of the s_i vector now correspond to s_2, s_3, ...

ix. Obtain k_{z2} from (4.19) and (4.21), selecting m such that the $\mathrm{Re}\{k_{z2}\}a$ product remains the in the reduced Brillouin zone $[-\pi, \pi]$.

x. From Fresnel reflection coefficient Γ_{12} and wave number k_{z2}, obtain the effective constitutive parameters μ_r and ε_r, using (4.23) and (4.25).

xi. Using (ε_r, μ_r) obtain the reflection coefficients of the homogeneous equivalents (i.e., homogeneous slabs with thicknesses $N_0 a$, $(N_0 + 1)a$, ... , $(N_0 + N - 1)a$): $[S_{11}'(N_0)\ S_{11}'(N_0 + 1) \ldots\ S_{11}'(N_0 + N - 1)]$.

xii. Obtain the mean square error (MSE) for the last 4 stacks, which is a heuristic choice for obtaining the error in homogenization:

$$\begin{aligned}\text{MSE} = &|S'_{11}(N_0+N-4) - S_{11}(N_0+N-4)|^2 \\ &+|S'_{11}(N_0+N-3) - S_{11}(N_0+N-3)|^2 \\ &+|S'_{11}(N_0+N-2) - S_{11}(N_0+N-2)|^2 \\ &+|S'_{11}(N_0+N-1) - S_{11}(N_0+N-1)|^2\end{aligned} \tag{4.30}$$

xiii. Find the optimum (N_0, M) pair in the least mean square (LMS) sense, following the steps i-xii for different possible choices of N_0 and M.

After the optimization algorithm, the final constitutive parameters of the homogeneous equivalent are obtained. In the frequency band, at some frequencies, both constitutive parameters are positive (i.e., DPS); at some frequencies, both constitutive parameters are negative (i.e., DNG); and for the rest of the frequencies they have alternative signs (i.e., SNG). For the frequencies at which the homogeneous equivalent is SNG, it is observed that two terms in the GPOF approximation are dominant: 1) the first term which gives the Fresnel term 2) the second term which gives the propagation constant. The higher order terms of the GPOF approximation are negligible. The propagation constant has a large and negative imaginary part, and the wave inside the metamaterial structure decays rapidly, which is related to the evanescent wave behavior of SNG metamaterials.

If more than 2 exponentials are used at these frequencies, the Fresnel term more or less stays the same, but the second exponential term is affected. Interestingly, the optimization algorithm may erroneously select the number of exponentials M to be more than 2, which may yield a better Fresnel coefficient for minimizing the MSE.

Here it should be noted that the optimization scheme and the LMS algorithm are dependent only on the reflection data, and they are much more dependent on Fresnel reflection than they are on the propagation constant. This is because

the Fresnel coefficient is the most dominant factor in the generalized reflection coefficient, and therefore optimization, since the metamaterial unit cell and total thickness of the metamaterial are very small.

For the SNG cases, because of the aforementioned reasons, we overrule the findings of the optimization algorithm. For SNG cases, the number of bias unit cells are selected as $N_0 = 1$, for the rapidly decaying wave to be able to bounce back, and the number of exponentials is selected as $M = 2$, because there should be 2 dominant terms in the GPOF approximation.

4.1.3 Numerical Results

Following the optimization procedure, and correction of the frequencies at which the metamaterial is SNG, the effective constitutive parameters of the homogeneous equivalent are obtained as in Fig. 4.8.

After the homogeneous equivalent is obtained, its scattering parameters, S_{11}, are compared with those of the metamaterial structure, in Fig. 4.9. There is a very good agreement between the scattering parameters over the frequency band.

The exponential approximations are tabulated in Table 4.1 as examples of three different situations: the SNG case at $f = 5$GHz, the DNG case at $f = 10.8$GHz and the DPS case at $f = 15$GHz.

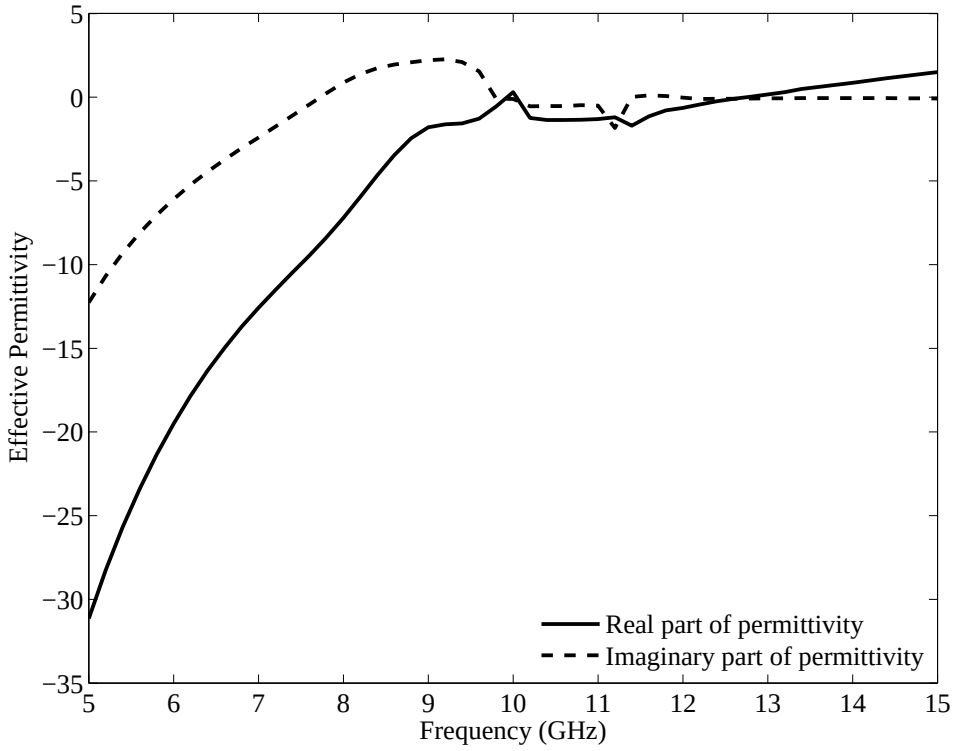

(a)

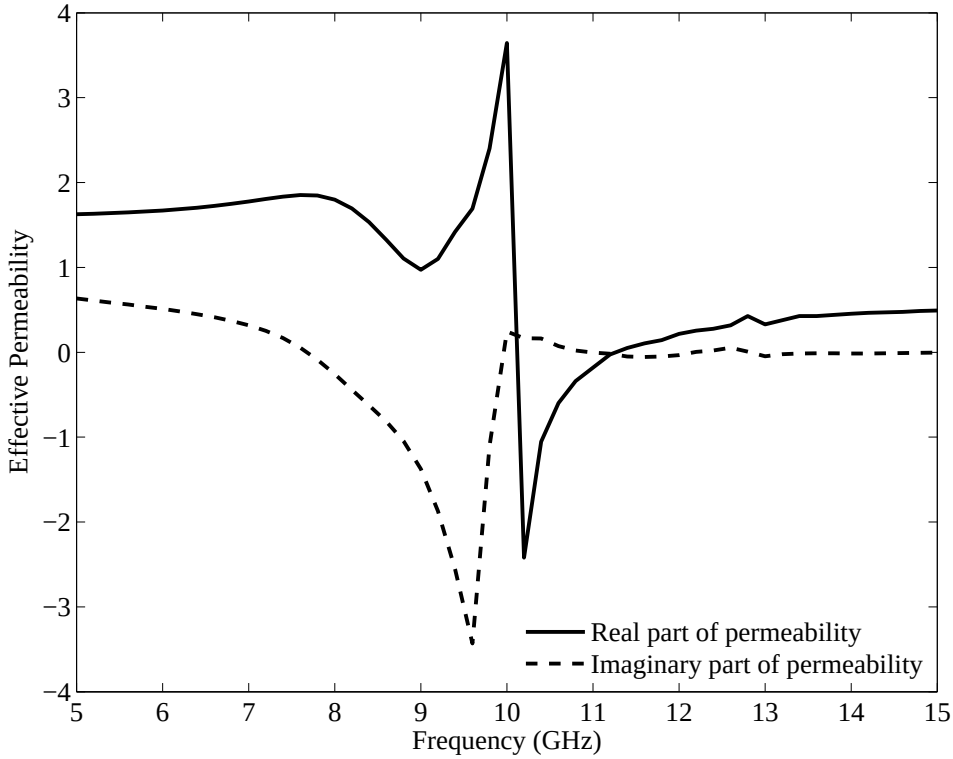

(b)

Figure 4.8: Effective homogenization parameters of the metamaterial over the 5GHz - 15GHz frequency band, (a) ε_r, (b) μ_r.

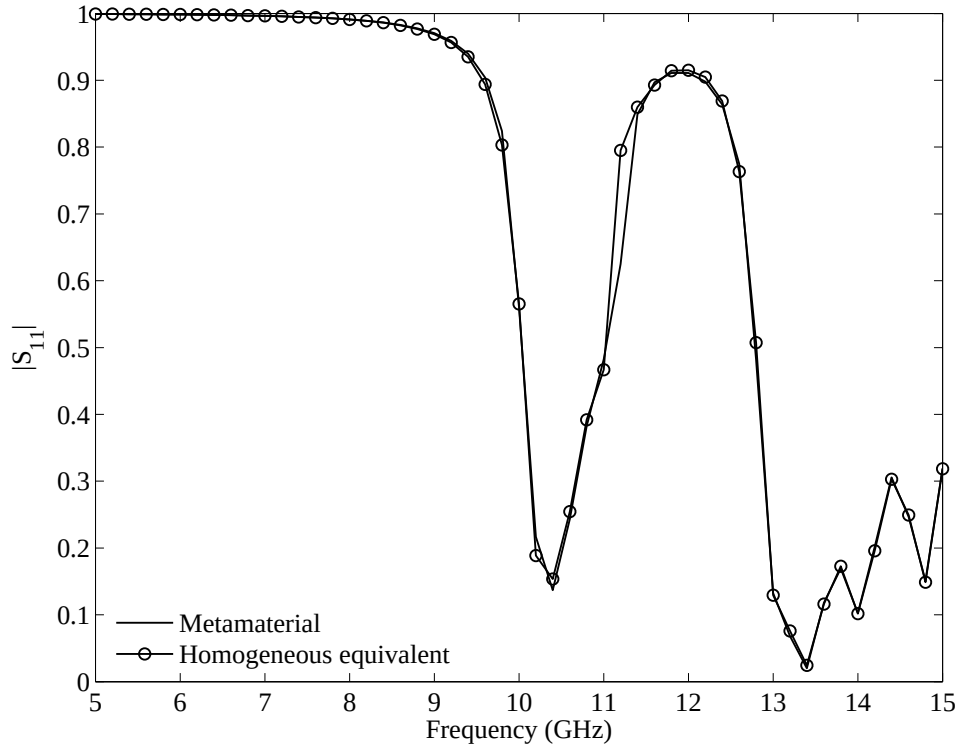

(a)

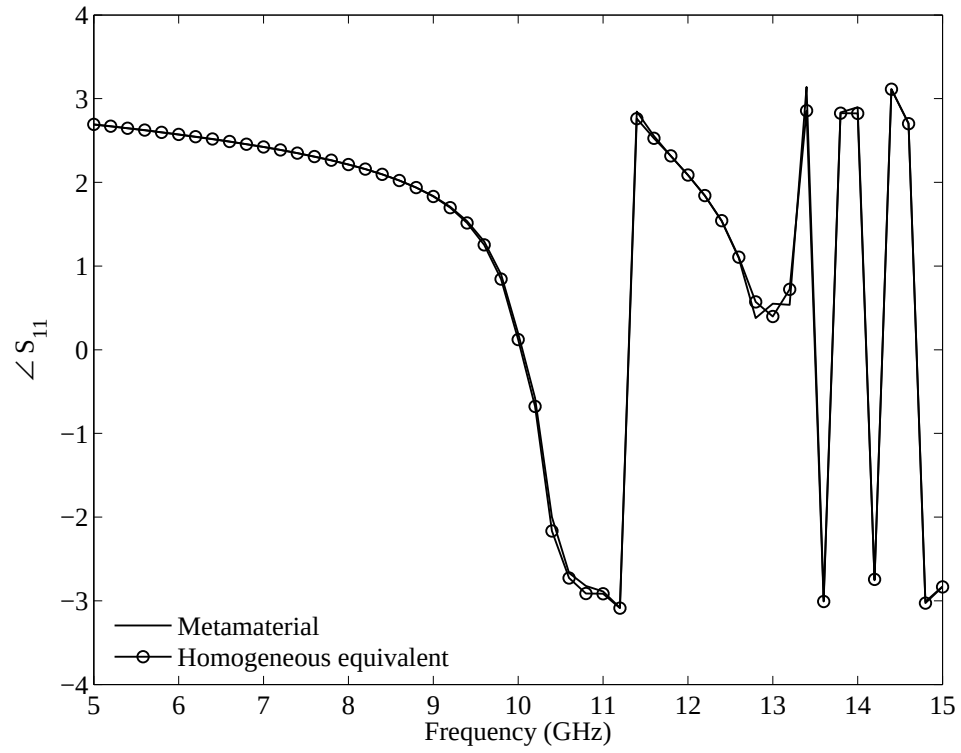

(b)

Figure 4.9: S_{11} vs. frequency, obtained from the metamaterial and its homogeneous equivalent.

Table 4.1: Parameters of the GPOF approximation

$f = 5\text{GHz}$

i	b_i	$s_i a$	$\text{Re}\{k_2\}a$
1	$-0.90 + j0.43$	$\approx 0.0 + j0.0$	
2	$-1.10 + j1.87$	$-3.73 - j1.46$	0.7294

$f = 10.8\text{GHz}$

i	b_i	$s_i a$	$\text{Re}\{k_2\}a$
1	$-0.35 - j0.09$	$\approx 0.0 + j0.0$	
2	$0.34 + j0.04$	$-0.11 + j0.87$	-0.389
3	$3.5 \times 10^{-3} - j0.1$	$-0.33 + j1.69$	-0.423
4	$2.4 \times 10^{-2} - j1.3 \times 10^{-3}$	$-0.22 - j1.59$	-0.782
5	$-1.4 \times 10^{-2} + j1.1 \times 10^{-3}$	$-0.10 - j2.63$	-0.456

$f = 15\text{GHz}$

i	b_i	$s_i a$	$\text{Re}\{k_2\}a$
1	$-0.27 + j9.8 \times 10^{-3}$	$\approx 0.0 + j0.0$	
2	$0.25 - j0.015$	$-0.041 - j1.35$	0.673
3	$0.029 - j1.9 \times 10^{-4}$	$-0.148 - j2.72$	0.679
4	$4.3 \times 10^{-3} - j5.4 \times 10^{-3}$	$-0.206 + j2.27$	0.669
5	$-1.1 \times 10^{-3} + j1.8 \times 10^{-3}$	$-0.025 - j2.09$	1.047
6	$-6.5 \times 10^{-4} - j1.7 \times 10^{-3}$	$-0.053 + j1.28$	0.500

As expected, $s_1 \approx 0 + j0$ for all of the frequencies given in Table 4.1. For $f = 10.8\text{GHz}$, the $\text{Re}\{k_2\}a$ product obtained from exponents s_2 and s_3, by reducing them to the reduced Brillouin zone, are close to each other. The products obtained from the higher order exponents, however, may not yield close results, since their corresponding coefficients are relatively very small. Similarly, for $f = 15\text{GHz}$ the $\text{Re}\{k_2\}a$ product obtained from exponents s_2, s_3 and s_4 are very close to each other, while higher order exponents may give different results, because of the explained reason. In summary, comparison of the $\text{Re}\{k_2\}a$ products obtained from the first exponents of the GPOF approximation can be used as a measure of quality of homogenization.

Note that the $\mathrm{Re}\{k_2\}a$ product is in the $[-\pi, 0]$ reduced Brillouin zone for the DNG case at $f = 10.8$GHz, whereas $\mathrm{Re}\{k_2\}a$ product is in the $[0, \pi]$ reduced Brillouin zone for the DPS case at $f = 15$GHz.

To better assess the quality of homogenization, the field distribution along the actual structure (i.e., metamaterial medium together with the air media surrounding it) is compared with the case where metamaterial medium is replaced with its homogeneous equivalent. The results for the frequencies of Table 4.1 are given in Figs. 4.10-4.11 (when $N_z = 20$ i.e., $d = 5$cm).

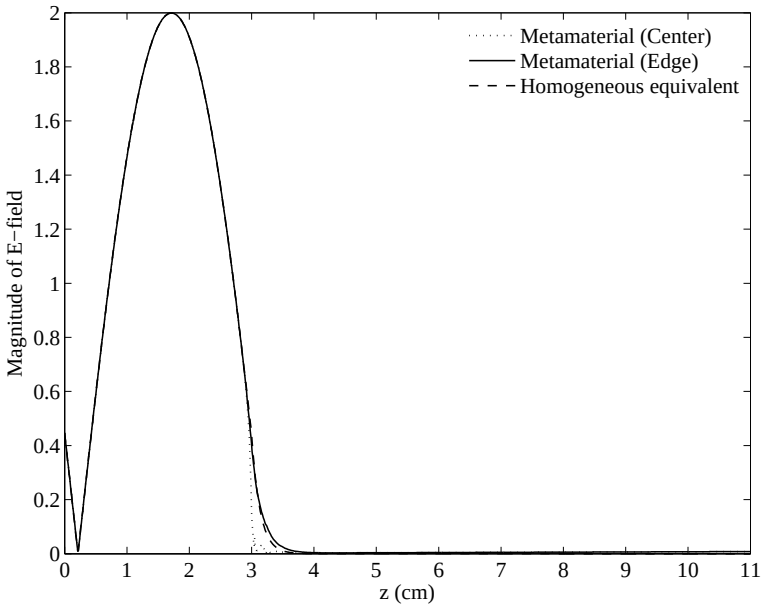

Figure 4.10: Magnitude of E-field inside and outside the metamaterial medium and its homogeneous equivalent at $f = 5$GHz.

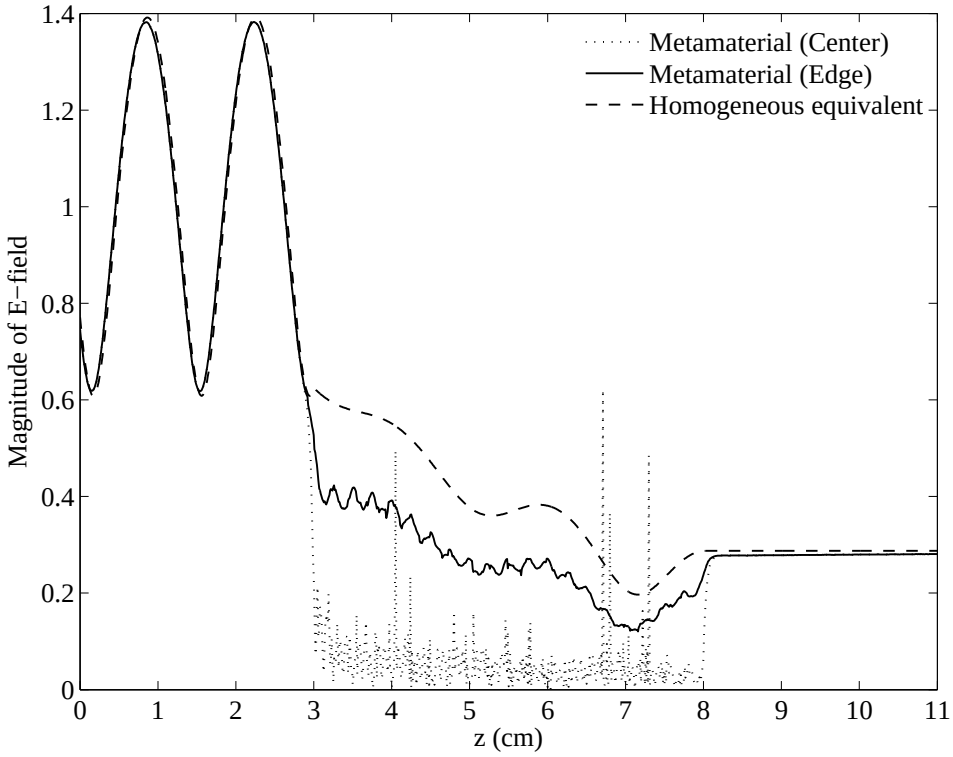

(a)

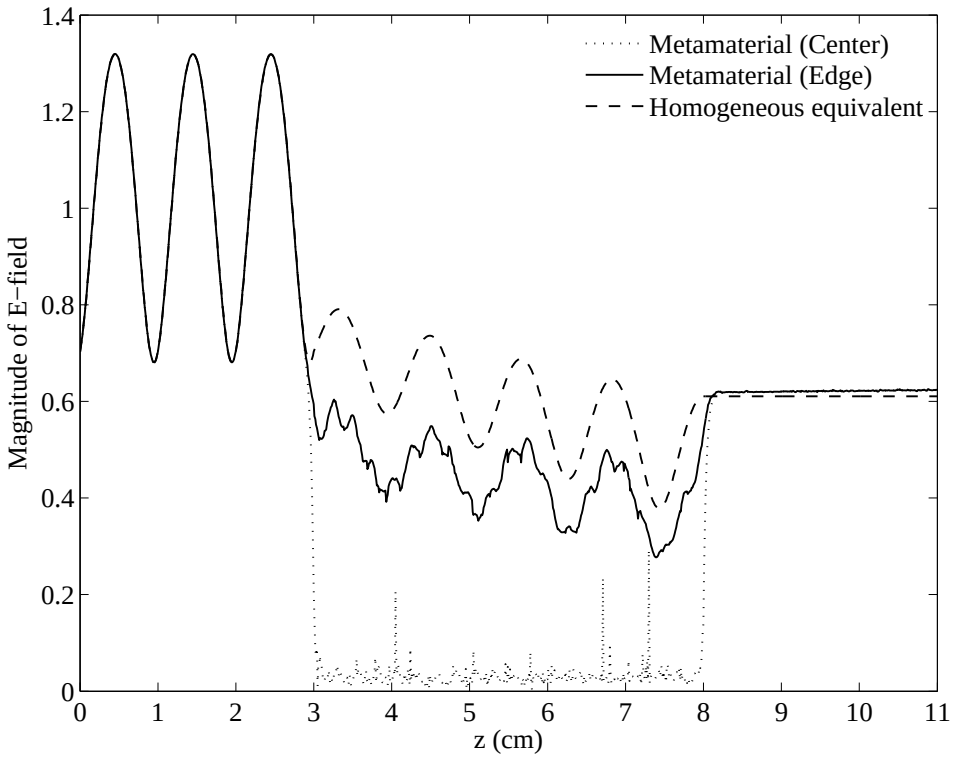

(b)

Figure 4.11: Magnitudes of E-field inside and outside the metamaterial medium and its homogeneous equivalent at (a) $f = 10.8$GHz, (b) $f = 15.0$GHz.

The field distributions show very good agreement between the metamaterial and its homogeneous equivalent in Medium 1 and Medium 3. Especially there is perfect agreement in Medium 1, since our method is based on reflection data and our optimization process strongly forces homogeneous equivalent to mimic the reflection properties of the metamaterial. The agreement in the transmitted field in Medium 3 is a sign of the success in homogenization. The field inside the metamaterial structure, passing through the centers of unit cells are close to zero and they are seen like noise. This is mainly because they are in the vicinity of metallic scatterers (i.e., the SRRs and the wire). For this reason, the field distributions are also recorded on another line, which passes from the edges of the unit cells (through one of the PMC walls). Although the exact mechanism inside the metamaterial region is not known, based on the unit cell geometry, a major portion of the medium is air. Hence, if the line is taken from the edge, we are at the furthest point from the SRR+wire combination, hence their coupling effects are minimized. Therefore, homogeneous equivalent is expected to resemble to the fields sampled at the edge.

4.1.4 Conclusion

In this section, a simple and versatile method for retrieval of the homogenization parameters of periodic structures is proposed. The method is tested with a typical 3D metamaterial structure, present in the literature. The homogenization quality of the metamaterial, compared with its homogeneous equivalent, is tested in terms of agreement in s-parameters, reduction of $\mathrm{Re}\{k_2\}a$ products into the reduced Brillouin zone and agreement in field distributions. Numerical results show that the method is very successful to retrieve the effective constitutive parameters of the metamaterial. As the future work, the method can be modified to incorporate also the transmission data, so that the homogeneous equivalent mimics the metamaterial more successfully in the transmission region.

4.2 Retrieval of Surface Wave Propagation Constants on a Grounded Dielectric Slab

4.2.1 Introduction

In this work our aim is to build an efficient and robust method to retrieve the surface wave propagation constants corresponding to each TM and TE mode that can propagate on the surface of a grounded dielectric slab, Fig. 4.12. The two-step method we propose in this work consists of modeling and simulating the problem geometry in a Finite Element Method (FEM) based electromagnetic simulator and then processing the electric field results obtained from the simulator to determine the surface wave propagation constants. The numerical results determined using our method are compared with their theoretical counterparts. Numerical results of the method are in good agreement with the theory, generally achieving less than 2% error. However, there are some geometries and special cases that the method requires improvement.

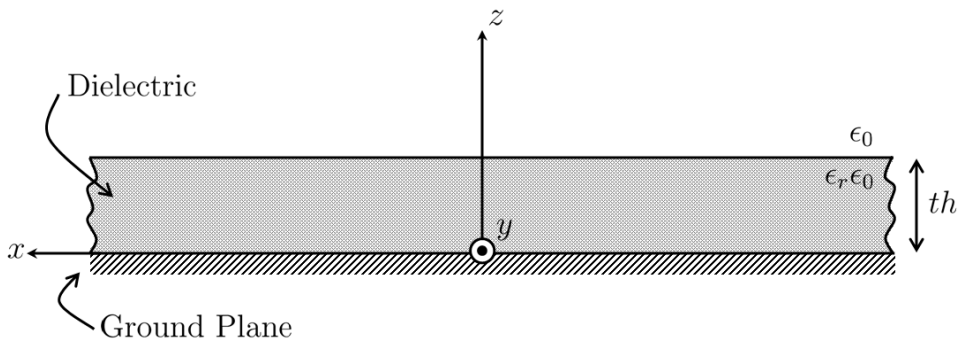

Figure 4.12: Geometry of a grounded dielectric slab.

The importance of our proposed method lies in its ability to be further generalized and applied to complex geometries. These complex geometries may include multi layered structures or periodically aligned metamaterial structures to create an artificial medium which may have negative effective electric permittivity and/or negative effective magnetic permeability. Surface waves, leaky waves and

evanescent waves related to metamaterials, electronic band gap (EBG) and photonic band gap (PBG) structures have created a flurry of interest among many researchers [34–77]. To the best of our knowledge, an efficient method to determine the propagation constants related to these waves has not been reported yet. Expansion of our method to include these geometries and structures will therefore meet an important need.

4.2.2 The Two-Step Method

High Frequency Structure Simulator (HFSS) Simulations

The first step of our method is modeling and simulating the problem geometry in a FEM based electromagnetic simulator. For this purpose we use the High Frequency Structure Simulator of Ansoft Corporation.

In theory, the ground plane and the dielectric slab is assumed to be of infinite extent in the x and y directions. In our simulator, due to memory and computational restrictions, the infinite geometry of the theory has to be truncated. However, HFSS provides a very useful tool to take into account the truncated parts of the geometry. HFSS allows the user to select radiation surfaces and impose Radiation Boundary Conditions (RBCs) on these surfaces/boundries, which in turn allows the waves to radiate infinitely far into space. For the accuracy of simulations, HFSS recommends the radiation boundary to be located at least one-quarter of a wavelength away from a radiating structure.

To create surface waves on the dielectric slab, we use a rectangular narrow patch at the surface of the slab and excite 1A constant current along the patch. The length of the patch is $L = 0.295\lambda_0$ and the width of the patch is $W = L/10 = 0.0295\lambda_0$, where $\lambda_0 = 1$cm at $f = 30$GHz. The geometry of the rectangular narrow patch and constant current excitation is depicted in Fig. 4.13.

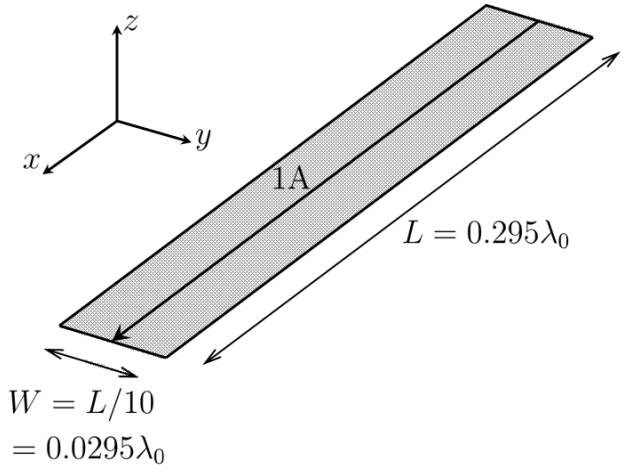

Figure 4.13: Geometry of the rectangular narrow patch and excitation.

To simulate the infinite ground plane, we use a PEC plate just beneath the dielectric substrate. We impose the Perfect Electric (PE) boundary condition on this plate together with the Infinite Ground Plane option being enabled.

As the dielectric substrate, we use a lossless dielectric material with dielectric constant $\varepsilon_r = 2.55$. The space above the dielectric slab is filled with ideal free space (vacuum). The outer boundaries of the vacuum and the dielectric substrate (excluding the infinite ground plane) are the radiation surfaces where Radiation Boundary Conditions are enforced. The outline of the entire problem geometry in HFSS is as given in Fig. 4.14.

Definitions: At this point it is useful to make some definitions, to which we will refer in the next sections.

- E-plane: xz plane (i.e., $y = 0$ plane).
- H-plane: yz plane (i.e., $x = 0$ plane).
- E-line: The line segment $(-x\_width/2 \leq x \leq x\_width/2, y = 0, z = th)$.
- H-line: The line segment $(x = 0, -y\_width/2 \leq y \leq y\_width/2, z = th)$.

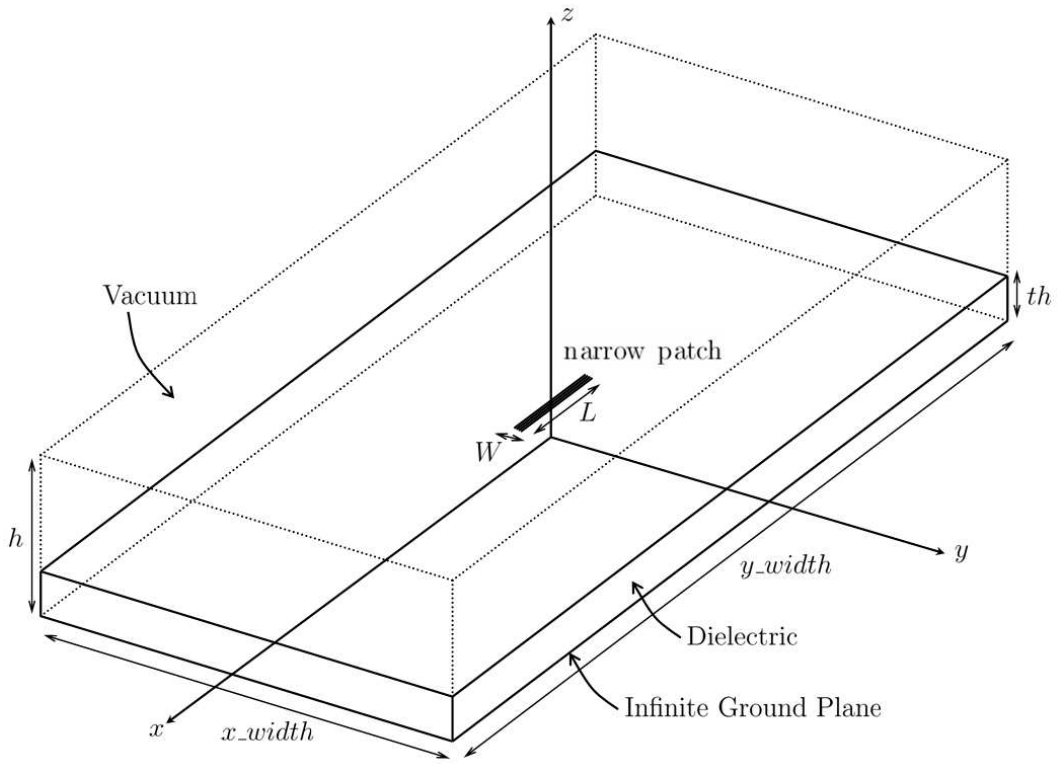

Figure 4.14: Entire problem geometry in HFSS.

As their names imply, E-line and H-line reside in the E-plane and H-plane, respectively. The E-plane and H-plane are defined with respect to the orientation of the narrow patch. Note that both E-line and H-line lie on the surface of the dielectric slab ($z = th$ plane).

Generalized Pencil of Function (GPOF) Method

Preliminaries:

The asymptotic expansion (for large lateral distances, ρ) of the Green's function of electric field for $\hat{x}$-directed filamentary microstrip dipoles, where the source is taken to be the origin, is formed as [78]:

$$G_{xx}^{E}(\rho) \sim \frac{Z_0}{2\pi}\left[\frac{\tan^2(k_0 d\sqrt{\varepsilon_r - 1})}{\varepsilon_r - 1}\sin^2\phi + \cos^2\phi\right]\frac{e^{-jk_0\rho}}{\rho^2} - \frac{Z_0}{2k_0}\frac{\varepsilon_r - 1}{\varepsilon_r} jRes_W(\beta_{TM}) \cdot \left\{\frac{\beta_{TM}^2}{2}\cos^2\phi\left[H_2^{(2)}(\beta_{TM}\rho) - H_0^{(2)}(\beta_{TM}\rho)\right] - \beta_{TM}\frac{\sin^2\phi}{\rho}H_1^{(2)}(\beta_{TM}\rho)\right\},$$

(4.31)

where $Z_0 = \sqrt{\mu_0/\varepsilon_0}$ is the intrinsic impedance of free space, $d = th$ is the thickness of the dielectric slab, β_{TM} is the propagation constant of the single proper TM pole and $Res_W(\beta_{TM})$ is the residue corresponding to the TM pole (where the function W is as given in [78]). The direction of propagation makes an angle ϕ with respect to the positive x-axis measured towards the positive y-axis.

The first term in (4.31) gives the space wave term:

$$\frac{Z_0}{2\pi}\left[\frac{\tan^2(k_0 d\sqrt{\varepsilon_r-1})}{\varepsilon_r-1}\sin^2\phi+\cos^2\phi\right]\frac{e^{-jk_0\rho}}{\rho^2}. \tag{4.32}$$

The second term in (4.31) shows the contribution from the TM surface wave:

$$-\frac{Z_0}{2k_0}\frac{\varepsilon_r-1}{\varepsilon_r}jRes_W(\beta_{TM}) \tag{4.33}$$
$$\times\left\{\frac{\beta_{TM}^2}{2}\cos^2\phi\left[H_2^{(2)}(\beta_{TM}\rho)-H_0^{(2)}(\beta_{TM}\rho)\right]-\beta_{TM}\frac{\sin^2\phi}{\rho}H_1^{(2)}(\beta_{TM}\rho)\right\}.$$

In the E-plane G_{xx}^E becomes:

$$G_{xx}^E(\rho,\phi=0)\approx\frac{Z_0}{2\pi}\frac{e^{-jk_0\rho}}{\rho^2} \tag{4.34}$$
$$-\frac{Z_0}{2k_0}\frac{\varepsilon_r-1}{\varepsilon_r}jRes_W(\beta_{TM})\frac{\beta_{TM}^2}{2}\left[H_2^{(2)}(\beta_{TM}\rho)-H_0^{(2)}(\beta_{TM}\rho)\right].$$

In the H-plane G_{xx}^E becomes:

$$G_{xx}^E(\rho,\phi=\frac{\pi}{2})\approx\frac{Z_0}{2\pi}\frac{\tan^2(k_0 d\sqrt{\varepsilon_r-1})}{\varepsilon_r-1}\frac{e^{-jk_0\rho}}{\rho^2} \tag{4.35}$$
$$+\frac{Z_0}{2k_0}\frac{\varepsilon_r-1}{\varepsilon_r}jRes_W(\beta_{TM})\frac{\beta_{TM}}{\rho}H_1^{(2)}(\beta_{TM}\rho).$$

Hence for large ρ, G_{xx}^E given in (4.35) and (4.36) have the following characteristics in the E- and H-planes, given in Table 4.2.

In our HFSS simulations we use an $\hat{x}$-directed narrow patch with constant current excitation to simulate the filamentary microstrip dipole mentioned in

Table 4.2: Space Wave and Surface Wave Characteristics in the E- and H-planes.

	Space Wave		Surface Wave	
Plane	Decay	Prop. Const.	Decay	Prop. Const.
E	$\sim \rho^{-2}$	k_0	$\sim \rho^{-1/2}$	β_{TM}
H	$\sim \rho^{-2}$	k_0	$\sim \rho^{-3/2}$	β_{TM}

[78]. In accordance with G_{xx}^E, we evaluate the E_x component of the electric field on the surface of the dielectric substrate (along E- and H-lines). The electric field data we have obtained in HFSS is then used in the GPOF method to determine the surface wave propagation constants.

On the Generalized Pencil of Function Method for Surface Wave Constant Determination:

Let y be a complex function, and $y[0], y[1], \ldots, y[N-1]$ be the N uniform samples of a real variable t, as shown in Fig. 4.15. These samples can be represented by M complex exponentials as

$$y[k] = \sum_{i=1}^{M} b_i e^{s_i \delta t k} = \sum_{i=1}^{M} b_i z_i^k \quad , \qquad k = 0, 1, \ldots, N-1 \tag{4.36}$$

where $z_i = e^{s_i \delta t}$ and δt is the sampling interval. Uniform sampling relates the samples k to the real variable t such that $t = \delta t k$. In (4.36), b_i's are called the residues, s_i's are called the exponents.

Now consider the case shown in Fig. 4.16, where $y(t)$ is shifted right by $t_0 = k_0 \delta t$. The shifted function $y(t - t_0)$ is sampled with N samples, again δt being the sampling interval, to form $y[k - k_0]$.

The shifted discrete complex signal sequence $y[k - k_0]$ can be can be represented by M complex exponentials as in (4.36).

$$y[k - k_0] = \sum_{i=1}^{M} b_i e^{s_i \delta t (k - k_0)} = \sum_{i=1}^{M} b_i z_i^{(k-k_0)}, \qquad k - k_0 = 0, 1, \ldots, N-1 \tag{4.37}$$

or equivalently,

$$y[k-k_0] = \sum_{i=1}^{M} b_i e^{s_i \delta t (k - k_0)} = \sum_{i=1}^{M} b_i z_i^{(k-k_0)}, \qquad k = k_0, k_0+1 \ldots, k_0+N-1 \tag{4.38}$$

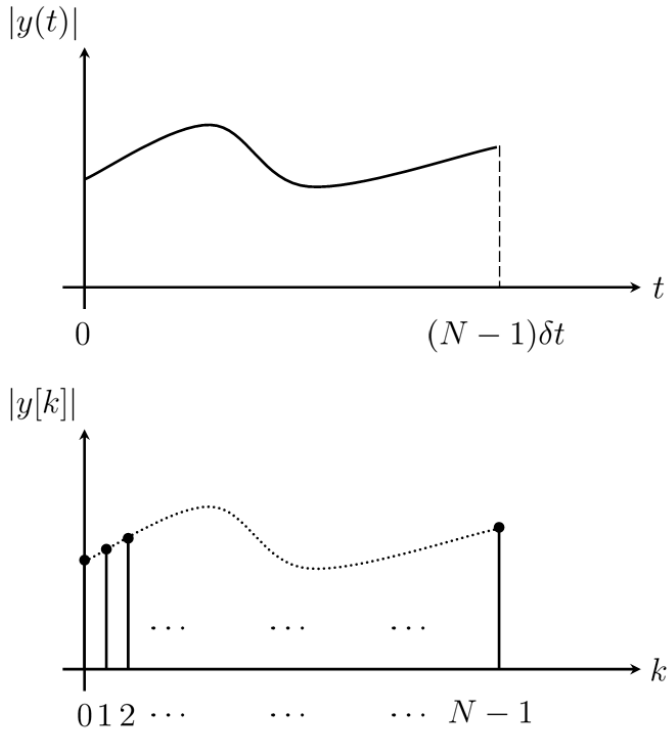

Figure 4.15: Magnitudes of complex function $y(t)$ and its N uniform samples $y[k]$.

Next sections will concentrate on the connection between the preliminaries and the formal definition of the GPOF Method.

Application of the GPOF Method on the E-Line:

As it is presented in the preliminaries section, for sufficiently large lateral distances ρ on the E-line, we expect the space wave term of the E_x component of the electric field to decay with ρ^{-2} whereas the surface wave term is expected to decay with $\rho^{-1/2}$. Now let us assume that there are M total propagating TM and TE modes and they all decay with $\rho^{-1/2}$. Therefore the E_x component of the electric field on the E-line can be written as a function of lateral distance ρ as follows

$$E_x(\rho) = \frac{A_0}{\rho^2} e^{-j\beta_0 \rho} + \sum_{i=1}^{M} \frac{A_i}{\sqrt{\rho}} e^{-j\beta_{SW}^i \rho}, \tag{4.39}$$

where β_0 is the space wave propagation constant, β_{SW}^i are the surface wave propagation constants, A_0 and A_i are the complex amplitudes of the space and

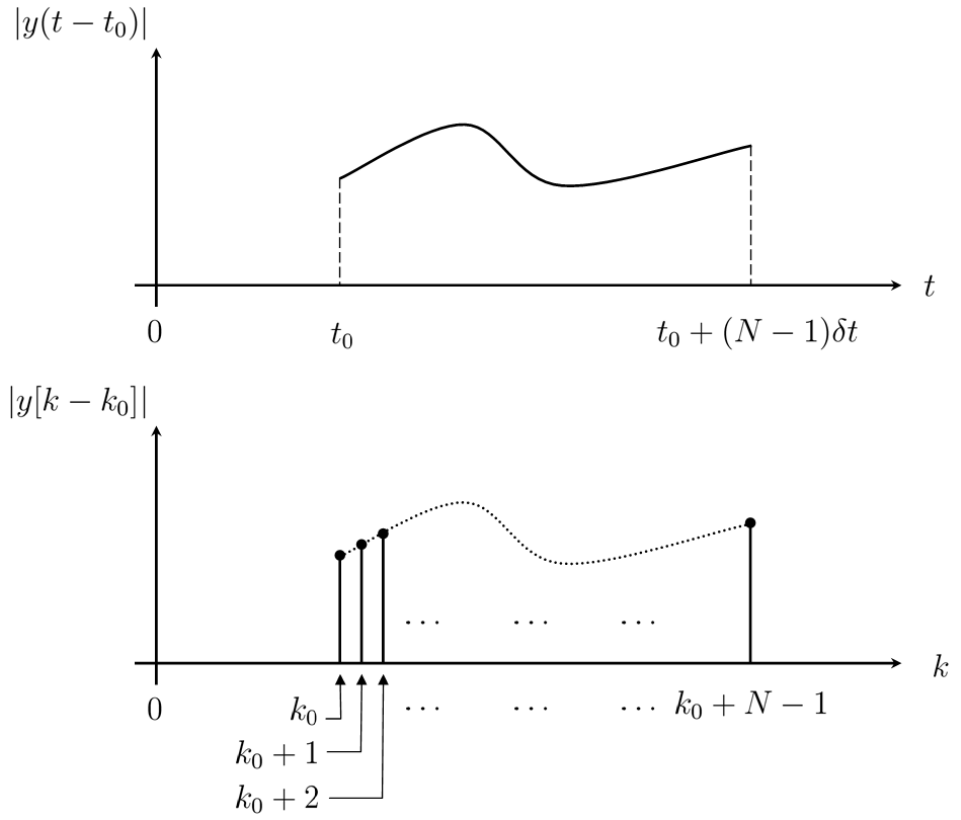

Figure 4.16: Magnitudes of complex function $y(t-t_0)$ and its N uniform samples $y[k-k_0]$.

surface wave terms excluding decay dependence. Multiplying (4.39) with $\sqrt{\rho}$ gives

$$\sqrt{\rho}E_x(\rho) = \frac{A_0}{\rho\sqrt{\rho}}e^{-j\beta_0\rho} + \sum_{i=1}^{M} A_i e^{-j\beta_{SW}^i\rho}. \tag{4.40}$$

Now let us rewrite (4.40) as

$$\sqrt{\rho}E_x(\rho) = \sum_{i=1}^{M} A_i e^{-j\beta_{SW}^i\rho} + N_{_E}(\rho), \tag{4.41}$$

where

$$N_{_E}(\rho) = \frac{A_0}{\rho\sqrt{\rho}}e^{-j\beta_0\rho}, \tag{4.42}$$

which comes from the space wave term contribution in (4.40).

For large lateral distances ρ, assuming $|A_0| \ll |A_i|$, with proper choices of sampling interval $\delta\rho$ and number of samples N, $N_{_E}(\rho)$ can be assumed as a noise term which can be discarded by the GPOF Method. In such a case, (4.41) can

be approximated as

$$\sqrt{\rho}E_x(\rho) \simeq \sum_{i=1}^{M} A_i e^{-j\beta_{SW}^i \rho}, \tag{4.43}$$

and can be represented with M complex exponentials utilizing the GPOF Method.

As it has been explained previously, for (4.39) to be valid and for (4.43) to be a correct approximation, the lateral distance ρ should be sufficiently large. Let us assume that the equations and approximations in (4.39)-(4.43) are correct when $\rho \geq \rho_0$, where ρ_0 is the starting value of the lateral distance to be used in the GPOF Method.

Fig. 4.17 shows the resemblance between $\sqrt{\rho}E_x(\rho)$ in (4.43) for $\rho \geq \rho_0$ and $y(t - t_0)$ of Fig. 4.16. Intuitively this suggests (4.38) to be used in representing (4.43) with M complex exponentials.

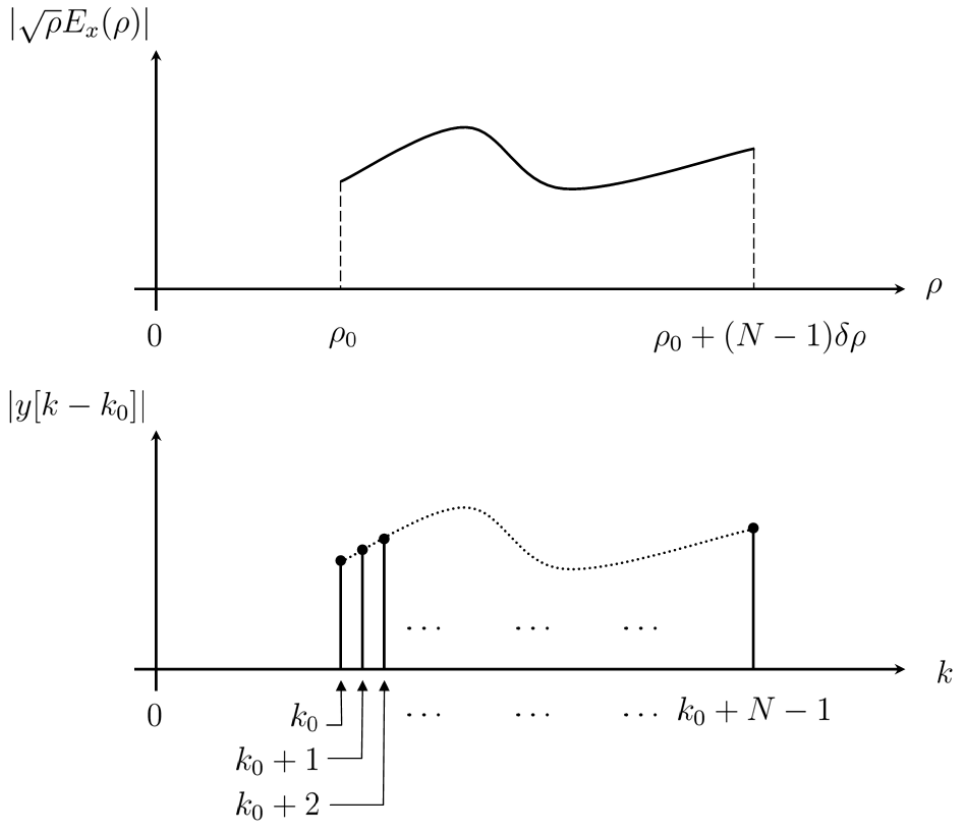

Figure 4.17: Magnitudes of $\sqrt{\rho}E_x(\rho)$ and its N uniform samples $y[k - k_0]$.

Therefore,

$$\sqrt{\rho}E_x(\rho) \simeq \sum_{i=1}^{M} A_i e^{-j\beta_{SW}^i \rho} \tag{4.44}$$

$$\equiv y[k-k_0] = \sum_{i=1}^{M} b_i e^{s_i \delta\rho (k-k_0)}, \qquad k = k_0, k_0+1, \ldots, k_0+N-1.$$

where $\rho = \delta\rho k$. It is obvious that $\rho_0 = \delta\rho k_0$ in Fig. 4.17. The left hand side of equivalence (4.44) is a continuous signal, whereas the right hand side is a discrete signal. Expressing the RHS also as a continuous signal, we get

$$\sum_{i=1}^{M} A_i e^{-j\beta_{SW}^i \rho} = \sum_{i=1}^{M} b_i e^{s_i(\rho-\rho_0)}, \tag{4.45}$$

$$A_i e^{-j\beta_{SW}^i \rho} = b_i e^{s_i(\rho-\rho_0)}, \tag{4.46}$$

$$A_i e^{-j\beta_{SW}^i \rho} = b_i e^{-s_i\rho_0} e^{s_i\rho}, \tag{4.47}$$

which gives

$$A_i = b_i e^{-s_i\rho_0} \quad , \quad \beta_{SW}^i = -\mathrm{Im}\{s_i\} \quad , \quad \mathrm{Re}\{s_i\} = 0, \tag{4.48}$$

Some Theoretical Examples (E-line):

Example 1: Consider the following case along E-line.

$$E_x(\rho) = \frac{A_0}{\rho^2} e^{-j\beta_0\rho} + \frac{A_1}{\sqrt{\rho}} e^{-j\beta_{SW}^1 \rho} \tag{4.49}$$

$$\sqrt{\rho}E_x(\rho) = \frac{A_0}{\rho\sqrt{\rho}} e^{-j\beta_0\rho} + A_1 e^{-j\beta_{SW}^1 \rho} \tag{4.50}$$

Assume $A_0 = 0$, $A_1 = -0.7 + j0.3$, $\beta_0 = 6.2832$, $\beta_{SW}^1 = 1.1\beta_0 = 6.9115$.

When $\sqrt{\rho}E_x(\rho)$ is used in the GPOF Method (in the $[5\lambda_0 - 8\lambda_0]$ interval with $N = 51$ samples) the following results are obtained.

$b_1 = 0.7 - j0.3$

$s_1 = 0 - j6.9115$

$\tilde{A}_1 = b_1 e^{-s_1 \rho_0} = -0.7 + j0.3$

$\tilde{\beta}^1_{SW} = -\text{Im}\{s_1\} = 6.9115$

Since $A_0 = 0$, the noise term $N_{_E}(\rho)$ becomes zero. $\text{Re}\{s_1\}$ is zero as expected. $\tilde{A}_1$ and $\tilde{\beta}^1_{SW}$ are retrieved exactly.

Example 2:

Consider Example 1 again, with the following assumptions

$A_0 = (-0.5 - j0.4) \times 10^{-n}$, $A_1 = -0.7 + j0.3$

$\beta_0 = 6.2832$, $\beta^1_{SW} = 1.1\beta_0 = 6.9115$.

When $\sqrt{\rho}E_x(\rho)$ is used in the GPOF Method (in the $[5\lambda_0 - 8\lambda_0]$ interval with $N = 51$ samples) the following results are obtained.

$\underline{n = 0 :}$

$b_1 = 0.6628 - j0.3464$

$s_1 = 0.0223 - j6.8886$

$\tilde{A}_1 = b_1 e^{-s_1 \rho_0} = -0.5537 + j0.3756$

$\tilde{A}'_1 = b_1 e^{-j\text{Im}\{s_1\}\rho_0} = -0.6189 + j0.4198$

$\tilde{\beta}^1_{SW} = -\text{Im}\{s_1\} = 6.8886$

$\underline{n = 1 :}$

$b_1 = 0.6963 - j0.3047$

$s_1 = 0.0024 - j6.9093$

$\tilde{A}_1 = b_1 e^{-s_1 \rho_0} = -0.6847 + j0.3087$

$\tilde{A}_1' = b_1 e^{-j\mathrm{Im}\{s_1\}\rho_0} = -0.6928 + j0.3124$

$\tilde{\beta}_{SW}^1 = -\mathrm{Im}\{s_1\} = 6.9093$

$\underline{n = 2:}$

$b_1 = 0.6996 - j0.3005$

$s_1 = 0.0002 - j6.9113$

$\tilde{A}_1 = b_1 e^{-s_1\rho_0} = -0.6985 + j0.3009$

$\tilde{A}_1' = b_1 e^{-j\mathrm{Im}\{s_1\}\rho_0} = -0.6993 + j0.3012$

$\tilde{\beta}_{SW}^1 = -\mathrm{Im}\{s_1\} = 6.9113$

$\underline{n = 3:}$

$b_1 = 0.7 - j0.3$

$s_1 = 0 - j6.9115$

$\tilde{A}_1 = b_1 e^{-s_1\rho_0} = -0.6998 + j0.3001$

$\tilde{A}_1' = b_1 e^{-j\mathrm{Im}\{s_1\}\rho_0} = -0.6999 + j0.3001$

$\tilde{\beta}_{SW}^1 = -\mathrm{Im}\{s_1\} = 6.9115$

$\underline{n = 4:}$

$b_1 = 0.7 - j0.3$

$s_1 = 0 - j6.9115$

$\tilde{A}_1 = b_1 e^{-s_1\rho_0} = -0.7 + j0.3$

$\tilde{A}_1' = b_1 e^{-j\mathrm{Im}\{s_1\}\rho_0} = -0.7 + j0.3$

$\tilde{\beta}_{SW}^1 = -\mathrm{Im}\{s_1\} = 6.9115$

In this particular example we see that when $|A_0|$ is comparable to $|A_1|$, the contribution of the space wave term shows a noise effect which cannot be easily discarded. In such a case $\mathrm{Re}\{s_1\} \neq 0$, which makes the theoretical $\tilde{A}_1 = b_1 e^{-s_1\rho_0}$ complex amplitude retrieval formula wrong. When $\mathrm{Re}\{s_1\} \neq 0$, the modified $\tilde{A}_1' = b_1 e^{-j\mathrm{Im}\{s_1\}\rho_0}$ formula yields better results for this purpose.

As n increases $|A_0| \ll |A_1|$, which leads $\tilde{A}_1 \simeq \tilde{A}_1' \simeq A_1$ and $\tilde{\beta}_{SW}^1 \simeq \beta_{SW}^1$.

Application of the GPOF Method on the H-Line:

The procedure for the H-line is very similar to the E-line case we have investigated in the previous section. For sufficiently large lateral distances ρ on the H-line, we again expect the space wave term of the E_x component of the electric field to decay with ρ^{-2} whereas in this case the surface wave terms are expected to decay with $\rho^{-3/2}$. Let us again assume that there are M total propagating TM and TE modes and they all decay with $\rho^{-3/2}$. Therefore the E_x component of the electric field on the H-line can be written as a function of lateral distance ρ as follows

$$E_x(\rho) = \frac{A_0}{\rho^2} e^{-j\beta_0\rho} + \sum_{i=1}^{M} \frac{A_i}{\rho\sqrt{\rho}} e^{-j\beta_{SW}^i\rho}. \tag{4.51}$$

Multiplying (4.51) with $\rho\sqrt{\rho}$ gives

$$\rho\sqrt{\rho}E_x(\rho) = \frac{A_0}{\sqrt{\rho}} e^{-j\beta_0\rho} + \sum_{i=1}^{M} A_i e^{-j\beta_{SW}^i\rho}. \tag{4.52}$$

Now let us rewrite (4.52) as

$$\rho\sqrt{\rho}E_x(\rho) = \sum_{i=1}^{M} A_i e^{-j\beta_{SW}^i\rho} + N_{_H}(\rho), \tag{4.53}$$

where

$$N_{_H}(\rho) = \frac{A_0}{\sqrt{\rho}} e^{-j\beta_0\rho}, \tag{4.54}$$

which comes from the space wave term contribution in (4.52).

Under the conditions presented in the previous section, $N_{H}(\rho)$ can be assumed as a noise term which can be discarded by the GPOF Method. In such a case, (4.53) can be approximated as

$$\rho\sqrt{\rho}E_x(\rho) \simeq \sum_{i=1}^{M} A_i e^{-j\beta_{SW}^{i}\rho}, \tag{4.55}$$

and can be represented with M complex exponentials utilizing the GPOF Method. Again with the assumption that the equations and approximations in (4.51)-(4.55) are correct when $\rho \geq \rho_0$, one can apply the same procedure in (4.44)-(4.48) and find out that

$$A_i = b_i e^{-s_i\rho_0} \quad , \quad \beta_{SW}^{i} = -\mathrm{Im}\{s_i\} \quad , \quad \mathrm{Re}\{s_i\} = 0. \tag{4.56}$$

The only difference for the H-line case appears in (4.44) where $\sqrt{\rho}E_x(\rho)$ has to be replaced with $\rho\sqrt{\rho}E_x(\rho)$.

On the other hand, $N_{E}(\rho)$ given in (4.42) decays with $\rho^{-3/2}$ whereas $N_{H}(\rho)$ in (4.54) decays with $\rho^{-1/2}$, which means application of GPOF Method on the E-line is less noise sensitive compared to the H-line case.

Some Theoretical Examples (H-line):

Example 3:

Consider the following case along H-line:

$$E_x(\rho) = \frac{A_0}{\rho^2}e^{-j\beta_0\rho} + \frac{A_1}{\rho\sqrt{\rho}}e^{-j\beta_{SW}^{1}\rho}, \tag{4.57}$$

$$\rho\sqrt{\rho}E_x(\rho) = \frac{A_0}{\sqrt{\rho}}e^{-j\beta_0\rho} + A_1 e^{-j\beta_{SW}^{1}\rho}. \tag{4.58}$$

Assume $A_0 = 0$, $A_1 = -0.7 + j0.3$, $\beta_0 = 6.2832$, $\beta_{SW}^{1} = 1.1\beta_0 = 6.9115$.

When $\rho\sqrt{\rho}E_x(\rho)$ is used in the GPOF Method (in the $[5\lambda_0 - 8\lambda_0]$ interval with $N = 51$ samples) the following results are obtained.

$b_1 = 0.7 - j0.3$

$s_1 = 0 - j6.9115$

$\tilde{A}_1 = b_1 e^{-s_1 \rho_0} = -0.7 + j0.3$

$\tilde{\beta}^1_{SW} = -\text{Im}\{s_1\} = 6.9115$

Since $A_0 = 0$, the noise term $N_{_H}(\rho)$ becomes zero. $\text{Re}\{s_1\}$ is zero as expected. $\tilde{A}_1$ and $\tilde{\beta}^1_{SW}$ are retrieved exactly. Note that the same results with Example 1 are obtained.

Example 4:

Consider Example 3 again, with the following assumptions

$A_0 = (-0.5 - j0.4) \times 10^{-n}$, $A_1 = -0.7 + j0.3$

$\beta_0 = 6.2832$, $\beta^1_{SW} = 1.1\beta_0 = 6.9115.$

When $\rho\sqrt{\rho}E_x(\rho)$ is used in the GPOF Method (in the $[5\lambda_0 - 8\lambda_0]$ interval with $N = 51$ samples) the following results are obtained.

$\underline{n = 0 :}$

$b_1 = 0.4925 - j0.5432$

$s_1 = 0.1149 - j6.7860$

$\tilde{A}_1 = b_1 e^{-s_1 \rho_0} = -0.0449 + j0.4104$

$\tilde{A}'_1 = b_1 e^{-j\text{Im}\{s_1\}\rho_0} = -0.0798 + j0.7289$

$\tilde{\beta}^1_{SW} = -\text{Im}\{s_1\} = 6.7860$

$\underline{n = 1 :}$

$b_1 = 0.6783 - j0.3249$

$s_1 = 0.0160 - j6.9008$

$\tilde{A}_1 = b_1 e^{-s_1 \rho_0} = -0.6091 + j0.3328$

$\tilde{A}'_1 = b_1 e^{-j\mathrm{Im}\{s_1\}\rho_0} = -0.6600 + j0.3606$

$\tilde{\beta}^1_{SW} = -\mathrm{Im}\{s_1\} = 6.9008$

$\underline{n = 2:}$

$b_1 = 0.6978 - j0.3025$

$s_1 = 0.0017 - j6.9105$

$\tilde{A}_1 = b_1 e^{-s_1 \rho_0} = -0.6905 + j0.3036$

$\tilde{A}'_1 = b_1 e^{-j\mathrm{Im}\{s_1\}\rho_0} = -0.6962 + j0.3061$

$\tilde{\beta}^1_{SW} = -\mathrm{Im}\{s_1\} = 6.9105$

$\underline{n = 3:}$

$b_1 = 0.6998 - j0.3002$

$s_1 = 0.0002 - j6.9114$

$\tilde{A}_1 = b_1 e^{-s_1 \rho_0} = -0.6990 + j0.3004$

$\tilde{A}'_1 = b_1 e^{-j\mathrm{Im}\{s_1\}\rho_0} = -0.6996 + j0.3006$

$\tilde{\beta}^1_{SW} = -\mathrm{Im}\{s_1\} = 6.9114$

$\underline{n = 4:}$

$b_1 = 0.7 - j0.3$

$s_1 = 0 - j6.9115$

$\tilde{A}_1 = b_1 e^{-s_1 \rho_0} = -0.6999 + j0.3$

$$\tilde{A}_1' = b_1 e^{-j\mathrm{Im}\{s_1\}\rho_0} = -0.7 + 0.3001$$

$$\tilde{\beta}_{SW}^1 = -\mathrm{Im}\{s_1\} = 6.9115$$

In this particular example we see that when $|A_0|$ is comparable to $|A_1|$, the contribution of the space wave term shows a noise effect which cannot be easily discarded. In such a case $\mathrm{Re}\{s_1\} \neq 0$, which makes the theoretical $\tilde{A}_1 = b_1 e^{-s_1\rho_0}$ complex amplitude retrieval formula wrong. When $\mathrm{Re}\{s_1\} \neq 0$, the modified $\tilde{A}_1' = b_1 e^{-j\mathrm{Im}\{s_1\}\rho_0}$ formula yields better results for this purpose.

As n increases $|A_0| \ll |A_1|$, which leads $\tilde{A}_1 \simeq \tilde{A}_1' \simeq A_1$ and $\tilde{\beta}_{SW}^1 \simeq \beta_{SW}^1$.

Also note that Example 2 for the E-line case works better than the H-line case examined here, as expected.

4.2.3 Implementation:

To determine the surface wave propagation constants accurately, the lateral distance ρ should be sufficiently large such that the space wave contribution to the electric field can be neglected compared with the surface wave contributions. On the other hand, the size of the problem geometry cannot exceed a threshold size which is predefined by the HFSS as a restriction. We want to investigate the cases where $0 \leq \rho \leq 10\lambda_0$, which means the size of the dielectric substrate must be $20\lambda_0 \times 20\lambda_0 \times th$. However this size is impossible to implement due to the aforementioned size restriction of HFSS. To solve this problem, we use different geometries for E-line and H-line cases. For the E-line case, dimensions of the substrate are $x\_width \times y\_width \times th$, where $x\_width < 20\lambda_0$ and $y\_width = 20\lambda_0$. For the H-line case, dimensions of the substrate are $x\_width \times y\_width \times th$, where $x\_width = 20\lambda_0$ and $y\_width < 20\lambda_0$. The problem geometries for the E- and H-line cases are shown in Fig. 4.18 and Fig. 4.19, respectively.

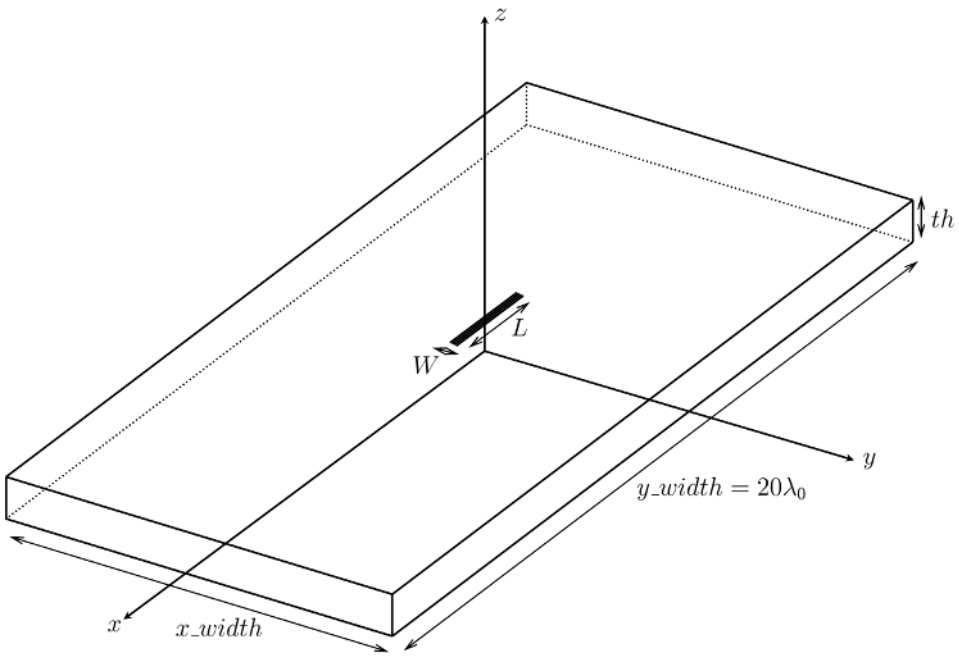

Figure 4.18: Problem geometry for the E-line case.

When the simulation is complete, the electric field data along the E-line or H-line are exported to a file (i.e., $\{\mathrm{Re}(E_x), \mathrm{Im}(E_x), \mathrm{Re}(E_y), \mathrm{Im}(E_y), \mathrm{Re}(E_z), \mathrm{Im}(E_z)\}$). This file is processed and the necessary E_x component of the electric field is formed. For the E-line case E_x is multiplied with $\sqrt{\rho}$, whereas for the H-line case E_x is multiplied with $\rho\sqrt{\rho}$.

Theoretically for both E-line and H-line cases we might use the $[\rho_0 \leq \rho \leq 10\lambda_0]$ interval in the GPOF Method, where ρ_0 can be taken $2\lambda_0 - 3\lambda_0$ intuitively. However on the E-line or H-line $\rho = 10\lambda_0$ corresponds to two of the surfaces where Radiation Boundary Conditions are set. In the simulation there will be small reflections from these surfaces, which will contaminate the results in their neighborhood. Therefore the logical interval to be used in the GPOF Method will be $[2\lambda_0 - 3\lambda_0 \leq \rho \leq 8\lambda_0 - 9\lambda_0]$.

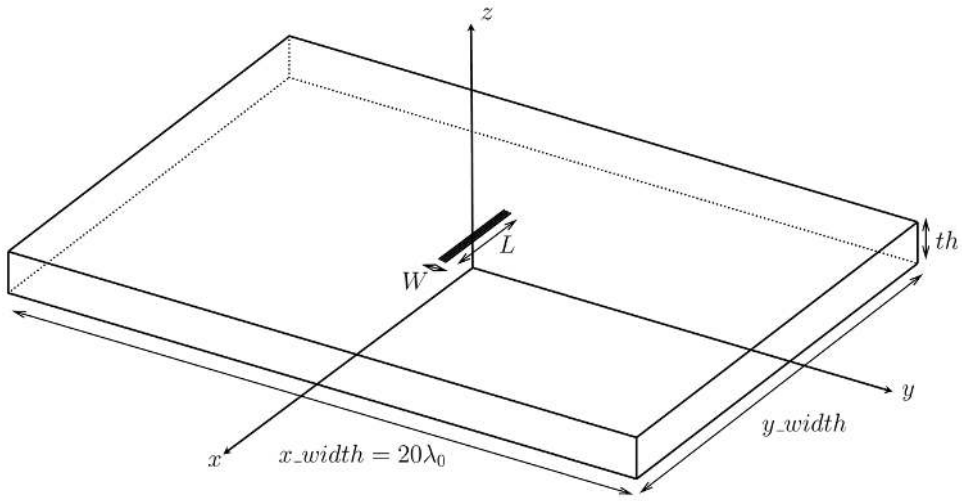

Figure 4.19: Problem geometry for the H-line case.

4.2.4 Numerical Results

Surface wave propagation constants retrieved from the E- and H-line data are compared with their analytical counterparts, which are calculated by solving the transcendental surface wave equations [79]. In the simulations, frequency is selected as $f = 30\text{GHz}$, therefore $\lambda_0 = 1\text{cm}$. The slab has a dielectric constant of $\varepsilon_r = 2.55$. The retrieval process is repeated for various thicknesses of the dielectric slab.

In the GPOF Method, HFSS results in the $[\rho_{start} - \rho_{end}]$ interval with N number of samples are used. In Table 4.3, for different intervals and using different number of samples, the surface wave propagation constant, β_{SW}^1, is retrieved from the E- and H-line data, when the thickness of the slab is $th = 0.1\lambda_0$.

The percentage error of the numerical results for TM_0 mode is calculated as

$$\%\text{Error} = \left| \frac{\beta_{SW}^1 - \beta_{TM_0}}{\beta_{TM_0}} \right| \times 100, \tag{4.59}$$

where $\beta_{TM_0} = 680.87 = 1.084\beta_0$ is the analytically found surface wave propagation constant for the TM_0 mode when $th = 0.1\lambda_0$.

For some of the cases given in Table 4.3, percentage errors are calculated:

$$\{\text{E-line}\ ,\ N = 51\ ,\ \rho_{start} = 5\lambda_0\ ,\ \rho_{end} = 8\lambda_0\} \ \rightarrow\ \%\text{Error} = 1.32$$

$$\{\text{E-line}\ ,\ N = 51\ ,\ \rho_{start} = 5\lambda_0\ ,\ \rho_{end} = 9\lambda_0\} \ \rightarrow\ \%\text{Error} = 1.41$$

$$\{\text{H-line}\ ,\ N = 51\ ,\ \rho_{start} = 5\lambda_0\ ,\ \rho_{end} = 8\lambda_0\} \ \rightarrow\ \%\text{Error} = 0.02$$

$$\{\text{H-line}\ ,\ N = 51\ ,\ \rho_{start} = 5\lambda_0\ ,\ \rho_{end} = 9\lambda_0\} \ \rightarrow\ \%\text{Error} = 0.53$$

As it is observed from Table 4.3 and percentage errors, both E-line and H-line cases give good results for most of the intervals and number of samples. Especially H-line case gives better results for this particular thickness of the dielectric substrate.

For $th = 0.15\lambda_0$, $\beta_{TM_0} = 749.32 = 1.193\beta_0$ and the results are tabulated in Table 4.4. For two of the intervals and number of samples the percentage errors can be found to be:

$$\{\text{E-line}\ ,\ N = 51\ ,\ \rho_{start} = 5\lambda_0\ ,\ \rho_{end} = 8\lambda_0\} \ \rightarrow\ \%\text{Error} = 0.04$$

$$\{\text{E-line}\ ,\ N = 51\ ,\ \rho_{start} = 5\lambda_0\ ,\ \rho_{end} = 9\lambda_0\} \ \rightarrow\ \%\text{Error} = 0.22$$

Examination of Table 4.4 shows that, E-line case gives very successful results. But for the H-line case the results are unsatisfactory.

When the thickness of the slab is increased to $th = 0.19\lambda_0$, the theoretical surface wave propagation constant increases to $\beta_{TM_0} = 805.81 = 1.282\beta_0$. The retrieved propagation constants are given in Table 4.5. The errors for two cases can be found as:

$$\{\text{E-line}\ ,\ N = 51\ ,\ \rho_{start} = 5\lambda_0\ ,\ \rho_{end} = 8\lambda_0\} \ \rightarrow\ \%\text{Error} = 0.63$$

$$\{\text{E-line}\ ,\ N = 51\ ,\ \rho_{start} = 5\lambda_0\ ,\ \rho_{end} = 9\lambda_0\} \ \rightarrow\ \%\text{Error} = 0.67$$

As it is seen from Table 4.5, E-line case gives acceptable results. But for the H-line case the results are again unsatisfactory.

For $th = 0.25\lambda_0$, except from the TM_0 mode, another mode emerges, which is TE_1. The analytically found surface wave propagation of these modes for $th = 0.25\lambda_0$ are $\beta_{TM_0} = 868.94 = 1.383\beta_0$ and $\beta_{TE_1} = 669.06 = 1.065\beta_0$, and the retrieved ones are tabulated in Table 4.6. For the TE_1 mode, percentage error is calculated as in (4.59).

$$\{\text{E-line}\ ,\ N = 51\ ,\ \rho_{start} = 4\lambda_0\ ,\ \rho_{end} = 8\lambda_0\} \ \rightarrow\ \%\text{Error}(\text{TM}_0) = 0.60$$

$$\%\text{Error}(\text{TE}_1) = 0.13$$

$$\{\text{E-line}\ ,\ N = 51\ ,\ \rho_{start} = 4\lambda_0\ ,\ \rho_{end} = 9\lambda_0\} \ \rightarrow\ \%\text{Error}(\text{TM}_0) = 0.89$$

$$\%\text{Error}(\text{TE}_1) = 0.15$$

$$\{\text{E-line}\ ,\ N = 21\ ,\ \rho_{start} = 4\lambda_0\ ,\ \rho_{end} = 9\lambda_0\} \ \rightarrow\ \%\text{Error}(\text{TM}_0) = 0.69$$

$$\%\text{Error}(\text{TE}_1) = 4.20$$

From Table 4.6 it is observed that E-line case gives acceptable results for the TM_0 mode. The results for this mode for the given intervals and number of samples yield approximately the same results. Along the E-line there are some problems for the TE_1 mode. For this mode, the best results are obtained in the $[4\lambda_0 - 8\lambda_0]$ and $[4\lambda_0 - 9\lambda_0]$ intervals with $N = 51$ samples. For the worst case, among the given intervals and number of samples, the percentage error is 4.20 for this mode. Along the H-line case the results are again unsatisfactory.

We have also simulated a case, where the dielectric substrate is very thin, $th = 0.05\lambda_0$. In this example, the surface propagation constant, $\beta_{TM_0} = 640.63 = 1.02\beta_0$, is very close to the space wave propagation constant. The results tabulated in Table 4.7 are far away from being successful for both E- and H-line cases. One thing to note is that, the surface wave propagation constants determined

using the GPOF Method are even smaller than the space wave propagation constant. The possible reason of failure for this particular thin case is propagation constants of space and surface wave terms being very close to each other.

Finally, the complex coefficients and exponentials found in the GPOF approximation are used for generating the electric field distribution along the E-line. In Figs. 4.20-4.23, the first two subplots of the figures show the field distribution inside the interval used for GPOF approximation. The last two subplots of the figures show the extrapolation of electric field distribution using the previously found complex coefficients and exponentials. HFSS data and GPOF approximation are in very good agreement. Also notice that GPOF method removes the noise in the HFSS data very well.

N	ρ_{start}	ρ_{end}	β^1_{SW}	β^1_{SW}/β_0
101	$4\lambda_0$	$8\lambda_0$	670.72	1.067
101	$5\lambda_0$	$8\lambda_0$	671.84	1.069
51	$4\lambda_0$	$8\lambda_0$	671.16	1.068
51	$5\lambda_0$	$8\lambda_0$	671.89	1.069
26	$4\lambda_0$	$8\lambda_0$	669.33	1.065
26	$5\lambda_0$	$8\lambda_0$	674.08	1.073
21	$4\lambda_0$	$8\lambda_0$	668.92	1.065
21	$5\lambda_0$	$8\lambda_0$	671.92	1.069
101	$4\lambda_0$	$9\lambda_0$	671.08	1.068
101	$5\lambda_0$	$9\lambda_0$	670.08	1.066
51	$4\lambda_0$	$9\lambda_0$	670.58	1.067
51	$5\lambda_0$	$9\lambda_0$	671.30	1.068
26	$4\lambda_0$	$9\lambda_0$	669.00	1.065
26	$5\lambda_0$	$9\lambda_0$	673.39	1.072
21	$4\lambda_0$	$9\lambda_0$	671.68	1.069
21	$5\lambda_0$	$9\lambda_0$	673.32	1.072

(a)

N	ρ_{start}	ρ_{end}	β^1_{SW}	β^1_{SW}/β_0
101	$4\lambda_0$	$8\lambda_0$	669.37	1.065
101	$5\lambda_0$	$8\lambda_0$	681.69	1.085
51	$4\lambda_0$	$8\lambda_0$	668.81	1.064
51	$5\lambda_0$	$8\lambda_0$	680.98	1.084
26	$4\lambda_0$	$8\lambda_0$	666.77	1.061
26	$5\lambda_0$	$8\lambda_0$	677.92	1.079
21	$4\lambda_0$	$8\lambda_0$	667.77	1.063
21	$5\lambda_0$	$8\lambda_0$	678.47	1.080
101	$4\lambda_0$	$9\lambda_0$	670.70	1.067
101	$5\lambda_0$	$9\lambda_0$	677.51	1.078
51	$4\lambda_0$	$9\lambda_0$	671.06	1.068
51	$5\lambda_0$	$9\lambda_0$	677.25	1.078
26	$4\lambda_0$	$9\lambda_0$	668.35	1.064
26	$5\lambda_0$	$9\lambda_0$	674.21	1.073
21	$4\lambda_0$	$9\lambda_0$	668.66	1.064
21	$5\lambda_0$	$9\lambda_0$	672.99	1.071

(b)

Table 4.3: Surface wave propagation constants retrieved from (a) E-line, (b) H-line. ($f = 30$GHz, $\lambda_0 = 1$cm, $th = 0.1\lambda_0$, $\varepsilon_r = 2.55$)

N	ρ_{start}	ρ_{end}	β^1_{SW}	β^1_{SW}/β_0
101	$4\lambda_0$	$8\lambda_0$	750.59	1.195
101	$5\lambda_0$	$8\lambda_0$	749.60	1.193
51	$4\lambda_0$	$8\lambda_0$	750.92	1.195
51	$5\lambda_0$	$8\lambda_0$	749.61	1.193
26	$4\lambda_0$	$8\lambda_0$	751.75	1.196
26	$5\lambda_0$	$8\lambda_0$	749.92	1.194
21	$4\lambda_0$	$8\lambda_0$	751.25	1.196
21	$5\lambda_0$	$8\lambda_0$	750.15	1.194
101	$4\lambda_0$	$9\lambda_0$	750.46	1.194
101	$5\lambda_0$	$9\lambda_0$	750.47	1.194
51	$4\lambda_0$	$9\lambda_0$	750.03	1.194
51	$5\lambda_0$	$9\lambda_0$	750.97	1.195
26	$4\lambda_0$	$9\lambda_0$	750.94	1.195
26	$5\lambda_0$	$9\lambda_0$	750.15	1.194
21	$4\lambda_0$	$9\lambda_0$	752.29	1.197
21	$5\lambda_0$	$9\lambda_0$	750.63	1.195

(a)

N	ρ_{start}	ρ_{end}	β^1_{SW}	β^1_{SW}/β_0
101	$4\lambda_0$	$8\lambda_0$	678.15	1.079
101	$5\lambda_0$	$8\lambda_0$	551.77	0.878
51	$4\lambda_0$	$8\lambda_0$	692.83	1.103
51	$5\lambda_0$	$8\lambda_0$	552.05	0.879
26	$4\lambda_0$	$8\lambda_0$	714.73	1.138
26	$5\lambda_0$	$8\lambda_0$	554.49	0.882
21	$4\lambda_0$	$8\lambda_0$	703.84	1.120
21	$5\lambda_0$	$8\lambda_0$	547.86	0.872
101	$4\lambda_0$	$9\lambda_0$	505.62	0.805
101	$5\lambda_0$	$9\lambda_0$	494.96	0.788
51	$4\lambda_0$	$9\lambda_0$	515.59	0.821
51	$5\lambda_0$	$9\lambda_0$	495.13	0.788
26	$4\lambda_0$	$9\lambda_0$	528.81	0.842
26	$5\lambda_0$	$9\lambda_0$	495.33	0.788
21	$4\lambda_0$	$9\lambda_0$	541.64	0.862
21	$5\lambda_0$	$9\lambda_0$	494.29	0.787

(b)

Table 4.4: Surface wave propagation constants retrieved from (a) E-line, (b) H-line. ($f = 30$GHz, $\lambda_0 = 1$cm, $th = 0.15\lambda_0$, $\varepsilon_r = 2.55$)

N	ρ_{start}	ρ_{end}	β^1_{SW}	β^1_{SW}/β_0
101	$4\lambda_0$	$8\lambda_0$	812.92	1.294
101	$5\lambda_0$	$8\lambda_0$	814.56	1.296
51	$4\lambda_0$	$8\lambda_0$	812.40	1.293
51	$5\lambda_0$	$8\lambda_0$	815.77	1.298
26	$4\lambda_0$	$8\lambda_0$	810.91	1.291
26	$5\lambda_0$	$8\lambda_0$	815.51	1.298
21	$4\lambda_0$	$8\lambda_0$	813.97	1.295
21	$5\lambda_0$	$8\lambda_0$	815.93	1.299
101	$4\lambda_0$	$9\lambda_0$	811.20	1.291
101	$5\lambda_0$	$9\lambda_0$	809.44	1.288
51	$4\lambda_0$	$9\lambda_0$	811.55	1.292
51	$5\lambda_0$	$9\lambda_0$	811.24	1.291
26	$4\lambda_0$	$9\lambda_0$	811.14	1.291
26	$5\lambda_0$	$9\lambda_0$	810.97	1.291
21	$4\lambda_0$	$9\lambda_0$	811.81	1.292
21	$5\lambda_0$	$9\lambda_0$	808.01	1.286

(a)

N	ρ_{start}	ρ_{end}	β^1_{SW}	β^1_{SW}/β_0
101	$4\lambda_0$	$8\lambda_0$	573.13	0.912
101	$5\lambda_0$	$8\lambda_0$	602.71	0.959
51	$4\lambda_0$	$8\lambda_0$	573.08	0.912
51	$5\lambda_0$	$8\lambda_0$	602.31	0.959
26	$4\lambda_0$	$8\lambda_0$	574.13	0.914
26	$5\lambda_0$	$8\lambda_0$	600.82	0.956
21	$4\lambda_0$	$8\lambda_0$	573.48	0.913
21	$5\lambda_0$	$8\lambda_0$	603.75	0.961
101	$4\lambda_0$	$9\lambda_0$	604.62	0.962
101	$5\lambda_0$	$9\lambda_0$	627.22	0.998
51	$4\lambda_0$	$9\lambda_0$	604.91	0.963
51	$5\lambda_0$	$9\lambda_0$	625.78	0.996
26	$4\lambda_0$	$9\lambda_0$	602.64	0.959
26	$5\lambda_0$	$9\lambda_0$	624.15	0.993
21	$4\lambda_0$	$9\lambda_0$	603.83	0.961
21	$5\lambda_0$	$9\lambda_0$	625.02	0.995

(b)

Table 4.5: Surface wave propagation constants retrieved from (a) E-line, (b) H-line. ($f = 30$GHz, $\lambda_0 = 1$cm, $th = 0.19\lambda_0$, $\varepsilon_r = 2.55$)

N	ρ_{start}	ρ_{end}	β^1_{SW}	β^1_{SW}/β_0	β^2_{SW}	β^2_{SW}/β_0
101	$4\lambda_0$	$8\lambda_0$	874.37	1.392	661.72	1.053
101	$5\lambda_0$	$8\lambda_0$	874.33	1.392	642.69	1.023
51	$4\lambda_0$	$8\lambda_0$	874.17	1.391	668.20	1.063
51	$5\lambda_0$	$8\lambda_0$	874.59	1.392	641.47	1.021
26	$4\lambda_0$	$8\lambda_0$	872.81	1.389	660.68	1.052
26	$5\lambda_0$	$8\lambda_0$	877.74	1.397	651.17	1.036
21	$4\lambda_0$	$8\lambda_0$	875.05	1.393	664.86	1.058
21	$5\lambda_0$	$8\lambda_0$	878.32	1.398	592.63	0.943
101	$4\lambda_0$	$9\lambda_0$	876.05	1.394	666.87	1.061
101	$5\lambda_0$	$9\lambda_0$	878.67	1.398	659.38	1.049
51	$4\lambda_0$	$9\lambda_0$	876.68	1.395	668.06	1.063
51	$5\lambda_0$	$9\lambda_0$	878.97	1.399	656.69	1.045
26	$4\lambda_0$	$9\lambda_0$	876.14	1.394	664.88	1.058
26	$5\lambda_0$	$9\lambda_0$	881.39	1.403	649.90	1.034
21	$4\lambda_0$	$9\lambda_0$	874.90	1.392	640.98	1.020
21	$5\lambda_0$	$9\lambda_0$	877.24	1.396	662.16	1.054

(a)

N	ρ_{start}	ρ_{end}	β^1_{SW}	β^1_{SW}/β_0	β^2_{SW}	β^2_{SW}/β_0
101	$4\lambda_0$	$8\lambda_0$	669.71	1.066	531.31	0.846
101	$5\lambda_0$	$8\lambda_0$	677.75	1.079	450.48	0.717
51	$4\lambda_0$	$8\lambda_0$	666.46	1.061	508.42	0.809
51	$5\lambda_0$	$8\lambda_0$	679.28	1.081	501.52	0.798
26	$4\lambda_0$	$8\lambda_0$	668.97	1.065	528.33	0.841
26	$5\lambda_0$	$8\lambda_0$	680.98	1.084	587.81	0.936
21	$4\lambda_0$	$8\lambda_0$	663.85	1.057	516.06	0.821
21	$5\lambda_0$	$8\lambda_0$	673.33	1.072	-422.74	-0.673
101	$4\lambda_0$	$9\lambda_0$	638.59	1.016	652.13	1.038
101	$5\lambda_0$	$9\lambda_0$	693.72	1.104	683.90	1.088
51	$4\lambda_0$	$9\lambda_0$	632.50	1.007	619.51	0.986
51	$5\lambda_0$	$9\lambda_0$	695.36	1.107	677.21	1.078
26	$4\lambda_0$	$9\lambda_0$	631.59	1.005	628.70	1.001
26	$5\lambda_0$	$9\lambda_0$	691.11	1.100	656.84	1.045
21	$4\lambda_0$	$9\lambda_0$	630.60	1.004	652.51	1.038
21	$5\lambda_0$	$9\lambda_0$	686.37	1.092	678.40	1.080

(b)

Table 4.6: Surface wave propagation constants retrieved from (a) E-line, (b) H-line. ($f = 30$GHz, $\lambda_0 = 1$cm, $th = 0.25\lambda_0$, $\varepsilon_r = 2.55$)

N	ρ_{start}	ρ_{end}	β^1_{SW}	β^1_{SW}/β_0
101	$4\lambda_0$	$8\lambda_0$	606.04	0.965
101	$5\lambda_0$	$8\lambda_0$	605.96	0.964
51	$4\lambda_0$	$8\lambda_0$	600.33	0.955
51	$5\lambda_0$	$8\lambda_0$	605.39	0.964
26	$4\lambda_0$	$8\lambda_0$	600.82	0.956
26	$5\lambda_0$	$8\lambda_0$	603.34	0.960
21	$4\lambda_0$	$8\lambda_0$	608.13	0.968
21	$5\lambda_0$	$8\lambda_0$	604.81	0.963
101	$4\lambda_0$	$9\lambda_0$	609.92	0.971
101	$5\lambda_0$	$9\lambda_0$	604.67	0.962
51	$4\lambda_0$	$9\lambda_0$	604.11	0.961
51	$5\lambda_0$	$9\lambda_0$	603.40	0.960
26	$4\lambda_0$	$9\lambda_0$	608.04	0.968
26	$5\lambda_0$	$9\lambda_0$	602.33	0.959
21	$4\lambda_0$	$9\lambda_0$	602.19	0.958
21	$5\lambda_0$	$9\lambda_0$	607.50	0.967

(a)

N	ρ_{start}	ρ_{end}	β^1_{SW}	β^1_{SW}/β_0
101	$4\lambda_0$	$8\lambda_0$	610.13	0.971
101	$5\lambda_0$	$8\lambda_0$	598.61	0.953
51	$4\lambda_0$	$8\lambda_0$	609.25	0.970
51	$5\lambda_0$	$8\lambda_0$	599.69	0.954
26	$4\lambda_0$	$8\lambda_0$	604.90	0.963
26	$5\lambda_0$	$8\lambda_0$	600.32	0.955
21	$4\lambda_0$	$8\lambda_0$	606.37	0.965
21	$5\lambda_0$	$8\lambda_0$	597.78	0.951
101	$4\lambda_0$	$9\lambda_0$	614.84	0.979
101	$5\lambda_0$	$9\lambda_0$	598.74	0.953
51	$4\lambda_0$	$9\lambda_0$	616.50	0.981
51	$5\lambda_0$	$9\lambda_0$	599.72	0.954
26	$4\lambda_0$	$9\lambda_0$	606.43	0.965
26	$5\lambda_0$	$9\lambda_0$	601.48	0.957
21	$4\lambda_0$	$9\lambda_0$	614.57	0.978
21	$5\lambda_0$	$9\lambda_0$	600.26	0.955

(b)

Table 4.7: Surface wave propagation constants retrieved from (a) E-line, (b) H-line. ($f = 30$GHz, $\lambda_0 = 1$cm, $th = 0.05\lambda_0$, $\varepsilon_r = 2.55$)

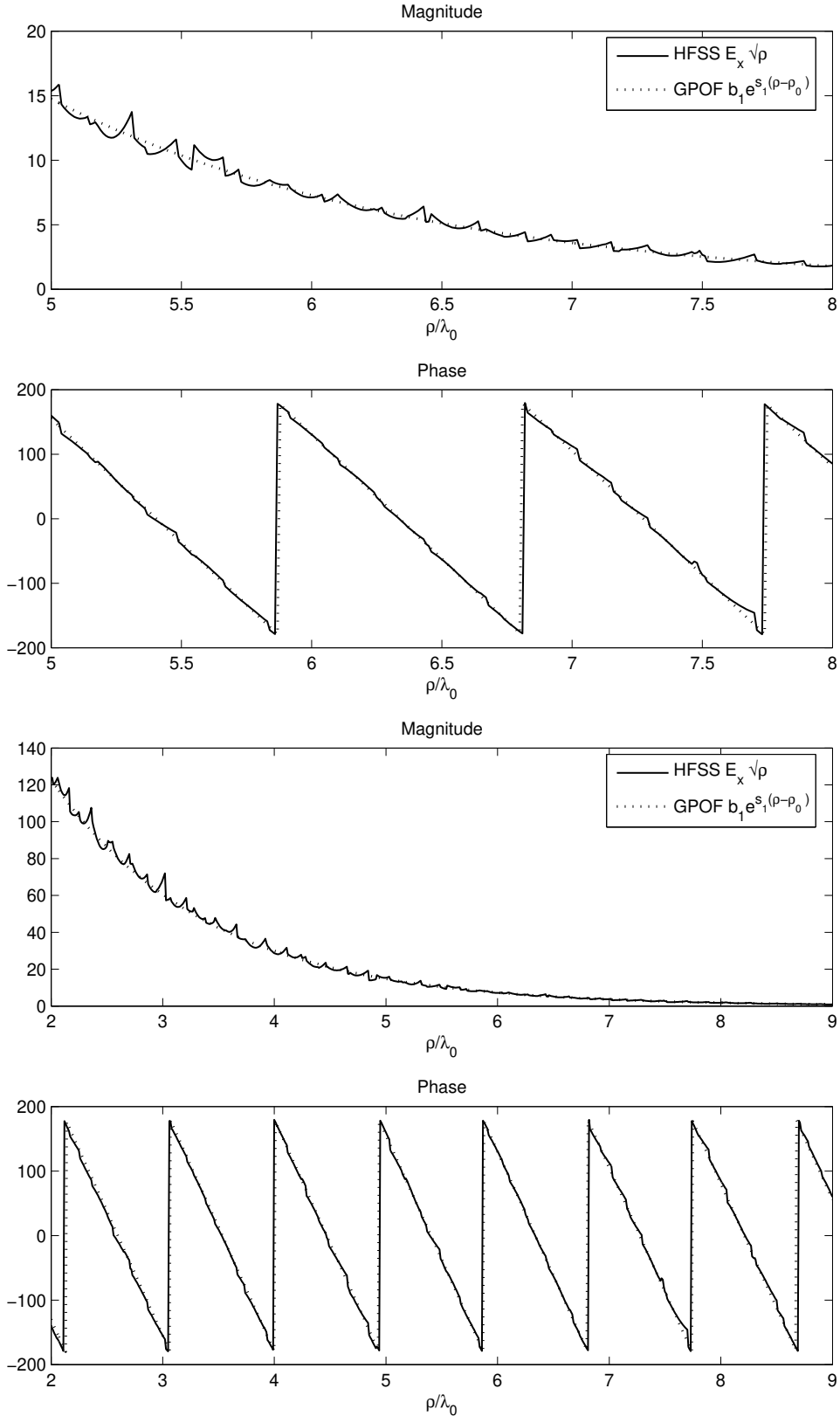

Figure 4.20: Comparison of GPOF approximation with HFSS data and its Extrapolation . (f = 30GHz, λ_0 = 1cm, $th = 0.1\lambda_0$, $\varepsilon_r = 2.55$, $\rho_{start} = 5\lambda_0$, $\rho_{end} = 8\lambda_0$, $N = 101$)

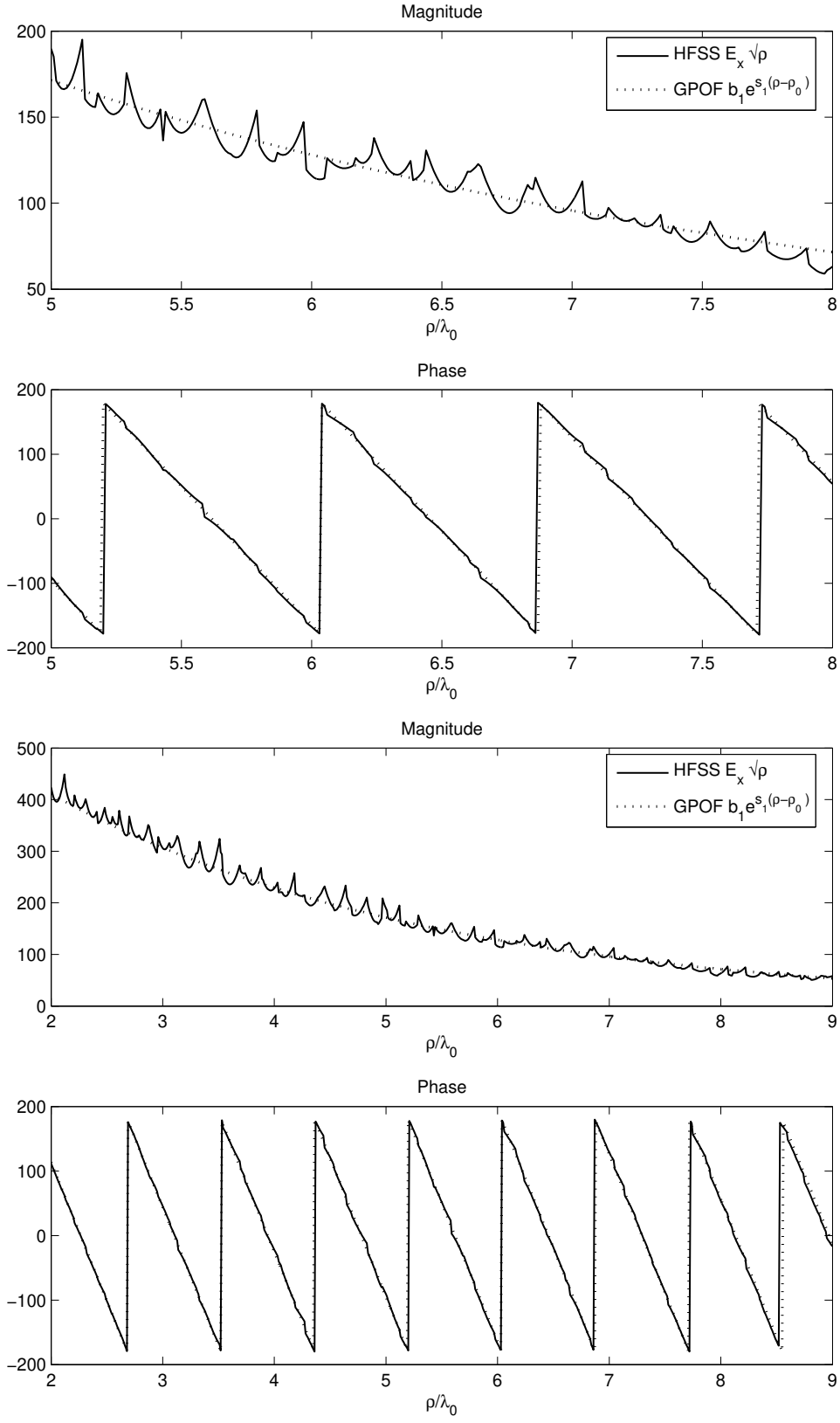

Figure 4.21: Comparison of GPOF approximation with HFSS data and its Extrapolation . (f = 30GHz, λ_0 = 1cm, $th = 0.15\lambda_0$, $\varepsilon_r = 2.55$, $\rho_{start} = 5\lambda_0$, $\rho_{end} = 8\lambda_0$, $N = 101$)

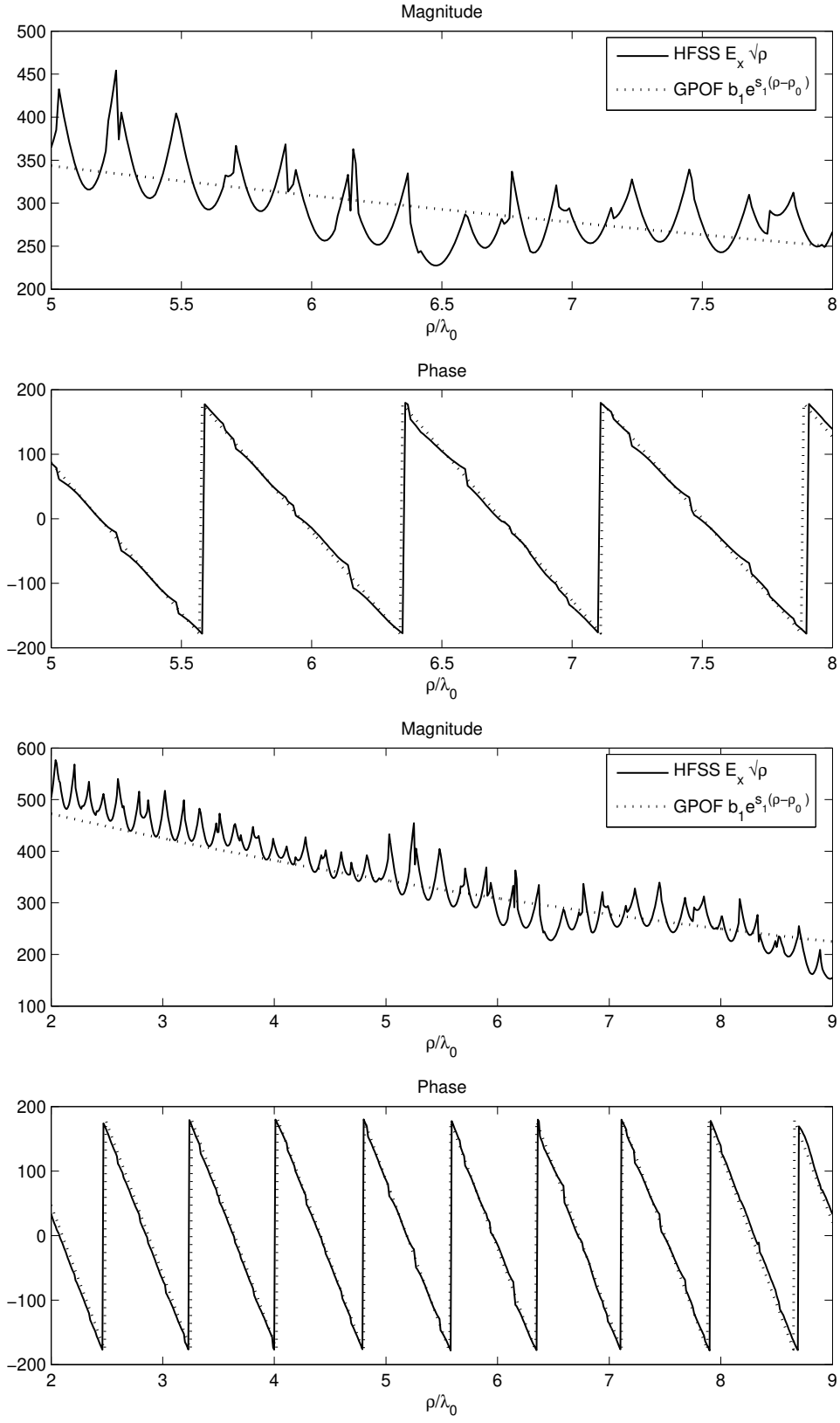

Figure 4.22: Comparison of GPOF approximation with HFSS data and its Extrapolation . (f = 30GHz, λ_0 = 1cm, $th = 0.19\lambda_0$, $\varepsilon_r = 2.55$, $\rho_{start} = 5\lambda_0$, $\rho_{end} = 8\lambda_0$, $N = 101$)

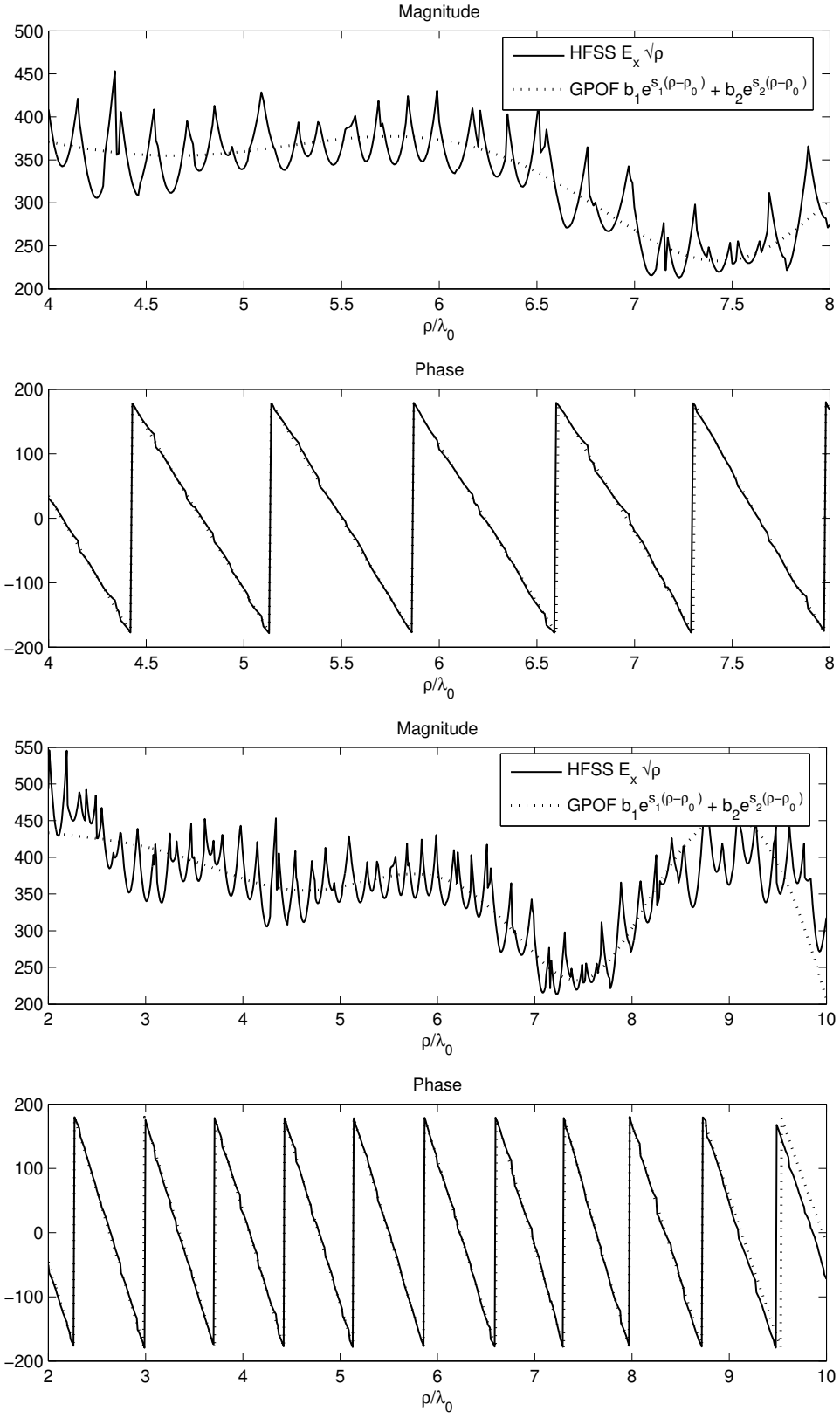

Figure 4.23: Comparison of GPOF approximation with HFSS data and its Extrapolation . (f = 30GHz, λ_0 = 1cm, $th = 0.25\lambda_0$, $\varepsilon_r = 2.55$, $\rho_{start} = 4\lambda_0$, $\rho_{end} = 8\lambda_0$, $N = 51$)

4.2.5 Conclusions

Numerical results and comparisons with theoretical calculations show that our method works quite successfully along the E-line. The only exception occurs in the $th = 0.05\lambda_0$ case. But along the H-line, successful results are obtained only in the $th = 0.1\lambda_0$ case.

In the implementation of the GPOF Method, the $[4\lambda_0 - 8\lambda_0]$, $[5\lambda_0 - 8\lambda_0]$, $[4\lambda_0 - 9\lambda_0]$ and $[5\lambda_0 - 9\lambda_0]$ intervals give good results. The reasons are: ρ should be sufficiently large and reflections from the radiation boundaries should decay not to contaminate the solutions.

The number of samples (N) is also important in the GPOF Method. Taking too many samples makes the system of equations solved in the method more linearly dependent, on the other hand taking not enough number of samples give inaccurate results because the behavior of the complex function to be approximated cannot be tracked correctly. In our method, we use $N = 51$ or $N = 101$ in the GPOF Method.

Another factor that affects the accuracy of the results is the ratio of the surface wave propagation constant to space wave propagation constant. When this ratio is very close to 1, the differentiation of the space wave and surface wave terms becomes difficult. This phenomena can be observed at the $th = 0.05\lambda_0$ case where surface wave propagation constant is very close to space wave propagation constant. As the thickness of the dielectric slab increases β_{TM_0} increases too. This increases the accuracy of results to determine β_{TM_0}. However when thickness is sufficiently large and TE_1 mode emerges, β_{TE_1} cannot be determined as accurate as β_{TM_0} is determined. For each mode that emerges recently, as the thickness increases, the results will not be very satisfactory at first. But as the thickness continues to increase the results will be more successful for this mode.

Chapter 5

CONCLUSIONS

In this thesis, electromagnetic scattering and transmission from metamaterial structures, such as metamaterial slabs, metamaterial cylinders and metamaterial coated conducting cylinders, are investigated. These structures are illuminated by electric line sources or plane waves. The formulation of these wave propagation problems is done in such a way that it remains valid for any kind of material used, having any sign combination of constitutive parameters and having any electric and/or magnetic losses.

For one of these propagation problems i.e., metamaterial coated conducting cylinders illuminated normally with plane waves, achieving transparency and maximizing scattering are investigated thoroughly. It is found out that, rigorous derivation of transparency and resonance conditions for PEC core cylinder case under the sub-wavelength limitations yields the same conditions of two electrically small concentric layers of conjugately paired cylinders, given in the literature (when the inner core layer is also taken to the PEC limit). These transparency and resonance conditions heavily depend on the permittivity of the metamaterial coating (for TE polarization) and the ratio of core-shell radii. The relations between the permittivity of the coating and the ratio of core-shell

radii are investigated for achieving transparency and scattering maximization. Numerical results show that these analytical relations are quite successful and work better when the cylindrical scatter is electrically very small. As the future work, similar analytical transparency and resonance conditions can be derived and tested for obliquely incident plane waves. Our preliminary numerical results for oblique incidence scenarios show the existence of such transparency and resonance conditions. As another future work, the infinite length metamaterial coated conducting cylinder can be truncated, while keeping other geometry and material parameters the same, and can be simulated in full wave simulators to see whether such transparency or resonance conditions exist for real-life geometries.

A novel homogenization method for the retrieval of effective constitutive parameters of metamaterials is proposed and implemented. The method is based on the simple idea that the total reflection coefficient from a finite metamaterial structure has to resemble the reflection from an homogeneous equivalent. While implementing the method, 1, 2, ..., 20 unit cells of the same metamaterial structure are stacked and their reflection coefficients are collected. The homogenization quality of the metamaterial is evaluated in terms of various factors, which showed that the method is very successful to retrieve the effective constitutive parameters of the metamaterial. Since the method is merely dependent on reflection, the homogeneous equivalent characterizes the reflection property of the metamaterial best. As the future work, the method can be modified to incorporate also the transmission data, so that the homogeneous equivalent mimics the metamaterial more successfully in the transmission region. Another future work can be homogenization in the oblique incidence case, since the method is already capable for this, if an efficient oblique incidence implementation scheme can be formed for the simulation of metamaterial.

Finally, another method has been proposed for the retrieval of surface wave propagation constants on any periodic or non-periodic grounded slab medium. As

a preliminary, the method is applied to grounded dielectric slabs. The numerical results generally show good agreement with their theoretical counterparts.

APPENDIX A

Bessel Functions

In cylindrical coordinate system, while solving the wave equation, Bessel's differential equation arises, which can be written as

$$x^2 \frac{d^2 y}{dx^2} + x \frac{dy}{dx} + \left(x^2 - p^2\right) y = 0. \tag{A.1}$$

Since Bessel's equation in (A.1) is a second order differential equation, it has two linearly independent solutions:

$$y(x) = A_1 J_p(x) + B_1 J_{-p}(x) \quad p \neq 0 \text{ or integer}, \tag{A.2}$$

$$y(x) = A_2 J_n(x) + B_2 Y_n(x) \quad p = n = 0 \text{ or integer}, \tag{A.3}$$

where $J_p(x)$ is referred to as the Bessel function of the first kind of order p and $Y_p(x)$ as the Bessel function of the second kind of order p (or sometimes as the Neumann function).

When $p = n =$ integer,

$$J_{-n}(x) = (-1)^n J_n(x), \tag{A.4}$$

$$J_n(-x) = (-1)^n J_n(x). \tag{A.5}$$

Small Argument Forms:

When the argument of the Bessel functions is small (i.e., $x \to 0$),

for $p = 0$:

$$J_0(x) \simeq 1, \tag{A.6}$$

$$Y_0(x) \simeq \frac{2}{\pi} \ln\left(\frac{\gamma x}{2}\right), \tag{A.7}$$

$$\gamma = 1.781, \tag{A.8}$$

for $p > 0$:

$$J_p(x) \simeq \frac{1}{p!}\left(\frac{x}{2}\right)^p, \tag{A.9}$$

$$Y_n(x) \simeq -\frac{(p-1)!}{\pi}\left(\frac{2}{x}\right)^p. \tag{A.10}$$

Large Argument Forms:

When the argument of the Bessel functions is large (i.e., $x \to \infty$),

$$J_p(x) \simeq \sqrt{\frac{2}{\pi x}} \cos\left(x - \frac{\pi}{4} - \frac{p\pi}{2}\right), \tag{A.11}$$

$$Y_p(x) \simeq \sqrt{\frac{2}{\pi x}} \sin\left(x - \frac{\pi}{4} - \frac{p\pi}{2}\right). \tag{A.12}$$

From electromagnetic point of view, these cosine and sine functions in Bessel functions of the first and second kinds represent standing waves. For wave propagation, it becomes more convenient to define Hankel functions:

$$H_p^{(1)}(x) = J_p(x) + jY_p(x), \tag{A.13}$$

$$H_p^{(2)}(x) = J_p(x) - jY_p(x), \tag{A.14}$$

where $H_p^{(1)}(x)$ is the Hankel function of the first kind of order p and $H_p^{(2)}(x)$ is the Hankel function of the second kind of order p.

For large arguments (i.e., $x \to \infty$):

$$H_p^{(1)}(x) \simeq \sqrt{\frac{2}{\pi x}} e^{j[x-p(\pi/2)-\pi/4]}, \tag{A.15}$$

$$H_p^{(2)}(x) \simeq \sqrt{\frac{2}{\pi x}} e^{-j[x-p(\pi/2)-\pi/4]}. \tag{A.16}$$

With the assumed $e^{j\omega t}$ time dependence, Hankel functions of the first kind represent inward propagating waves, whereas Hankel functions of the second kind represent outward propagating waves.

For the derivatives of Bessel and Hankel functions, the following recurrence relation can be used:

$$\frac{dF_p(x)}{dx} = \frac{1}{2}\left[F_{p-1}(x) - F_{p+1}(x)\right], \tag{A.17}$$

where $F(x)$ represents any kind of Bessel or Hankel function. Other alternative forms of the recurrence relations and many other properties of Bessel and Hankel functions of integer and non-integer orders can be found in [80].

APPENDIX B

Derivation of the ϕ Components of Electric and Magnetic Fields: TM^z Polarization

To find the ϕ components of the electric and magnetic fields, we will use Maxwell's Equations:

$$\nabla \times \mathbf{E} = -j\omega\mu\mathbf{H} \quad \rightarrow \quad \mathbf{H} = -\frac{1}{j\omega\mu}\nabla \times \mathbf{E}, \tag{B.1}$$

$$H_\rho = -\frac{1}{j\omega\mu}\left(\frac{1}{\rho}\frac{\partial E_z}{\partial \phi} - \frac{\partial E_\phi}{\partial z}\right), \tag{B.2}$$

$$H_\phi = -\frac{1}{j\omega\mu}\left(\frac{\partial E_\rho}{\partial z} - \frac{\partial E_z}{\partial \rho}\right), \tag{B.3}$$

$$H_z = -\frac{1}{j\omega\mu}\frac{1}{\rho}\left[\frac{\partial}{\partial \rho}\left(\rho E_\phi\right) - \frac{\partial E_\rho}{\partial \phi}\right]. \tag{B.4}$$

$$\nabla \times \mathbf{H} = j\omega\varepsilon\mathbf{E} \quad \rightarrow \quad \mathbf{E} = \frac{1}{j\omega\varepsilon}\nabla \times \mathbf{H}, \tag{B.5}$$

$$E_\rho = \frac{1}{j\omega\varepsilon}\left(\frac{1}{\rho}\frac{\partial H_z}{\partial \phi} - \frac{\partial H_\phi}{\partial z}\right), \tag{B.6}$$

$$E_\phi = \frac{1}{j\omega\varepsilon}\left(\frac{\partial H_\rho}{\partial z} - \frac{\partial H_z}{\partial \rho}\right), \tag{B.7}$$

$$E_z = \frac{1}{j\omega\varepsilon}\frac{1}{\rho}\left[\frac{\partial}{\partial \rho}\left(\rho H_\phi\right) - \frac{\partial H_\rho}{\partial \phi}\right]. \tag{B.8}$$

In the following derivations, all derivatives of Bessel and Hankel functions are taken with respective to their entire arguments.

$\underline{H^i_\phi}$:

$$H^i_\phi = -\frac{1}{j\omega\mu_0}\left(\frac{\partial E^i_\rho}{\partial z} - \frac{\partial E^i_z}{\partial \rho}\right) \tag{B.9}$$

$$H^i_\phi = -\frac{1}{j\omega\mu_0}\left[\frac{\partial E^i_\rho}{\partial z} - \frac{\partial}{\partial \rho}\left(E_0 \sin\theta_0 e^{jk_0 z\cos\theta_0}\sum_{n=-\infty}^{+\infty} j^{-n}J_n(k_0\rho\sin\theta_0)e^{jn(\phi-\phi_0)}\right)\right] \tag{B.10}$$

$$H^i_\phi = -\frac{1}{j\omega\mu_0}\left(\frac{\partial E^i_\rho}{\partial z} - E_0 k_0 \sin^2\theta_0 e^{jk_0 z\cos\theta_0}\sum_{n=-\infty}^{+\infty} j^{-n}J'_n(k_0\rho\sin\theta_0)e^{jn(\phi-\phi_0)}\right) \tag{B.11}$$

$$E^i_\rho = \frac{1}{j\omega\varepsilon_0}\left(\frac{1}{\rho}\frac{\partial H^i_z}{\partial \phi} - \frac{\partial H^i_\phi}{\partial z}\right) \tag{B.12}$$

Since $H^i_z = 0$,

$$E^i_\rho = -\frac{1}{j\omega\varepsilon_0}\frac{\partial H^i_\phi}{\partial z} \tag{B.13}$$

We also know that all field variations in the z direction are in the form of $e^{jk_0 z\cos\theta_0}$. Therefore,

$$E^i_\rho = -\frac{k_0\cos\theta_0}{\omega\varepsilon_0}H^i_\phi \tag{B.14}$$

Substituting (B.14) in (B.11),

$$H^i_\phi = -\frac{1}{j\omega\mu_0}\left(-\frac{k_0\cos\theta_0}{\omega\varepsilon_0}\frac{\partial H^i_\phi}{\partial z} - E_0 k_0 \sin^2\theta_0 e^{jk_0 z\cos\theta_0}\sum_{n=-\infty}^{+\infty} j^{-n}J'_n(k_0\rho\sin\theta_0)e^{jn(\phi-\phi_0)}\right) \tag{B.15}$$

$$H^i_\phi = -\frac{1}{j\omega\mu_0}\left(-\frac{jk_0^2\cos^2\theta_0}{\omega\varepsilon_0}H^i_\phi - E_0 k_0 \sin^2\theta_0 e^{jk_0 z\cos\theta_0}\sum_{n=-\infty}^{+\infty} j^{-n}J'_n(k_0\rho\sin\theta_0)e^{jn(\phi-\phi_0)}\right) \tag{B.16}$$

$$H^i_\phi = \left(\frac{k_0^2\cos^2\theta_0}{\omega^2\mu_0\varepsilon_0}H^i_\phi + \frac{E_0 k_0\sin^2\theta_0}{j\omega\mu_0}e^{jk_0 z\cos\theta_0}\sum_{n=-\infty}^{+\infty} j^{-n}J'_n(k_0\rho\sin\theta_0)e^{jn(\phi-\phi_0)}\right) \tag{B.17}$$

Since $k_0 = \omega\sqrt{\mu_0\varepsilon_0}$,

$$(1-\cos^2\theta_0)H_\phi^i = \sin^2\theta_0 H_\phi^i = \frac{E_0 k_0 \sin^2\theta_0}{j\omega\mu_0} e^{jk_0 z\cos\theta_0} \sum_{n=-\infty}^{+\infty} j^{-n} J_n'(k_0\rho\sin\theta_0) e^{jn(\phi-\phi_0)} \tag{B.18}$$

$$\begin{aligned} H_\phi^i &= \frac{E_0 k_0}{j\omega\mu_0} e^{jk_0 z\cos\theta_0} \sum_{n=-\infty}^{+\infty} j^{-n} J_n'(k_0\rho\sin\theta_0) e^{jn(\phi-\phi_0)} \\ &= -j\frac{E_0}{\eta_0} e^{jk_0 z\cos\theta_0} \sum_{n=-\infty}^{+\infty} j^{-n} J_n'(k_0\rho\sin\theta_0) e^{jn(\phi-\phi_0)} \end{aligned} \tag{B.19}$$

$\underline{E_\phi^i}$:

$$E_\phi^i = \frac{1}{j\omega\varepsilon_0}\left(\frac{\partial H_\rho^i}{\partial z} - \frac{\partial H_z^i}{\partial \rho}\right) \tag{B.20}$$

Since $H_z^i = 0$ and $\frac{\partial}{\partial z} = jk_0\cos\theta_0$,

$$E_\phi^i = \frac{k_0\cos\theta_0}{\omega\varepsilon_0} H_\rho^i \tag{B.21}$$

$$H_\rho^i = -\frac{1}{j\omega\mu_0}\left(\frac{1}{\rho}\frac{\partial E_z^i}{\partial\phi} - \frac{\partial E_\phi^i}{\partial z}\right) \tag{B.22}$$

$$H_\rho^i = -\frac{1}{j\omega\mu_0}\left[\frac{1}{\rho}\frac{\partial}{\partial\phi}\left(E_0\sin\theta_0 e^{jk_0 z\cos\theta_0}\sum_{n=-\infty}^{+\infty} j^{-n} J_n(k_0\rho\sin\theta_0)e^{jn(\phi-\phi_0)}\right) - \frac{\partial E_\phi^i}{\partial z}\right] \tag{B.23}$$

$$H_\rho^i = -\frac{1}{j\omega\mu_0}\left[\frac{1}{\rho}\left(jE_0\sin\theta_0 e^{jk_0 z\cos\theta_0}\sum_{n=-\infty}^{+\infty} nj^{-n} J_n(k_0\rho\sin\theta_0)e^{jn(\phi-\phi_0)}\right) - \frac{\partial E_\phi^i}{\partial z}\right] \tag{B.24}$$

Substituting (B.21) in (B.24)

$$\begin{aligned} H_\rho^i = -\frac{1}{j\omega\mu_0}\Bigg[&\frac{1}{\rho}\left(jE_0\sin\theta_0 e^{jk_0 z\cos\theta_0}\sum_{n=-\infty}^{+\infty} nj^{-n} J_n(k_0\rho\sin\theta_0)e^{jn(\phi-\phi_0)}\right) \\ &- \frac{jk_0^2\cos^2\theta_0}{\omega\varepsilon_0} H_\rho^i\Bigg] \end{aligned} \tag{B.25}$$

$$H_\rho^i = -\frac{E_0\sin\theta_0}{\omega\mu_0\rho} e^{jk_0 z\cos\theta_0}\sum_{n=-\infty}^{+\infty} nj^{-n} J_n(k_0\rho\sin\theta_0)e^{jn(\phi-\phi_0)} + \frac{k_0^2\cos^2\theta_0}{\omega^2\mu_0\varepsilon_0} H_\rho^i \tag{B.26}$$

$$(1-\cos^2\theta_0)H_\rho^i = \sin^2\theta_0 H_\rho^i = -\frac{E_0\sin\theta_0}{\omega\mu_0\rho}e^{jk_0z\cos\theta_0}\sum_{n=-\infty}^{+\infty} nj^{-n}J_n(k_0\rho\sin\theta_0)e^{jn(\phi-\phi_0)} \tag{B.27}$$

$$H_\rho^i = -\frac{E_0}{\omega\mu_0\rho\sin\theta_0}e^{jk_0z\cos\theta_0}\sum_{n=-\infty}^{+\infty} nj^{-n}J_n(k_0\rho\sin\theta_0)e^{jn(\phi-\phi_0)} \tag{B.28}$$

Substituting (B.28) in (B.21) gives

$$E_\phi^i = -\frac{E_0k_0\cos\theta_0}{\omega^2\mu_0\varepsilon_0\rho\sin\theta_0}e^{jk_0z\cos\theta_0}\sum_{n=-\infty}^{+\infty} nj^{-n}J_n(k_0\rho\sin\theta_0)e^{jn(\phi-\phi_0)} \tag{B.29}$$

$$E_\phi^i = -\frac{E_0\cos\theta_0}{k_0\rho\sin\theta_0}e^{jk_0z\cos\theta_0}\sum_{n=-\infty}^{+\infty} nj^{-n}J_n(k_0\rho\sin\theta_0)e^{jn(\phi-\phi_0)} \tag{B.30}$$

$\underline{E_\phi^s}$:

$$E_\phi^s = \frac{1}{j\omega\varepsilon_0}\left(\frac{\partial H_\rho^s}{\partial z} - \frac{\partial H_z^s}{\partial\rho}\right) \tag{B.31}$$

$$E_\phi^s = \frac{1}{j\omega\varepsilon_0}\Big(jk_0\cos\theta_0 H_\rho^s \tag{B.32}$$
$$-E_0k_0\sin^2\theta_0 e^{jk_0z\cos\theta_0}\sum_{n=-\infty}^{+\infty} j^{-n}\widetilde{c}_nH_n^{(2)'}(k_0\rho\sin\theta_0)e^{jn(\phi-\phi_0)}\Big)$$

$$E_\phi^s = \frac{k_0\cos\theta_0}{\omega\varepsilon_0}H_\rho^s - \frac{E_0k_0\sin^2\theta_0}{j\omega\varepsilon_0}e^{jk_0z\cos\theta_0}\sum_{n=-\infty}^{+\infty} j^{-n}\widetilde{c}_nH_n^{(2)'}(k_0\rho\sin\theta_0)e^{jn(\phi-\phi_0)} \tag{B.33}$$

$$H_\rho^s = -\frac{1}{j\omega\mu_0}\left(\frac{1}{\rho}\frac{\partial E_z^s}{\partial\phi} - \frac{\partial E_\phi^s}{\partial z}\right) \tag{B.34}$$

$$H_\rho^s = -\frac{1}{j\omega\mu_0}\left(\frac{1}{\rho}jE_0\sin\theta_0 e^{jk_0z\cos\theta_0}\sum_{n=-\infty}^{+\infty} nj^{-n}c_nH_n^{(2)}(k_0\rho\sin\theta_0)e^{jn(\phi-\phi_0)}\right.$$
$$\left.-jk_0\cos\theta_0E_\phi^s\right) \tag{B.35}$$

$$H_\rho^s = -\frac{E_0\sin\theta_0}{\omega\mu_0\rho}e^{jk_0z\cos\theta_0}\sum_{n=-\infty}^{+\infty} nj^{-n}c_nH_n^{(2)}(k_0\rho\sin\theta_0)e^{jn(\phi-\phi_0)} + \frac{k_0\cos\theta_0}{\omega\mu_0}E_\phi^s \tag{B.36}$$

Substituting (B.36) in (B.33) gives

$$E_\phi^s = \frac{k_0\cos\theta_0}{\omega\varepsilon_0}\left(-\frac{E_0\sin\theta_0}{\omega\mu_0\rho}e^{jk_0z\cos\theta_0}\sum_{n=-\infty}^{+\infty} nj^{-n}c_nH_n^{(2)}(k_0\rho\sin\theta_0)e^{jn(\phi-\phi_0)} + \frac{k_0\cos\theta_0}{\omega\mu_0}E_\phi^s\right) - \frac{E_0k_0\sin^2\theta_0}{j\omega\varepsilon_0}e^{jk_0z\cos\theta_0}\sum_{n=-\infty}^{+\infty} j^{-n}\widetilde{c}_nH_n^{(2)'}(k_0\rho\sin\theta_0)e^{jn(\phi-\phi_0)} \tag{B.37}$$

$$E_\phi^s = -\frac{E_0k_0\sin\theta_0\cos\theta_0}{\omega^2\mu_0\varepsilon_0\rho}e^{jk_0z\cos\theta_0}\sum_{n=-\infty}^{+\infty} nj^{-n}c_nH_n^{(2)}(k_0\rho\sin\theta_0)e^{jn(\phi-\phi_0)} + \frac{k_0^2\cos^2\theta_0}{\omega^2\mu_0\varepsilon_0}E_\phi^s - \frac{E_0k_0\sin^2\theta_0}{j\omega\varepsilon_0}e^{jk_0z\cos\theta_0}\sum_{n=-\infty}^{+\infty} j^{-n}\widetilde{c}_nH_n^{(2)'}(k_0\rho\sin\theta_0)e^{jn(\phi-\phi_0)} \tag{B.38}$$

$$E_\phi^s = -\frac{E_0\cos\theta_0}{k_0\rho\sin\theta_0}e^{jk_0z\cos\theta_0}\sum_{n=-\infty}^{+\infty} nj^{-n}c_nH_n^{(2)}(k_0\rho\sin\theta_0)e^{jn(\phi-\phi_0)} - \frac{E_0k_0}{j\omega\varepsilon_0}e^{jk_0z\cos\theta_0}\sum_{n=-\infty}^{+\infty} j^{-n}\widetilde{c}_nH_n^{(2)'}(k_0\rho\sin\theta_0)e^{jn(\phi-\phi_0)} \tag{B.39}$$

$$E_\phi^s = -\frac{E_0\cos\theta_0}{k_0\rho\sin\theta_0}e^{jk_0z\cos\theta_0}\sum_{n=-\infty}^{+\infty} nj^{-n}c_nH_n^{(2)}(k_0\rho\sin\theta_0)e^{jn(\phi-\phi_0)} + jE_0\eta_0e^{jk_0z\cos\theta_0}\sum_{n=-\infty}^{+\infty} j^{-n}\widetilde{c}_nH_n^{(2)'}(k_0\rho\sin\theta_0)e^{jn(\phi-\phi_0)} \tag{B.40}$$

$\underline{H_\phi^s}$:

$$H_\phi^s = -\frac{1}{j\omega\mu_0}\left(\frac{\partial E_\rho^s}{\partial z} - \frac{\partial E_z^s}{\partial\rho}\right) \tag{B.41}$$

$$H_\phi^s = -\frac{1}{j\omega\mu_0}\left(jk_0\cos\theta_0E_\rho^s - E_0k_0\sin^2\theta_0e^{jk_0z\cos\theta_0}\sum_{n=-\infty}^{+\infty} j^{-n}c_nH_n^{(2)'}(k_0\rho\sin\theta_0)e^{jn(\phi-\phi_0)}\right) \tag{B.42}$$

$$H_\phi^s = -\frac{k_0\cos\theta_0}{\omega\mu_0}E_\rho^s + \frac{E_0k_0\sin^2\theta_0}{j\omega\mu_0}e^{jk_0z\cos\theta_0}\sum_{n=-\infty}^{+\infty} j^{-n}c_nH_n^{(2)'}(k_0\rho\sin\theta_0)e^{jn(\phi-\phi_0)} \tag{B.43}$$

$$E_\rho^s = \frac{1}{j\omega\varepsilon_0}\left(\frac{1}{\rho}\frac{\partial H_z^s}{\partial \phi} - \frac{\partial H_\phi^s}{\partial z}\right) \tag{B.44}$$

$$E_\rho^s = \frac{1}{j\omega\varepsilon_0}\left(\frac{1}{\rho} jE_0 \sin\theta_0 e^{jk_0 z\cos\theta_0} \sum_{n=-\infty}^{+\infty} nj^{-n}\widetilde{c}_n H_n^{(2)}(k_0\rho\sin\theta_0)e^{jn(\phi-\phi_0)} - jk_0\cos\theta_0 H_\phi^s\right) \tag{B.45}$$

$$E_\rho^s = \frac{E_0\sin\theta_0}{\omega\varepsilon_0\rho} e^{jk_0 z\cos\theta_0} \sum_{n=-\infty}^{+\infty} nj^{-n}\widetilde{c}_n H_n^{(2)}(k_0\rho\sin\theta_0)e^{jn(\phi-\phi_0)} - \frac{k_0\cos\theta_0}{\omega\varepsilon_0} H_\phi^s \tag{B.46}$$

Substituting (B.46) in (B.43) gives

$$H_\phi^s = -\frac{k_0\cos\theta_0}{\omega\mu_0}\left(\frac{E_0\sin\theta_0}{\omega\varepsilon_0\rho} e^{jk_0 z\cos\theta_0} \sum_{n=-\infty}^{+\infty} nj^{-n}\widetilde{c}_n H_n^{(2)}(k_0\rho\sin\theta_0)e^{jn(\phi-\phi_0)} - \frac{k_0\cos\theta_0}{\omega\varepsilon_0} H_\phi^s\right) + \frac{E_0 k_0\sin^2\theta_0}{j\omega\mu_0} e^{jk_0 z\cos\theta_0} \sum_{n=-\infty}^{+\infty} j^{-n} c_n H_n^{(2)'}(k_0\rho\sin\theta_0)e^{jn(\phi-\phi_0)} \tag{B.47}$$

$$H_\phi^s = -\frac{E_0 k_0\sin\theta_0\cos\theta_0}{\omega^2\mu_0\varepsilon_0\rho} e^{jk_0 z\cos\theta_0} \sum_{n=-\infty}^{+\infty} nj^{-n}\widetilde{c}_n H_n^{(2)}(k_0\rho\sin\theta_0)e^{jn(\phi-\phi_0)} + \frac{k_0^2\cos^2\theta_0}{\omega^2\mu_0\varepsilon_0} H_\phi^s + \frac{E_0 k_0\sin^2\theta_0}{j\omega\mu_0} e^{jk_0 z\cos\theta_0} \sum_{n=-\infty}^{+\infty} j^{-n} c_n H_n^{(2)'}(k_0\rho\sin\theta_0)e^{jn(\phi-\phi_0)} \tag{B.48}$$

$$H_\phi^s = -\frac{E_0\cos\theta_0}{k_0\rho\sin\theta_0} e^{jk_0 z\cos\theta_0} \sum_{n=-\infty}^{+\infty} nj^{-n}\widetilde{c}_n H_n^{(2)}(k_0\rho\sin\theta_0)e^{jn(\phi-\phi_0)} + \frac{E_0 k_0}{j\omega\mu_0} e^{jk_0 z\cos\theta_0} \sum_{n=-\infty}^{+\infty} j^{-n} c_n H_n^{(2)'}(k_0\rho\sin\theta_0)e^{jn(\phi-\phi_0)} \tag{B.49}$$

$$H_\phi^s = -\frac{E_0\cos\theta_0}{k_0\rho\sin\theta_0} e^{jk_0 z\cos\theta_0} \sum_{n=-\infty}^{+\infty} nj^{-n}\widetilde{c}_n H_n^{(2)}(k_0\rho\sin\theta_0)e^{jn(\phi-\phi_0)} - j\frac{E_0}{\eta_0} e^{jk_0 z\cos\theta_0} \sum_{n=-\infty}^{+\infty} j^{-n} c_n H_n^{(2)'}(k_0\rho\sin\theta_0)e^{jn(\phi-\phi_0)} \tag{B.50}$$

$\underline{E_\phi^t}$:

$$E_\phi^t = \frac{1}{j\omega\varepsilon}\left(\frac{\partial H_\rho^t}{\partial z} - \frac{\partial H_z^t}{\partial \rho}\right) \tag{B.51}$$

$$E_\phi^t = \frac{1}{j\omega\varepsilon}\left(jk_0\cos\theta_0 H_\rho^t - E_0 k\sin\theta_0\sin\theta_1 e^{jk_0 z\cos\theta_0}\sum_{n=-\infty}^{+\infty} j^{-n}\widetilde{a}_n J_n'(k\rho\sin\theta_1)e^{jn(\phi-\phi_0)}\right) \tag{B.52}$$

$$E_\phi^t = \frac{k_0\cos\theta_0}{\omega\varepsilon}H_\rho^t - \frac{E_0 k\sin\theta_0\sin\theta_1}{j\omega\varepsilon}e^{jk_0 z\cos\theta_0}\sum_{n=-\infty}^{+\infty} j^{-n}\widetilde{a}_n J_n'(k\rho\sin\theta_1)e^{jn(\phi-\phi_0)} \tag{B.53}$$

$$H_\rho^t = -\frac{1}{j\omega\mu}\left(\frac{1}{\rho}\frac{\partial E_z^t}{\partial\phi} - \frac{\partial E_\phi^t}{\partial z}\right) \tag{B.54}$$

$$H_\rho^t = -\frac{1}{j\omega\mu}\left(\frac{1}{\rho}jE_0\sin\theta_0 e^{jk_0 z\cos\theta_0}\sum_{n=-\infty}^{+\infty} nj^{-n}a_n J_n(k\rho\sin\theta_1)e^{jn(\phi-\phi_0)} - jk_0\cos\theta_0 E_\phi^t\right) \tag{B.55}$$

$$H_\rho^t = -\frac{E_0\sin\theta_0}{\omega\mu\rho}e^{jk_0 z\cos\theta_0}\sum_{n=-\infty}^{+\infty} nj^{-n}a_n J_n(k\rho\sin\theta_1)e^{jn(\phi-\phi_0)} + \frac{k_0\cos\theta_0}{\omega\mu}E_\phi^t \tag{B.56}$$

Substituting (B.56) in (B.53) gives

$$\begin{aligned}E_\phi^t = &\frac{k_0\cos\theta_0}{\omega\varepsilon}\left(-\frac{E_0\sin\theta_0}{\omega\mu\rho}e^{jk_0 z\cos\theta_0}\sum_{n=-\infty}^{+\infty} nj^{-n}a_n J_n(k\rho\sin\theta_1)e^{jn(\phi-\phi_0)}\right.\\ &\left.+\frac{k_0\cos\theta_0}{\omega\mu}E_\phi^t\right)\\ &-\frac{E_0 k\sin\theta_0\sin\theta_1}{j\omega\varepsilon}e^{jk_0 z\cos\theta_0}\sum_{n=-\infty}^{+\infty} j^{-n}\widetilde{a}_n J_n'(k\rho\sin\theta_1)e^{jn(\phi-\phi_0)}\end{aligned} \tag{B.57}$$

$$\begin{aligned}E_\phi^t = &-\frac{E_0 k_0\sin\theta_0\cos\theta_0}{\omega^2\mu\varepsilon\rho}e^{jk_0 z\cos\theta_0}\sum_{n=-\infty}^{+\infty} nj^{-n}a_n J_n(k\rho\sin\theta_1)e^{jn(\phi-\phi_0)} + \frac{k_0^2\cos^2\theta_0}{\omega^2\mu\varepsilon}E_\phi^t\\ &-\frac{E_0 k\sin\theta_0\sin\theta_1}{j\omega\varepsilon}e^{jk_0 z\cos\theta_0}\sum_{n=-\infty}^{+\infty} j^{-n}\widetilde{a}_n J_n'(k\rho\sin\theta_1)e^{jn(\phi-\phi_0)}\end{aligned} \tag{B.58}$$

Since

$$\frac{k_0^2\cos^2\theta_0}{\omega^2\mu\varepsilon} = \frac{k_0^2\cos^2\theta_0}{k^2} = \cos^2\theta_1 \tag{B.59}$$

$$\begin{aligned}E_\phi^t = &-\frac{E_0 k_0\sin\theta_0\cos\theta_0}{k^2\rho\sin^2\theta_1}e^{jk_0 z\cos\theta_0}\sum_{n=-\infty}^{+\infty} nj^{-n}a_n J_n(k\rho\sin\theta_1)e^{jn(\phi-\phi_0)}\\ &-\frac{E_0 k\sin\theta_0}{j\omega\varepsilon\sin\theta_1}e^{jk_0 z\cos\theta_0}\sum_{n=-\infty}^{+\infty} j^{-n}\widetilde{a}_n J_n'(k\rho\sin\theta_1)e^{jn(\phi-\phi_0)}\end{aligned} \tag{B.60}$$

$$E_\phi^t = -\frac{E_0 k_0 \sin\theta_0 \cos\theta_0}{k^2 \rho \sin^2\theta_1} e^{jk_0 z\cos\theta_0} \sum_{n=-\infty}^{+\infty} n j^{-n} a_n J_n(k\rho\sin\theta_1) e^{jn(\phi-\phi_0)}$$
$$+ jE_0\eta \frac{\sin\theta_0}{\sin\theta_1} e^{jk_0 z\cos\theta_0} \sum_{n=-\infty}^{+\infty} j^{-n} \widetilde{a}_n J_n'(k\rho\sin\theta_1) e^{jn(\phi-\phi_0)} \tag{B.61}$$

$\underline{H_\phi^t}$:

$$H_\phi^t = -\frac{1}{j\omega\mu}\left(\frac{\partial E_\rho^t}{\partial z} - \frac{\partial E_z^t}{\partial \rho}\right) \tag{B.62}$$

$$H_\phi^t = -\frac{1}{j\omega\mu}\left(jk_0\cos\theta_0 E_\rho^t \right. \tag{B.63}$$
$$\left. - E_0 k \sin\theta_0 \sin\theta_1 e^{jk_0 z\cos\theta_0} \sum_{n=-\infty}^{+\infty} j^{-n} a_n J_n'(k\rho\sin\theta_1) e^{jn(\phi-\phi_0)}\right)$$

$$H_\phi^t = -\frac{k_0\cos\theta_0}{\omega\mu} E_\rho^t + \frac{E_0 k\sin\theta_0\sin\theta_1}{j\omega\mu} e^{jk_0 z\cos\theta_0} \sum_{n=-\infty}^{+\infty} j^{-n} a_n J_n'(k\rho\sin\theta_1) e^{jn(\phi-\phi_0)} \tag{B.64}$$

$$E_\rho^t = \frac{1}{j\omega\varepsilon}\left(\frac{1}{\rho}\frac{\partial H_z^t}{\partial\phi} - \frac{\partial H_\phi^t}{\partial z}\right) \tag{B.65}$$

$$E_\rho^t = \frac{1}{j\omega\varepsilon}\left(\frac{1}{\rho} jE_0\sin\theta_0 e^{jk_0 z\cos\theta_0} \sum_{n=-\infty}^{+\infty} n j^{-n}\widetilde{a}_n J_n(k\rho\sin\theta_1) e^{jn(\phi-\phi_0)} - jk_0\cos\theta_0 H_\phi^t\right) \tag{B.66}$$

$$E_\rho^t = \frac{E_0\sin\theta_0}{\omega\varepsilon\rho} e^{jk_0 z\cos\theta_0} \sum_{n=-\infty}^{+\infty} n j^{-n}\widetilde{a}_n J_n(k\rho\sin\theta_1) e^{jn(\phi-\phi_0)} - \frac{k_0\cos\theta_0}{\omega\varepsilon} H_\phi^t \tag{B.67}$$

Substituting (B.67) in (B.64) gives

$$H_\phi^t = -\frac{k_0\cos\theta_0}{\omega\mu}\left(\frac{E_0\sin\theta_0}{\omega\varepsilon\rho} e^{jk_0 z\cos\theta_0} \sum_{n=-\infty}^{+\infty} n j^{-n}\widetilde{a}_n J_n(k\rho\sin\theta_1) e^{jn(\phi-\phi_0)} \right.$$
$$\left. - \frac{k_0\cos\theta_0}{\omega\varepsilon} H_\phi^t\right)$$
$$+ \frac{E_0 k\sin\theta_0\sin\theta_1}{j\omega\mu} e^{jk_0 z\cos\theta_0} \sum_{n=-\infty}^{+\infty} j^{-n} a_n J_n'(k\rho\sin\theta_1) e^{jn(\phi-\phi_0)} \tag{B.68}$$

$$H_\phi^t = -\frac{E_0 k_0 \sin\theta_0\cos\theta_0}{\omega^2\mu\varepsilon\rho} e^{jk_0 z\cos\theta_0} \sum_{n=-\infty}^{+\infty} n j^{-n}\widetilde{a}_n J_n(k\rho\sin\theta_1) e^{jn(\phi-\phi_0)} \tag{B.69}$$
$$+ \frac{k_0^2\cos^2\theta_0}{\omega^2\mu\varepsilon} H_\phi^t + \frac{E_0 k\sin\theta_0\sin\theta_1}{j\omega\mu} e^{jk_0 z\cos\theta_0} \sum_{n=-\infty}^{+\infty} j^{-n} a_n J_n'(k\rho\sin\theta_1) e^{jn(\phi-\phi_0)}$$

Since

$$\frac{k_0^2\cos^2\theta_0}{\omega^2\mu\varepsilon}=\frac{k_0^2\cos^2\theta_0}{k^2}=\cos^2\theta_1 \tag{B.70}$$

$$\begin{aligned}H_\phi^t=&-\frac{E_0k_0\sin\theta_0\cos\theta_0}{k^2\rho\sin^2\theta_1}e^{jk_0z\cos\theta_0}\sum_{n=-\infty}^{+\infty}nj^{-n}\widetilde{a}_nJ_n(k\rho\sin\theta_1)e^{jn(\phi-\phi_0)}\\&+\frac{E_0k\sin\theta_0}{j\omega\mu\sin\theta_1}e^{jk_0z\cos\theta_0}\sum_{n=-\infty}^{+\infty}j^{-n}a_nJ_n'(k\rho\sin\theta_1)e^{jn(\phi-\phi_0)}\end{aligned} \tag{B.71}$$

$$\begin{aligned}H_\phi^t=&-\frac{E_0k_0\sin\theta_0\cos\theta_0}{k^2\rho\sin^2\theta_1}e^{jk_0z\cos\theta_0}\sum_{n=-\infty}^{+\infty}nj^{-n}\widetilde{a}_nJ_n(k\rho\sin\theta_1)e^{jn(\phi-\phi_0)}\\&-j\frac{E_0}{\eta}\frac{\sin\theta_0}{\sin\theta_1}e^{jk_0z\cos\theta_0}\sum_{n=-\infty}^{+\infty}j^{-n}a_nJ_n'(k\rho\sin\theta_1)e^{jn(\phi-\phi_0)}\end{aligned} \tag{B.72}$$

APPENDIX C

Derivation of the Transparency Condition

For achieving transparency with metamaterial coated conducting cylinders at normal incidence and TE^z polarization, numerator of the scattering coefficients, c_n, given in (2.240) should be zero:

$$\begin{aligned} \text{num}\{c_n\} &= \zeta J_n(k_0 b)\left[J_n'(k_c a)Y_n'(k_c b) - J_n'(k_c b)Y_n'(k_c a)\right] \\ &\quad - J_n'(k_0 b)\left[J_n'(k_c a)Y_n(k_c b) - J_n(k_c b)Y_n'(k_c a)\right] \\ &= 0. \end{aligned} \tag{C.1}$$

Let T_1 and T_2 be the the two terms of the numerator of c_n:

$$T_1 = \zeta J_n(k_0 b)\left[J_n'(k_c a)Y_n'(k_c b) - J_n'(k_c b)Y_n'(k_c a)\right], \tag{C.2}$$

$$T_2 = -J_n'(k_0 b)\left[J_n'(k_c a)Y_n(k_c b) - J_n(k_c b)Y_n'(k_c a)\right], \tag{C.3}$$

such that $T_1 + T_2 = 0$.

Using the small argument approximations and the recurrence relation,

$$T_1 = \zeta \frac{1}{n!}\left(\frac{k_0 b}{2}\right)^n \left[\left(\frac{\frac{1}{(n-1)!}\left(\frac{k_c a}{2}\right)^{n-1} - \frac{1}{(n+1)!}\left(\frac{k_c a}{2}\right)^{n+1}}{2}\right)\right. \tag{C.4}$$

$$\times \left(\frac{-\frac{(n-2)!}{\pi}\left(\frac{2}{k_c b}\right)^{n-1} + \frac{n!}{\pi}\left(\frac{2}{k_c b}\right)^{n+1}}{2} \right)$$
$$- \left(\frac{\frac{1}{(n-1)!}\left(\frac{k_c b}{2}\right)^{n-1} - \frac{1}{(n+1)!}\left(\frac{k_c b}{2}\right)^{n+1}}{2} \right)$$
$$\times \left(\frac{-\frac{(n-2)!}{\pi}\left(\frac{2}{k_c a}\right)^{n-1} + \frac{n!}{\pi}\left(\frac{2}{k_c a}\right)^{n+1}}{2} \right) \Bigg],$$

$$T_2 = - \left(\frac{\frac{1}{(n-1)!}\left(\frac{k_0 b}{2}\right)^{n-1} - \frac{1}{(n+1)!}\left(\frac{k_0 b}{2}\right)^{n+1}}{2} \right) \tag{C.5}$$
$$\times \left[\left(\frac{\frac{1}{(n-1)!}\left(\frac{k_c a}{2}\right)^{n-1} - \frac{1}{(n+1)!}\left(\frac{k_c a}{2}\right)^{n+1}}{2} \right) \left(-\frac{(n-1)!}{\pi}\left(\frac{2}{k_c b}\right)^{n} \right) \right.$$
$$\left. - \left(\frac{1}{n!}\left(\frac{k_c b}{2}\right)^{n} \right) \left(\frac{-\frac{(n-2)!}{\pi}\left(\frac{2}{k_c a}\right)^{n-1} + \frac{n!}{\pi}\left(\frac{2}{k_c a}\right)^{n+1}}{2} \right) \right],$$

$$T_1 = \zeta \frac{1}{n!}\left(\frac{k_0 b}{2}\right)^{n} \frac{1}{4\pi} \tag{C.6}$$
$$\times \left[\left\{ -\frac{1}{(n-1)}\left(\frac{a}{b}\right)^{n-1} + n\left(\frac{a}{b}\right)^{n-1} \frac{4}{(k_c b)^2} \right.\right.$$
$$\left. + \frac{1}{(n+1)n(n-1)}\left(\frac{a}{b}\right)^{n-1} \frac{(k_c a)^2}{4} - \frac{1}{(n+1)}\left(\frac{a}{b}\right)^{n+1} \right\}$$
$$- \left\{ -\frac{1}{(n-1)}\left(\frac{b}{a}\right)^{n-1} + n\left(\frac{b}{a}\right)^{n-1} \frac{4}{(k_c a)^2} \right.$$
$$\left.\left. + \frac{1}{(n+1)n(n-1)}\left(\frac{b}{a}\right)^{n-1} \frac{(k_c b)^2}{4} - \frac{1}{(n+1)}\left(\frac{b}{a}\right)^{n+1} \right\} \right],$$

$$T_2 = -\frac{1}{4\pi}\left(\frac{1}{(n-1)!}\left(\frac{k_0 b}{2}\right)^{n-1} - \frac{1}{(n+1)!}\left(\frac{k_0 b}{2}\right)^{n+1} \right) \tag{C.7}$$
$$\times \left[-\left(\frac{a}{b}\right)^{n-1}\left(\frac{2}{k_c b}\right) + \frac{1}{(n+1)n}\left(\frac{a}{b}\right)^{n}\left(\frac{k_c a}{2}\right) \right.$$
$$\left. + \frac{1}{(n+1)n}\left(\frac{b}{a}\right)^{n-1}\left(\frac{k_c b}{2}\right) - \left(\frac{b}{a}\right)^{n}\left(\frac{2}{k_c a}\right) \right].$$

Since $k_c a \ll 1$ and $k_c b \ll 1$, we can keep only the dominant terms in T_1 and T_2 (i.e., the terms where $k_c a$ and $k_c b$ are in the denominator):

$$T_1 = \zeta \frac{1}{n!} \left(\frac{k_0 b}{2}\right)^n \frac{1}{4\pi} \left[n \left(\frac{a}{b}\right)^{n-1} \frac{4}{(k_c b)^2} - n \left(\frac{b}{a}\right)^{n-1} \frac{4}{(k_c a)^2} \right], \tag{C.8}$$

$$\begin{aligned} T_2 = \frac{1}{4\pi} & \left(\frac{1}{(n-1)!} \left(\frac{k_0 b}{2}\right)^{n-1} - \frac{1}{(n+1)!} \left(\frac{k_0 b}{2}\right)^{n+1} \right) \\ & \times \left[\left(\frac{a}{b}\right)^{n-1} \left(\frac{2}{k_c b}\right) + \left(\frac{b}{a}\right)^n \left(\frac{2}{k_c a}\right) \right]. \end{aligned} \tag{C.9}$$

Writing

$$\frac{1}{(n-1)!} \left(\frac{k_0 b}{2}\right)^{n-1} = \frac{1}{n!} \left(\frac{k_0 b}{2}\right)^n n \left(\frac{2}{k_0 b}\right), \tag{C.10}$$

$$\frac{1}{(n+1)!} \left(\frac{k_0 b}{2}\right)^{n+1} = \frac{1}{n!} \left(\frac{k_0 b}{2}\right)^n \frac{1}{(n+1)} \left(\frac{k_0 b}{2}\right), \tag{C.11}$$

$$\begin{aligned} \left(\frac{1}{(n-1)!} \left(\frac{k_0 b}{2}\right)^{n-1} - \frac{1}{(n+1)!} \left(\frac{k_0 b}{2}\right)^{n+1} \right) & \\ = \frac{1}{n!} \left(\frac{k_0 b}{2}\right)^n & \left[n \left(\frac{2}{k_0 b}\right) - \frac{1}{(n+1)} \left(\frac{k_0 b}{2}\right) \right] \\ \simeq \frac{1}{n!} \left(\frac{k_0 b}{2}\right)^n & n \left(\frac{2}{k_0 b}\right), \end{aligned} \tag{C.12}$$

T_2 becomes

$$T_2 = \frac{1}{n!} \left(\frac{k_0 b}{2}\right)^n \frac{1}{4\pi} \left[n \left(\frac{a}{b}\right)^{n-1} \frac{4}{k_0 k_c b^2} + n \left(\frac{b}{a}\right)^n \frac{4}{k_0 k_c a b} \right], \tag{C.13}$$

$$\begin{aligned} T_1 + T_2 = \frac{1}{n!} & \left(\frac{k_0 b}{2}\right)^n \frac{1}{4\pi} \\ & \times \left[\zeta n \left(\frac{a}{b}\right)^{n-1} \frac{4}{k_c^2 b^2} - \zeta n \left(\frac{b}{a}\right)^{n-1} \frac{4}{k_c^2 a^2} \right. \\ & \left. + n \left(\frac{a}{b}\right)^{n-1} \frac{4}{k_0 k_c b^2} + n \left(\frac{b}{a}\right)^n \frac{4}{k_0 k_c a b} \right] \\ = 0. & \end{aligned} \tag{C.14}$$

Therefore,

$$\zeta\left(\frac{a}{b}\right)^{n-1}\frac{1}{k_c^2b^2}-\zeta\left(\frac{b}{a}\right)^{n-1}\frac{1}{k_c^2a^2}+\left(\frac{a}{b}\right)^{n-1}\frac{1}{k_0k_cb^2}+\left(\frac{b}{a}\right)^{n}\frac{1}{k_0k_cab}=0 \quad \text{(C.15)}$$

Note that,

$$\zeta=\frac{\eta_c}{\eta_0}=\frac{\sqrt{\frac{\mu_c}{\varepsilon_c}}}{\sqrt{\frac{\mu_0}{\varepsilon_0}}}=\sqrt{\frac{\mu_c\varepsilon_0}{\mu_0\varepsilon_c}}, \quad \text{(C.16)}$$

$$k_c=\omega\sqrt{\mu_c\varepsilon_c}, \quad \text{(C.17)}$$

$$k_0=\omega\sqrt{\mu_0\varepsilon_0}. \quad \text{(C.18)}$$

Hence,

$$\begin{aligned}0=&\left(\frac{a}{b}\right)^{n-1}\sqrt{\frac{\mu_c\varepsilon_0}{\mu_0\varepsilon_c}}\frac{1}{\omega^2\mu_c\varepsilon_c}\frac{1}{b^2}-\left(\frac{b}{a}\right)^{n-1}\sqrt{\frac{\mu_c\varepsilon_0}{\mu_0\varepsilon_c}}\frac{1}{\omega^2\mu_c\varepsilon_c}\frac{1}{a^2}\\&+\left(\frac{a}{b}\right)^{n-1}\frac{1}{\omega^2\sqrt{\mu_0\varepsilon_0}\sqrt{\mu_c\varepsilon_c}}\frac{1}{b^2}+\left(\frac{b}{a}\right)^{n}\frac{1}{\omega^2\sqrt{\mu_0\varepsilon_0}\sqrt{\mu_c\varepsilon_c}}\frac{1}{ab},\end{aligned} \quad \text{(C.19)}$$

or dividing each term by $\omega^2\zeta$,

$$\begin{aligned}0=&\left(\frac{a}{b}\right)^{n-1}\frac{1}{\mu_c\varepsilon_c}\frac{1}{b^2}-\left(\frac{b}{a}\right)^{n-1}\frac{1}{\mu_c\varepsilon_c}\frac{1}{a^2}\\&+\left(\frac{a}{b}\right)^{n-1}\sqrt{\frac{\mu_0\varepsilon_c}{\mu_c\varepsilon_0}}\frac{1}{\sqrt{\mu_0\varepsilon_0\mu_c\varepsilon_c}}\frac{1}{b^2}+\left(\frac{b}{a}\right)^{n}\sqrt{\frac{\mu_0\varepsilon_c}{\mu_c\varepsilon_0}}\frac{1}{\sqrt{\mu_0\varepsilon_0\mu_c\varepsilon_c}}\frac{1}{ab},\end{aligned} \quad \text{(C.20)}$$

$$\begin{aligned}0&=\left(\frac{a}{b}\right)^{n-1}\frac{1}{\mu_c\varepsilon_c}\frac{1}{b^2}-\left(\frac{b}{a}\right)^{n-1}\frac{1}{\mu_c\varepsilon_c}\frac{1}{a^2}+\left(\frac{a}{b}\right)^{n-1}\frac{1}{\mu_c\varepsilon_0}\frac{1}{b^2}+\left(\frac{b}{a}\right)^{n}\frac{1}{\mu_c\varepsilon_0}\frac{1}{ab}\\&=\frac{a^n}{b^n}\frac{b}{a}\frac{1}{\mu_c\varepsilon_c}\frac{1}{b^2}-\frac{b^n}{a^n}\frac{a}{b}\frac{1}{\mu_c\varepsilon_c}\frac{1}{a^2}+\frac{a^n}{b^n}\frac{b}{a}\frac{1}{\mu_c\varepsilon_0}\frac{1}{b^2}+\frac{b^n}{a^n}\frac{1}{\mu_c\varepsilon_0}\frac{1}{ab}\\&=\frac{1}{\mu_cab}\left[\frac{a^n}{b^n}\frac{1}{\varepsilon_c}-\frac{b^n}{a^n}\frac{1}{\varepsilon_c}+\frac{a^n}{b^n}\frac{1}{\varepsilon_0}+\frac{b^n}{a^n}\frac{1}{\varepsilon_0}\right].\end{aligned} \quad \text{(C.21)}$$

Denoting $\gamma=a/b$,

$$\frac{\gamma^n}{\varepsilon_c}-\frac{\gamma^{-n}}{\varepsilon_c}+\frac{\gamma^n}{\varepsilon_0}+\frac{\gamma^{-n}}{\varepsilon_0}=0, \quad \text{(C.22)}$$

$$\gamma^n \left(\frac{1}{\varepsilon_c} + \frac{1}{\varepsilon_0} \right) = \gamma^{-n} \left(\frac{1}{\varepsilon_c} - \frac{1}{\varepsilon_0} \right), \tag{C.23}$$

$$\gamma^{2n} = \frac{\frac{1}{\varepsilon_c} - \frac{1}{\varepsilon_0}}{\frac{1}{\varepsilon_c} + \frac{1}{\varepsilon_0}} = \frac{\varepsilon_0 - \varepsilon_c}{\varepsilon_0 + \varepsilon_c}, \tag{C.24}$$

$$\gamma = \sqrt[2n]{\frac{\varepsilon_0 - \varepsilon_c}{\varepsilon_0 + \varepsilon_c}}. \tag{C.25}$$

APPENDIX D

Derivation of the Resonance Condition

For scattering maximization (i.e., resonance) with metamaterial coated conducting cylinders at normal incidence and TE^z polarization, denominator of the scattering coefficients, c_n, given in (2.241) should be zero:

$$\begin{aligned}\text{den}\{c_n\} &= -\zeta H_n^{(2)}(k_0 b)\left[J_n'(k_c a)Y_n'(k_c b) - J_n'(k_c b)Y_n'(k_c a)\right] \\ &\quad + H_n^{(2)'}\left[J_n'(k_c a)Y_n(k_c b) - J_n(k_c b)Y_n'(k_c a)\right] \\ &= 0.\end{aligned} \tag{D.1}$$

Let R_1 and R_2 be the the two terms of the denominator of c_n:

$$R_1 = -\zeta H_n^{(2)}\left[J_n'(k_c a)Y_n'(k_c b) - J_n'(k_c b)Y_n'(k_c a)\right], \tag{D.2}$$

$$R_2 = H_n^{(2)'}\left[J_n'(k_c a)Y_n(k_c b) - J_n(k_c b)Y_n'(k_c a)\right], \tag{D.3}$$

such that $R_1 + R_2 = 0$.

Using the small argument approximations and the recurrence relation,

$$R_1 = -\zeta\left(\frac{1}{n!}\left(\frac{k_0 b}{2}\right)^n + j\frac{(n-1)!}{\pi}\left(\frac{2}{k_0 b}\right)^n\right) \tag{D.4}$$

$$\times \left[\left(\frac{\frac{1}{(n-1)!}\left(\frac{k_c a}{2}\right)^{n-1} - \frac{1}{(n+1)!}\left(\frac{k_c a}{2}\right)^{n+1}}{2} \right) \left(\frac{-\frac{(n-2)!}{\pi}\left(\frac{2}{k_c b}\right)^{n-1} + \frac{n!}{\pi}\left(\frac{2}{k_c b}\right)^{n+1}}{2} \right) \right.$$
$$\left. - \left(\frac{\frac{1}{(n-1)!}\left(\frac{k_c b}{2}\right)^{n-1} - \frac{1}{(n+1)!}\left(\frac{k_c b}{2}\right)^{n+1}}{2} \right) \left(\frac{-\frac{(n-2)!}{\pi}\left(\frac{2}{k_c a}\right)^{n-1} + \frac{n!}{\pi}\left(\frac{2}{k_c a}\right)^{n+1}}{2} \right) \right],$$

$$R_2 = \left(\frac{\frac{1}{(n-1)!}\left(\frac{k_0 b}{2}\right)^{n-1} - \frac{1}{(n+1)!}\left(\frac{k_0 b}{2}\right)^{n+1}}{2} - j\frac{-\frac{(n-2)!}{\pi}\left(\frac{2}{k_0 b}\right)^{n-1} + \frac{n!}{\pi}\left(\frac{2}{k_0 b}\right)^{n+1}}{2} \right)$$
$$\times \left[\left(\frac{\frac{1}{(n-1)!}\left(\frac{k_c a}{2}\right)^{n-1} - \frac{1}{(n+1)!}\left(\frac{k_c a}{2}\right)^{n+1}}{2} \right) \left(-\frac{(n-1)!}{\pi}\left(\frac{2}{k_c b}\right)^{n} \right) \right.$$
$$\left. - \left(\frac{1}{n!}\left(\frac{k_c b}{2}\right)^{n} \right) \left(\frac{-\frac{(n-2)!}{\pi}\left(\frac{2}{k_c a}\right)^{n-1} + \frac{n!}{\pi}\left(\frac{2}{k_c a}\right)^{n+1}}{2} \right) \right], \tag{D.5}$$

$$R_1 = -\zeta \left(\frac{1}{n!}\left(\frac{k_0 b}{2}\right)^{n} + j\frac{(n-1)!}{\pi}\left(\frac{2}{k_0 b}\right)^{n} \right) \frac{1}{4\pi} \tag{D.6}$$
$$\times \left[\left\{ -\frac{1}{(n-1)}\left(\frac{a}{b}\right)^{n-1} + n\left(\frac{a}{b}\right)^{n-1} \frac{4}{(k_c b)^2} \right.\right.$$
$$\left. + \frac{1}{(n+1)n(n-1)}\left(\frac{a}{b}\right)^{n-1} \frac{(k_c a)^2}{4} - \frac{1}{(n+1)}\left(\frac{a}{b}\right)^{n+1} \right\}$$
$$- \left\{ -\frac{1}{(n-1)}\left(\frac{b}{a}\right)^{n-1} + n\left(\frac{b}{a}\right)^{n-1} \frac{4}{(k_c a)^2} \right.$$
$$\left.\left. + \frac{1}{(n+1)n(n-1)}\left(\frac{b}{a}\right)^{n-1} \frac{(k_c b)^2}{4} - \frac{1}{(n+1)}\left(\frac{b}{a}\right)^{n+1} \right\} \right],$$

$$R_2 = \frac{1}{2\pi} \left(\frac{\frac{1}{(n-1)!}\left(\frac{k_0 b}{2}\right)^{n-1} - \frac{1}{(n+1)!}\left(\frac{k_0 b}{2}\right)^{n+1}}{2} - j\frac{-\frac{(n-2)!}{\pi}\left(\frac{2}{k_0 b}\right)^{n-1} + \frac{n!}{\pi}\left(\frac{2}{k_0 b}\right)^{n+1}}{2} \right)$$
$$\times \left[-\left(\frac{a}{b}\right)^{n-1}\left(\frac{2}{k_c b}\right) + \frac{1}{(n+1)n}\left(\frac{a}{b}\right)^{n}\left(\frac{k_c a}{2}\right) \right.$$
$$\left. + \frac{1}{(n+1)n}\left(\frac{b}{a}\right)^{n-1}\left(\frac{k_c b}{2}\right) - \left(\frac{b}{a}\right)^{n}\left(\frac{2}{k_c a}\right) \right]. \tag{D.7}$$

Since $k_c a \ll 1$ and $k_c b \ll 1$, we can keep only the dominant terms in R_1 and R_2 (i.e., the terms where $k_c a$ and $k_c b$ are in the denominator):

$$R_1 = -j\zeta \frac{(n-1)!}{\pi} \left(\frac{2}{k_0 b}\right)^n \frac{1}{4\pi} \left[n \left(\frac{a}{b}\right)^{n-1} \frac{4}{(k_c b)^2} - n \left(\frac{b}{a}\right)^{n-1} \frac{4}{(k_c a)^2} \right], \quad \text{(D.8)}$$

$$\begin{aligned} R_2 = j \frac{1}{4\pi} & \left(-\frac{(n-2)!}{\pi} \left(\frac{2}{k_0 b}\right)^{n-1} + \frac{n!}{\pi} \left(\frac{2}{k_0 b}\right)^{n+1} \right) \\ & \times \left[\left(\frac{a}{b}\right)^{n-1} \left(\frac{2}{k_c b}\right) + \left(\frac{b}{a}\right)^n \left(\frac{2}{k_c a}\right) \right]. \end{aligned} \quad \text{(D.9)}$$

Writing

$$-\frac{(n-2)!}{\pi} \left(\frac{2}{k_0 b}\right)^{n-1} = -\frac{(n-1)!}{\pi} \left(\frac{2}{k_0 b}\right)^n \frac{1}{(n-1)} \left(\frac{k_0 b}{2}\right), \quad \text{(D.10)}$$

$$\frac{n!}{\pi} \left(\frac{2}{k_0 b}\right)^{n+1} = -\frac{(n-1)!}{\pi} \left(\frac{2}{k_0 b}\right)^n (-n) \left(\frac{2}{k_0 b}\right), \quad \text{(D.11)}$$

$$\begin{aligned} & \left(-\frac{(n-2)!}{\pi} \left(\frac{2}{k_0 b}\right)^{n-1} + \frac{n!}{\pi} \left(\frac{2}{k_0 b}\right)^{n+1} \right) \\ & \qquad = -\frac{(n-1)!}{\pi} \left(\frac{2}{k_0 b}\right)^n \left[\frac{1}{(n-1)} \left(\frac{k_0 b}{2}\right) - n \left(\frac{2}{k_0 b}\right) \right] \\ & \qquad \simeq \frac{(n-1)!}{\pi} \left(\frac{2}{k_0 b}\right)^n n \left(\frac{2}{k_0 b}\right), \end{aligned} \quad \text{(D.12)}$$

R_2 becomes

$$R_2 = j \frac{1}{4\pi} \frac{(n-1)!}{\pi} \left(\frac{2}{k_0 b}\right)^n n \left(\frac{2}{k_0 b}\right) \left[\left(\frac{a}{b}\right)^{n-1} \left(\frac{2}{k_c b}\right) + \left(\frac{b}{a}\right)^n \left(\frac{2}{k_c a}\right) \right], \quad \text{(D.13)}$$

$$\begin{aligned} R_1 + R_2 = -j \frac{1}{4\pi} \frac{n!}{\pi} & \left(\frac{2}{k_0 b}\right)^n \\ & \times \left[\zeta \left(\frac{a}{b}\right)^{n-1} \frac{4}{(k_c b)^2} - \zeta \left(\frac{b}{a}\right)^{n-1} \frac{4}{(k_c a)^2} \right. \\ & \quad \left. - \left(\frac{2}{k_0 b}\right) \left(\frac{a}{b}\right)^{n-1} \left(\frac{2}{k_c b}\right) - \left(\frac{2}{k_0 b}\right) \left(\frac{b}{a}\right)^n \left(\frac{2}{k_c a}\right) \right] \\ = 0. & \end{aligned} \quad \text{(D.14)}$$

Therefore,

$$\zeta\left(\frac{a}{b}\right)^{n-1}\frac{1}{k_c^2b^2}-\zeta\left(\frac{b}{a}\right)^{n-1}\frac{1}{k_c^2a^2}-\left(\frac{a}{b}\right)^{n-1}\frac{1}{k_0k_cb^2}-\left(\frac{b}{a}\right)^{n}\frac{1}{k_0k_cab}=0 \quad \text{(D.15)}$$

Note that,

$$\zeta=\frac{\eta_c}{\eta_0}=\frac{\sqrt{\frac{\mu_c}{\varepsilon_c}}}{\sqrt{\frac{\mu_0}{\varepsilon_0}}}=\sqrt{\frac{\mu_c\varepsilon_0}{\mu_0\varepsilon_c}}, \quad \text{(D.16)}$$

$$k_c=\omega\sqrt{\mu_c\varepsilon_c}, \quad \text{(D.17)}$$

$$k_0=\omega\sqrt{\mu_0\varepsilon_0}. \quad \text{(D.18)}$$

Hence,

$$\begin{aligned}0=&\left(\frac{a}{b}\right)^{n-1}\sqrt{\frac{\mu_c\varepsilon_0}{\mu_0\varepsilon_c}}\frac{1}{\omega^2\mu_c\varepsilon_c}\frac{1}{b^2}-\left(\frac{b}{a}\right)^{n-1}\sqrt{\frac{\mu_c\varepsilon_0}{\mu_0\varepsilon_c}}\frac{1}{\omega^2\mu_c\varepsilon_c}\frac{1}{a^2}\\&-\left(\frac{a}{b}\right)^{n-1}\frac{1}{\omega^2\sqrt{\mu_0\varepsilon_0}\sqrt{\mu_c\varepsilon_c}}\frac{1}{b^2}-\left(\frac{b}{a}\right)^{n}\frac{1}{\omega^2\sqrt{\mu_0\varepsilon_0}\sqrt{\mu_c\varepsilon_c}}\frac{1}{ab},\end{aligned} \quad \text{(D.19)}$$

or dividing each term by $\omega^2\zeta$,

$$\begin{aligned}0=&\left(\frac{a}{b}\right)^{n-1}\frac{1}{\mu_c\varepsilon_c}\frac{1}{b^2}-\left(\frac{b}{a}\right)^{n-1}\frac{1}{\mu_c\varepsilon_c}\frac{1}{a^2}\\&-\left(\frac{a}{b}\right)^{n-1}\sqrt{\frac{\mu_0\varepsilon_c}{\mu_c\varepsilon_0}}\frac{1}{\sqrt{\mu_0\varepsilon_0\mu_c\varepsilon_c}}\frac{1}{b^2}-\left(\frac{b}{a}\right)^{n}\sqrt{\frac{\mu_0\varepsilon_c}{\mu_c\varepsilon_0}}\frac{1}{\sqrt{\mu_0\varepsilon_0\mu_c\varepsilon_c}}\frac{1}{ab},\end{aligned} \quad \text{(D.20)}$$

$$\begin{aligned}0&=\left(\frac{a}{b}\right)^{n-1}\frac{1}{\mu_c\varepsilon_c}\frac{1}{b^2}-\left(\frac{b}{a}\right)^{n-1}\frac{1}{\mu_c\varepsilon_c}\frac{1}{a^2}-\left(\frac{a}{b}\right)^{n-1}\frac{1}{\mu_c\varepsilon_0}\frac{1}{b^2}-\left(\frac{b}{a}\right)^{n}\frac{1}{\mu_c\varepsilon_0}\frac{1}{ab}\\&=\frac{a^n}{b^n}\frac{b}{a}\frac{1}{\mu_c\varepsilon_c}\frac{1}{b^2}-\frac{b^n}{a^n}\frac{a}{b}\frac{1}{\mu_c\varepsilon_c}\frac{1}{a^2}-\frac{a^n}{b^n}\frac{b}{a}\frac{1}{\mu_c\varepsilon_0}\frac{1}{b^2}-\frac{b^n}{a^n}\frac{1}{\mu_c\varepsilon_0}\frac{1}{ab}\\&=\frac{1}{\mu_cab}\left[\frac{a^n}{b^n}\frac{1}{\varepsilon_c}-\frac{b^n}{a^n}\frac{1}{\varepsilon_c}-\frac{a^n}{b^n}\frac{1}{\varepsilon_0}-\frac{b^n}{a^n}\frac{1}{\varepsilon_0}\right].\end{aligned} \quad \text{(D.21)}$$

Denoting $\gamma=a/b$,

$$\frac{\gamma^n}{\varepsilon_c}-\frac{\gamma^{-n}}{\varepsilon_c}-\frac{\gamma^n}{\varepsilon_0}-\frac{\gamma^{-n}}{\varepsilon_0}=0, \quad \text{(D.22)}$$

$$\gamma^n \left(\frac{1}{\varepsilon_c} - \frac{1}{\varepsilon_0} \right) = \gamma^{-n} \left(\frac{1}{\varepsilon_c} + \frac{1}{\varepsilon_0} \right), \tag{D.23}$$

$$\gamma^{2n} = \frac{\frac{1}{\varepsilon_c} + \frac{1}{\varepsilon_0}}{\frac{1}{\varepsilon_c} - \frac{1}{\varepsilon_0}} = \frac{\varepsilon_0 + \varepsilon_c}{\varepsilon_0 - \varepsilon_c}, \tag{D.24}$$

$$\gamma = \sqrt[2n]{\frac{\varepsilon_0 + \varepsilon_c}{\varepsilon_0 - \varepsilon_c}}. \tag{D.25}$$

Bibliography

[1] C. Li and Z. Shen, "Electromagnetic scattering by a conducting cylinder coated with metamaterials," *Progress In Electromagnetics Research*, vol. 42, pp. 91–105, 2003.

[2] X. Zhou and G. Hu, "Design for electromagnetic wave transparency with metamaterials," *Phys. Rev. E*, vol. 74, pp. 026607/1–8, Aug. 2006.

[3] J. B. Pendry, D. Schurig, and D. R. Smith, "Controlling electromagnetic fields," *Science*, vol. 312, pp. 1780–1782, June 2006.

[4] S. A. Cummer, B. I. Popa, D. Schurig, D. R. Smith, and J. Pendry, "Full-wave simulations of electromagnetic cloaking structures," *Phys. Rev. E*, vol. 74, pp. 036621/1–5, Sep. 2006.

[5] A. Alù and N. Engheta, "Achieving transparency with plasmonic and metamaterial coatings," *Phys. Rev. E*, vol. 72, pp. 016623/1–9, July 2005.

[6] A. Alù and N. Engheta, "Plasmonic materials in transparency and cloaking problems: mechanism, robustness, and physical insights," *Optics Express*, vol. 15, pp. 3318–3332, March 2007.

[7] A. Alù and N. Engheta, "Pairing an epsilon-negative slab with a mu-negative slab: Resonance, tunneling and transparency," *IEEE Trans. Antennas Propagat.*, vol. 51, pp. 2558–2571, Oct. 2003.

[8] A. Alù and N. Engheta, "Resonances in sub-wavelength cylindrical structures made of pairs of double-negative and double-positive or epsilon-negative and mu-negative coaxial shells," in *Proc. Int. Conf. on Electromagnetics in Advanced Applications*, (Torino, Italy), pp. 435–438, Sep. 8-12 2003.

[9] A. Alù and N. Engheta, "Sub-wavelength resonant structures containing double-negative (DNG) or single-negative (SNG) media: Planar, cylindrical and spherical cavities, waveguides, and open scatterers," in *Progress in Electromagnetic Research Symp.*, (Waikiki, HI), p. 12, Oct. 13-16 2003.

[10] A. Alù and N. Engheta, "Peculiar radar cross section properties of double-negative and single-negative metamaterials," in *Proc. of the 2004 IEEE Radar Conf.*, (Philadelphia, PA, USA), Apr. 26-29 2004.

[11] A. Alù and N. Engheta, "Polarizabilities and effective parameters for collections of spherical nano-particles formed by pairs of concentric double-negative (DNG), single-negative (SNG) and/or double-positive (DPS) metamaterial layers," *J. Appl. Phys*, vol. 97, pp. 094310/1–12, Apr. 2005.

[12] A. Alù, N. Engheta, and R. W. Ziolkowski, "FDTD simulation of tunneling and "growing exponential" in a pair of epsilon-negative and mu-negative slabs," in *USNC-URSI Nat. Radio Science Meeting Dig.*, (Monterey, CA), p. 18, Jun. 20-26 2004.

[13] S. Arslanagic and O. Breinbjerg, "Electric-line-source illumination of a circular cylinder of lossless double-negative material: an investigation of near field, directivity, and radiation resistance," *IEEE Antennas Propagat. Mag.*, vol. 48, pp. 38–54, June 2006.

[14] S. Arslanagic, R. W. Ziolkowski, and O. Breinbjerg, "Excitation of an electrically small metamaterial-coated cylinder by an arbitrarily located line

source," *Microwave and Optical Technology Letters*, vol. 48, pp. 2598–2606, Dec. 2006.

[15] R. W. Ziolkowski and A. D. Kipple, "Application of double negative materials to increase the power radiated by electrically small antennas," *IEEE Trans. Antennas Propagat.*, vol. 51, pp. 2626–2640, Oct. 2003.

[16] A. Erentok and R. W. Ziolkowski, "Efficient electrically small antenna design using an electric dipole in a multi-layered ENG metamaterial shell," in *Int. Workshop on Antenna Technology: Small Antennas and Novel Metamaterials*, (White Plains, New York), pp. 400–403, March 6-8 2006.

[17] R. W. Ziolkowski and A. Erentok, "Metamaterial-based efficient electrically small antennas," *IEEE Trans. Antennas Propagat.*, vol. 54, pp. 2113–2130, July 2006.

[18] D. R. Smith, D. C. Vier, N. Krol, and S. Schultz, "Direct calculation of permeability and permittivity for a left-handed metamaterial," *Appl. Phys. Lett.*, vol. 77, pp. 2246–2248, Oct. 2000.

[19] D. R. Smith and J. B. Pendry, "Homogenization of metamaterials by field averaging," *J. Opt. Soc. Am. B*, vol. 23, pp. 391–403, Mar. 2006.

[20] D. R. Smith, S. Shultz, P. Markos, and C. M. Soukoulis, "Determination of effective permittivity and permeability of metamaterials from reflection and transmission coefficients," *Phys. Rev. B*, vol. 65, p. 195104, 2002.

[21] D. R. Smith, D. C. Vier, T. Koschny, and C. M. Soukoulis, "Electromagnetic parameter retrieval from inhomogeneous metamaterials," *Phys. Rev. E*, vol. 71, p. 036617, 2005.

[22] T. Koschny, M. Kafesaki, E. N. Economou, and C. M. Soukoulis, "Effective medium theory of left-handed materials," *Phys. Rev. Lett*, vol. 93, p. 107402, 2004.

[23] J. B. Pendry, "Negative refraction makes a perfect lens," *Phys. Rev. Lett.*, vol. 85, pp. 3966–3969, Oct. 2000.

[24] P. M. Valanju, R. M. Walser, and A. P. Valanju, "Wave refraction in negative-index media: Always positive and very inhomogeneous," *Phys. Rev. Lett.*, vol. 88, p. 187401, Apr 2002.

[25] R. W. Ziolkowski and E. Heyman, "Wave propagation in media having negative permittivity and permeability," *Phys. Rev. E*, vol. 64, pp. 056625/1–15, Nov. 2001.

[26] D. R. Smith and N. Kroll, "Negative refractive index in left-handed materials," *Phys. Rev. Lett.*, vol. 85, pp. 2933–2936, Oct. 2000.

[27] C. A. Balanis, *Advanced Engineering Electromagnetics*. New York: Wiley, 1989.

[28] R. F. Harrington, *Time-Harmonic Electromagnetic Fields*. New York: McGraw-Hill, 1961.

[29] J. R. Wait, *Electromagnetic Radiation from Cylindrical Structures*. London: Peter Peregrinus Ltd., 1988.

[30] R. W. Ziolkowski, "Design, fabrication and testing of double negative metamaterials," *IEEE Trans. Antennas Propagat.*, vol. 65, pp. 1516–1529, July 2003.

[31] N. Kinayman and M. I. Aksun, *Modern Microwave Circuits*. Artech House, Norwood, MA, 2005.

[32] Y. Hua and T. K. Sarkar, "Generalized pencil-of-function method for extracting poles of an em system from its transient response," *IEEE Trans. Antennas Propagat.*, vol. 37, pp. 229–234, Feb. 1989.

[33] Çağatay Tokgöz, "Derivation of closed-form Green's functions for cylindrically stratified media," Master's thesis, Middle East Technical University, 1997.

[34] S. Maci, M. Caiazzo, A. Cucini, and M. Casaletti, "A pole-zero matching method for ebg surfaces composed of a dipole fss printed on a grounded dielectric slab," *IEEE Trans. Antennas Propagat.*, vol. 53, pp. 70–81, Jan. 2005.

[35] N. Engheta and R. W. Ziolkowski, "A positive future for double-negative metamaterials," vol. 53, pp. 1535–1556, Apr. 2005.

[36] X. S. Rao and C. K. Ong, "Amplification of evanescent waves in a lossy left-handed material slab," *Phys. Rev. B, Condens. Matter*, vol. 68, no. 11. Paper 113103.

[37] C. Caloz and T. Itoh, "Array factor approach of leaky-wave antennas and application to 1-d/2-d composite right/left-handed (crlh) structures," vol. 14, pp. 274–276, June 2004.

[38] A. P. Feresidis, G. Apostolopoulos, N. Serfas, and J. C. Vardaxoglou, "Closely coupled metallodielectric electromagnetic band-gap structures formed by double-layer dipole and tripole arrays," *IEEE Trans. Antennas Propagat.*, vol. 52, pp. 1149–1158, May 2004.

[39] A. D. Boardman, P. Egan, L. Velasco, and N. King, "Control of planar nonlinear guided waves and spatial solitons with a left-handed medium," *J. Opt. A: Pure Appl. Opt.*, vol. 7, pp. 57–67, Jan. 2005.

[40] S. Maci, M. Casaletti, M. Caiazzo, and A. Cucini, "Dispersion analysis of printed periodic structures by using a pole-zero network synthesis," in *17th International Conference on Applied Electromagnetics and Communications, ICECom 2003*, (Dubrovnik, Croatia), pp. 300–303, Oct. 2003.

[41] S. Maci, M. Camletti, M. Caiazzo, and C. Boffa, "Dispersion properties of periodic grounded structures via equivalent network synthesis," in *IEEE Antennas and Propagation Society International Symposium, 2003*, vol. 1, pp. 493–496, June 2003.

[42] D. Artigas and L. Torner, "Dyakonov surface waves in photonic metamaterials," *Phys. Rev. Lett.*, vol. 94, Jan. 2005. Paper 013901.

[43] P. Baccarelli, P. Burghignoli, F. Frezza, A. Galli, P. Lampariello, G. Lovat, and S. Paulotto, "Effects of leaky-wave propagation in metamaterial grounded slabs excited by a dipole source," vol. 53, pp. 32–44, Jan. 2005.

[44] Y. Guo, G. Goussetis, A. P. Feresidis, and J. C. Vardaxoglou, "Efficient modeling of novel uniplanar left-handed metamaterials," vol. 53, pp. 1462–1468, Apr. 2005.

[45] F. D. M. Haldane, "Electromagnetic Surface Modes at Interfaces with Negative Refractive Index make a "Not-Quite-Perfect" Lens," *ArXiv Condensed Matter e-prints*, June 2002.

[46] C. Caloz, C. J. Lee, D. R. Smith, J. B. Pendry, and T. Itoh, "Existence and properties of microwave surface plasmons at the interface between a right-handed and a left-handed media," in *IEEE Antennas and Propagation Society International Symposium, 2004*, vol. 3, pp. 3151–3154, June 2004.

[47] R. Ruppin, "Extinction properties of a sphere with negative permittivity and permeability," *Solid State Commun.*, vol. 116, pp. 411–415, Aug. 2000.

[48] P. Baccarelli, P. Burghignoli, F. Frezza, A. Galli, P. Lampariello, G. Lovat, and S. Paulotto, "Fundamental modal properties of surface waves on metamaterial grounded slabs," vol. 53, pp. 1431–1442, Apr. 2005.

[49] F. Capolino, D. R. Jackson, and D. R. Wilton, "Fundamental properties of the field at the interface between air and a periodic artificial material excited

by a line source," *IEEE Trans. Antennas Propagat.*, vol. 53, pp. 91–99, Jan. 2005.

[50] K. Y. Kim, *Guided and Leaky Modes of Circular Open Electromagnetic Waveguides Dielectric, Plasma, and Metamaterial Columns.* PhD thesis, The Graduate School, Kyungpook National University, Dec. 2004.

[51] R. S. Kshetrimayum and L. Zhu, "Guided-wave characteristics of waveguide based periodic structures loaded with various fss strip layers," *IEEE Trans. Antennas Propagat.*, vol. 53, pp. 120–124, Jan. 2005.

[52] A. Alu, F. Bilotti, N. Engheta, and L. Vegni, "How metamaterials may significantly affect the wave transmission through a sub-wavelength hole in a flat perfectly conducting screen," in *IEE Workshop on Metamaterials for Microwave and (Sub)millimetre Wave Applications: Photonic Bandgap and Double Negative Designs, Components and Experiments*, (London, UK), Nov. 2003.

[53] X. Yina, L. Hesselink, Z. Liu, N. Fang, and X. Zhang, "Large positive and negative lateral optical beam displacements due to surface plasmon resonance," *Appl. Phys. Lett.*, vol. 85, pp. 372–374, July 2004.

[54] C. Caloz, S. Lim, C. Allen, and T. Itoh, "Leakage phenomena from negative refractive index structures," in *URSI Int. Electromagnetic Theory Symp.*, (Pisa, Italy), May 2004.

[55] A. A. Oliner and D. R. Jackson, "Leaky surface-plasmon theory for dramatically enhanced transmission through a subwavelength aperture, part i: Basic features," in *IEEE Antennas and Propagation Society International Symposium, 2003*, vol. 2, pp. 1091–1094, Aug. 2003.

[56] C. A. Allen, C. Caloz, and T. Itoh, "Leaky-waves in a metamaterial-based two-dimensional structure for a conical beam antenna application,"

in *Microwave Symposium Digest, 2004 IEEE MTT-S International*, vol. 1, pp. 305–308, June 2004.

[57] A. K. Iyer and G. V. Eleftheriades, "Leaky-wave radiation from planar negative-refractive-index transmission-line metamaterials," in *IEEE Antennas and Propagation Society International Symposium, 2004*, vol. 2, pp. 1411– 1414, June 2004.

[58] A. Alu, F. Bilotti, N. Engheta, and L. Vegni, "Metamaterial covers over a small aperture." Submitted to *IEEE Trans. Antennas Propagat.* under review.

[59] A. J. Viitanen and S. A. Tretyakov, "Metawaveguides formed by arrays of small resonant particles over a ground plane," *J. Opt. A: Pure Appl. Opt.*, vol. 7, pp. 133–140, Jan. 2005.

[60] P. Baccarelli, P. Burghignoli, F. Frezza, A. Galli, P. Lampariello, G. Lovat, and S. Paulotto, "Modal properties of surface and leaky waves propagating at arbitrary angles along a metal strip grating on a grounded slab," *IEEE Trans. Antennas Propagat.*, vol. 53, pp. 36–46, Jan. 2005.

[61] P. Baccarelli, P. Burghignoli, F. Frezza, A. Galli, P. Lampariello, G. Lovat, and S. Paulotto, "New dispersion characteristics and surface-wave suppression in double-negative metamaterial grounded slabs," in *URSI Int. Electromagnetic Theory Symp.*, (Pisa, Italy), pp. 379–381, May 2004.

[62] I. V. Shadrivov, A. A. Sukhorukov, Y. S. Kivshar, A. A. Zharov, A. D. Boardman, and P. Egan, "Nonlinear surface waves in left-handed materials," *Phys. Rev. E*, vol. 69, Jan. 2004. Paper 016617.

[63] P. Baccarelli, P. Burghignoli, F. Frezza, A. Galli, G. Lovat, and S. Paulotto, "Novel analytical representations of the continuous-spectrum current in multilayer stripline structures," vol. 47, pp. 17–27, Feb. 2005.

[64] A. Alu and N. Engheta, "Pairing an epsilon-negative slab with a mu-negative slab: Resonance, tunneling and transparency," *IEEE Trans. Antennas Propagat.*, vol. 51, pp. 2558–2571, Oct. 2003.

[65] S. A. Ramakrishna, "Physics of negative refractive index materials," *Rep. Prog. Phys.*, vol. 68, pp. 449–521, Jan. 2005.

[66] T. Itoh, "Invited paper: Prospects for metamaterials," *Electron. Lett.*, vol. 40, pp. 972–973, Aug. 2004.

[67] M. Beruete, M. Sorolla, I. Campillo, and J. S. Dolado, "Subwavelength slotted corrugated plate with enhanced quasioptical millimeter wave transmission," vol. 15, pp. 286–288, Apr. 2005.

[68] R. Ruppin, "Surface polaritons and extinction properties of a left-handed material cylinder," *J. Phys.: Condens. Matter*, vol. 16, pp. 5991–5998, Aug. 2004.

[69] C. J. Tang and L. Gao, "Surface polaritons and imaging properties of a multi-layer structure containing negative-refractive-index materials," *J. Phys.: Condens. Matter*, vol. 16, pp. 4743–4751, June 2004.

[70] R. Ruppin, "Surface polaritons of a left-handed material slab," *J. Phys.: Condens. Matter*, vol. 13, pp. 1811–1819, Jan. 2001.

[71] R. Ruppin, "Surface polaritons of a left-handed medium," *Phys. Rev. A*, vol. 277, pp. 61–64, Oct. 2000.

[72] I. V. Shadrivov, A. A. Sukhorukov, Y. S. Kivshar, A. D. Boardman, and A. A. Zharov, "Surface polaritons of nonlinear left-handed materials," in *Quantum Electronics Conference, 2003*, p. 55, June 2003.

[73] S. Ancey, Y. Decanini, A. Folacci, and P. Gabrielli, "Surface polaritons on left-handed cylinders: A complex angular momentum analysis," *Phys. Rev. B*, vol. 72, Aug.

[74] P. Baccarelli, P. Burghignoli, G. Lovat, and S. Paulotto, "Surface-wave suppression in a double-negative metamaterial grounded slab," vol. 2, pp. 269–272, 2003.

[75] P. Baccarelli, P. Burghignoli, F. Frezza, A. Galli, P. Lampariello, G. Lovat, and S. Paulotto, "The nature of radiation from leaky waves on single- and double-negative metamaterial grounded slabs," in *Microwave Symposium Digest, 2004 IEEE MTT-S International*, vol. 1, pp. 309–312, June 2004.

[76] P. Baccarelli, P. Burghignoli, F. Frezza, A. Galli, G. Lovat, and D. R. Jackson, "Uniform analytical representation of the continuous spectrum excited by dipole sources in a multilayer dielectric structure through weighted cylindrical leaky waves," *IEEE Trans. Antennas Propagat.*, vol. 52, pp. 653–665, Mar. 2004.

[77] G. Gomez-Santos, "Universal features of the time evolution of evanescent modes in a left-handed perfect lens," *Phys. Rev. Lett.*, vol. 90, Feb. 2003. Paper 077401.

[78] P. R. Haddad and D. M. Pozar, "Anomalous mutual coupling between microstrip antennas," *IEEE Trans. Antennas Propagat.*, vol. 42, pp. 1545–1549, Nov. 1994.

[79] D. M. Pozar, *Microwave Engineering*. Wiley, New York, 1998.

[80] M. Abramowitz and I. A. Stegun, *Handbook of Mathematical Functions with Formulas, Graphs, and Mathematical Tables*. New York: Dover, 1964.